INVESTIGATING ACTIVE GALACTIC NUCLEI WITH LOW FREQUENCY RADIO OBSERVATIONS

by

MATTHEW LAZELL

A thesis submitted to
The University of Birmingham
for the degree of
DOCTOR OF PHILOSOPHY

School of Physics & Astronomy
College of Engineering and Physical Sciences
The University of Birmingham
March 2015

Abstract

Low frequency radio astronomy allows us to look at some of the fainter and older synchrotron emission from the relativistic plasma associated with active galactic nuclei in galaxies and clusters. In this thesis, we use the Giant Metrewave Radio Telescope to explore the impact that active galactic nuclei have on their surroundings. We present deep, high quality, 150–610 MHz radio observations for a sample of fifteen predominantly cool-core galaxy clusters. We investigate a selection of these in detail, uncovering interesting radio features and using our multi-frequency data to derive various radio properties. For well-known clusters such as MS0735, our low noise images enable us to see in improved detail the radio lobes working against the intracluster medium, whilst deriving the energies and timescales of this event.

Our excellent field of view allowed us to explore the point-source like radio AGN for a subsample of our clusters. We used additional optical and infra-red data to identify cluster members, remove radio contamination from star forming galaxies, and thus investigate the energetics of the many cluster galaxies. We find that low mass radio-loud AGN can easily quench the star formation at their core, and possibly enough to eject the gas from the system given some assumptions. We compare our observations with the results of cosmological hydrodynamical simulations (cosmo-OWLS), and explore the mechanical and binding energy levels over a large range of galaxy masses.

We look at the radio powers of our sample and compare these to the published X-ray cavity powers. We find an improved relation from our integrated luminosities, allowing a more accurate estimation of jet powers when X-ray or radio observations are unavailable. The question of what radio jets are made of is still an unknown variable in AGN physics today. Our observations rule out a relativistic electron/positron plasma, we find that a heavier solution is required. Our deepest low-frequency radio observations of these well-known clusters will yield valuable information about the nature of feedback when combined with X-ray observations of comparable depth. We present results from such combined work in this thesis.

Acknowledgements

Family

Friends

Dr. Somak Raychaudhury

Prof. Trevor Ponman

Dr. Ian Stevens

Prof. Matt Jarvis

David Stops

Dr. Ian McCarthy

Dr. Chris Haines

Dr. Ishwara Chandra

Dr. Ewan O'Sullivan, Dr. Alastair Sanderson, Dr. Samuel George

Contents

List of Figures

List of Tables

Chapter 1

Radio galaxies in clusters

1.1 What causes radio emission?

There are many processes in the Universe that can emit radiation in the radio frequency. Every object emits thermal radiation. The Rayleigh-Jeans Law is a well known approximation that can give the flux density in the radio band for a thermal source. It is the limit of the Planck law when $h\nu \ll kT$. This is easily satisfied in the radio regime for generally encountered astrophysical temperatures.

$$S = (2kT/\lambda^2)d\Omega \tag{1.1}$$

S is the source flux density, λ is the observed wavelength, k is Boltzmann's constant, Ω is the solid angle of the emission, and T is the temperature.

As λ is so large at the radio end of the electromagnetic spectrum, the resulting flux densities are very small. This may lead you to conclude that the radio sky is not very interesting to observe. Observations show that in many cases, flux densities increase as you go to longer wavelengths. This is opposite to what is expected observing thermal radiation only. However, thermal radiation is not the only process that will result in radio emission. A significant part is from non-thermal emission, mainly synchrotron radiation, due to relativistic charged particles accelerating through a magnetic field.

1.1.1 Synchrotron radiation

When a particle is accelerated, it emits electromagnetic radiation. Take first the case of an energetic particle moving at a non-relativistic velocity. When in the vicinity of a magnetic field it spirals around it rather than travelling across it. The acceleration in this case is its centripetal acceleration. The frequency in which it spirals will be dependent on the initial velocity of the particle, and secondly on the strength of the magnetic field. The polarisation of the radiation is perpendicular to that of the magnetic field, where the radiation is emitted in a narrow cone towards the direction of motion. The observed spectrum of synchrotron emission arises from combining the individual emission spectrum from each particle, which is typically an electron. This emits radiation as it spirals within the magnetic field, with a range of frequencies peaking at ν_c, the critical frequency.[1] This peak will move towards longer wavelengths as the electron continues to lose energy spiralling in the magnetic field. Summing these individual electron spectra will give a characteristic spectrum for synchrotron emission. An ensemble of electrons radiating with frequencies ν to $\nu + d\nu$, has energies in the range E to $E + dE$. We can assume this to have a power law of $N(E)\,dE = CE^{-p}\,dE$, with p the power law index; observations of broad-band radio spectra show evidence of having a power-law form. A power law distribution of relativistic electrons will give a synchrotron spectrum where flux decreases with frequency as a power law:

$$S(\nu) \propto \nu^{\alpha} \tag{1.2}$$

where α is the spectral index for the object, and $\alpha = (1 - p)/2$.

These spectra usually 'turn-over', or be curved, at low and high frequencies, this is discussed further below. The addition of any thermal contributions will also cause a spectral curvature at higher frequencies (e.g. Condon, 1992).

The synchrotron spectrum of an isolated electron has a (logarithmic) slope of

$$\frac{d\log P(\nu)}{d\log\nu} \sim \frac{1}{3} \tag{1.3}$$

---

[1] e.g. `http://astronomy.swin.edu.au/cosmos/s/synchrotron+emission`

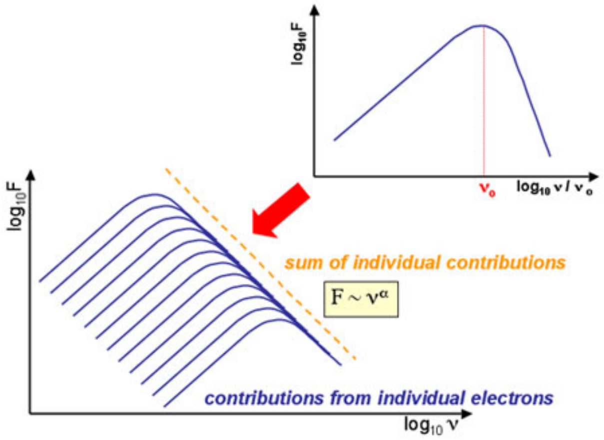

Figure 1.1: Summing the synchrotron spectra for each individual electron gives a characteristic spectrum with $S(\nu) \propto \nu^{\alpha}$. Image from Swinburne Astronomy Online.[1]

at low frequencies, falling off sharply at the high frequency end.[1] The frequency at which the emission peaks is the critical frequency $\nu_c \sim E^2 B_{\perp}$. An optically thin plasma has a low-frequency radio spectrum that is the superposition of the spectra from a population of single electrons, and so the (logarithmic) slope of its spectrum has to be shallower than or equal to $1/3$. At the high end, this slope is found to be ~ 0.7 for many astronomical sources.

Synchrotron radiative timescales

The power radiated by a synchrotron electron can be written as follows, by transforming the Larmor formula from restframe of the electron into that of the observer, where the electron is moving relativistically:

$$P_{\text{rad}} = \frac{4}{3} \sigma_T \, c \, U_{\text{mag}} \left(\frac{v}{c}\right)^2 \gamma^2 \tag{1.4}$$

where σ_T is the Thomson cross-section, γ is the Lorentz factor and $U_{\text{mag}} = \dfrac{B^2}{\mu_0}$ is the magnetic energy density in the observer's frame. If we assume that the relativistic electrons only lose energy by synchrotron radiation, then $-\dfrac{dE}{dt} \propto B^2 E^2$ (e.g. Longair, 2008). From this, we can see that in a population of electrons with a distribution of energies $N(E)$, it is the higher energy electrons that will radiate away their energy first. The high-frequency cutoff is due to this; above a certain frequency there will be no high-energy electrons left to radiate, as the only

---

[1] `http://www.cv.nrao.edu/course/astr534/SynchrotronSpectrum.html`

electrons that remain have synchrotron lifetimes that are longer than the time since they were accelerated. This can be seen in powerful radio sources, such as FR-IIs (see §1.2.2). If we make the assumption that the last location where the plasma was accelerated was at the hotspot, we will be able to see this 'break' frequency decreasing as we observe the older plasma in the radio lobes. §4.2 will look at this in more detail using actual radio observations.

1.1.2 What causes radio emission in galaxies?

Radio emission from galaxies can be caused by a variety of extragalactic objects. Condon (1992) has a review of the radio emission from normal galaxies, which we will briefly summarise.

Radio supernovae are one potential source of radio emission. Synchrotron radiation is emitted from the ultra-relativistic electrons accelerated at the expanding supernova shock. The origin of the magnetic field needed is not well understood, but believed to be from the progenitor star wind (Mioduszewski et al., 2001). These sources are quite short-lived; the compact sources disappear on the order of months after first being observed (typically following type II or type Ib supernovae).

Supernova remnants on the other hand remain visible at radio frequencies for thousands of years. The radio luminosity is proportional to the kinetic energy of the supernova, which supplies energy to the cosmic ray electrons in the shocked ISM (Thompson et al., 2009). The cause of these supernova remnants is the main reason for radio emission in normal galaxies. Massive stars of at least $\sim 8\,\mathrm{M}_\odot$ produce the supernovae, but also ionise the H ɪɪ regions around them. This free-free emission has a very flat spectral index, but corresponds well to far-infrared observations. The non-thermal synchrotron emission is dominant at lower frequencies, and it is the electrons that radiate whilst spiralling through the interstellar medium magnetic fields that trace the supernova rate, from which the star formation rate can be derived.

1.2 Active galactic nuclei

The centre of the galaxy is usually the dominant component of radio emission in a galaxy. The active galactic nucleus (AGN) is the compact region at the centre of a galaxy that has a high luminosity over the electromagnetic spectrum. The radiation from the AGN is from the release of gravitational potential energy as matter is accreted onto the supermassive black hole (SMBH) at the centre of the host galaxy.

Radio galaxies are AGN that are very luminous at radio wavelengths. The radio emission is from synchrotron radiation described in the above section. We can tell this due to the broadband nature of the spectrum and its high degree of polarisation.

1.2.1 Basic model of extragalactic radio sources

The jet-powered radio source model has been improved upon over the years, but the basic model by Scheuer (1974) remains the same. Within or near the AGN, cold, highly collimated, high velocity flows are formed. These propagate without much dissipation until they reach the ends of the radio lobes, where they shock and terminate. The majority of the kinetic energy in the bulk flow of the jet is then converted into relativistic electrons where the jet meet the ambient medium (Kellermann and Owen, 1988). The momentum of the jet moves the hot spots forward into the surrounding medium, and the lobes grow in size and luminosity (Carilli et al., 1991).

1.2.2 Radio source structures

Radio sources are observed having many similar features; some more prominent than others. Here is a brief list to summarise the different source structures.

- Cores: The radio core is associated with the powerful source at the nucleus of the active galaxy, from which the jets emerge. It has a compact, flat spectrum. At lower frequencies, the shape of the synchrotron spectrum cuts off, due to a process called synchrotron self-absorption. This is because the radiation at that frequency is not being observed by a distant observer, instead it is interacting with one of the synchrotron electrons. This scattering can occur many times before the photon can leave the source, resulting in the material becoming ‘optically-thick’. The self-absorption cross-section is greater at low frequencies, so one can only observe a thin shell from which the photons can escape. Moving to higher frequencies allows photons from deeper within the source to be observed, and therefore this results in the flat spectrum seen at the core (e.g. Athreya et al., 1997; Mościbrodzka and Falcke, 2013, and references within).

- Jets: Jets are the structures linking the core to the hotspots. Jets are defined by Bridle and Perley (1984) as being at least four times long as wide, separable from extended structure by observations, and aligned with a radio core. At high resolution, they can be discerned from the radio lobe by brightness contrast or spatially. The jets trace the path of a collimated flow, carrying energetic particles from the central engine out into the lobes. The jets trap and confine the twisted magnetic field within the plasma. The composition of these jets is still unknown. Due to charge neutrality, the jets must either have positrons or protons in addition to relativistic electrons. The ratio of energy carried by heavy particles to electrons is also an unknown factor, we explore this more in Chapter 4.

- Lobes: Lobes are the extended regions of radio emitting plasma. They usually appear either side of the AGN, and often are very large when present, some being up to megaparsecs in size. Lobes can come in different morphologies; there are some common terms to use when describing them. Plumes are mostly found in less luminous sources, these are usually quite elongated and fade gradually with distance from the galaxy. Tails occur when the lobe interacts with an external medium and is deflected back, giving a definite elongated structure. An example can be seen in §5.8.1. There are also bridges and haloes which contain older plasma and look like their namesakes.

- Hotspots: These are high luminosity components at the edge of the lobes, where the jet meets the intergalactic medium. This creates a strong shock and converts the kinetic energy of the jet into the relativistic particles we observe.

Radio sources can usually be described as either core-dominated or lobe-dominated.

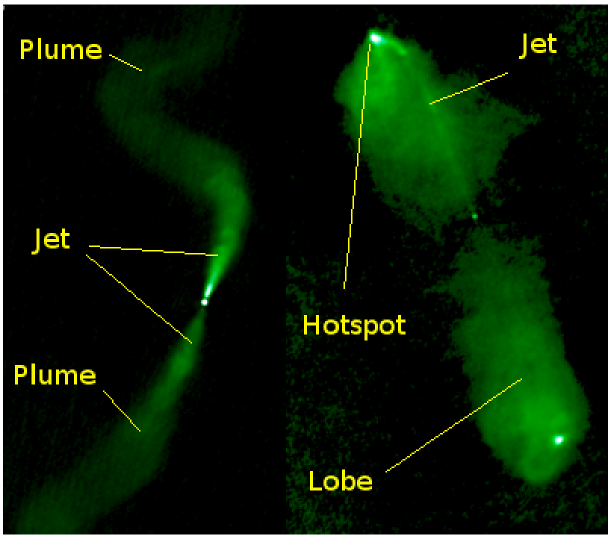

Figure 1.2: 3C31 on the left is classified as an FR-I source, and 3C98 (right) is a FR-II source.

Fanaroff-Riley classification

Most extended radio sources can be classified as one of two types, first identified by Fanaroff and Riley (1974).

- FR I: These generally are lower luminosity, with bright jets in centre, the sources become fainter toward the outer edges of the lobes. Spectra there are steepest, indicating that the radiating particles have aged the most.
- FR II: Have a higher luminosity, large scale structure that is edge-brightened, and with bright outer hotspots. Possess faint jets and appear to transport energy more efficiently to the end of the lobes, whereas FR I jets radiate significant amount of energy away as they travel.

1.3 Galaxy formation and evolution

It is emerging from multiwavelength studies of galaxies, that AGN play a crucial role in the formation and evolution of galaxies in a variety of environments. An important aspect of understanding the contribution of AGN is to study how black holes grow in the centres of galaxies, and to study the flow of mass and energy connected with SMBHs.

1.3.1 Estimating black hole masses

There are multiple methods used to derive the mass of a black hole. These will be briefly covered below.

Stellar dynamics: The primary method is to use dynamical evidence from the motions of stars nearby to the black hole. This requires the ability to track their paths over an extended period of time, in order to ascertain the mass of the object they are orbiting. The construction of the *Hubble Space Telescope* enhanced our ability to find more black holes due to its higher spatial resolution. However, in more distant galaxies it is not possible to resolve the individual orbits of each star near the black hole. Recent techniques use the luminosity-weighted line-of-sight velocity distribution, building on methods such as the orbit superposition method of Schwarzschild (1979) to determine constraints on the black hole mass and stellar mass-to-light ratios (Onken et al., 2014). Kormendy and Ho (2013) has further reading material.

The supermassive black hole at the heart of our own Milky Way galaxy is a special case of the stellar dynamics method. This area can be completely resolved, and along with the short orbital periods means that we can carefully track the individual orbits of the stars in the galactic centre, see Figure 1.3. From this, a mass of $\sim 4 \times 10^6\ \mathrm{M}_\odot$ is calculated for the object known in the radio spectrum as Sagittarius A* (Ghez et al., 2008; Gillessen et al., 2009).

Gas dynamics: This involves observing the emission lines from the nuclear gas disc and measuring their equivalent widths, and thus velocities and velocity dispersions. A model of the gravitational potential is computed consisting of the stellar distribution and the central mass source. This central mass (the black hole) is a free parameter, which is varied to best fit the data (Barth, 2004). There are, however, some potential drawbacks to this method. One assumption at the core of using gas dynamics is that the gas is mostly affected by the gravitational pull of the black hole. Non-gravitational forces, such as magnetic fields, turbulence and shocks, will lead to non-Keplerian orbits that complicate the models needed to represent the black hole mass.

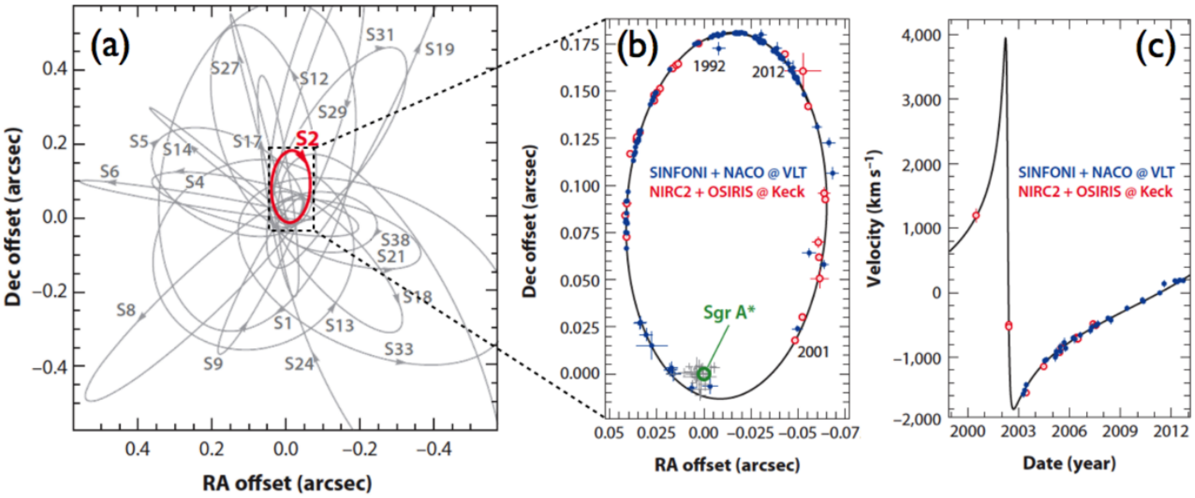

Figure 1.3: a) The orbits of a number of stars near the galactic centre. b) A closer look at the star labelled S2, shown over a 20 yr period. It has an orbital period of ∼15 yr (Gillessen et al., 2009), with the pericentre occurring near the location of Sagittarius A*. Images adapted from Kormendy and Ho (2013).

Reverberation mapping: The technique of reverberation mapping relies on the assumption that in active galaxies, the luminosity of the broad-line region (BLR) around a supermassive black hole varies as a result of changes in the brightness of the AGN continuum. These changes occur with a time delay, equal to the light travel time across the line-emitting region (Blandford and McKee, 1982; Peterson and Horne, 2004). This timescale is proportional to the AGN luminosity, and the observations needed typically last several months (Denney et al., 2010). Therefore, this technique has been predominantly used to measure lesser luminosity AGN at lower redshifts. High-luminosity quasars require prolonged observational periods and have to counter cosmological time dilation effects, because they are typically found at high redshifts (Kaspi et al., 2007).

If we assume the motion of the BLR is dominated by the gravity of the central black hole, the mass of the black hole can then be defined by:

$$M_{BH} = \frac{c\tau\,(\Delta V)^2 f}{G} \tag{1.5}$$

where M_{BH} is the black hole mass, $c\tau$ will give the radius of the broad-line region (τ is the lag time), ΔV is the BLR velocity dispersion and G is the gravitational constant. f is a scaling factor used to take into account the geometry and dynamics of the BLR; estimates of this coefficient range from 2.8 to 5.5 (Onken et al., 2014).

1.3.2 Black hole scaling relations

Relationships between the black holes and their host galaxies were derived empirically from observational data. Studies of galaxies in the local universe uncovered a strong relationship between the mass of a black hole (M_{BH}) and the luminosity of the host galaxy (Kormendy and Richstone, 1995; Magorrian et al., 1998). Magorrian et al. (1998) calculated a black hole mass to bulge mass ratio of 0.006. Their measurements of masses for the black holes relied on the dynamical methods described earlier, using photometry from *Hubble*, but ground-based kinematics. Results using other techniques found a ratio that was an order of magnitude smaller, so further work was needed.

The M_{BH}–σ relation: Further independent observations by Ferrarese and Merritt (2000) and Gebhardt et al. (2000) at the turn of the millennium resulted in two differing values for β in the following equation, where $M_{BH}$is the black hole mass and σ is the velocity dispersion of the host galaxy:

$$\log\left(\frac{M_{BH}}{M_{\odot}}\right) = \alpha + \beta \log\left(\frac{\sigma}{\sigma_0}\right) \tag{1.6}$$

Ferrarese and Merritt (2000) used a sample of 12 galaxies to derive $\beta = 4.8 \pm 0.5$, with measurements of the BH masses obtained predominantly from absorption-line stellar spectra or from the motion of the nuclear gas disks. Gebhardt et al. (2000) had a sample double the size, with black hole estimates from masers, gas kinematics, and stellar kinematics with three-integrals axisymmetric dynamical models. They found a slope of 3.75 ± 0.30.

Figure 1.4 shows the published log–log plots from both of these papers. What is remarkable is the very small scatter associated with each value, despite the range in black hole masses covering almost three orders of magnitude. These are quoted as being almost entire due to observation errors.

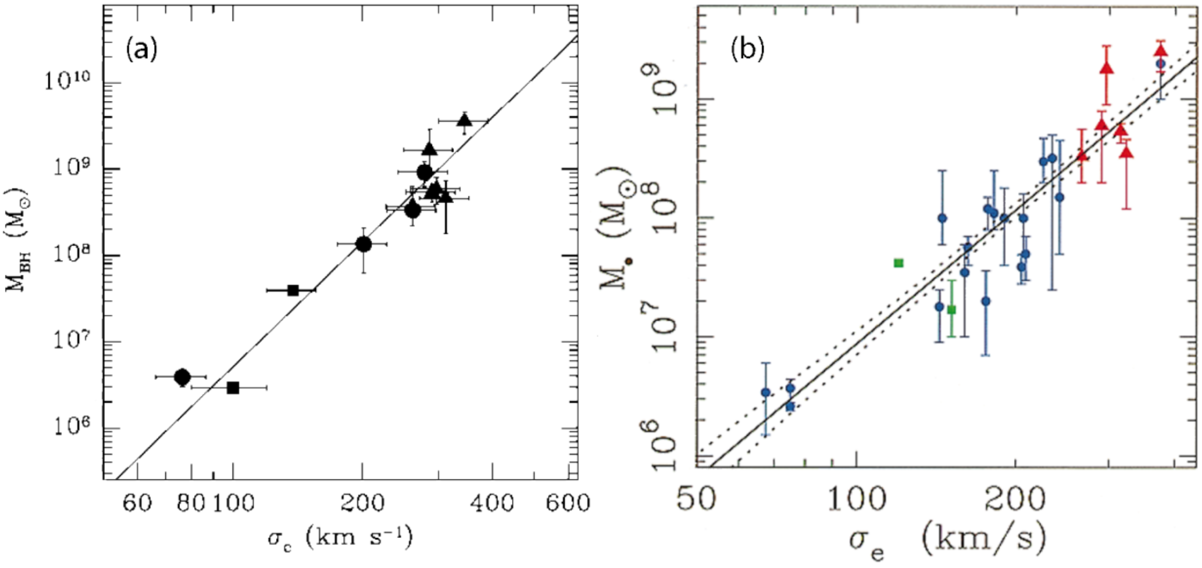

Figure 1.4: M–σ plots from Ferrarese and Merritt (2000) (left) and Gebhardt et al. (2000) (right). A strong correlation was found between the black hole mass and the velocity dispersion of the host galaxy. Whilst both have a small amount of scatter, there is a significant difference between the resulting gradients, quoted as 4.8 and 3.75 respectively.

There are a few potential reasons for the discrepancies in the gradients of these two works. Tremaine et al. (2002) suggest the main cause were the different methods used in calculating the velocity dispersion, which would lead to the slope being dependent on what measure was used. Other reasons include differing statistical techniques used to estimate the gradient, and potential biases introduced by varying resolutions of the black hole mass measurements. The most recent results by Kormendy and Ho (2013) find a slope of $\beta = 4.38 \pm 0.29$ with a scatter of 0.29 ± 0.02 dex.

The fact we find a close correlation between the black hole mass and velocity dispersion is important for a couple of reasons. Firstly, it allows us to make estimates of the black hole mass from easy to gather spectral observations. Secondly, it implies that the growth of black holes and galaxies are tightly linked.

Supermassive black holes at the centres of galaxies grow via the flow of gas from its parent galaxy, and also from minor mergers. This inflow has been observed within the inner kiloparsecs of nearby galaxies, from IFU (Integral Field Unit) studies of the cores of galaxies, mapping the Doppler velocities of emission lines such as $H\alpha$ and N II (e.g. Fathi et al., 2006; Schnorr-Müller et al., 2014). The mass inflow appears to be the major factor in the growth of SMBHs over time (e.g. Marconi et al., 2004), and AGN growth is seen to peak in comoving number density between redshift $z = 2{-}3$ (e.g. Brandt and Alexander, 2010). This growth is regulated by outflows, which are also directly detected in these velocity fields (e.g. Storchi-Bergmann et al., 2010). These inject energy into the surrounding medium, which loses their cold material through star formation and an efficient AGN feedback process (e.g. Dubois et al., 2012). We discuss the effect of AGN feedback on galaxy evolution below.

1.4 Clusters of galaxies

There have been various simulations which try to model and reproduce the structure in the Universe that we observe. One example is the Millennium simulation (Springel et al., 2005), which uses the cold dark matter (ΛCDM) model and cosmic inflation to show how the growth of mass fluctuations in the early Universe reproduce very large scale structures that are almost indistinguishable by eye. Alpaslan et al. (2014) used a two-point correlation function in their analysis to confirm that their mock galaxy catalogues, based on the simulation, reproduced the observed distribution of galaxies at large scales. These dark matter halos grow hierarchically, with the largest of these building up at the intersection of the large scale dark matter filaments.

The most significant constituent of galaxy clusters is dark matter. The baryonic component consists of the stars in the galaxies ($\sim$ 1%) and the hot intracluster gas between them ($\sim$ 10%). These can be observed over a wide range of wavelengths. We can estimate the masses of galaxy clusters using three different techniques. If we assume hydrostatic equilibrium, we can use the temperature of the intracluster gas from X-ray measurements to derive the total gravitating mass within it. Another technique is to use the velocity dispersion of the galaxies to find a dynamical mass estimate. We can also use gravitational lensing estimates, which have the advantage of not being subject to the previous assumption of hydrostatic equilibrium, but does require extensive modelling. A mixture of the above is normally used to constrain the masses of galaxy clusters. Typically, clusters have masses on the order of $10^{15}\,\mathrm{M}_{\odot}$ and are usually around a megaparsec in radius.

The Sunyaev-Zel'dovich effect

Another important physical effect in clusters of galaxies that has proved to be useful in cosmological applications is the Sunyaev-Zel'dovich effect (for a review, see Birkinshaw, 1999). Cosmic microwave background (CMB) photons, which are everywhere, stream to us along certain lines of sight, passing through clusters of galaxies. The hot plasma in the gravitational potential of the cluster contains highly energetic electrons, which interact with the CMB photons. These, due to the inverse Compton effect, gain energy from the electrons. This causes a depletion of lower energy CMB photons and a corresponding gain in higher energy ones. This results in a reduced intensity of the CMB being measured at frequencies lower than 218 GHz.

The magnitude of the decrement depends on the mass of the cluster, and this method has been used to measure masses of clusters independently of the assumption of hydrostatic equilibrium that X-ray derived masses require. Since the X-ray emission (thermal bremsstrahlung) of the cluster depends on n_e^2, where n_e is the column density of electrons in a hot plasma along the line of sight, while the Sunyaev-Zel'dovich effect depends on the average n_e, the Sunyaev-Zel'dovich effect is sensitive to the clumpiness of the potential and produces a projected mass map of a cluster (e.g. Carlstrom et al., 2002). Since the effect is independent of redshift, it is also very useful is measuring masses of clusters at high redshift (e.g. Planck Collaboration et al., 2014).

1.4.1 Cool-cores and non-cool-cores

In the core of dense, relaxed galaxy clusters, the thermal gas generally has a cooling time that is shorter than the Hubble time (Fabian and Nulsen, 1977). The cooling time is the ratio between the thermal energy content and the energy loss rate for a gas component. This can be through radiative or conductive cooling. If there are no sources of heating, then this gas should cool as it radiates, and the cooling time will be inversely proportional to the density of the gas. As gas in cluster cores is more dense due to hydrostatic equilibrium, it will cool first compared to gas further away. As it cools it will lose pressure, so gas must flow in and form a “cooling flow” to maintain hydrostatic equilibrium (Fabian, 1994). The gas will accrete onto the central cluster galaxy, where it will form stars in dense molecular clouds within the cooling radius. These could reach a mass of up to $10^{12}\,M_{\odot}$ over the lifetime of the cluster.

However, X-ray observations of clusters from XMM-Newton grating observations have not shown the emission lines below 2 keV that would illustrate the presence of this cooling gas (Tamura et al., 2001; Peterson et al., 2001). There are a lack of Fe-L-shell lines (Fe xvii-xxiv), which are sensitive to the lower temperatures that should be expected from a cooling flow (Böhringer et al., 2002). The transition energy for these lines is related to the degree of ionisation of the Fe ions, which in turn is proportional to the temperature of the hot plasma. The absence of evidence of these lines suggests that the cooling rates are an order of magnitude less than first estimated (Fabian et al., 2001; McNamara and Nulsen, 2007). Observations at other wavelengths have also not found evidence for the large reservoirs of cold gas that should be seen at the centre of these cooling flow – or cool-core clusters as they are now termed. This, along with the lack of extreme star formation rates being found, is known as the 'cooling flow problem', and was a significant problem for models of galaxy formation and evolution (Silk, 1977; Rees and Ostriker, 1977).

Sanderson et al. (2009) separate cool-core and non-cool-clusters using X-ray observations and investigated the gas entropy profiles of the intracluster medium (ICM). They found a difference between the entropy profiles, demonstrating that there are two distinct cluster types. Figure 1.5 shows this split between them. We will divide our sample of clusters (see §4.1) into cool-core and non-cool-core using the standard method of comparing the temperature profiles as a function of radius (e.g. Sanderson et al., 2006).

1.4.2 AGN feedback

Simulations also struggled to replicate the basic properties that we see in real observed galaxies. Baryonic matter and the associated gas physics were included, but the simulations found too many faint and too many bright galaxies. They also predict that the largest galaxies in our Universe should be blue and star forming as opposed to the red, passive galaxies that are generally seen (Benson et al., 2003). This means that there must be some source of heating in

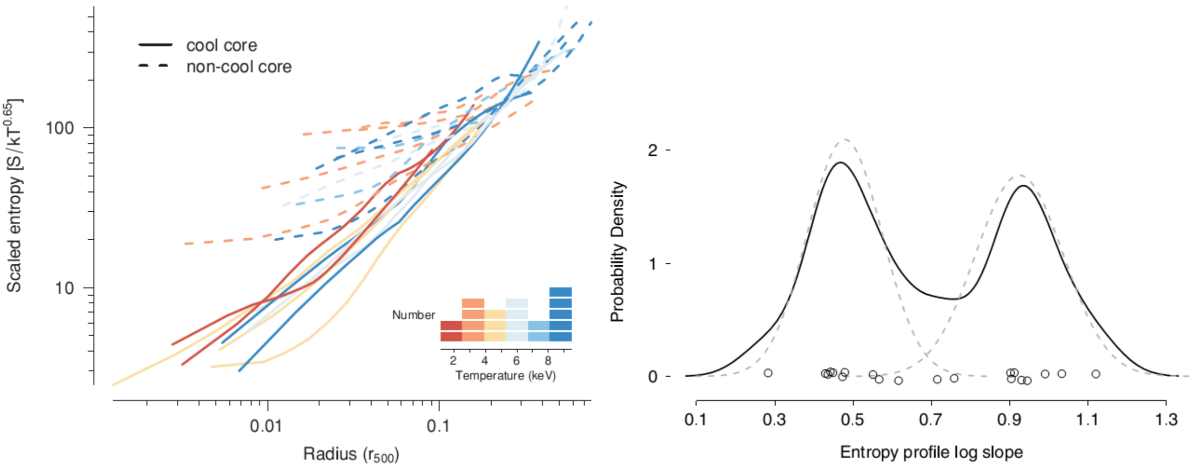

Figure 1.5: Clusters can be separated according to the presence or absence of a cool core. Left: Gas entropy profiles are plotted as a function of radius. The non-cool-clusters are found to have a significantly higher entropy level in the core, with the scatter in normalisation suggesting different heating mechanisms. Right: The bimodality of clusters is shown here as a function of entropy profile log slope. The clusters above the split of 0.7 are cool core clusters. Images from Sanderson et al. (2009).

the galaxy, as this extra energy would stop the gas being able to cool and form stars. With the star formation suppressed, the galaxy would then passively evolve over time, becoming redder in colour. There are several suggestions on what could cause the excess heating: gravitational heating, supernovae, galaxy mergers and thermal conduction. The most plausible and popular candidate though is 'AGN feedback'. This is the energy that is injected by relativistic jets from supermassive black holes at the centres of galaxy clusters into the intracluster medium.

A primary reason why AGN feedback is one of the favoured processes for feedback is observationally there are AGN found in many of the massive red galaxies, that do not appear in the previous simulations. These older simulations did not have a mechanism for feedback, which resulted in an excess of cool gas. This led to very large star forming galaxies at the centres of galaxy clusters with no major process for quenching star formation on timescales comparable to the cooling time; a result that is not backed up by observations. Observations with the *Chandra* X-ray telescope find a clear positive correlation between the presence of a cool core in a cluster and the central galaxy hosting a radio source (Mittal et al., 2009). This is consistent with the theory that the cool gas is fuelling the supermassive black hole in the centre of the galaxy, leading to an AGN radio outburst.

Chandra images of cool-core clusters have shown that in many cases, there are clear surface depressions visible in the X-ray band. These cavities are created by the interaction between the powerful radio source and the surrounding hot gas. The radio jets of the AGN displace the cluster atmosphere, leaving a surface brightness depression in X-ray images. Evidence for this is seen from the positions of the radio lobes appearing to match these depressions when they are overlaid. The cavities are lower density than their surroundings so they will rise buoyantly. Cavities are old enough to provide enough energy to suppress cooling in clusters.

It is important to note that this is theorised to be a feedback loop. The estimated power that is being injected into the cluster is the same magnitude as the X-ray luminosity. If the power were too little, then this would have little affect on the cluster so this problem would not exist. If the power were too much, the entropy would be raised and the cooling time would increase to the Hubble time, so the cool-cores would not develop. Cool-core clusters are observed in $> 50\%$ of the luminous X-ray cluster population below $z < 0.4$, so the cool-core must remain for a significant amount of time. Supernova feedback was once touted as a way to achieve the necessary energy input into the cluster, but has since been shown to fall orders of magnitude short (e.g. Voit and Donahue, 2005).

1.4.3 AGN feedback modes

The classical view of an AGN has cold gas being accreted onto a central supermassive black hole, via a radiatively efficient, geometrically thin, optically thick accretion disc (Shakura and Sunyaev, 1973). This emits radiation across a wide range of the electromagnetic spectrum, from ultra-violet to X-ray. Optical emission lines are sometimes observed when material near the black hole is photoionised, as seen in broad and narrow line regions. Unified models suggest that these emission lines can be obscured by a dusty torus structure between the black hole and the observer (Antonucci, 1993). This would result in the torus reradiating at infrared wavelengths, with the nuclear hard X-ray emission still being detectable (Hardcastle et al., 2007). For these typical features of an AGN to be observed, the accretion disc must be radiatively efficient – the energy released by the inspiralling gas is efficiently radiated away. This assumes that the accretion disc is optically thick and geometrically thin, from being flattened by rotation, as in the model of Shakura and Sunyaev (1973).

This model is sufficient when compared to observations of radio-quiet galaxies. The inclusion of radio jets into the unified model seems to be broadly consistent with radio-loud galaxy observations. There is, however, a population of radio galaxies where the strong, high excitation, narrow line optical emission lines that are expected from standard AGNs are absent. This dichotomy in the optical spectral properties of radio galaxies was first noted by Hine and Longair (1979) and expanded upon by Laing et al. (1994) among others. This difference cannot be consolidated with the unified AGN model as it is not due to the orientation or obscuration of the AGN. Buttiglione et al. (2010) used an optical sample of 113 3CR radio galaxies (with $z < 0.3$) to investigate the bimodality in the population of AGNs, separating them by a combination of spectral lines. Their 'excitation index' was defined as a function of four emission-line ratios:

$$EI = \log_{10}\left([O\,\textsc{iii}]/H\beta\right) - \frac{1}{3}\left[\log_{10}\left([N\,\textsc{ii}]/H\alpha\right) + \log_{10}\left([S\,\textsc{ii}]/H\alpha\right) + \log_{10}\left([O\,\textsc{i}]/H\alpha\right)\right] \quad (1.7)$$

An index value of 0.95 was used as the cut-off point between high and low excitation galaxies.

One of the main differences between these two types of galaxies is how efficiently they radiate. The current consensus is that these low-excitation radio galaxies (hereafter LERGs) have a radiatively *inefficient* accretion flow (hereafter RIAF), and so do not display the optical and X-ray signatures that the high-excitation radio galaxies (HERGs) do (e.g. Hardcastle et al., 2007). What could cause this lack of efficiency?

The standard model of an accretion disc has gas moving in a near-circular orbit around a central black hole. In order to accrete material, gas at large radii must lose angular momentum otherwise it cannot be captured by the gravitational centre (black hole). To conserve angular momentum, other gas must be transported outwards as a result of a loss of angular momentum. This occurs by a 'viscous' torque being applied; the mechanism causing this change of angular momentum is still unknown, but possibilities include magneticorotational instabilities (Balbus and Hawley, 1991), winds and other turbulent electromagnetic stresses (Shakura and Sunyaev, 1973; Krolik, 1999). These stresses result in the disc heating up, and the heat then being efficiently radiated away.

In the above thin disc case, the accretion rate needs to be high in order for the gas density to be sufficient to cool efficiently. An accretion rate of $0.01-1\,\dot{\mathrm{M}}_{\mathrm{Edd}}$, is generally thought to be the range for these AGN, where $M_{Edd} = L_{Edd}/\epsilon c^2$ or,

$$\dot{M}_{Edd} = GM\frac{4\pi m_p}{\sigma_T c} \tag{1.8}$$

where m_p is the mass of a proton, and σ_T is the Thomson cross-section.

When the mass accretion rate drops further ($\dot{M} \ll \dot{M}_{Edd}$), a lower gas density means the gas will be unable to radiate the gravitational potential energy released from accretion. The heating of the accretion disc is theorised to preferentially act on the ions, whereas electrons lose their energy via radiative losses, synchrotron radiation and Componization of low-energy photons (Fernandes et al., 2015). The protons in the gas are thus heated to high (virial) temperatures. Thermal equilibrium of the ions and electrons is hampered by the weak Coulomb coupling between the particles. This thermal timescale is inversely proportional to the ion density, which is directly related to the accretion flow rate. With a low mass accretion rate, the number density of ions drops. When this timescale is larger than the accretion timescale, a two-temperature plasma is predicted to form (e.g. Fernandes et al., 2015, and references therein). Without this two-temperature plasma assumption, the electrons would become highly relativistic and therefore would radiate efficiently, such as in the standard thin disc model (and consequently would drop in temperature).

One example of a radiatively inefficient accretion flow is known as an ‘accretion-dominated advection flow’ (hereafter ADAF: Narayan and Yi, 1995). As the name suggests, these flows are cooled by advection as heat is transported by the matter inwards towards the centre. As it is radiatively inefficient, the excess heat will cause the accretion disc to expand in thickness, becoming more quasi-spherical in shape. ADAFs are also much less luminous than the Shakura and Sunyaev (1973) model, due to the reduced radiation. Other radiatively inefficient solutions such as the 'adiabatic inflow–outflow solution' (ADIOS: Blandford and Begelman, 1999) and 'convection-domination accretion flow' (CDAF: Quataert and Gruzinov, 2000) have also been proposed (D'Angelo et al., 2014, and references therein).

It is generally accepted that the nature of the accreting gas determines the rate and type of accretion. Cold gas is theorised to be needed for the thin disc, radiatively efficient model (HERGs), whereas hotter gas accretion could result in the geometrically thick, advection dominated flow described above (LERGs) (e.g. Hardcastle et al., 2007).

This gives us a clue as to where these galaxies are typically found. The hot, X-ray emitting gas found at the centres of galaxy clusters is a prime candidate for the material needed for a LERG to form. Instead of radiating their gravitational energy, it is thought that the energy is being channelled into the radio jets (Mingo et al., 2014). Indeed, lower luminosity radio galaxies, such as FR-I class galaxies, are typically found to be LERGs (e.g. Buttiglione et al., 2010; Saripalli, 2012). This makes radio surveys an essential part of detecting these kind of galaxies, and this type of AGN activity is also known as 'radio-mode'. This mode of AGN activity is also known as 'radio-mode', compared to the emission line rich 'quasar-mode', which is associated with those objects.

HERGs on the other hand require a supply of cold gas in order to accrete efficiently. An excellent source of this cold material comes from galaxy interactions, e.g. galaxy mergers (Ramos Almeida et al., 2011, 2012, 2013, and references within). Ramos Almedia et al. concluded that the more powerful radio galaxies were elliptical galaxies that have recently undergone a merger or significant interaction, with the new cold gas substantial enough to trigger the AGN. HERGs are also more dominant at high redshift ($z > 1$), where the supply of cold gas is plentiful (e.g. Best et al., 2014). This is in line with the evolution of star formation in the Universe.

FR-I galaxies are almost always LERGs, but there is a substantial population of LERG FR-IIs as well in the nearby Universe ($z < 0.5$). HERGs on the other hand, are almost exclusively FR-IIs.

To summarise, spectroscopic studies in optical, radio and X-ray emission find a picture that suggests in radio-loud AGN, HERGs are fuelled at high rates by means of radiatively efficient accretion disks, fuelled by cold gas infalling from interactions with neighbours or mergers. LERGs instead result from radiatively inefficient flows, from hot gas associated with X-ray haloes surrounding massive galaxies, in groups or clusters, resulting from AGN feedback. The environmental basis of this dichotomy necessitates the use multi-wavelength observations, but it also means that the complex way in which the various contributing factors relate to each other gives rise to the wide diversity of modes of galaxy evolution we see today (e.g. Best and Heckman, 2012; Hardcastle et al., 2006).

1.4.4 Environmental effects

The cluster environment appears to play a role in the triggering of AGN activity. Both the mass of the supermassive black hole and the local environment of the host galaxy are important to AGN energetics (Alexander and Hickox, 2012). At higher redshifts, AGN activity is seen to be significantly higher in overdense regions compared to that of the field (e.g. Best, 2004; Heckman and Best, 2014). In more massive dark matter haloes, quiescent galaxies are found to host lower accretion rate radio-loud AGN. The quenching of colder gas in these massive dark matter haloes could be aided by large scale outflows high in mechanical energy, but which may not be bright in radiation.

The dependence on radio-loud AGN fraction with galaxy mass supports this picture (e.g. Alexander and Hickox, 2012, for a review). The brightest galaxies in groups and clusters are more likely to host powerful radio sources (Eilek and Owen, 2007, and many others) and even the satellite galaxies in group and cluster environments are more likely to be active in the X-rays (Martini et al., 2007) and possibly the radio (Best et al., 2007). These satellite galaxies could have a significant impact on the total energy balance of the ICM. A distributed population of AGNs could help answer the 'cooling flow' problem (Nusser et al., 2006) if the energy output from satellites needs to be at least comparable to the output of the central galaxy.

1.5 Sample selection

Our sample of galaxy clusters has been selected to include the known systems that host X-ray cavities that are able to be observed with the Giant Metrewave Radio Telescope (GMRT: see §2.4). This limits us to clusters with a redshift $z \lesssim 0.2$, except in cases where the cavities are exceptionally large (e.g. MS0735). The samples of Rafferty et al. (2006) and Bîrzan et al. (2008) are selected as a base for our selections. It is important to try and select a large and varied sample, so as to probe a range of radio and jet powers. We use the GMRT for its access to low frequencies and decent resolution. It has a typical resolution of ~5 arcsec at 610 MHz, which is one of the low frequencies that we will observe at. A 5 arcsec resolution will be able to detect radio emission on scales the order of ~15 kpc at a redshift of $z = 0.2$, approximately the radius of the Milky Way [1]. As well as being able to detect radio emission from individual galaxies at that redshift, we will be able to observe detailed structure of extended emission, with some radio lobes reaching linear sizes of megaparsecs (Machalski et al., 2008).

Not all clusters with cavities have associated radio emission ('ghost cavities'). When observed at lower frequencies, this emission becomes visible, as the loss of energy over time causes the electrons to radiate at low frequencies. We also investigate the composition of the radio lobes, where fluxes measured at low frequencies will help constrain the energy ratio of massive particles to electrons. Multiple frequencies are observed to enable the construction of spectral index maps, showing the interactions between the AGN and the ICM.

Our collaborators were also awarded significant time with *Chandra* for several of these clusters, to try and achieve the best measurements of cavity power amongst others.

For some of our observations, the large field of view afforded by the GMRT (see §2.8) is larger than the virial radius of the cluster. This enables us to also study the cluster radio AGN population. In Chapter 3, we look at the energetics of all radio galaxies (central and non-central) in four well-studied clusters. Thereafter, in Chapters 4 & 5, we present results

---

[1] e.g. `https://heasarc.gsfc.nasa.gov/docs/cosmic/milkyway_info.html`

Table 1.1: Our sample of galaxy clusters. The X-ray information is from Rafferty et al. (2006) and Cavagnolo et al. (2009).

Cluster Name	RA$_{J2000}$ ($^{\mathrm{h}\ \mathrm{m}\ \mathrm{s}}$)	Dec$_{J2000}$ ($^\circ$,$'$,$''$)	z	t_{buoy} (Myr)	L_X (10^{42} erg s^{-1})	T_X (keV)
2A0335	03:38:35.3	09:57:54.7	0.0349	58.1	338	2.9
A478	04:13:20.7	10:28:35.0	0.0881	19.0	1440	7.8
MS0735	07:41:44.5	74:14:39.5	0.216	294	450	7.7
Hydra A	09:18:05.7	-12:05:44.0	0.0549	189	282	7.4
RBS797	09:47:12.9	76:23:12.8	0.354	40.1	3100	3.0
A1795	13:49:00.5	26:35:06.7	0.0625	37.2	625	6.7
A1835	14:01:02.1	02:52:41.9	0.253	33.1	3160	9.2
A2029	15:10:56.0	05:44:40.9	0.0773	69.9	1160	3.6
A2052	15:16:45.5	07:00:01.1	0.0355	14.4	97	7.1
A2218	16:35:54.0	66:13:00.1	0.176			4.2
Hercules A	16:51:08.1	04:59:33.3	0.154	127	210	4.3
RXJ1720	17:20:08.9	26:38:06.0	0.164			5.5
A2390	21:53:34.6	17:40:10.9	0.228			6.4
A2597	23:25:18.0	-12:06:29.9	0.0852	68.1	470	5.6

from our whole sample, concentrating particularly on the extended sources seen in these observations at multiple GMRT frequencies.

Chapter 2

Principles of imaging with radio telescopes

When we look up at the night sky, we see only a tiny fraction of the amount that is emitted. Astronomical objects radiate at frequencies from radio waves to gamma rays, but historically our visibility of these has been limited due to their absorption and reflection by the Earth's atmosphere.

Radio astronomy covers the largest range of wavelengths in the electromagnetic (EM) spectrum. It covers the longest wavelengths and ranges from millimetres to several metres. Most radio astronomy occurs between a few millimetres (50 GHz) to around 10 m (30 MHz). This is because the atmosphere is effectively transparent to EM waves at these wavelengths. Low frequency radio astronomy is considered to be at frequencies less than the GHz range, and is the area that we will be using to investigate our selected extragalactic sources.

2.1 Detecting radio waves

An electromagnetic wave has both amplitude and phase. In astronomy, typically the square of the amplitude is detected and the phase information is lost. In radio astronomy, the incoming radiation is transformed into electrical signals that are proportional to the amplitude of the electric field, whilst preserving the phase.

Radio waves, like other imaging systems, are diffraction limited, and so will follow Rayleigh's criterion.

$$\theta \sim \frac{\lambda}{D} \tag{2.1}$$

where θ is the angular resolution of the telescope, λ is the wavelength of the observed radiation and D is the size of the aperture. As radio waves have a large wavelength, the angular resolution will be low. To achieve roughly the same resolution as that of a typical 1 m optical telescope, either the diameter of the radio telescope must increase, or the frequency of the radiation that is observed must increase. The size of the telescope would have to go up to several hundred kilometres in size, which is clearly unachievable. Alternatively, observing at centimetre and sub-mm wavelengths provides better angular resolution, but the sources may not be bright at those frequencies. To look for interactions between the AGN and the surrounding medium, we need to look at physical scales of a few kiloparsecs. For a redshift of $z = 0.1$ this equates to around 5.5 arcsec / 10 kpc. If we take the largest single aperture radio telescope at Arecibo, it has a physical diameter of 300 m. At the low frequencies that we wish to look at, the best resolution it would be able to achieve is ~6 arcminutes, several orders of magnitude less than needed. A solution to this is interferometry.

2.2 Interferometric imaging

The most basic interferometer is one with two elements. A two-element interferometer provides limited information about the two-dimensional projected structure of the source. To obtain this structure information, we need to move the telescopes, and repeat the observations several times, in order to change the baselines. We can also increase the number of telescopes to increase the number of baselines available, since for N telescopes, there would be $N(N-1)/2$ unique baselines. Each baseline contributes an independent Fourier component to the image. A simple example is the Australian Telescope Compact Array, which has 5 telescopes on a railroad track 3 km long, running East-West.

Enhanced uv plane coverage can be obtained by rotating the array, and this is achieved in most current observatories by using the rotation of the Earth to fill in the uv plane. As the Earth rotates, each telescope moves along an elliptical path in the uv plane, with the various baselines resulting from the spacings of the N telescopes contributing to the filling of the uv plane. The greater the coverage, the more information about the source is obtained. This is known as aperture synthesis. Briefly, if we take an image of the sky (in (θ, ϕ) coordinates) and obtain its Fourier transform, the resulting image is in what is called the 'uv-plane'. Figure 2.4 shows an example of how we want to fill in this uv-plane. We now go into a more detailed look at interferometry.

We start by making a number of assumptions. First of all, we assume that the sources in the radio sky that we are observing are non-variable over the time periods that we are measuring. This will be true for the sources that we are interested in, such as AGN, but would not be for sources such as pulsars that are rapidly variable on timescales that are much shorter than the span of the observation. Secondly, we assume the source is distant from the antenna, so that we can treat it as measurable in only two dimensions. We also assume that the radiation is monochromatic, and following Taylor et al. (1999) we ignore polarisation in order to simplify the measured electric field to a scalar quantity. Finally, we take the space between the source and us to be a vacuum, so we can describe the electric field propagation by Maxwell's equations.

We can start by taking the electric field in a vacuum as

$$E(t) = \int_0^\infty E(\nu) e^{i[\phi(\nu) - 2\pi\nu t]}\, d\nu \tag{2.2}$$

where we assume the signal to be essentially monochromatic, $d\nu/\nu \ll 1$. This small bandwidth is what we actually measure in practice. We can then express this as a Fourier series,

$$\mathbf{E}_\nu(\mathbf{r}) = \iiint P_\nu(\mathbf{R}, \mathbf{r})\, \mathbf{E}_\nu(\mathbf{R})\, dx\, dy\, dz \tag{2.3}$$

where $P_\nu(\mathbf{R}, \mathbf{r})$ is the propagator function. This shows how the source electric field affects the electric field measured at $\mathbf{r}$, where $\mathbf{R}$ is the position of the radio source, and $\mathbf{r}$ is the location of the observer.

If we take our assumptions listed earlier, and considering the electric field as a scalar, we can simplify this equation for an empty space (e.g. Clark, 1995).

$$E_\nu(\mathbf{r}) = \int \mathbf{E}_\nu(\mathbf{R}) \frac{e^{2\pi i\nu|\mathbf{R}-\mathbf{r}|/c}}{|\mathbf{R}-\mathbf{r}|}\, dS \tag{2.4}$$

where dS is an element of surface area on the celestial sphere.

We take the most simple example of a two element monochromatic interferometer. The voltage induced is measured at either end of the interferometer, at $\mathbf{r}_1$ and $\mathbf{r}_2$. We can measure the correlation of the field at these points, i.e. how similar the electromagnetic field at those two positions are, and is given by

$$V_\nu(\mathbf{r}_1, \mathbf{r}_2) = \langle \mathbf{E}_\nu(\mathbf{r}_1)\mathbf{E}^*_\nu(\mathbf{r}_2)\rangle \tag{2.5}$$

where * is the complex conjugate and $\langle\rangle$ denotes an expectation value. From this, we follow Clark (1999) to obtain the spatial coherence function. As noted by Clark, an interferometer is a device for measuring this spatial coherence function.

$$V_\nu(\mathbf{r}_1, \mathbf{r}_2) \approx \int I_\nu(\mathbf{s})\, e^{-2\pi i\nu \mathbf{s}\cdot(\mathbf{r}_1-\mathbf{r}_2)/c}\, d\Omega \tag{2.6}$$

where I is the intensity of the radiation field, $\mathbf{s}$ is the unit vector pointing to the direction of $\mathbf{R}$, and Ω is the solid angle subtended by the radio source.

This equation can be inverted under certain conditions, so that the intensity distribution of the source can be reconstructed. To apply this to real interferometers, we need to choose an applicable set of coordinates. We pick a coordinate system that is in a plane, where the unit vector $\mathbf{s}$ can be defined by its projections on the (u, v, w) axes: $l = \cos(\alpha)$, $m = \cos(\beta)$ and

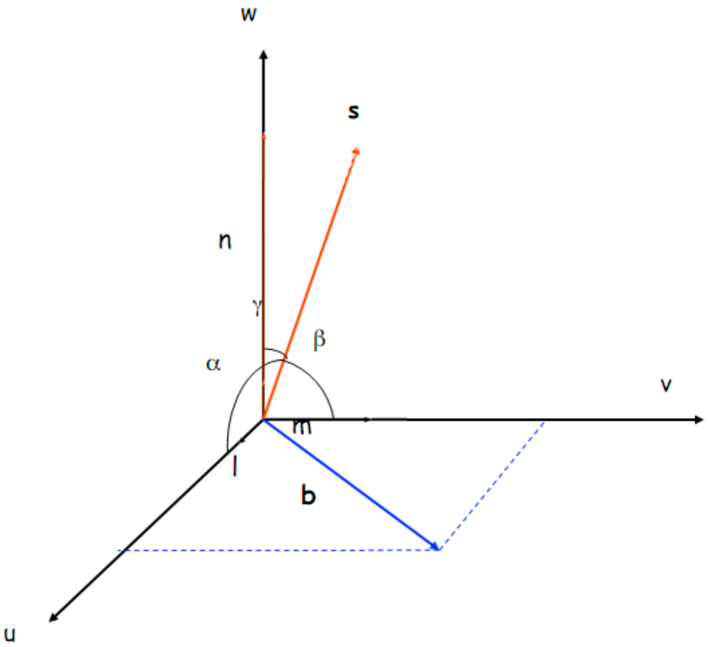

Figure 2.1: The (u, v, w) imaging geometry. (l,m,n) are the three direction cosines of the source with respect to the three axes, and α, β and γ are the corresponding angles. $l = \cos(\alpha)$, $m = \cos(\beta)$ and $n = \cos(\gamma) = \sqrt{1 - l^2 - m^2}$.

$n = \cos(\gamma) = \sqrt{1 - l^2 - m^2}$. Figure 2.1 shows this graphically. The baseline vector **b** can be found from $\mathbf{b} = (\lambda u, \lambda v, \lambda w) = (\lambda u, \lambda v, 0)$.

This simplification of having all measurements confined to a plane, i.e. $w = 0$, gives

$$V_\nu(u, v, w = 0) = \iint \frac{I_\nu(l, m)}{\sqrt{1 - l^2 - m^2}} e^{-2\pi i(ul+vm+wn)} \, dl \, dm \tag{2.7}$$

Alternatively, we can assume that all sources are in a small region of the sky. Therefore, we can write $\mathbf{s} = \mathbf{s}_0 + \sigma$, where $\mathbf{s}_0$ points from the antenna to the phase tracking centre, and σ is perpendicular to $\mathbf{s}_0$.

$$V_\nu(u, v) = \iint A_\nu(l, m) \, I_\nu(l, m) \, e^{-2\pi i(ul+vm)} \, dl \, dm \tag{2.8}$$

This Fourier transform relation again can be inverted to obtain the intensity of the source. Here, we have also introduced a factor needed due to the fact that the antennae are dishes: the normalised antenna response, $A_\nu(l, m)$. Near the field centre, $A_\nu(l, m) \sim 1$. The Fourier transform can be simply divided through by this factor to obtain the final image. As we

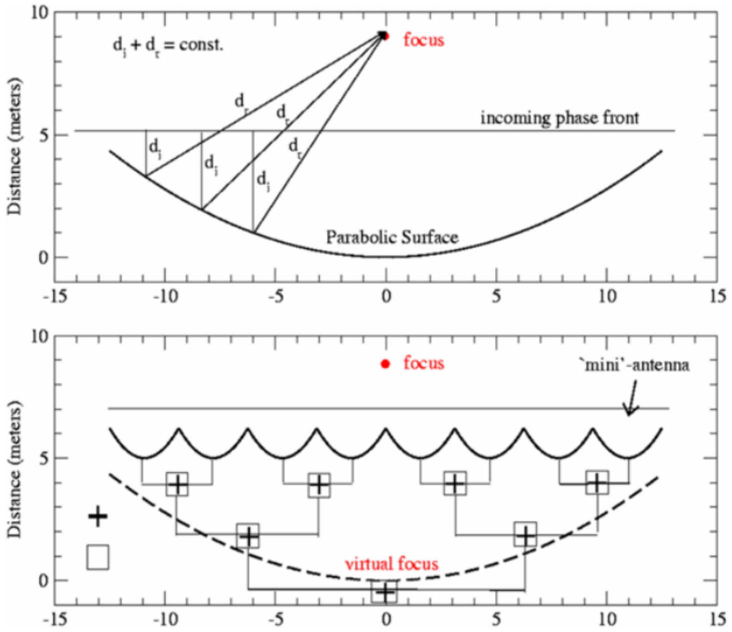

Figure 2.2: Instead of building a large telescope, the same effect can be created by using many smaller antennae. This is the idea behind interferometry. Image from an NRAO presentation by Di Francesco. `https://science.nrao.edu/science/meetings/presentation/jdf.webinar.2.pdf`

mentioned before, the majority of the sources in the radio sky are non-variable. This means that is is not necessary to measure the entire wavefront at any given time. For an interferometric array, pairs of signals from N elements are measured and combined. If there are N antennas, there are $N(N-1)/2$ pairs to combine in order to measure a set of Fourier components at a time. Each of these pairs will have a different baseline, and hence a different measure of the visibility function. The baselines are described in terms of the uv–plane, mentioned earlier. It is important to measure as many samples of the uv–plane as possible in order to be able to deconvolve them and obtain a good quality image. One can take advantage of the fact that as the Earth rotates, the projected baseline between two antenna changes from the perspective of the source. This is a great help in filling in the uv coverage, and is known as (Earth rotation) aperture synthesis. An example is shown in §2.3. The angular coverage or 'primary beam' from this will have a radius of $\theta_{\rm PB} \sim \frac{\lambda}{D}$, where D is the diameter of a single antenna. The resulting image will have a maximum resolution of $\theta \sim \frac{\lambda}{B}$, where B is the length of the longest baseline of the array. For the GMRT (§2.4), this will give a resolution of $\sim 4''$ at 610 MHz.

2.3 Sensitivity & uv−coverage

To image the faint diffuse emission that we are investigating, it is imperative to achieve good sensitivity. The rms noise level for our observations can be obtained by

$$S_{\text{rms}} = \frac{2kT_{\text{sys}}}{A_{\text{eff}}\sqrt{N(N-1)\,t_{\text{int}}\,\Delta\nu}} \tag{2.9}$$

where k is the Boltzmann constant, T_{sys} is the system temperature, A_{eff} is the effective area of the antennae, N is the number of antennae, t_{int} is the integration time and $\Delta\nu$ is the bandwidth.

The need for long observations is clear here, for example compared to a quick 5 min observation, a good 6 h integration time decreases the theoretical rms noise levels by a factor of ~ 8.

The time on source is important not only for the increased number of visibilities, but also for the larger coverage of the uv−plane. Figures 2.3 and 2.4 show the uv−coverage of a 10 and 300 min observation respectively. The (x,y) on the plots corresponds to the (u,v) plane, which is measured in units of kλ.

An ideal case would be to completely fill the uv plane, making measurements at every baseline length and orientation out to some distance, so that the fully sampled Fourier transform contains exactly the same information as the image of an equivalently sized single dish telescope. The rotation of the Earth is used to fill the uv−plane azimuthally. Another method to help with uv−coverage is bandwidth. As the uv−plane is measured in units of wavelength, choosing different frequencies will have the effect of filling in the uv−plane radially. It was soon discovered that an image needs much less uv−coverage for it still to be scientifically useful, using non-linear deconvolution algorithms such as the CLEAN algorithm (Högbom, 1974).

2.4 The GMRT

The Giant Metrewave Radio Telescope (GMRT) is located near Pune, India. It is an interferometric array of 30 telescopes observing at frequencies from 150 to 1420 MHz. Each dish is 45 m

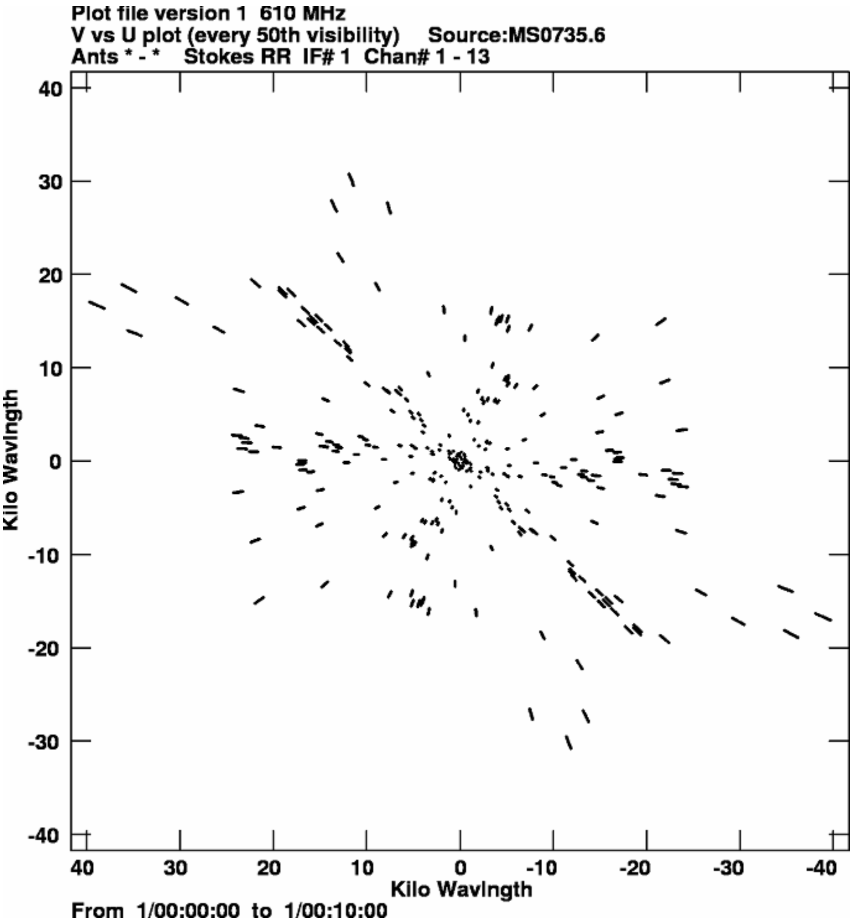

Figure 2.3: The uv−coverage shown for the observation of MS0735, but for only a 10 minute snapshot.

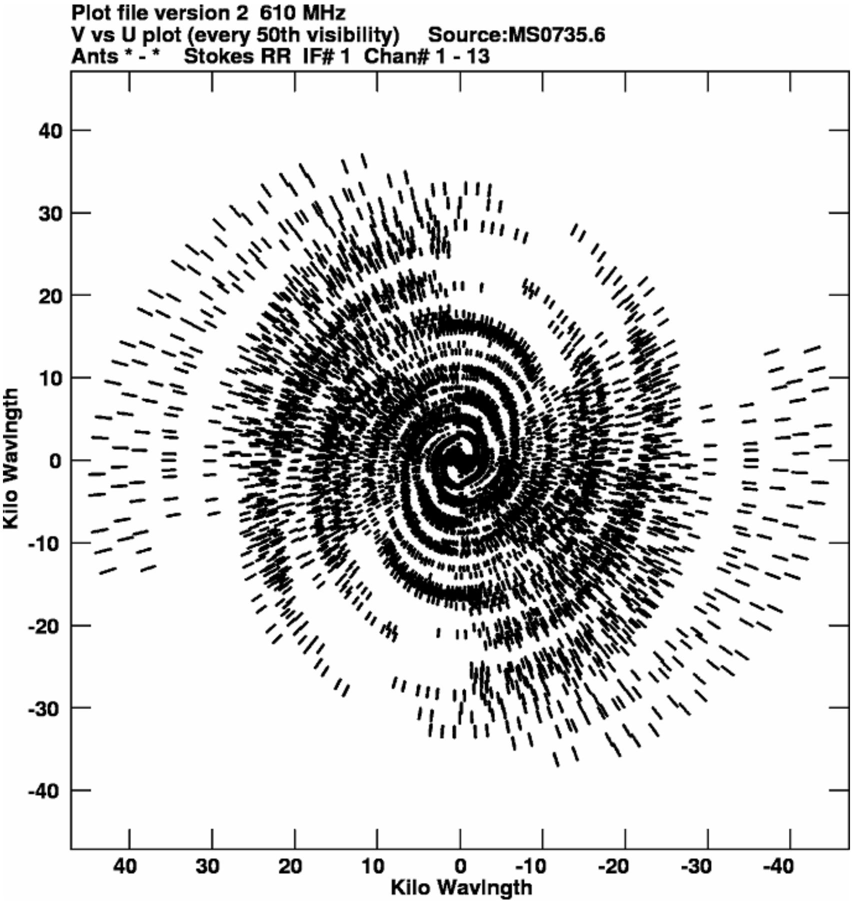

Figure 2.4: The uv−coverage shown for the observation of MS0735, for the full ~6 hour integration time. The rotation of the Earth has clearly filled in much more of the uv−plane.

Table 2.1: The measured system parameters of the GMRT, taken from the GMRT manual.

System Properties	150	235 (MHz)	325	610
Primary beam (arcmin) [a]	186	114	81	43
Synthesised beam (arcsec) [b]	20	13	9	5
T_{sys} (K)	615	237	106	102
Best RMS noise (mJy) [c]	0.7	0.25	0.04	0.02
Typical dynamic range [c]	> 1500	> 1500	> 1500	> 2000

---

[a] Half power beam width (HPBW)
[b] Full width half maximum (FWHM)
[c] Anecdotal; from GMRT observer's manual

in diameter and the longest baseline is approximately 25 km long. This gives it typical angular resolutions on the scale of arcseconds. 14 of the antennas are arranged pseudo-randomly in a 1 km long 'central square'. These are important to cover the short baselines needed for observing large extended sources. The other 16 dishes are set out in a Y-shape pattern (see Figure 2.5).

The GMRT has 6 different feeds, offering frequency bands at of 150, 235, 325, 610 and 1420 MHz. They are placed at the prime focus of the parabolic antennas. These feeds are circularly polarised except for the 1420 MHz feed which is linear. Table 2.1 shows the system properties of the GMRT at the different frequencies it offers. With such a large field of view it is important to take into account any strong sources that are on the edges of the primary beam.

The GMRT was constructed in India for various reasons. Firstly, the cost of building an array in India is cheaper due to reduced labour and construction costs, as well as the nature of the design of the dishes. Thin stainless steel wire ropes were used to create a lightweight mesh approximating a parabolic surface (see Figure 2.6). This design has been coined as the 'SMART' concept: Stretch Mesh Attached to Rope Trusses. More details can be found on the GMRT website.[1] Secondly, the radio frequency interference (RFI), at these low frequencies is considerably less compared to other countries (especially man-made RFI). Further information can be found in §2.5. Thirdly, the latitude of the array is such that it can cover declinations from

---

[1] `http://www.ncra.tifr.res.in/ncra/gmrt/`

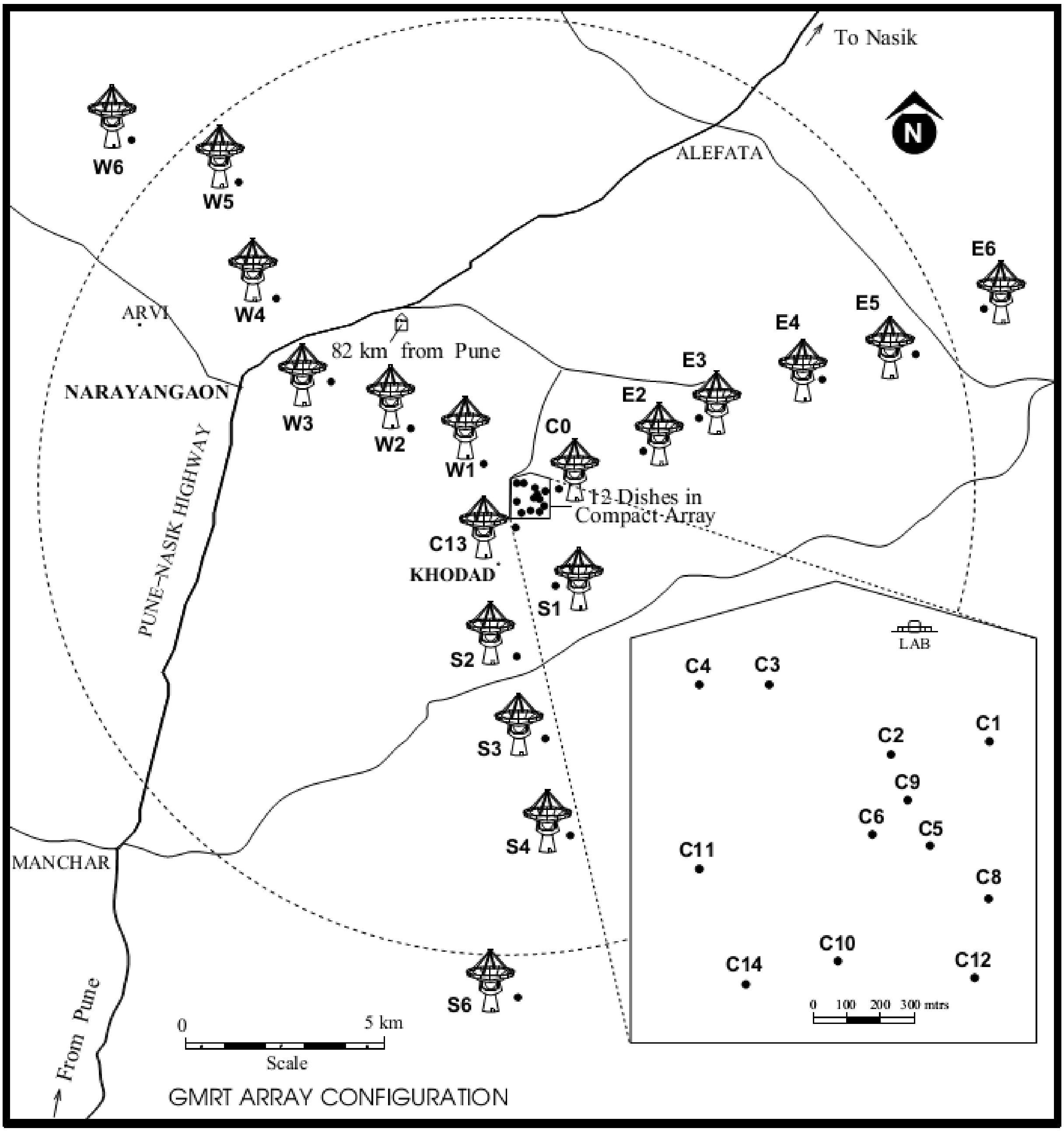

Figure 2.5: The GMRT array configuration. The three arms are shown here in the customary Y-formation, along with the central square of dishes to provide good short baseline coverage. Image from `http://gmrt.ncra.tifr.res.in/gmrt_hpage/Users/doc/GMRT-specs.pdf`.

+90° to −53°. The TIFR GMRT Sky Survey (TGSS)[1] is a 150 MHz sky survey with coverage of the sky north of −30°, with future plans to image at declinations down to −53°.

2.5 Radio frequency interference

Radio Frequency Interference (RFI) is a major problem for radio telescopes at lower frequencies. There are two types: narrowband and broadband. Narrowband RFI effects only a small frequency range, and is usually from intentional transmissions. Examples of narrowband RFI are radio, TV stations and mobile phones. Figure 2.7 shows that narrowband RFI is only a major problem if it is near any frequencies that are being observed in. For the GMRT, 150 and 235 MHz appear to be relatively free from narrowband RFI, although there is a concern if the RFI leaks out into other frequencies.

Broadband RFI covers a wider range in frequencies and is usually less powerful. It is commonly caused as a secondary effect of electrical objects. Power transmission lines and electric motors are two causes of broadband RFI. This type of RFI is most damaging to observations as it covers more of the observational band and is more difficult to remove from the data. RFI can be a one-off spike or constant over the entire observation. It is important to not confuse RFI with data, as a lot of short spacings can contain RFI, and short spacings are most important in our observations as they obtain the extended emission. Local RFI will also be correlated on short spacings since nearby antennae will pick up the same source of noise. This can be troublesome to correct as it would appear like a signal in the data. At our low frequencies, the RFI tends to decrease during the night, so this is when we decided to observe.

---

[1] `http://tgss.ncra.tifr.res.in`

Figure 2.6: One of the GMRT antennae found in the central square. Two others can be seen in the background. This picture was taken by me during one of my visits to the GMRT array, after a long night of observing!

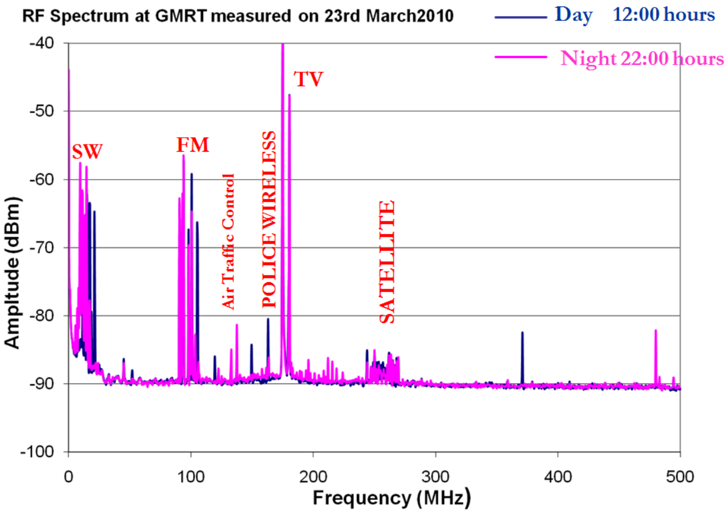

Figure 2.7: The GMRT radio frequency spectrum from 0–500 MHz. The spikes from RFI are easily visible. Image is from Raybole (2010).

2.6 Data Reduction

After observing our radio sources at the GMRT, they need to be reduced. We use NRAO Astronomical Image Processing Software ($\mathcal{AIPS}$)[1] for this process. A brief overview of the reduction method is presented below.

2.6.1 Preparation

The raw data from the observatory is first converted into the more commonly used FITS (Flexible Image Transport System) format. This file is typically around a gigabyte in size, depending on the length of the observations and the integration time per visibility.

As an example, we will use the observation of MS0735.6+7421. It contains 547,230 visibilities, with an integration time of 16.9 sec per visibility. The file contains the combined observations of MS0735, and the calibrator sources. These calibration sources are important to observe, without these it would not be possible to calculate even the basic information such as the flux density of the source. There are two types of calibrator, the primary flux calibrator and the phase calibrator. We used two flux calibrators during the course of this particular observation: 3C147 and 3C286. These two sources are quasars, therefore bright and compact. Their flux density has been measured at many frequencies and determined to be stable over many decades, making them ideal as flux calibrators (Perley and Butler, 2013).

During the observation, there are slow ionospheric and instrumental gain variations in amplitude and phase that occur on timescales of tens of minutes. In order to allow for this, a good phase calibrator has to be stable over timescales much longer than the length of the observation, so that the amplitude and phase of the antennas in the array can be corrected. Why can't we just use the flux calibrator again? The answer is because the calibrator needs to be close to the object that we are observing. Apart from the time needed to slew between our object source and the calibrators, the area of sky around the flux calibrator will be different to that around our object source. Ionospheric effects (e.g. refraction) will change the phase of

---

[1] `http://www.aips.nrao.edu`

```
Scan      Source      Qual  Calcode Sub         Timerange          FrqID   START
   1 3C147           : 0231           1  0/20:45:30 -   0/21:00:16     1       1
   2 0834+555        : 0081  C        1  0/21:04:02 -   0/21:08:35     1   24361
   3 MS0735.6+74     : 0216           1  0/21:12:21 -   0/21:43:29     1   32191
   4 0834+555        : 0081  C        1  0/21:45:22 -   0/21:49:56     1   83086
   5 MS0735.6+74     : 0216           1  0/21:53:41 -   0/22:24:34     1   90916
   ...
```

Figure 2.8: Output from the *AIPS* tool LISTR, for the start of the observing run on MS0735.6+7421.

the object, and will be very different when comparing the phase calibrator and the object we are interested in. Thus we pick a known phase calibrator source that is closest to our object source. Figure 2.8 shows some output of the LISTR tool, for the start of the observing run on MS0735.6+7421. The phase calibrator in this example is named as 0834+555. At the start and end of our observations, we observe the primary flux calibrator. We use two in this example as the first flux calibrator, 3C147, had set. We then alternate between observing the phase calibrator and the object source, spending 5 minutes on the calibrator, followed by 30 minutes on the object source. The first few seconds of each scan are typically of bad quality, so they are cut using the *AIPS* QUACK tool.

We set the flux density of the flux calibrators using the *AIPS* SETJY implementation of the scale of Perley and Butler (2013).

2.6.2 Flagging & calibration

We now have the data in a state that can be worked on. The primary concern that we have with GMRT is the high amount of RFI that will corrupt the image of the source. The first stage is to visually inspect the data, we initially use the interative flagging tool, TVFLG, shown in Figure 2.9. This tool presents the data as a plot of time against antenna baseline pair, with the amplitude or phase of each visibility shown. Only one channel is shown at a time with this tool.

With our MS0735 source there are 512 channels, each of which are 65 MHz in width. We start by selecting a relatively clean channel close to the middle of the frequency range, and make the assumption that all of the strong RFI which is present will also be throughout the observation. Some of the baseline pairs may also not be working, or ‘dead’, and can be marked

```
PHS DIFF  (0.00-12.95)  CH 239  IF 1  AVG 1  BLC 1 1  TRC 1056 318  ONE-CH  ALL-IF  ANT.PR  ALL-SOURCE  SCAN 3  SHOW RR  STOKES, FLAG RR
```

Figure 2.9: TVFLG, the interactive flagging tool, is shown here. Antenna-baseline pairs are shown along the x-axis, and time increases from top to bottom. In this instance, the phase difference is being shown – where darker pixels indicate a larger phase difference. This difference is just the modulus of the difference between the phase of the data and a running 'scan average'. Here, after some flagging, we see that there are only minor patches of phase inconsistency, and only on a scale of a few degrees.

appropriately. Here, we are only interested in the amplitude and phase calibrators, which should be stable. Any baselines that differ significantly and quickly in amplitude and phase during the observations are noted down, and then flagged for all channels. This also applies for any baselines that are anomalously large or small. These are sometimes only short periods, minutes, where only that range can be flagged. The term 'flagging' means that these visibilities are marked as not to be used for any of the subsequent reduction. In radio reduction, it is much more preferable to flag aggressively and delete potential good data, rather than to keep any bad data.

After preliminary flagging of the data set has been completed, initial calibration can be started. The $\mathcal{AIPS}$ task CALIB is used to compute the antenna based complex gain solutions for the flux density and phase calibrators. The solution interval is initially set to 1 min, too long a solution interval and it will not be able to track the variable ionosphere, too small and the signal-to-noise ratio will not be adequate.

We then bootstrap the flux information from the flux calibrators onto the phase calibrator. This value can then be compared to the VLA Calibrator Manual[1], which has a list of fluxes for many used calibrator sources.

---

[1] `http://www.vla.nrao.edu/astro/calib/manual/csource.html`

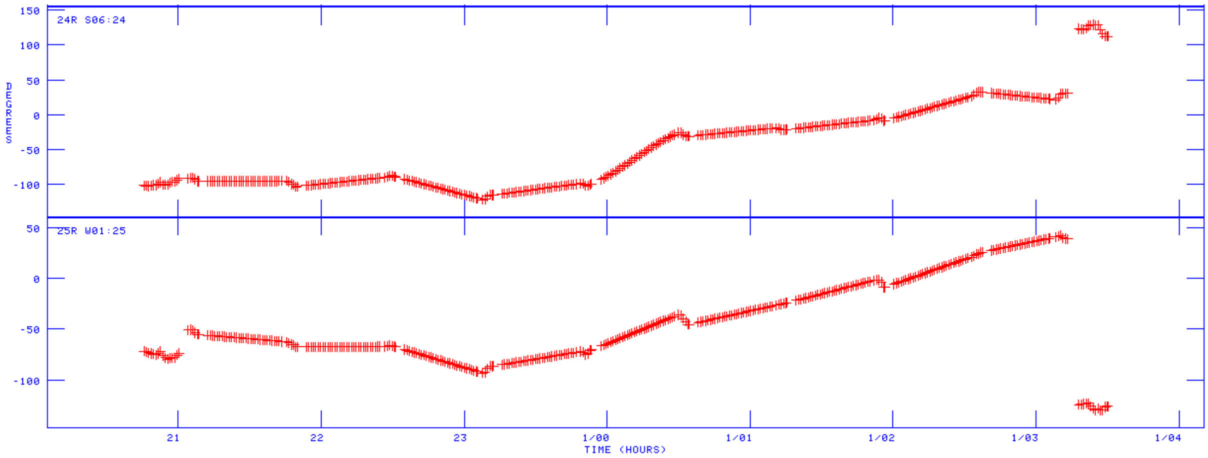

Figure 2.10: The SNPLT tool is shown here, with the calculated phase solutions every thirty minutes. We have interpolated these solutions, providing a first estimate of the gains required for the target source.

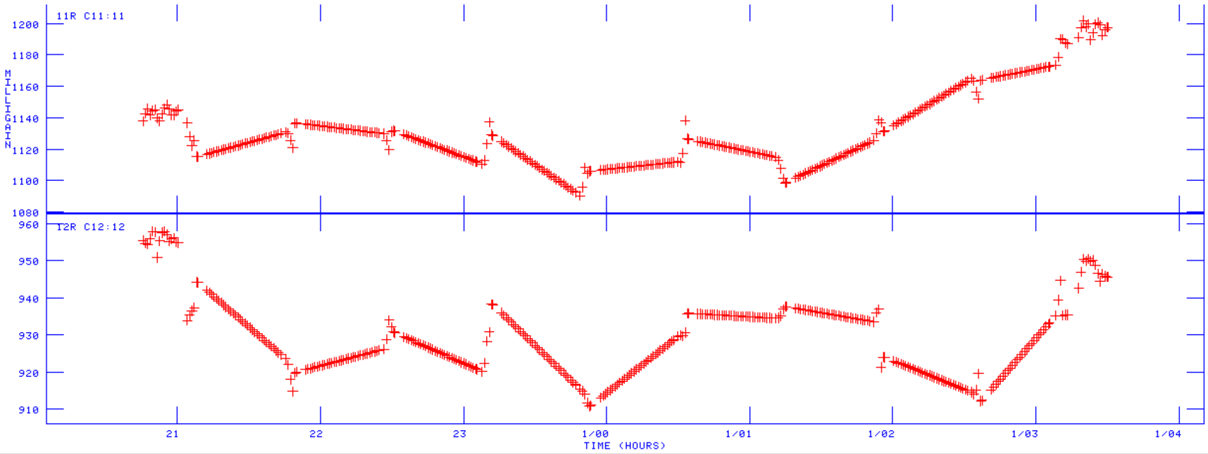

Figure 2.11: The SNPLT tool is shown here, with the calculated amplitude solutions every thirty minutes. We have interpolated these solutions, providing a first estimate of the gains required for the target source.

This process is then repeated, flagging and calibrating until the RFI level has been greatly reduced and the CALIB routine gives us good solutions. We can check the quality of these solutions using the SNPLT tool, shown in Figure 2.10. We expect relatively smooth gradient for the phases, along with a similar distribution near unity for amplitude. The phase calibrators are observed every 30 minutes, and so the solutions for the target source are interpolated from these.

Line RFI, which only affects a very narrow frequency range, will also need to be filtered out. The bandpass is the relative gain response of each antenna as a function of frequency, calculated in $\mathcal{AIPS}$ with the BPASS tool (e.g. Rupen, 1999). From this, we can use POSSM to

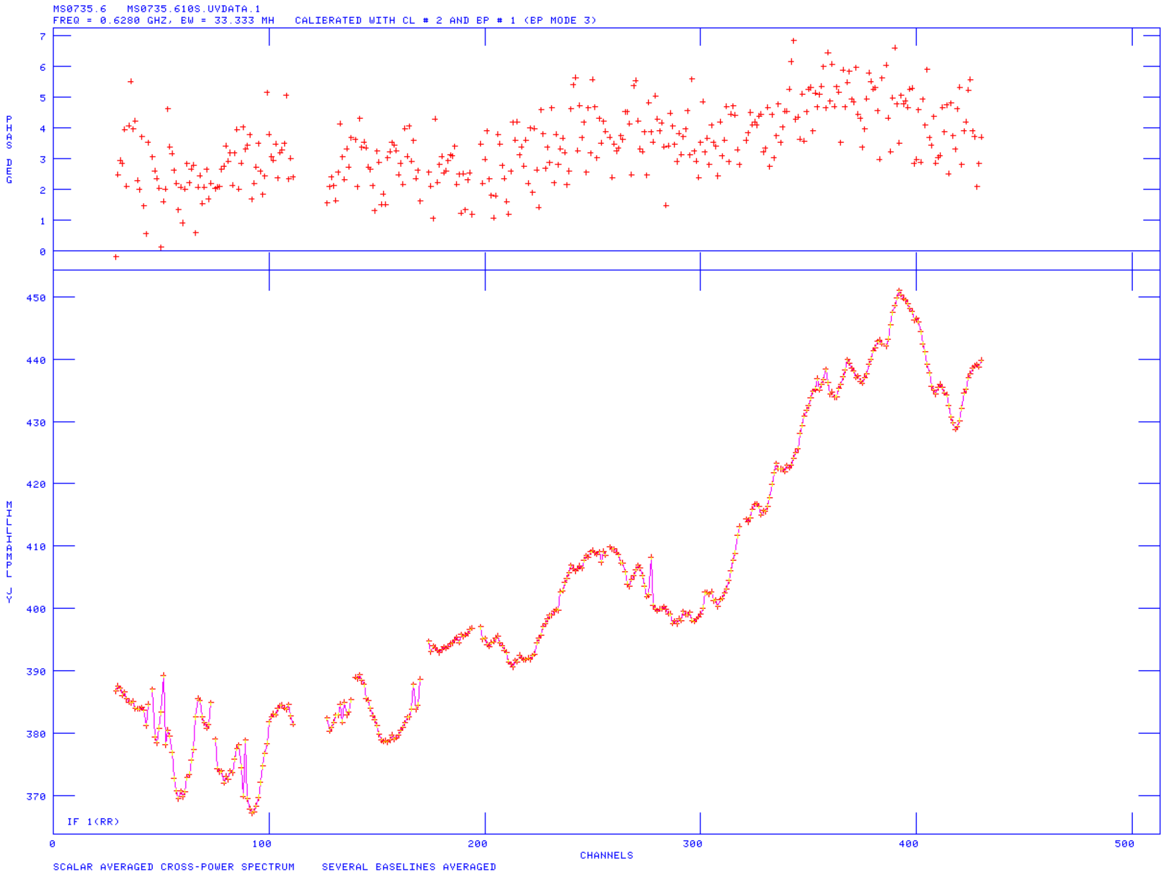

Figure 2.12: The time and baseline-averaged plot of amplitude (and phase) against channel (frequency), created using POSSM. Gaps in the plot are due to some channels being flagged out due to narrow-band RFI.

plot the time-averaged, baseline-averaged spectrum, so that each frequency channel can be compared easily, see Figure 2.12. A completely linear relation is the ideal case, any channels with large spikes due to RFI at a specific frequency can be easily seen and flagged. It is possible to increase the signal-to-noise ratio by collapsing several channels into one. Instead of having 512 channels of 65 MHz each, averaging 16 channels into one will give 32 channels of 2 MHz each. Care must be taken not to collapse too many channels due to bandwidth smearing effects.

Bandwidth smearing is a process that occurs due to radiation not being monochromatic, but in a frequency range $\Delta\nu$, around a central frequency ν where $\Delta\nu \ll \nu$. Averaging these frequencies is equivalent to averaging visibilities in the radial direction of the uv plane. This means any small scale structure in the uv plane is 'smeared out' or reduced in amplitude. These correspond to sources which are located far from the phase centre of the image, and so at

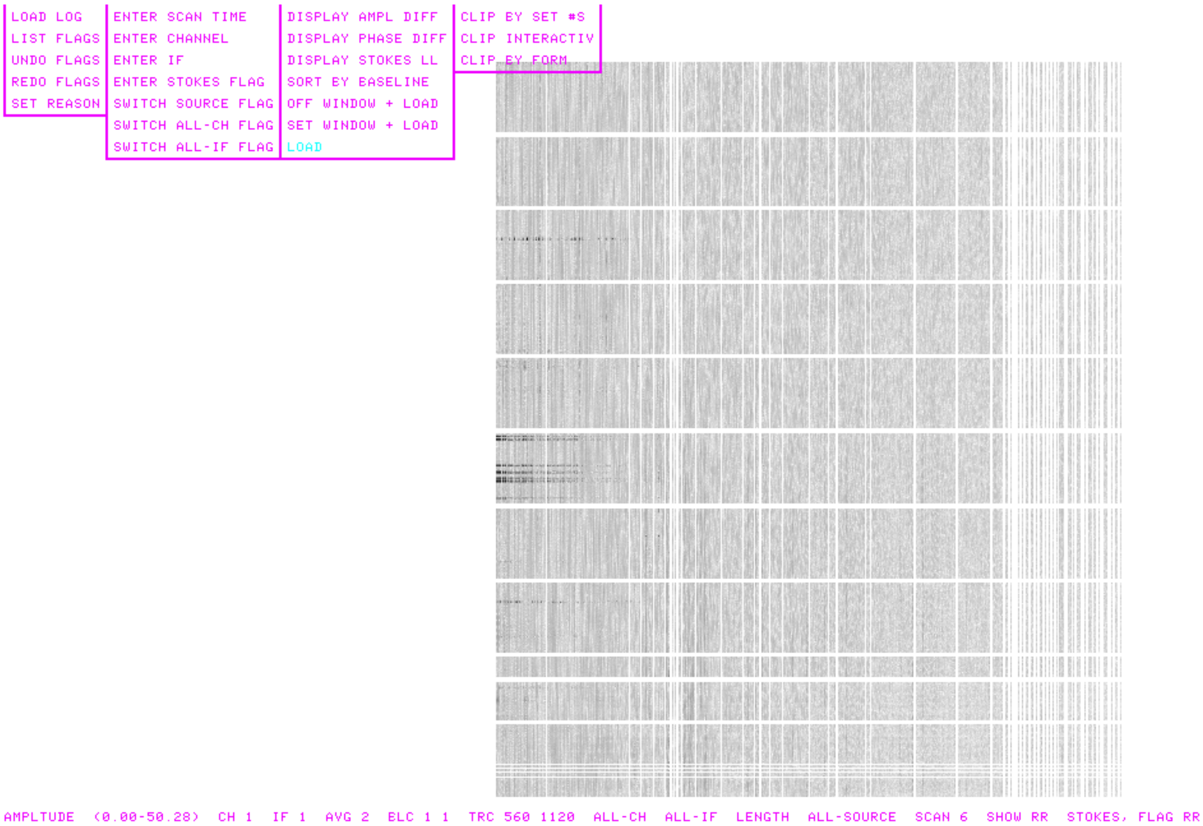

Figure 2.13: The x-axis is sorted now by baselength length, from short to long. Darker pixels now represent higher amplitudes. We see some dark peaks of RFI which only occur for very short periods, these will need to be flagged. Amplitude errors will result in symmetric structure appearing in the image.

the edges of the image the sources are radially smeared and some of their flux is distributed throughout the image, increasing the noise.

For the 610 MHz observation, 2 MHz is the practical limit per channel, and 1 MHz for the 235 MHz observation. It is important to note that when averaging multiple channels they have to be CLEAN of RFI, otherwise the RFI will be collapsed in with the real data and it will be very difficult to remove afterwards. The collapsed channels are then calibrated using the same technique as before, this time with a stronger signal-to-noise ratio. Averaging will also speed up processing, and results in smaller file sizes. After careful visual inspection, the target source is extracted and the calibrated solutions are applied, in preparation for imaging the source. Any future flagging or calibration will be done on this target source, as in Figure 2.13.

2.6.3 Imaging

Once the uv data has been collapsed and calibrated, the imaging stage can begin. First of all, we use the GMRT observers manual[1] to find the sizes of the primary beam and expected synthesised beam (spatial resolution). This varies as a function of frequency. Once we have this, it is important to find other bright radio sources in the field of view so that these can be taken into account. This is done by cross-correlating with a table of known NVSS sources, and a 'box' file (a simple list) is created with the coordinates of these sources. These bright sources need to be taken into account during the imaging phase, otherwise their flux will be distributed throughout the final image, dramatically increasing the noise level. At the low frequencies that we are observing at, we need to make use of wide-field imaging techniques described in §2.8. The task SETFC will use the beam size information to calculate the number of facets needed in order to cover the field of view.

Convolution

We would like to make use of the Fast Fourier Transform (FFT) algorithm, which is much faster than simple Fourier summations. This requires that our data are on a regularly spaced grid, so our uvdata are first convolved onto one in a technique known as gridding. We specified a cellsize of 1.3 arcsec/px, and an image size of 512 x 512 pixels.

Our sampling of the uv plane is not complete, there are many gaps (e.g. Figure 2.4). We can define a sampling function $S(u,v)$ that is 1 where we have a measured visibility and zero elsewhere. Our measured visibilities will thus be $[S(u,v)V(u,v)]$, where $V(u,v)$ are the 'true' visibilities.

$$V(u,v) = \iint I(l,m)\, e^{-2\pi i(ul+vm)}\, dl\, dm \tag{2.10}$$

An initial image can be made by taking the inverse Fourier transform of the sampled visibility function:

$$I'(x,y) = \mathcal{F}^{-1}\left[S(u,v)V(u,v)\right] \tag{2.11}$$

---

[1] `http://gmrt.ncra.tifr.res.in/gmrt_hpage/Users/doc/GMRT-specs.pdf`

and using the convolution theorem

$$I'(x, y) = B(x, y) * I(x, y) \tag{2.12}$$

where

$$B(x, y) = \mathcal{F}^{-1} S(u, v) \tag{2.13}$$

is the point source function (PSF). $I'(x, y)$ is known as the 'dirty map', and $B(x, y)$ is the 'dirty beam'. The PSF or 'clean beam' is usually a Gaussian function of the same FWHM as the central component of the dirty beam (Schwarz, 1978).

$I(x, y)$ is the true sky brightness and is our final goal – we want to deconvolve the dirty map by the dirty beam to achieve this.

IMAGR

IMAGR is the main imaging task in $\mathcal{AIPS}$, and it makes use of the CLEAN algorithm for deconvolution (Högbom, 1974). This is the most well known deconvolution algorithm in radio astronomy, and we will briefly describe it next.

An *a priori* assumption is that the sky consists of a limited collection of point sources on an otherwise empty background. CLEAN starts off by computing the dirty map and dirty beam as above. The CLEAN algorithm is an iterative procedure which operates on the dirty map (Rich et al., 2008, e.g.).

1. A residual map is created from the dirty map, and a 'clean component' list is initialised to empty.
2. The maximum brightness point in the residual map is identified as a point source.
3. The strength of this peak is then multiplied by a gain factor (typically 10%) to generate a clean component at that location.
4. This clean component is convolved with the dirty beam, and this is then subtracted from the dirty map.

5. The location and amplitude of the clean component are added to the clean component list.
6. Goto step 2, and repeat until a stopping criterion has been met.

The process ends when the residual map maximum goes below a certain flux threshold or the maximum number of iterations has been completed. The flux threshold is usually set to be some multiple of the rms noise, this occurs when it becomes noise limited. Alternatively, it can be equal to a fraction of the dirty map max, in cases where it is limited by dynamic range. While the loop gain factor (g) is typically set to 10%, for sources with extended emission a lower value is used. This does take more computational time, but can give better results.

The result of this process is a residual map, which should only include noise and any weak source structure that was below the clean cutoff limit. A list of clean components (flux and position) is also constructed. These are convolved with the clean beam and summed onto the residual map to return the final (or restored) image.

Further *a priori* information can be added when running this task in interactive mode. Instead of occurring over the entire image, clean components can be restricted to areas in user-defined boxes. These are drawn around sources that can be identified by eye, and are useful because they stop additional background noise from being added to the clean components list and reduce processing time. An example of this is shown in Figure 2.14. IMAGR can also be run in automatic mode, with the list of boxes (boxfile) taken from previous imaging runs.

2.6.4 Self-calibration

After the primary round of imaging, it is not unusual for the image to be very noisy. This is because we have only derived the initial gain corrections from our calibrator sources, but these are only first estimates. Figure 2.10 shows this interpolation, a simple linear function is used to connect the end of one calibrator scan to the beginning of the next. These gains will clearly be incorrect, as they were derived at a different time and in a different direction.

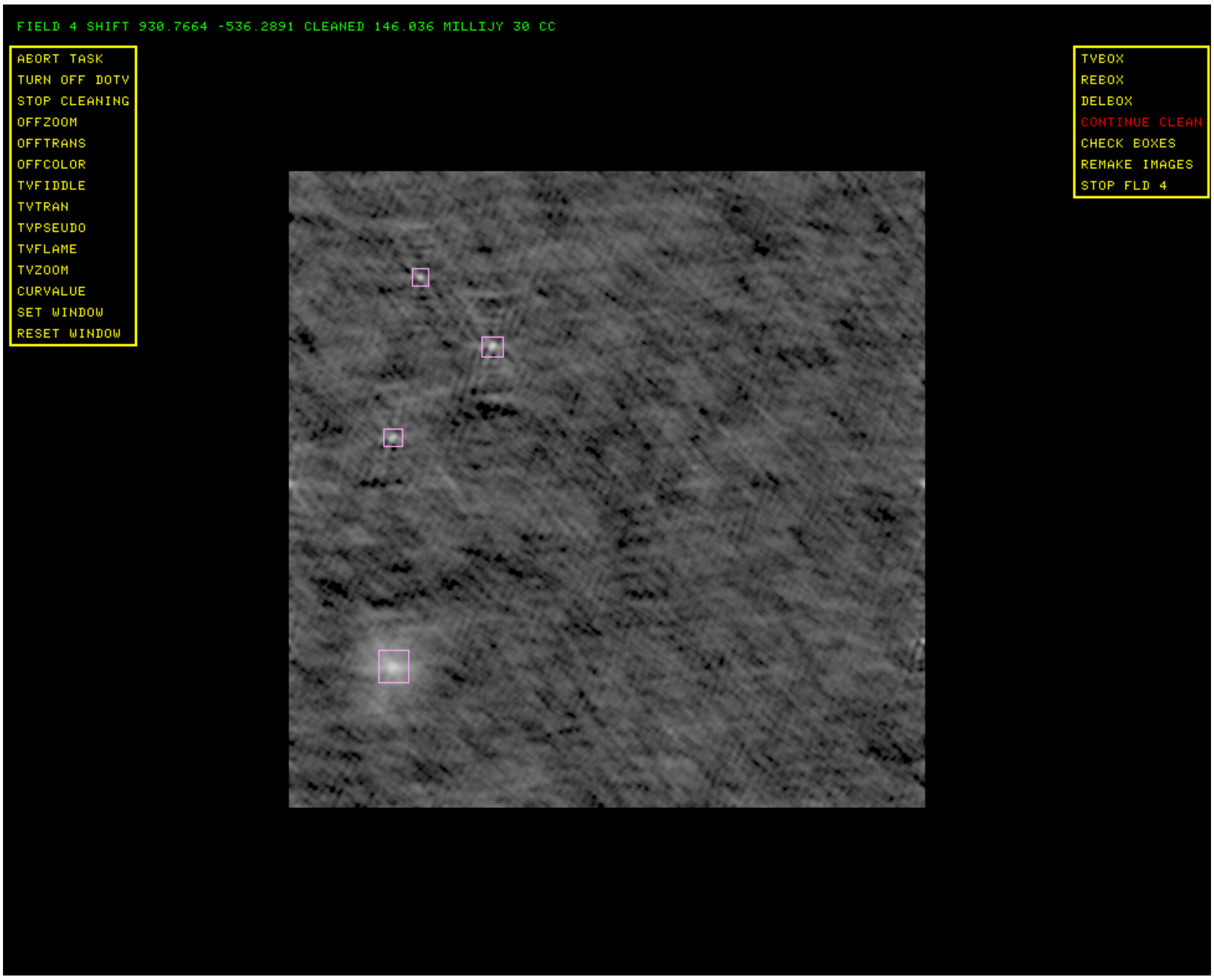

```
FIELD 4 SHIFT 930.7664 -536.2891 CLEANED 146.036 MILLIJY 30 CC
```

Figure 2.14: IMAGR is shown here in interactive mode. Boxes are placed around visible sources of radio emission, clean components will be generated from the peaks within these boxes. This will be repeated for all of the facets in the image, until such point that the majority of the easily seen point sources have been removed from the image. This will greatly aid in the calibration of the image.

With a strong enough source, a technique called self-cal can be used to calibrate itself to achieve a more accurate image. The basic calibration equation is as follows:

$$\tilde{V}_{i,j}(t) = g_i(t)g_j^*(t) \cdot b_i(\nu)b_j^*(\nu) \cdot V_{i,j}(t,\nu) + e_{i,j}(t,\nu) \tag{2.14}$$

where $\tilde{V}_{i,j}(t)$ is the observed visibility on baseline (i, j) at a time t and frequency ν. $V_{i,j}(t,\nu)$ is the true visibility as above, $g_i(t)$ is the complex gain for antenna i, $b_i(\nu)$ is the complex frequency bandpass and $e_{i,j}(t,\nu)$ is the noise.

Self-calibration uses a model of the target source to find improved values for the complex gains of each antenna. The gains are solved using a least-squares algorithm minimising the difference between the observed and model visibilities. This model comes from the previous round of imaging of the source.

The number of baselines ($N(N-1)/2$) is greater than the number of antennae (N). We are using antenna based gains, so we can use the redundancy of the extra baselines to add constraints on the computed solutions (e.g. Chengalur et al., 2007). An iterative process of imaging and self-calibration is used to enhance the image quality, using smaller solution intervals in each iteration (for stability). Self-calibration is usually only done for the phase solutions initially, amplitude is added in for the last iteration. Figure 2.15 shows the enhanced quality of the solutions compared to the interpolated results from before.

The final image is then corrected for the primary beam using PBCOR.[1]

2.7 Stripe removal

A useful technique that was used in the data reduction of our GMRT maps was the adaptation of the 'stripe removal' method from Basu et al. (2012). As the GMRT operates at a low frequency, it is susceptible to a significant amount of RFI (see §2.5) and other causes of bad baselines. These will cause artefacts in the image plane, which can be hard to identify. To narrow down which baseline(s) are causing the problems, we can measure the angular spacing of the ripples, and

---

[1] http://www.ncra.tifr.res.in:8081/~ngk/primarybeam/beam.html

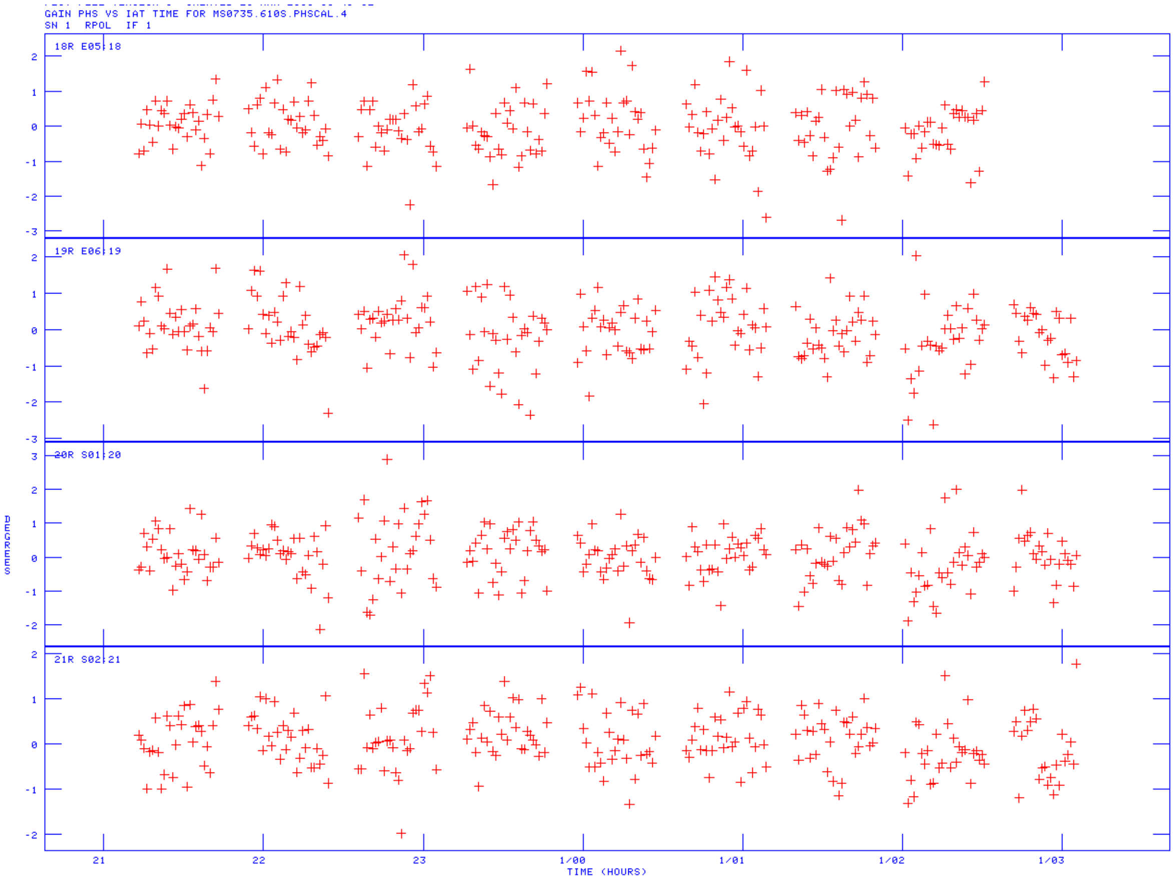

Figure 2.15: Instead of the straight line separating the calibrator sources at the start of our data reduction, here we see the temporally resolved phase solutions for the target source. This is from a direct result of using self-calibration.

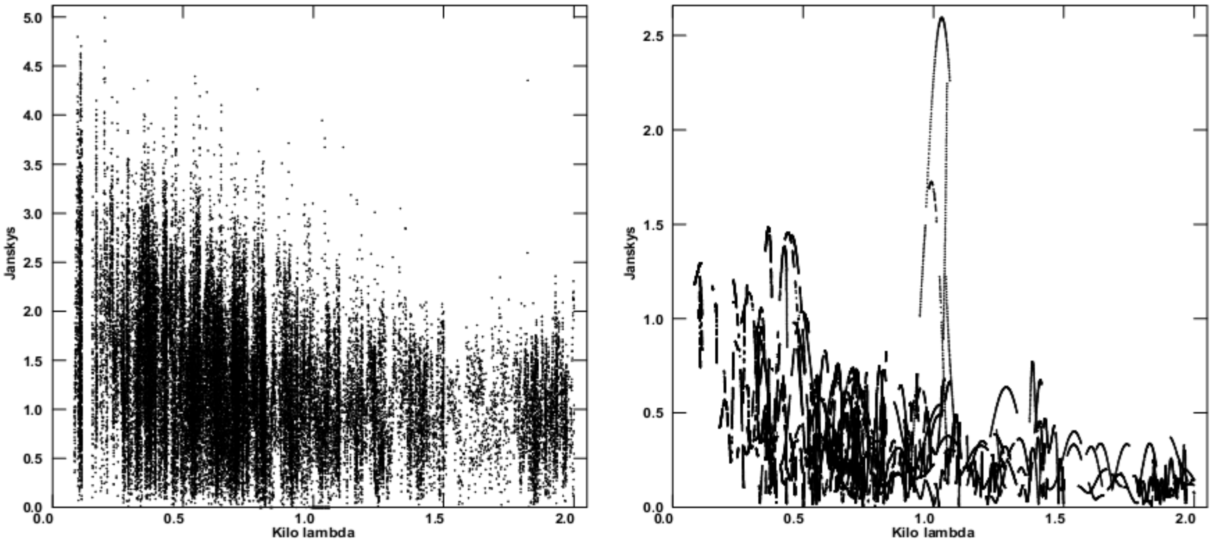

Figure 2.16: Left: The uv−plot of the raw data. No obvious bad baselines are prominent so it is difficult to make progress. Right: The uv−plot of the model generated data. Here, we can see there is some clearly anomalous data, which can be inspected and removed. Image taken from Basu et al. (2012).

can calculate the distance in the uv−plane. This will not give the identity of the bad baseline, as there are normally many baselines with similar uv distances. We can use this knowledge to inspect the visibilities, however, looking at the raw data it is normally difficult to find any obvious bad baselines that have not already been flagged.

To get around this, we have to simulate what the uv−data would look like considering only the stripes. We start by creating a uv−data file that has a noise level similar to our actual data. It is creating using only the points on the uv−plane that we had gathered in our observations. Next, we take a cutout of the stripes in the image plane in a region where there are no sources present. This is then Fourier transformed and added to the noise, resulting in a uv−file that we can inspect. The bad baseline should be more obvious as the contribution of the stripe has been singled out. We can then remove this from our original data, and iterate the process to gradually improve our image. Figure 2.16 shows the difference between the uv−plots of the raw and model generated data. The AIPS commands that are used for this are: UVMOD, SUBIM and UVSUB.

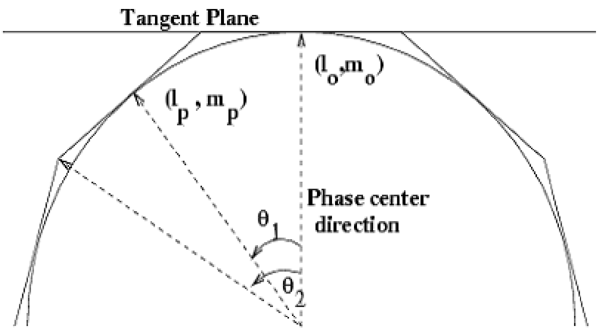

Figure 2.17: A diagram showing the use of multiple facets for wide-field imaging. Image from the NRAO Synthesis Imaging Workshop presentations.

2.8 Wide-field imaging

At low frequencies, the field of view is much greater than what is typical for other wavelengths of astronomy. At 610 MHz, which is the highest frequency we observe with the GMRT, the field of view extends to a radius of ~0.75°. In order to image such a wide field, we can no longer simply assume that the w term in Equation 2.7 is negligible. Instead, one option to take this into account is to split up the celestial sphere into a number of smaller tangential planes, or 'facets'. From this, we can use our previous 2D approximation and imaging techniques and then re-project the facet images back onto a single 2D image. This significantly improves the images created, with the downside that it is computationally expensive to make so many images. This technique is implemented in the current version of IMAGR in the AIPS software. Figure 2.18 shows an image of the field of view of RBS797. This is observed at 150 MHz, and covers an area of 9 deg^2.

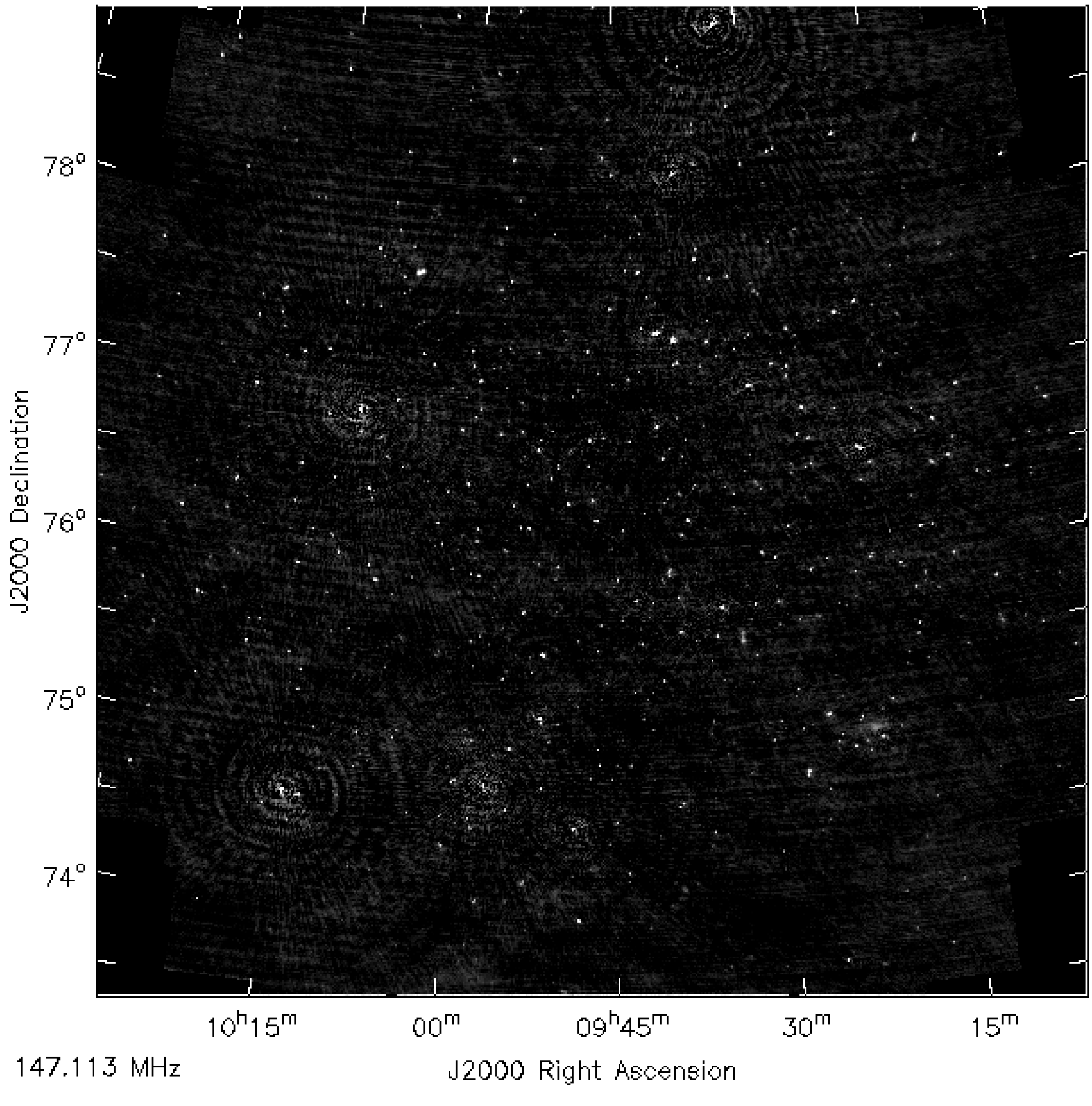

Figure 2.18: The wide field of RBS797, shown here at 150 MHz. This image has not been corrected for the primary beam. The rms noise is ~1 mJy beam^{-1}. The individual facets can be seen around the outskirts of the image. It is important to be able to image the bright sources away from the centre of the image as well, as otherwise their flux would be distributed throughout the image as noise.

Chapter 3

The energetics of the radio AGN population in clusters

3.1 Introduction

Supermassive black holes (SMBH) play a vital role in the life of a galaxy. At the heart of our own Milky Way galaxy is a strong compact radio source, named Sagittarius A*. Observed at the galactic centre is a collection of stars whose individual orbits were tracked around this central source for a number of years. With this lengthy amount of data it is then simple enough to calculate the mass and size of the object the stars are orbiting – a SMBH with mass $\sim 4 \times 10^6$ $M_\odot$ (Ghez et al., 2008; Gillessen et al., 2009). The M–σ relation (Ferrarese and Merritt, 2000; Gebhardt et al., 2000; King, 2003) suggests that the formation and evolution of the SMBH and galaxy are interlinked, and hence these black holes are ubiquitous at the centres of galaxies (Tremaine et al., 2002).

One way that a SMBH can grow is to accrete matter from its host galaxy, leading to an active galactic nucleus (AGN). Studying AGN is important to understanding both the origin and growth of black holes, as well as the formation and evolution of galaxies throughout the universe. Gas within the inner regions of the galaxy is drawn into the black hole accretion disk, where it will feed the SMBH. During the accretion process, a large amount of energy is released. The energy released by the growth of the black hole can be shown as $E_{\mathrm{BH}} = \epsilon M_{\mathrm{BH}} c^2$, where $\epsilon = 0.1$ is the radiative efficiency of the accretion process, normally estimated at around 10% (Fabian, 2012).

The binding energy of the galaxy can be simply approximated as $E_{\rm bind} \approx \mathrm{M}_\star \sigma^2$, with σ being the velocity dispersion of the galaxy as above. Comparing these two equations and inputting standard galaxy values (e.g. $M_{BH} \sim 1.4 \times 10^{-3}\,\mathrm{M}_{\rm gal}$, $\sigma \sim 300\,\mathrm{km\,s^{-1}}$), it is clear that there is more than enough energy available for the AGN to easily expel the reservoir of gas from its host galaxy. Whether this occurs is down to how much of this energy actually interacts with the galaxy. If even a small fraction of the energy available can be transferred to the gas, the AGN would play a large role in the evolution of its host galaxy. There are two major forms of AGN feedback that have been identified, differing predominantly in the rate of accretion of material onto their black holes (see e.g. Best and Heckman, 2012).

In this paper, we report results of observations of AGN at radio wavelengths, with the emission coming mostly from synchrotron radiation due to AGN jets emanating from the black hole. These jets can transfer energy by a variety of processes to the surrounding gas and potentially eject gas from the system. We use the Giant Metrewave Radio Telescope (GMRT) to take deep radio observations of a sample of galaxies in at least two low frequencies. These low frequencies provide the best tracers to the total energy output of the radio jets. This, along with quality infra-red data from *LoCuSS* (see §3.4.1), will enable us to take an in-depth look at the energies involved and investigate how the mechanical power from the AGN jets compare to the gravitational binding energy of the galaxy. We compare our results to recent simulations to ascertain how well the models correlate with what we observe.

Once the black hole fuel is exhausted, the black hole becomes dormant and the galaxy is no longer classified as an AGN. We define the duty cycle of an AGN as the ratio of the length of time that the AGN is active, to its total lifetime (i.e. $t_{\rm on}/(t_{\rm on} + t_{\rm off})$). It is an important factor to quantify in order to gauge the importance of AGN feedback (Shabala et al., 2008). Determining the fraction of galaxies that host a radio AGN gives an insight into the duty cycle of black hole growth. Best et al. (2005a) found a strong dependence of the radio-loud fraction with galaxy mass in the local universe, implying larger galaxies trigger the radio jets more often than smaller ones. With our deeper GMRT data, we will look at this relationship and how it varies with radio luminosity. Our sample, with a mean $z \sim 0.2$, extends to a higher redshift than that of Best et al. (2005a).

The paper is organised as follows. Section 3.2 outlines the details of our radio observations and reduction process. Section 3.3 describes the construction of our source catalogue. In Section 3.4, we describe the galaxy properties of our sample and detail our radio analysis and the process we use to remove contaminating radio emission from star-forming galaxies. In Section 3.5 we present our results on the properties and energetics of our radio AGN sample and compare to recent simulations. Our conclusions are presented in Section 3.6.

Throughout this work, we have adopted a lambda cold dark matter (ΛCDM) cosmology with $H_0 = 71\,\mathrm{km\,s^{-1}\,Mpc^{-1}}$, $\Omega_m = 0.27$ and $\Omega_\Lambda = 0.73$. Optical and infra-red magnitudes have been normalised to the AB system.

3.2 GMRT Radio Observations & Reduction

3.2.1 Observations

Radio observations were taken using the *Giant Metrewave Radio Telescope (GMRT)*, located near Pune, India. Our sample consisted of four clusters: Abell 1835, Abell 2218, RXJ 1720.1+2638 and Abell 2390. These clusters are described in Table 3.1, and the observation details are summarised in Table 3.2. They were observed for several hours at 235 and 610 MHz in the GMRT cycles 16, 18, 19 & 20, between May 2009 and July 2011. The observations were carried out in spectral line mode, using the GMRT Software Backend (GSB; Roy et al., 2010) (except for Abell 1835, which used the hardware backend as it was in cycle 16). The dual frequency circular polarization mode was used so that both frequencies could be observed simultaneously.

The observations were recorded at 610 MHz using both the upper and lower side bands (USB & LSB), giving a total of 256 channels available, each with a spectral resolution of 130 kHz/channel. The number of usable channels for 235 MHz was lower, typically 6 MHz in

Table 3.1: List of Galaxy Clusters

Cluster Name	RA_{J2000} ($^{\mathrm{h\ m\ s}}$)	Dec_{J2000} ($^{\circ}$,$'$,$''$)	z	$S_{1.4\,\mathrm{GHz}}$ [a] (mJy)	$\log P_{1.4\,\mathrm{GHz}}$ ($\mathrm{W\,Hz^{-1}}$)	Scale ($\mathrm{kpc}\,''^{-1}$)
Abell 1835	14:01:02.1	02:52:41.9	0.2532	32.2	24.79	3.913
Abell 2218	16:35:54.0	66:13:00.1	0.1756	[b] 4.7	23.60	2.949
RXJ 1720.1+2638	17:20:08.9	26:38:06.0	0.1640	89.0	24.81	2.789
Abell 2390	21:53:34.6	17:40:10.9	0.2280	63.0	24.98	3.621

---

[a] From Bîrzan et al. (2008)

[b] From Giovannini and Feretti (2000)

bandwidth. RXJ1720 was a more recent observation, and hence had double the number of channels available, with a resolution of 65 kHz/channel.

3.2.2 Reduction

The datasets were calibrated and analysed using the NRAO Astronomical Image Processing System ($\mathcal{AIPS}$) package. The data were visually inspected for radio frequency interference (RFI) before being calibrated. The usual VLA amplitude calibrators were observed at the beginning and end of the observing run, and the flux density was set using the $\mathcal{AIPS}$ SETJY implementation of the scale of Perley and Butler (2013). Phase calibrators were observed between each observation of the target source, to correct for ionospheric and instrumental gain variations. The flux and phase calibrators were then used on a central channel free of RFI to obtain the bandpass correction for each antenna. A few channels near the edges of the band were removed due to excessive noise. To increase the signal-to-noise, the channels were combined to give some averaged channels of ~2 MHz each at 610 MHz, and ~0.7 MHz at 235 MHz. Bandwidth smearing is not a problem at this level of averaging.

Further careful inspection of the averaged channels was completed before the bandpass calibration was applied and the target source was split from the multi-source data. Several rounds of phase-only self calibration and imaging were then undertaken for each data set, using the wide-field imaging technique, in order to account for the non-planar nature of the sky. This is because of the wide field of view (~0.4 deg^2 for 610 MHz, ~3 deg^2 for 235 MHz) of

Table 3.2: GMRT Observation Details

Cluster	Obs. Date dd/mm/yy	Project code	ν (MHz)	Bandwidth (MHz)	Int. Time (min)	Beam, PA (″ × ″, °)	rms (mJy beam^{-1})
Abell 1835	06/05/09	16_051	610	27.5	203	9.5 × 4.9, 60.4	0.070
	06/05/09	16_051	235	5.6	203	18.9 × 13.6, 42.3	1.1
Abell 2218	19/05/10	18_015	610	31.0	484	7.4 × 5.6, 66.5	0.027
	19/05/10	18_015	235	6.0	484	15.1 × 14.0, −53.3	0.39
RXJ 1720	23/07/11	20_016	610	33.0	346	6.6 × 4.3, 61.1	0.060
	23/07/11	20_016	235	12.0	346	14.9 × 12.0, 60.2	0.45
Abell 2390	23/12/10	19_010	610	29.0	309	5.6 × 4.9, −68.2	0.13
	23/12/10	19_010	235	6.2	309	13.2 × 10.7, 63.9	0.73

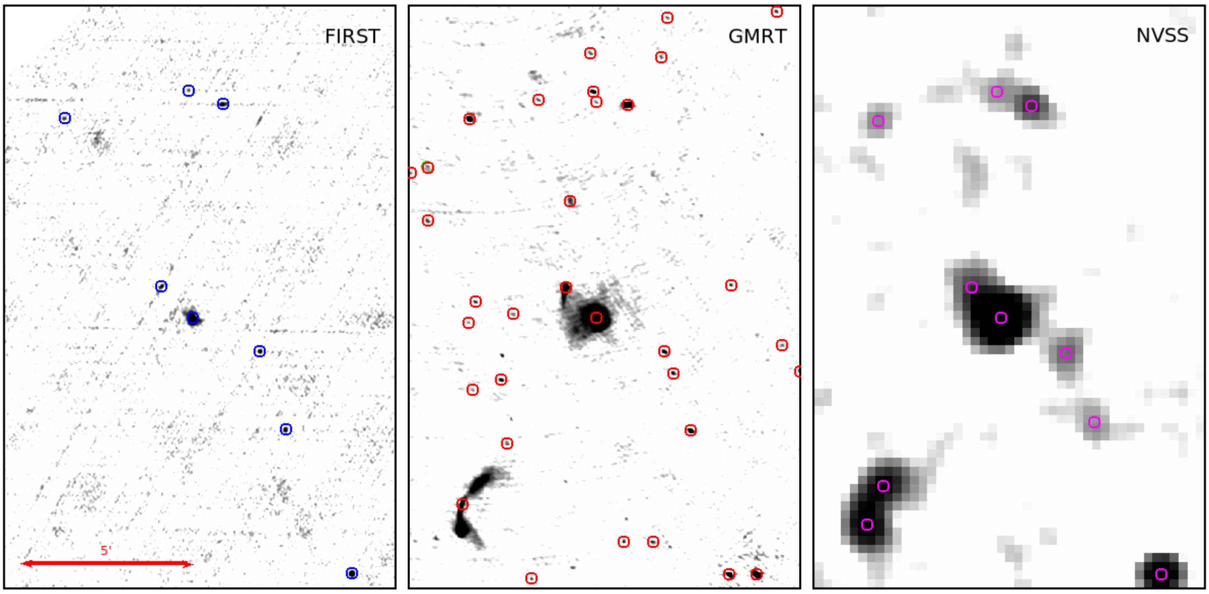

Figure 3.1: Comparison between the radio sources detected in GMRT (centre), FIRST (left) and NVSS (right) for the RXJ1720 cluster. Circles show the positions of detected radio sources, which may have some extended emission. The red arrow in the bottom-left corner shows 5 arcmin.

the GMRT. 109 facets were used for each observation to cover the field, each being imaged separately before being combined into one image.

Amplitude and phase self-calibration was completed before the final images were produced using the multi-scale CLEAN algorithm in the IMAGR task. These were then corrected for the primary beam.[1] This was applied out to a radius where the correction factor is 10, any further than this was blanked out. This corresponds to angular radii of 35.3 and 102.7 arcmin for 610 and 235 MHz respectively.

---

[1] `http://ncra.tifr.res.in/~ngk/primarybeam/beam.html`

Our deep GMRT data enables us to explore our sample in much greater detail than possible with other radio surveys. We have data at lower frequencies that allow emission from earlier epochs to be observed. Figure 3.1 gives an example of the quality of our GMRT data at 610 MHz, compared to that of the 1.4 GHz frequency images from the FIRST and NVSS surveys (see §3.3.3). One clear example is the double source to the south-east of the image; it is not resolved when viewing with the NVSS, whereas it is resolved out when using the FIRST survey. This underlines the importance of having good coverage of the uv plane, allowing us to have both good resolution and sensitivity to extended sources.

Using the full uv range (~0.1–50 kλ and ~0.05–20 kλ at 610 and 235 MHz respectively), gives us a typical resolution of ~6 arcsec at 610 MHz, and ~13 arcsec at 235 MHz, as well as good sensitivity to extended sources. The rms noise level (1σ) for our full-resolution images drops to as low as 20 µJy for our deepest observations, an illustration showing the typical local rms across the field is shown in Figure 3.2.

The average residual amplitude errors on each individual antenna are $\leq 5\%$ at 610 MHz and $\leq 8\%$ at 235 MHz. (e.g., Chandra et al., 2004). Therefore, we assume the absolute flux density calibration is accurate to within these error margins.

3.3 The source catalogue

3.3.1 Source extraction

Various source extraction techniques were explored but many had problems with the high rms on the outskirts of the field, and the need to detect faint sources near the centre. This resulted in either too many false positives, or poor sensitivity to fainter sources. Therefore, a local rms map was created to take into account the varying sensitivity levels across the field. This was made by finding the rms inside a 100 by 100 pixel square surrounding each pixel in the image. The $\mathcal{AIPS}$ task SAD was used along with the local rms map to detect all sources in the image that had a peak value $\geq 5\sigma$. Gaussian models are then fitted to the image by the least-squares method and the measured positions and fluxes of the sources are output to a file and subtracted from the image.

This file was then used to make a radio source catalogue. This source finding technique is optimised for point sources, so extended and double sources needed to be located in a different manner. This was done by looking at the point source subtracted image and finding the (usually obvious) extended sources. Their fluxes and positions were then recorded manually using the TVSTAT tool. This record was then merged with the point source catalogue and an internal match of radius 10 arcsec was performed using the TOPCAT[1] software (Taylor, 2005). Each source was visually inspected and codified according to the morphology of the radio source. Any sources that were identified more than once (e.g. an extended source split up into multiple components), take the flux and position of the manually recorded entry. This leaves the final radio source catalogue.

3.3.2 Catalogue cross-correlation and matching

A catalogue of galaxies within the *UKIRT/WFCAM* K-band images was created for each of the clusters. More information on the infra-red data can be found in §3.4.1. The radio and infra-red catalogues were then cross-correlated within a radius of 10 arcsec. Multiple matches were resolved by visual inspection, which was done for all radio sources. Typically the positions of the radio source and the corresponding infra-red source were within 3 arcsec. Information such as cluster membership, redshift, and hence radio luminosity are then calculated. Upper limits in the radio are then calculated using the local rms map and using the 5σ value at each source position in the infra-red catalogue. As shown in Figure 3.2, the rms is affected by several things; the quality/depth of the data, proximity of bright sources, and the distance from the centre of the image. Figure 3.3 shows the fluxes and apparent magnitudes observed for each galaxy. We observe that the most luminous galaxies at radio wavelengths also tend to be optically brightest, we will discuss this further in §3.5.1.

---

[1] `http://www.starlink.ac.uk/topcat/`

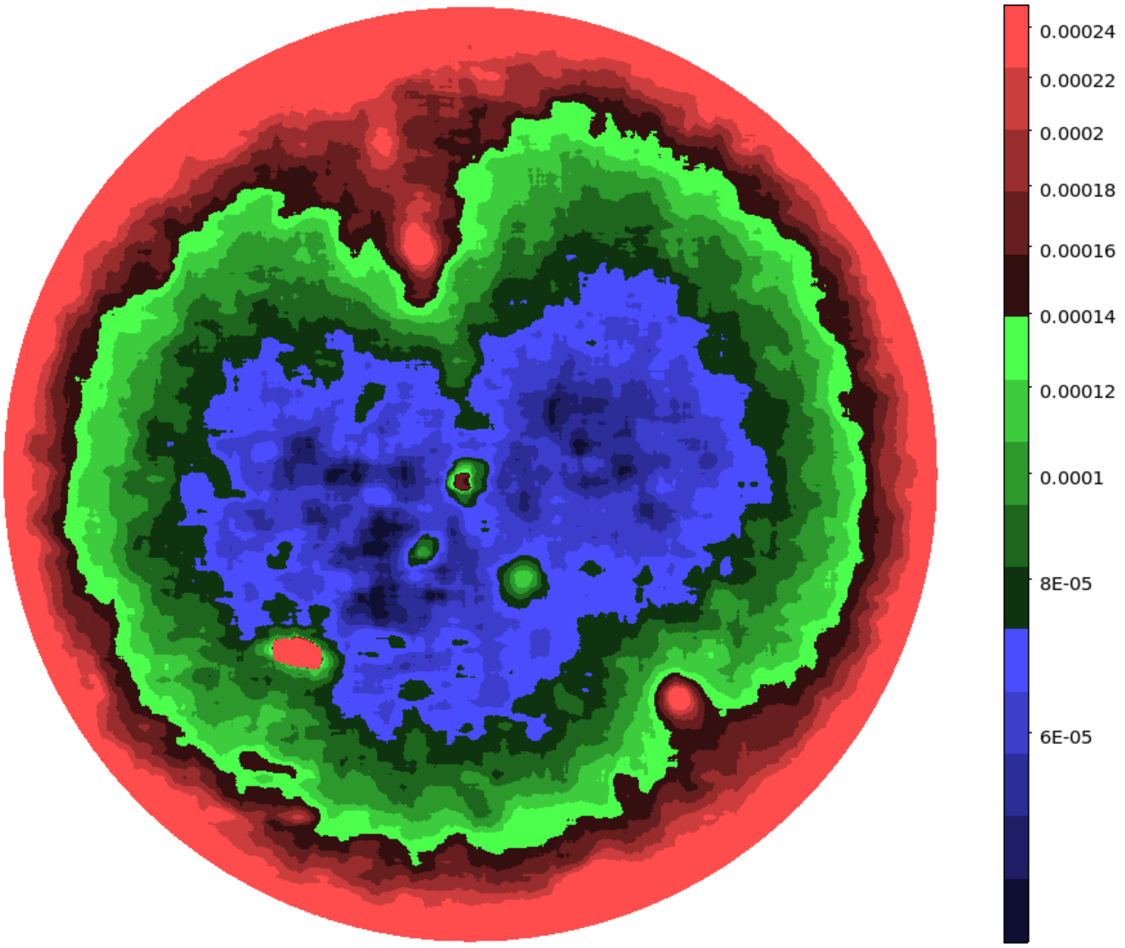

Figure 3.2: The local rms map for the cluster RXJ1720, the colourbar scale has units of Jy. A square of dimensions 100 by 100 pixels is used to calculate the rms for each point of the map. As is standard with radio observations, the sensitivity decreases as a function of radius from the centre. Other regions of higher noise are due to being near bright sources.

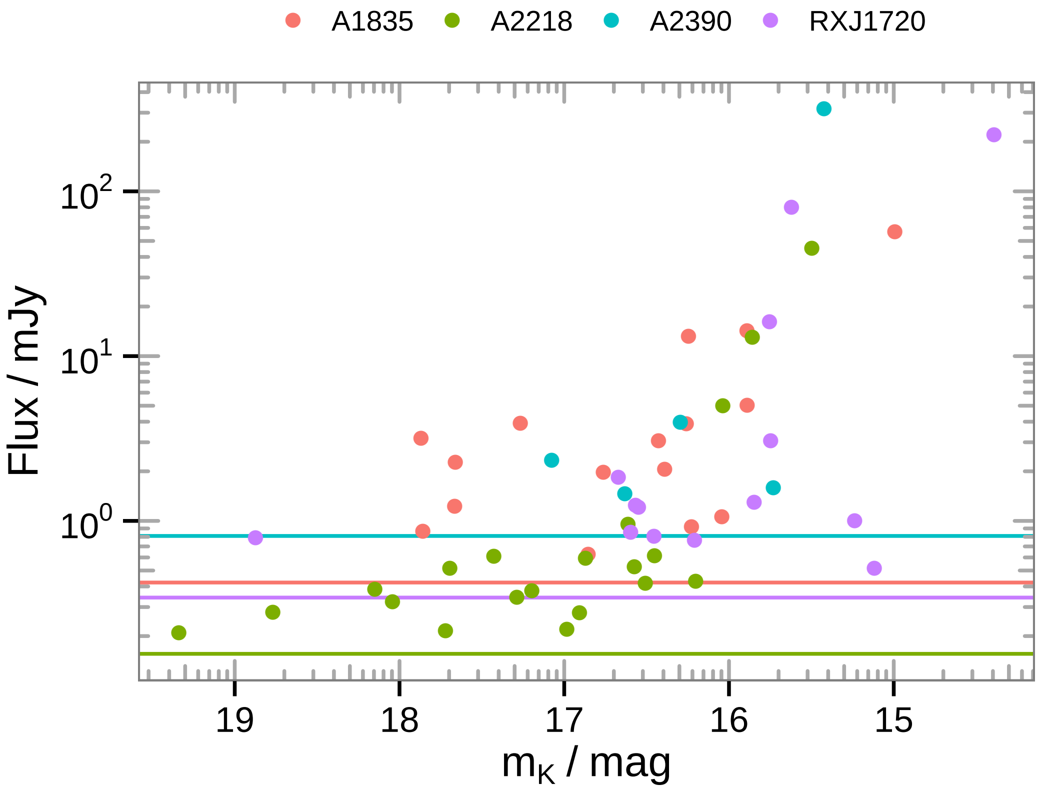

Figure 3.3: Detected radio flux density as a function of K-band apparent magnitude. Horizontal lines are the median upper flux limits (5σ) for each cluster. Different coloured points correspond to the different clusters for each detected galaxy.

3.3.3 Comparison with other radio catalogues

Two major radio frequency surveys are the NRAO VLA Sky Survey (NVSS; Condon et al., 1998) and the Faint Images of the Radio Sky at Twenty-cm survey (FIRST: Becker et al., 1995).

The NVSS is a 1.4 GHz continuum survey covering the entire northern sky. It is complete to ∼2.5 mJy and the rms brightness fluctuations are ∼0.45 mJy beam^{-1}.[1] The NVSS images are made using a large restoring beam, giving a resolution of 45 arcsec. The FIRST survey also uses the VLA to take three minute snapshots of the northern sky at 1.4 GHz. The survey area is designed to overlap that of the SDSS, so that optical counterparts to the radio sources can be identified. These observations are taken in the B-configuration of the VLA, giving a resolution of ∼5 arcsec. The typical rms in the survey is 0.15 mJy, and at the 1 mJy source detection threshold there are ∼ 90 sources per square degree.[2] Figure 3.4 plots all of the observed radio sources in our sample as a function of frequency. We link with a connecting line a galaxy detected at multiple frequencies, so spectral indices can then be easily calculated. We have also cross-correlated our sample with the two VLA snapshot surveys above, and these are also plotted at 1.4 GHz. Our observations at 610 MHz are clearly deeper than previous surveys at higher frequencies, with several detections unmatched at the bottom of the figure. Our 235 MHz sensitivity limits are comparable to NVSS and FIRST, despite sources typically being much brighter at these lower radio frequencies. Figure 3.1 shows the difference between the surveys visually. Another advantage is that our low frequency data come from a single observatory and are analysed uniformly. This improves our flux density and spectral index measurements compared to mixed archival source data. Best et al. (2005a) investigate radio sources detected in NVSS/FIRST with a flux density above 5 mJy. This corresponds to $L_{1.4\,\mathrm{GHz}} \sim 10^{23}$ W Hz^{-1} at $z \sim 0.1$. A 5 mJy source at 1.4 GHz would be 9.7 mJy at 610 MHz, assuming a spectral index of −0.8.[3]

---

[1] `http://www.cv.nrao.edu/nvss/`

[2] `http://sundog.stsci.edu/first/description.html`

[3] We define the spectral index α, as $S_\nu \propto \nu^\alpha$.

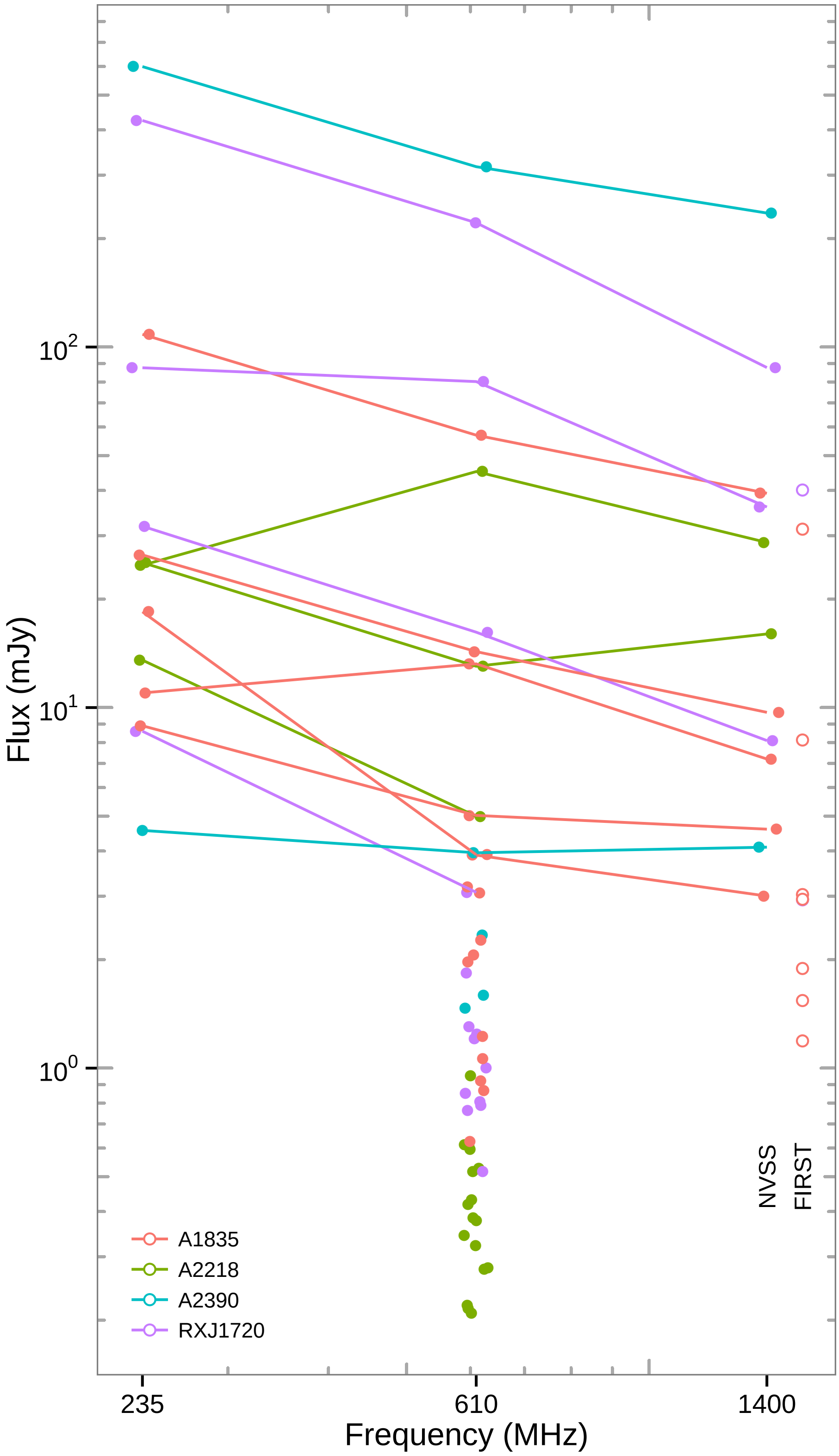

Figure 3.4: Each cluster source is shown here for each frequency it is detected at. Each connected line is a single cluster source. Points have been position-jittered in the x-axis to reduce overlapping. The filled sources at 1.4 GHz are from the NVSS, and the open circles are taken from FIRST. Both are at the same frequency. Not all sources are detected with both NVSS & FIRST. Typical errors in flux are 5 and 8 % for 610 and 235 MHz respectively.

3.4 Galaxy properties

3.4.1 LoCuSS

LoCuSS is a multi-wavelength survey of a morphologically-unbiased sample of 80 X-ray luminous clusters in the redshift range $0.15 < z < 0.30$ drawn from the *ROSAT* All Sky Survey cluster catalogues. It is primarily aimed at calibrating the mass-observable scaling relations obtained from weak-lensing, X-ray or Sunyaev-Zel'dovich analyses (Haines et al., 2013). The four clusters in this work are all drawn from the first batch of 30 clusters, for which we have obtained a particularly rich multi-wavelength dataset, including: Subaru/Suprime-Cam optical imaging (Okabe et al., 2010), *Spitzer*/MIPS 24 µm maps, *Herschel*/PACS+SPIRE 100–500 µm maps, *Chandra* X-ray data, and near-infrared (NIR; J, K) imaging. All of these data embrace at least $25' \times 25'$ fields of view, centred on each cluster, and thus probe the clusters out to $\sim$1.5–2 virial radii (Smith et al., 2010).

All four of our clusters have extensive spectroscopic data as part of the recently-completed Arizona Cluster Redshift Survey (ACReS), which provides highly complete redshift coverage of cluster members down to $M_K^\star + 2.0$, obtained using the Hectospec multi-object spectrograph on the 6.5 m MMT telescope at Mount Hopkins, Arizona. For the clusters A1835, A2390 and RXJ1720 targets were selected from the available UKIRT/WFCAM J, K-band imaging, providing coverage over a $52' \times 52'$ field of view and sensitive to galaxies down to $K \sim 19$, $J \sim 21$, while for A2218 targets were selected from comparably deep J, K-band imaging obtained with the $27' \times 27'$ NEWFIRM instrument on the 4.0 m Mayall telescope at Kitt Peak. We also include those redshifts obtained from previous studies of these clusters, in particular Yee et al. (1996) for A2390 (134 additional cluster members), Czoske (2004) for A1835 and Owers et al. (2011) for RXJ1720. Overall, our spectroscopic coverage is 87% complete for cluster galaxies within r_{200} and brighter than $M_K^\star + 2.0$. We prioritized those targets detected at 24 µm, such that we are 100% complete for probable cluster members with $f_{24} > 0.4$ mJy. There is little variation with cluster-centric radius, as we observed each of the four clusters with 4 or 5 configurations,

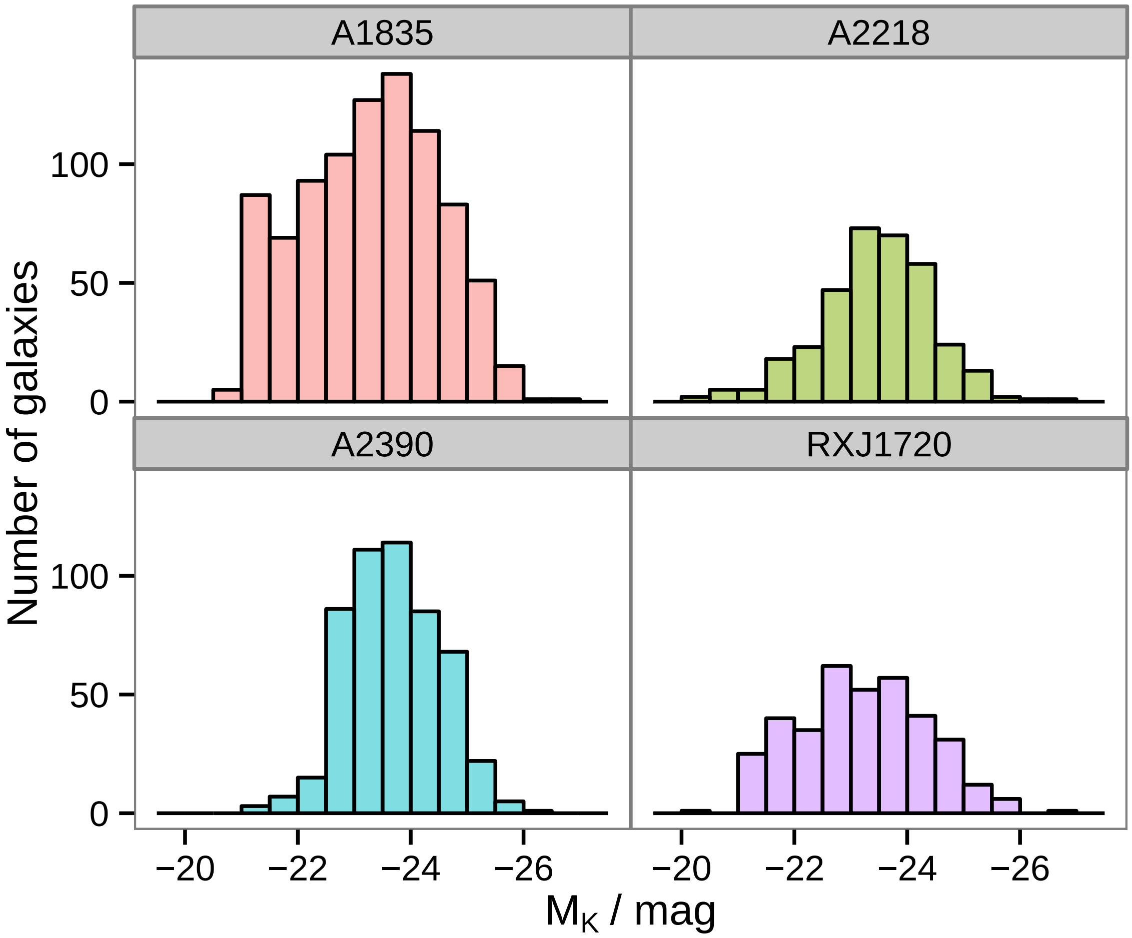

Figure 3.5: A histogram of the distribution of galaxy K-band absolute magnitudes in each of the clusters.

thus minimizing the effects of fiber collisions on incompleteness, while the previous targetted surveys from the literature tended to fill in any residual incompleteness in the densest parts of the cluster cores. Figure 3.5 shows the distribution of K-band light for each of the cluster members in our sample.

3.4.2 Star formation rates

Radio AGN are not the only extragalactic source of radio emission, so it is important to consider what effect other potential sources have on our data. The most important possible contaminant is that of star forming galaxies. These can contribute a significant amount of radio luminosity, especially at the lower mass end where their number density dominates over AGN (Best et al., 2005b).

To distinguish between the two sources of radio luminosity, each cluster was observed across a 25′ × 25′ field of view at 24 µm with MIPS (Rieke et al., 2004) on board the *Spitzer Space Telescope*, reaching typical 90% completeness limits of 0.4 mJy. *Herschel* PACS/SPIRE imaging from the LoCuSS *Herschel* Key Programme provides 100–500 µm photometry for matched 25′ × 25′, reaching comparable sensitivities in terms of obscured star formation rates (SFR) and allowing us to obtain total infrared luminosities and distinguish between infrared emission powered by AGN and star formation. For each 24 µm-detected galaxy with known redshift, its rest-frame 24 µm luminosity is estimated by comparison of its 24 µm flux to the luminosity-dependent template infrared spectral energy distributions of Rieke et al. (2009). The latter is then converted to a SFR using the calibration of Rieke et al. (2009), shown in Equation 3.1,

$$\mathrm{SFR}\left(\mathrm{M}_{\odot}\,\mathrm{yr}^{-1}\right) = 7.8 \times 10^{-10}\,\mathrm{L}\left(24\,\mu\mathrm{m}, L_{\odot}\right) \tag{3.1}$$

which is valid for either a Kroupa or Chabrier IMF. The data are sensitive to obscured SFRs in cluster galaxies down to 1–2 $\mathrm{M}_{\odot}\,\mathrm{yr}^{-1}$.

For each galaxy with detected radio emission, we compare our infrared data from *Spitzer* and *Herschel*. The dust around the SMBH is heated to above 200 K, emitting radiation peaking at 20–30 µm (e.g. Del Moro et al., 2013). The deficiency of colder gas reduces any emission at wavelengths longer than λ >30 µm. However, dust is heated to a wide range of temperatures via star formation, and emits radiation across the entire infrared spectrum. Three galaxies in our sample with 24 µm emission are not detected with *Herschel*, and thus their emission is likely due to dust heated by AGN rather than star formation. They are identified as QSOs from spectroscopy and are unresolved in optical images. We thus consider their SFR to be negligible. The three brightest cluster galaxies (BCGs) with radio emission have been studied previously in Rawle et al. (2012). They confirm that their infrared emission is produced mostly by star formation. §3.4.7 details how we remove the estimated star formation contribution from the detected radio flux.

3.4.3 X-ray data

The deprojected dark matter densities, gas densities and gas temperature profiles for each cluster were derived by fitting the phenomenological cluster models of Ascasibar and Diego (2008) to a series of annular spectra extracted for each cluster from the *Chandra* data (Sanderson and Ponman, 2010). The best-fitting cluster models were used to estimate r_{500} and r_{200}, the radii enclosing mean overdensities of 500 and 200 with respect to the critical density of the Universe at the cluster redshift.

The *Chandra* data were also used to identify X-ray AGN among the cluster members as described in Haines et al. (2012). The survey limit of six broad (0.3–7 keV) X-ray counts allows us to detect any X-ray AGN with $L_X > 1.5 \times 10^{41}$ erg s^{-1} associated with any of the four clusters in our sample. Of the 2110 cluster members in our sample, only 17 (0.8%) are detected in the X-ray with *Chandra*, of which 7 are radio-loud. This includes three BCGs.

3.4.4 Stellar masses

Stellar masses are estimated using a combination of the K-band data from LoCuSS, and colour information from optical SDSS magnitudes (York et al., 2000). The mass-to-light ratio used to derive the stellar masses was taken from Bell et al. (2003), and is shown in the following equation:

$$\log\left(\frac{M}{L_K}\right) = a_K + \left(b_K \times (g - r)\right) \tag{3.2}$$

where a_K and b_K are coefficients from Bell et al. (2003), g and r are SDSS magnitudes in those filters, and the M/L_K ratio is in solar units. The difference between a normal Salpeter IMF and the 'diet' version is that it only has 70% of the mass because of a lower number of faint low-mass stars (Bell, 2003). 0.1 was subtracted from the zeropoint (a_K) to convert from a 'diet' Salpeter to a Chabrier IMF – this is the IMF we used earlier (Dutton and van den Bosch, 2009).

The mass-to-light ratios from this relationship were calculated to be between 0.69–0.94 for the 10–90 per cent quantiles. This resulted in stellar masses ranging from $\sim 10^{10}$–10^{12} M$_{\odot}$ for our cluster members. As K-band light is a good indicator of stellar mass, the mass-to-light ratio is less sensitive to (g-r) colours. Other ways of estimating stellar masses of these galaxies include from calculating velocity dispersions from the virial theorem, and by scaling from their luminosities using full spectral energy distribution (SED) modelling. We use K-band data here as the required measurements for the other methods were not available to us. A2218 is not within the SDSS footprint, so we do not have colour information for these galaxies. The mean of the other K-band mass-to-light ratios, $0.8\,\Upsilon_\odot$ was therefore assumed. To maintain homogeneity of data, we restricted our study to the SDSS.

3.4.5 Binding energies

Using the stellar masses calculated earlier, we can estimate the halo mass, M_{200}, *that a galaxy would have if it was not incorporated into a galaxy cluster.* From this we can approximate the amount of energy needed to unbind gas from that galaxy.

Our halo mass estimates are obtained using halo abundance matching following results in simulations from Moster et al. (2010). The cold dark matter model of the Universe makes predictions about the abundance of collapsed objects at any given epoch. We make the assumption that the number of dark matter halos expected should match with the number of galaxies observed. This enables us to obtain a link between the stellar mass of a galaxy and the dark halo halo mass; this method is called 'abundance matching' and is one of the tools used in semi-analytic simulations of galaxy formation (Ferrero et al., 2012).

$$\frac{m(M)}{M} = 2\left(\frac{m}{M}\right)_0 \left[\left(\frac{M}{M_1}\right)^{-\beta} + \left(\frac{M}{M_1}\right)^{\gamma}\right]^{-1} \tag{3.3}$$

where the parameters given in the literature are $M_1 = 10^{11.899}$, $\left(\frac{m}{M}\right)_0 = 0.02817$, $\beta = 1.068$, $\gamma = 0.611$. M_{200} was calculated for all of our galaxies, from which r_{200} can be calculated using

$$r_{200} = \left(\frac{3\,M_{200}}{4\pi\,\rho_{crit} \times 200}\right)^{1/3} \tag{3.4}$$

where $\rho_{\rm crit} = \dfrac{3H}{8\pi G} = 9.30 \times 10^{27}\,\mathrm{kg\,m^{-3}}$.

Written simply, r_{200} is the radius of a sphere within which the average overdensity is 200 times the density of matter in the universe. m_{200} is the mass of a sphere with radius r_{200}.

We then use the following binding energy calculation, which is approximated using

$$E_{\text{bind}} \sim \frac{G f_b {M_{200}}^2}{r_{200}} \tag{3.5}$$

where the universal baryonic mass fraction, $f_b = \dfrac{\Omega_b}{\Omega_m} = 0.175$ (Spergel et al., 2007). This essentially approximates the amount of energy needed to eject the gas from a dark matter halo to infinity, and is better than just ejecting it to the outskirts of the system, where it would just fall back in again. This approximation is accurate enough for our purposes.

3.4.6 Radio analysis

Radio powers for each frequency are calculated using Equation 3.6,

$$P_\nu = 4\pi\, D_L^2\, (1+z)^{-(\alpha+1)}\, S_\nu \tag{3.6}$$

where D_L is the luminosity distance to the source, z is the redshift, α is the spectral index and S_ν is the flux density of the source at the frequency ν. If no spectral index is known for the source, we set $\alpha = -0.8$, a typical value for extragalactic radio sources (Condon, 1992).

Table 3.3 shows a summary of the key properties and results for each of the detected radio cluster members.

3.4.7 Removing contamination from star-forming galaxy radio emission

Figure 3.6 compares the detected star formation rate as a function of galaxy stellar mass. If a galaxy is detected in our radio data, it is plotted as a filled point. Of the 2110 cluster members in our sample, 319 have an estimated SFR. Only ~10% of the galaxies in this star-forming subsample have detected radio emission at 610 MHz.

Table 3.3: This table describes the galaxy properties for the 56 radio-loud cluster members in our sample. Column 1 gives the name of the cluster that the galaxy is in, and column 2 has the ID number of that galaxy within the cluster. Columns 3–5 give the RA, Dec and redshift of the galaxy, and columns 6–7 have the K-band apparent magnitude and 610 MHz radio fluxes respectively. Column 8 shows the estimated star formation rate for each galaxy in solar masses per year (see §3.4.2 for calculations, uncertainties not listed in original source of data), and columns 9 and 10 have the derived stellar and halo masses. The halo mass is found using the halo abundance matching described in §3.4.5. Column 11 displays the mechanical power output estimated from the radio jets of the AGN, further described in §3.5.2.

Cluster	ID	RA_{J2000} (deg)	Dec_{J2000} (deg)	z	m_K (mag)	S_{610} (mJy)	SFR ($M_\odot\,yr^{-1}$)	$M_\star$ ($10^{10}\,M_\odot$)	M_{200} ($10^{12}\,M_\odot$)	P_{mech} ($10^{42}\,erg\,s^{-1}$)
A1835	25292	210.1326	2.9120	0.2505	13.99	5.02	2.8	46	310	38
A1835	30299	210.2462	2.9337	0.2498	14.36	3.90	0.	35	150	29
A1835	30309	210.2451	2.8854	0.2611	14.86	1.97	7.8	17	27	19
A1835	30409	210.2586	2.8785	0.2518	13.09	57.0	170	83	1400	210
A1835	30605	210.2687	2.9069	0.2486	14.53	3.07	0.	29	100	24
A1835	31139	210.4376	2.8926	0.2491	14.14	1.06	42	37	180	11
A1835	31847	210.3654	2.9350	0.2647	15.76	2.26	0.	7.0	3.2	22
A1835	35524	210.4928	3.0211	0.2529	14.95	0.626	4.8	17	24	8.1
A1835	45956	210.0024	2.6740	0.2581	14.33	0.921	0.	35	150	11
A1835	50106	210.2813	2.8754	0.2570	15.96	0.867	0.	8.4	4.6	10
A1835	50147	210.2620	2.8691	0.2443	15.37	3.91	0.	14	14	56
A1835	50296	210.2560	2.8617	0.2521	15.97	3.18	0.	7.5	3.7	26
A1835	51642	210.2786	2.7047	0.2473	15.76	1.23	8.1	7.6	3.8	13
A1835	52167	210.3173	2.7537	0.2447	14.49	2.06	0.	30	110	18
A1835	55669	210.5956	2.8096	0.2473	13.99	14.3	0.	48	350	77
A1835	71086	210.3589	2.4933	0.2457	14.35	13.2	0.	35	160	200
A2218	2	248.8322	65.9723	0.1731	13.60	45.1	0.	29	100	500
A2218	1496	249.3231	66.0953	0.1706	14.71	0.954	12	11	7.7	5.8
A2218	2104	248.9001	66.1457	0.1785	15.30	0.378	2.5	6.1	2.5	3.2
A2218	2394	249.0477	66.1696	0.1651	14.61	0.419	1.6	12	10	3.0
A2218	2759	249.0169	66.1945	0.1748	14.55	0.613	0.	12	11	4.4
A2218	2835	248.9797	66.1975	0.1686	16.87	0.280	3.7	1.5	0.58	2.4
A2218	2876	248.8856	66.2008	0.1667	16.14	0.323	2.3	2.9	0.98	2.6
A2218	2919	248.9640	66.2020	0.1740	17.44	0.209	1.5	0.86	0.41	2.0
A2218	3183	249.2353	66.2216	0.1722	15.79	0.516	1.6	3.9	1.4	3.8
A2218	3241	249.2786	66.2241	0.1714	16.25	0.384	1.1	2.6	0.89	3.0
A2218	3278	248.9218	66.2297	0.1809	14.14	4.99	0.	18	27	21
A2218	3428	248.9473	66.2457	0.1686	13.96	13.0	0.	21	44	37
A2218	4198	249.1114	66.2770	0.1751	15.08	0.220	0.	7.5	3.6	2.1
A2218	4729	248.9739	66.2818	0.1811	14.97	0.595	3.8	8.2	4.4	4.5
A2218	4821	249.0317	66.3066	0.1795	15.01	0.277	2.8	7.9	4.1	2.6
A2218	5130	248.9701	66.2769	0.1808	15.82	0.216	3.5	3.8	1.3	2.2
A2218	5238	249.2102	66.2684	0.1766	15.53	0.608	9.9	5.0	1.8	4.4
A2218	5319	248.9864	66.2638	0.1649	15.39	0.344	1.1	5.8	2.3	2.6
A2218	5506	248.7336	66.2451	0.1738	14.67	0.527	0.	11	8.3	3.9
A2218	5823	249.1361	66.4400	0.1729	14.30	0.432	3.7	15	19	3.3
A2390	25489	328.3809	17.6927	0.2459	15.18	2.34	0.	11	8.5	20
A2390	30070	328.4034	17.6955	0.2300	13.52	316	5.7	51	430	600
A2390	37462	328.7656	17.7682	0.2296	14.40	3.96	0.	27	83	45
A2390	45377	328.3718	17.5165	0.2252	13.83	1.59	0.	47	330	13
A2390	51058	328.4719	17.4700	0.2276	14.73	1.47	0.	17	26	12
RXJ1720	5352	260.0135	26.8875	0.1626	13.85	3.07	0.	20	39	13
RXJ1720	25001	260.0418	26.6255	0.1600	12.49	221	0.	69	900	260
RXJ1720	27481	259.8168	26.7416	0.1547	16.97	0.788	0.	1.0	0.46	4.3
RXJ1720	30167	260.0577	26.6411	0.1625	13.85	16.2	0.	21	44	41
RXJ1720	30183	260.0557	26.6820	0.1579	14.77	1.84	0.	8.8	5.1	8.1
RXJ1720	30535	260.0864	26.6273	0.1523	14.55	0.808	2.8	8.9	5.1	4.3
RXJ1720	31011	260.1325	26.6723	0.1589	13.34	1.00	2.7	29	100	5.3
RXJ1720	31061	260.1323	26.6984	0.1599	13.95	1.30	0.	19	33	6.5
RXJ1720	45503	260.0002	26.5989	0.1565	14.65	1.21	8.0	11	7.9	5.9
RXJ1720	46870	259.8241	26.5673	0.1580	14.31	0.763	7.5	12	9.9	4.3
RXJ1720	47261	259.8591	26.5620	0.1538	13.22	0.517	2.5	35	160	3.2
RXJ1720	47443	259.8732	26.5762	0.1589	14.67	1.24	8.9	7.8	4.0	6.2
RXJ1720	51548	260.1146	26.5330	0.1594	13.72	80.2	0.	24	58	220
RXJ1720	52067	260.0972	26.4585	0.1632	14.70	0.852	6.7	8.6	4.9	4.9

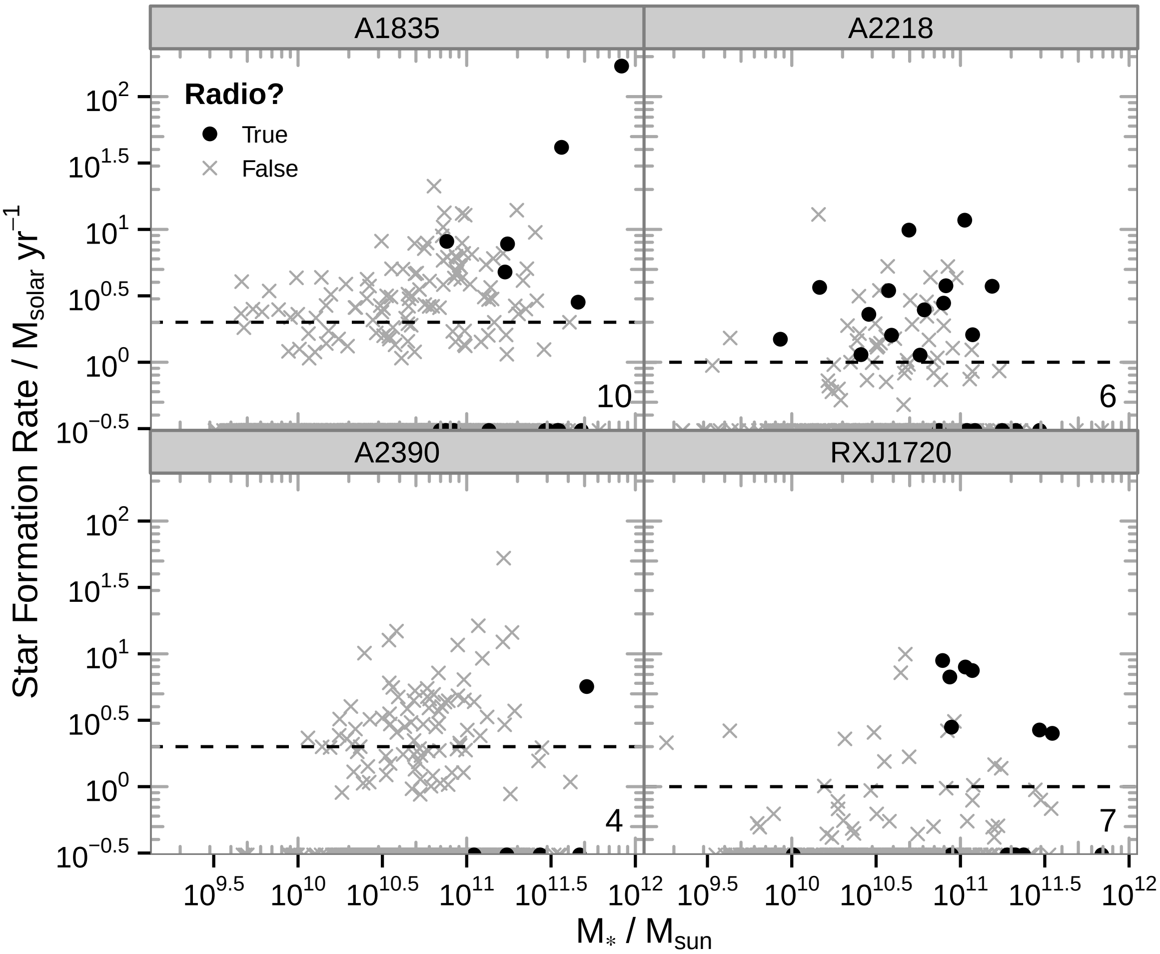

Figure 3.6: Star formation rates as a function of stellar mass are plotted here for all cluster members, with the radio sources shown as filled points. Numbers in the bottom-right corner show the number of radio-loud members with no detected star formation. The galaxies without a star formation rate appear on the bottom axis, to show their derived stellar mass. The horizontal dashed lines show the quoted upper limits for which we are complete with the *Spitzer* data.

In optical surveys, contamination from star forming galaxies was separated by using methods such as optical emission-line diagnostics (e.g. Best and Heckman, 2012). These methods sometimes give false results, such as characterising a radio-loud star forming galaxy as an AGN due to their emission lines (e.g. Kauffmann et al., 2003). Our use of infrared observations gives us reliable star formation rates, therefore making it easier to distinguish between true radio-loud AGN and radio-quiet AGN with associated star formation. Each of the star formation rates is converted to an estimate of the radio luminosity contributed by this process.

We use the following relationship from Bell (2003), converted from 1.4 GHz to 610 MHz fluxes assuming a spectral index of $\alpha = -0.8$.

$$\left(\frac{L_{610\,\mathrm{MHz}}}{\mathrm{W\,Hz^{-1}}}\right) = \begin{cases} 3.52 \times 10^{21} \left(\dfrac{\psi}{\mathrm{M_{\odot}\,yr^{-1}}}\right) & \text{if } L > L_c \\ 3.52 \times 10^{21} \times \zeta \left(\dfrac{\psi}{\mathrm{M_{\odot}\,yr^{-1}}}\right) & \text{if } L \leq L_c \end{cases} \tag{3.7}$$

where $\zeta = 0.1 + 0.9\left(L_{610\,\mathrm{MHz}}/L_c\right)^{0.3}$, and $L_c = 3.29 \times 10^{21}\,\mathrm{W\,Hz^{-1}}$ is the radio luminosity at 610 MHz of a $\sim L_{\star}$ galaxy (with $\psi \approx 1\,\mathrm{M_{\odot}\,yr^{-1}}$, where ψ is the star formation rate).

Using Equation 3.7, we simply subtract the expected radio emission from star formation, L_{SFR}, from our observed radio emission, L_{610}. The resulting value is the radio emission attributed to the AGN, L_{AGN}, and is what we use for our analysis.

Figure 3.8 shows the removal of the SF radio emission from our cluster members. Only one galaxy has $L_{\mathrm{SFR}} > L_{610}$, and hence is no longer defined as radio-loud. L_{SFR} is also subtracted from our upper limits, when applicable. An alternative method is to remove sources which lie between the dashed lines in Figure 3.7, as their estimated L_{610} from SFR is within a factor or 2 of the observed L_{610}. This removes 6 galaxies: 1 from A1835, 4 from A2218, 0 from A2390 and 1 from RXJ1720. The results do not change significantly when using the alternative method. It is worth noting that there are a few galaxies that have an expected L_{610} from star formation above our sensitivity levels, but which are not detected. This illustrates that there are uncertainties in the predicted L_{SFR}, which Bell et al. (2003) estimates to be a factor of 2 on a galaxy-by-galaxy basis.

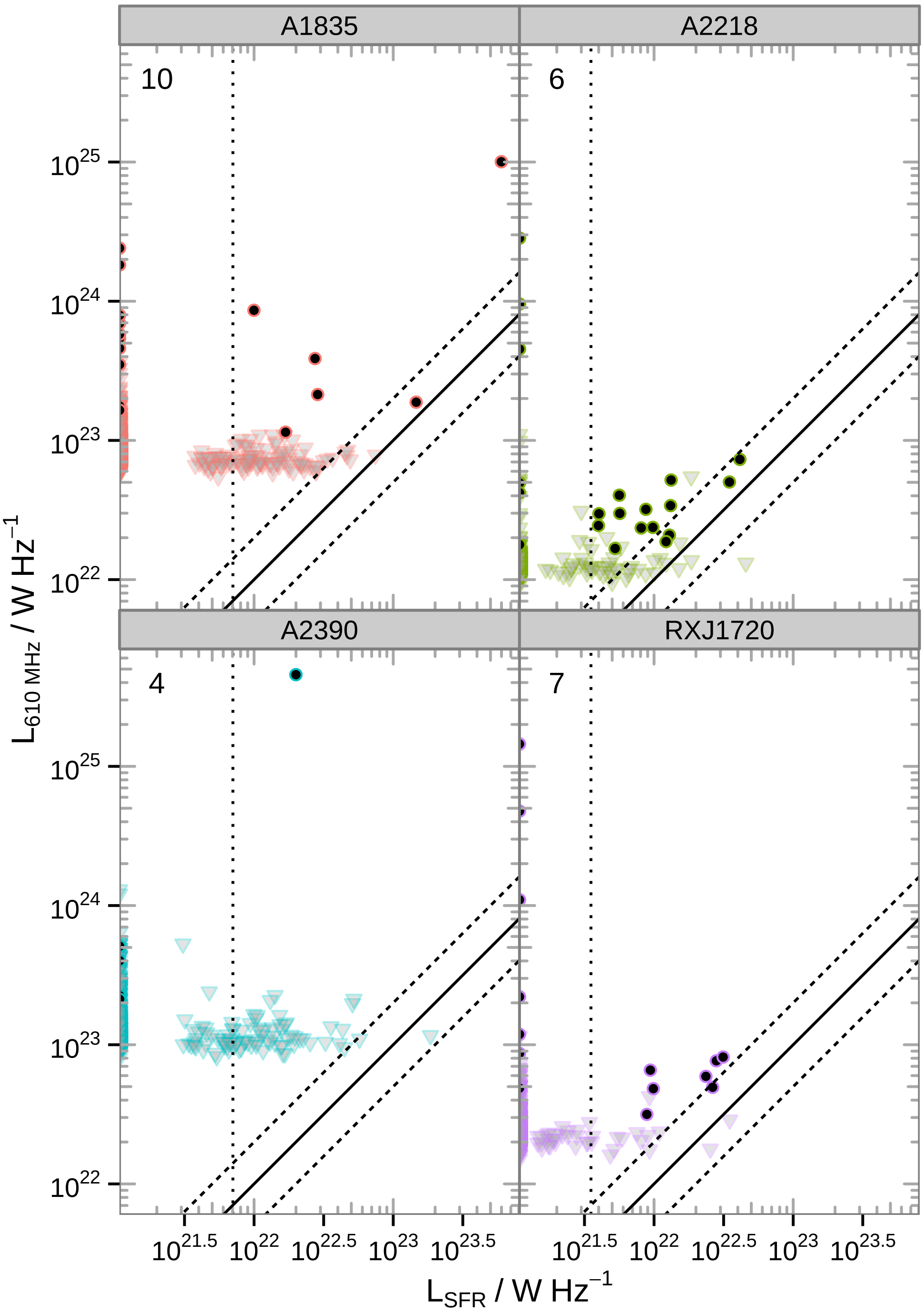

Figure 3.7: The observed radio luminosity is plotted as a function of the expected radio luminosity for a galaxy with a given star formation rate. Filled points are detected radio sources, the shaded triangles are radio upper limits. The solid line is equality, and the dashed lines shows a factor of two difference. The vertical dotted line shows the upper limits to the expected L_{SFR}, given the SFR upper limits for completeness of 1 and 2 $\mathrm{M_{\odot}\ yr^{-1}}$. Numbers in the top left corner show the number of radio-loud galaxies observed without a detected star formation rate. The galaxies without a star formation rate appear on the left axis, to show their observed radio luminosity.

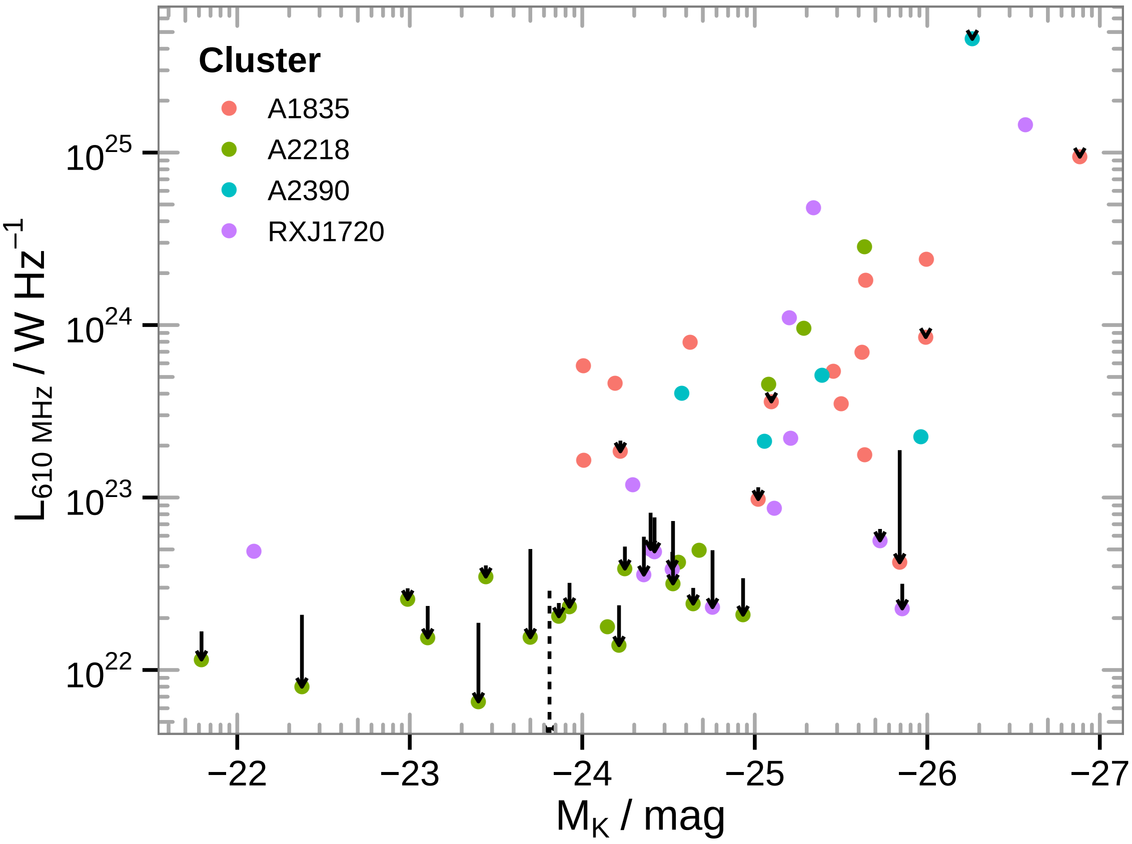

Figure 3.8: AGN-related radio luminosity is shown as a function of K-band absolute magnitude. Arrows show the amount of radio emission from star formation that has been subtracted. The dashed arrow signifies that for this galaxy the radio emission observed was all due to star formation.

3.4.8 Final AGN radio luminosities

Figure 3.9 shows the SF-corrected 610 MHz radio luminosity (hereafter L_{AGN}) of our four cluster sample, observed with the GMRT. Each cluster source is plotted, with the black filled points detected in the radio, and a shaded triangle for upper limits. A yellow fill means they have been detected in X-ray.

The field

We also select a number of galaxies that are not cluster members, but field galaxies in well defined redshift ranges either side of the clusters, where we should be spectroscopically com-

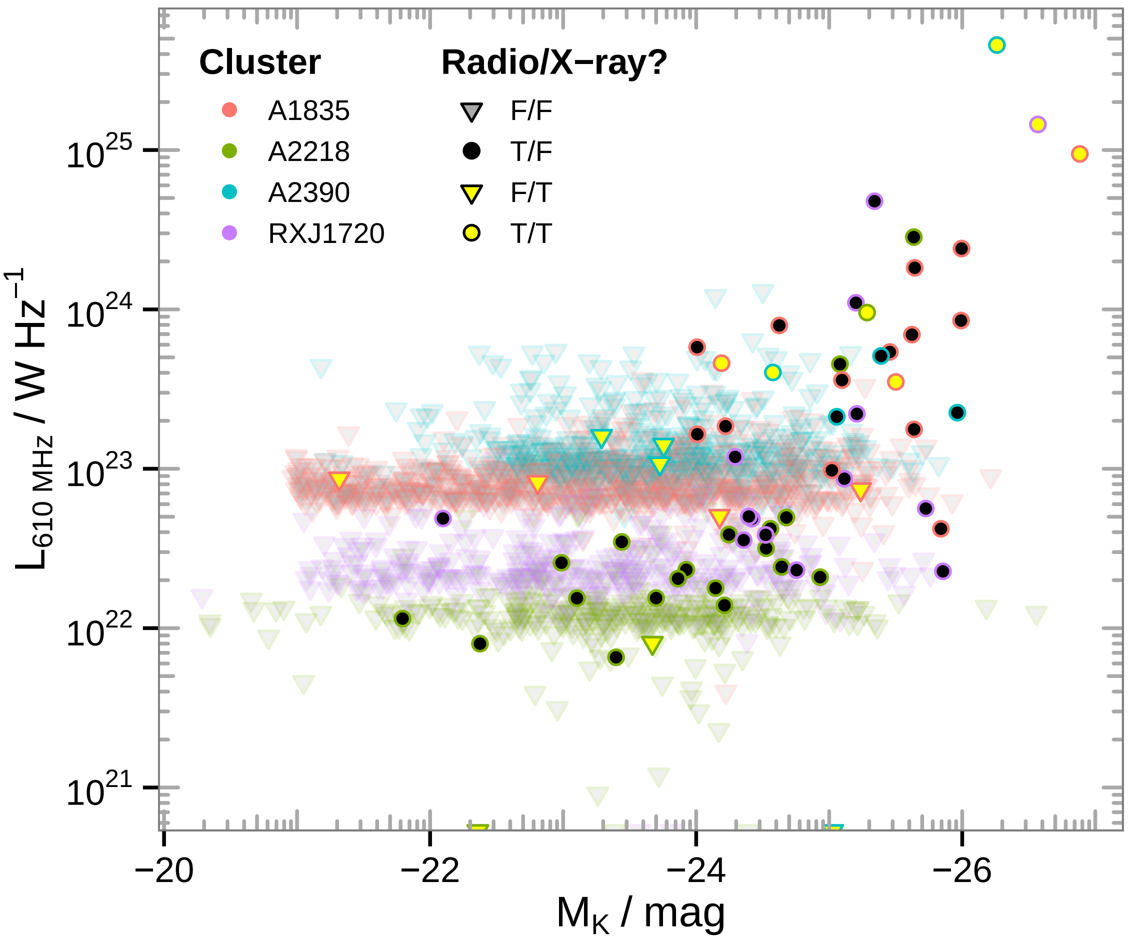

Figure 3.9: 610 MHz luminosity plotted against absolute *K*-band magnitude. The contribution from star formation has been subtracted from X-ray bright sources are the filled yellow points.

plete. There are 679 galaxies in this field sample, with a redshift range of $0.17 < z < 0.3$. This is selected to be similar to our cluster sample, to be useful for comparison. We have the same multi-wavelength coverage for this sample of galaxies.

3.5 Radio AGN in the galaxy population

In the following analysis, we consider our data as a sample of *individual* galaxies, for which we have collected good quality multiwavelength observations. M_{200} for galaxies refers to the halo mass a galaxy would have, if it was considered as an individual system, as described in §3.4.5.

3.5.1 The radio-loud AGN fraction

We define a **radio-loud** AGN as a galaxy detected (at 610 MHz) in our radio catalogue with a radio luminosity (corrected for star formation contamination, as described in §3.4.7) greater than $L_{\mathrm{AGN}} \geq 7 \times 10^{21}\,\mathrm{W\,Hz^{-1}}$.

Our data are substantially complete at the $2 \times 10^{23}\,\mathrm{W\,Hz^{-1}}$ level, with 95% of our upper limits below this value, and 23 of our radio-loud galaxies exceed this luminosity. Using different cut-off values, we can explore the data to compare our results with either maximum sensitivity of our catalogue, or maximum completeness but with fewer galaxies. As stated previously, other definitions have been used in the literature to classify a galaxy as being radio-loud. Alexander and Hickox (2012) define a radio AGN as having $L_{1.4\,\mathrm{GHz}} > 10^{24}\,\mathrm{W\,Hz^{-1}}$, whereas Best et al. (2005b) use the 4000 Å break to separate AGN from SFGs. We believe our method should probe more lower luminosity AGN without being significantly contaminated by star forming galaxies.

Figure 3.10 shows the fraction of cluster galaxies with a 610 MHz radio luminosity above various cut-off levels. The relation, $f_{\text{radio-loud}} \propto \mathrm{M_{\star}}^{\beta}$ can then be calculated, where β is the slope of the best-fit. The bivariate correlated error and intrinsic scatter (BCES) algorithm (Akritas and Bershady, 1996) was used to perform linear regression fits to the data, determining the best-fitting power-law relationship between the fraction of radio-loud AGN and the stellar mass of the galaxies. The orthogonal BCES regression was used to fit the parameters in log space. Errors are estimated assuming a binomial distribution,

$$\sigma_{\rm frac} = \frac{\sqrt{Np(1-p)}}{N} \tag{3.8}$$

where N is the number of galaxies and p is the fraction of galaxies that host a radio-loud AGN. Best et al. (2005a) give $\beta = 2.5$ for their sample at 1.4 GHz, independent of cut-off (10^{23}, 10^{24} and 10^{25} W Hz^{-1}), whereas ours varies depending on our choice of cut-off.

Our four cut-off values in Figure 3.10 were chosen to be 10^{22}, 4×10^{22}, 10^{23} and 2×10^{23} W Hz^{-1}, encompassing differing levels of sensitivity and completeness. At all cut-off levels, we find a similar radio-loud fraction for high mass galaxies to Best et al. (2005a) of ~30−40%. However, we find $\beta = 1.27 \pm 0.07$ for our most sensitive cut-off level, and a slope of 2.03 ± 0.05 for our most complete cut-off level. This could mean that there are more lower mass galaxies that host radio-loud AGN than previously thought.

What could cause this flattening of the slope at lower radio luminosities? We have already subtracted the star formation contribution from L_{610} as described in §3.4.7, reducing the likelihood of star forming galaxies being confused with radio-loud AGN, which would cause a shallower gradient.

Although we do have deep data, the number of radio-loud galaxies in our sample is not large. At the lower mass end, where radio-loud AGN are increasingly rare, one or two galaxies will increase the fraction significantly. This is reflected in the large errorbars in Figure 3.10. We find the flattest slope for our lowest luminosity cut-off. However, as some of our data does not have the sensitivity to observe that deeply, we will miss other radio-loud AGN that would have been detected with our deepest observations.

Note, our highest cut-off value of 2×10^{23} W Hz^{-1} at 610 MHz corresponds to a 1.4 GHz value of ~10^{23} W Hz^{-1}, which is comparable to or lower than the lowest radio luminosities that most radio AGN literature consider (e.g. Best et al., 2005a).

One explanation for the greater radio-loud fraction in higher mass galaxies could be due to their possession of more powerful central engines, and thus more luminous radio emission.

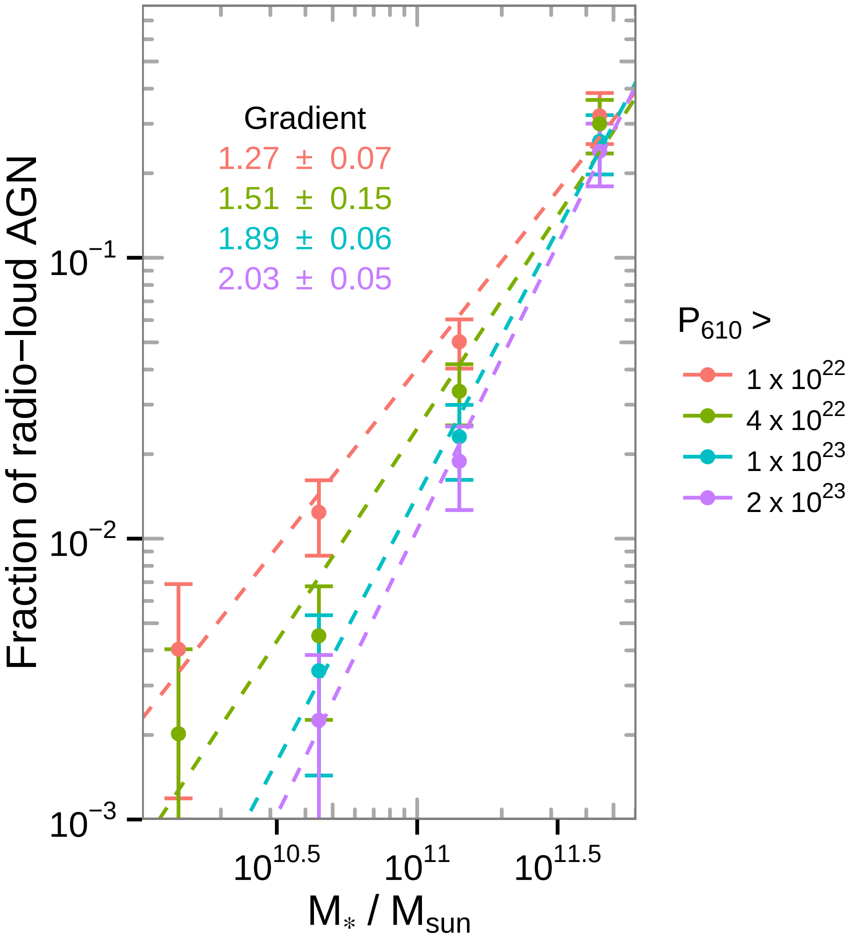

Figure 3.10: The fraction of cluster galaxies that have a radio luminosity above a cutoff in W Hz^{-1}. Galaxies are allocated into bins based on their derived stellar mass. We find a shallower gradient for our lowest luminosity cut-off.

To investigate this, we consider galaxies with a threshold radio luminosity that has been normalised by stellar mass, i.e. $\frac{L_{\mathrm{AGN}}}{\mathrm{M}_\star} > \kappa \left(\frac{\mathrm{W\,Hz^{-1}}}{\mathrm{M_\odot\,yr^{-1}}}\right)$, where κ is an arbitrary fixed limit. This radio-loudness gives an indication to how active the nucleus is in comparison to the stellar mass of the galaxy. This is equivalent to defining a galaxy as radio-loud if it is radiating above some fixed fraction of the Eddington limit (Best et al., 2005a).

We still find that the fraction of radio-loud AGN increases with mass when using this definition, despite normalising by mass, which should remove the mass dependence if having a bigger nucleus was the only factor having an effect.

Figure 3.11 shows the ratio of the star formation corrected radio luminosity to stellar mass as a function of $\mathrm{M}_\star$. The top-right three points of the plot are the BCGs of their respective clusters. This figure does not change significantly when the non-corrected luminosities are plotted instead. This mass-normalised radio luminosity is essentially similar to that of radio-loudness, $\mathcal{R} \equiv L_{\nu_5}/L_{\nu_B}$, which is the ratio of the 5 GHz and blue-band luminosities.

Woo and Urry (2002) found no dependence with black hole mass, but Sikora et al. (2007) find that radio-loudness increases as a function of black hole mass and with decreasing Eddington ratio. Table 3.4 displays the result of various correlation tests between the data. Because of our differing sensitivities in our clusters, we have an unusual distribution of upper limits that will stop us finding galaxies with low mass and low radio-loudness. This would lead to an artificial negative correlation for a normal distribution. However, we see some evidence for a positive correlation between the mass-normalised radio luminosity and stellar mass for our data set, with a p−value of < 0.05.

Table 3.4 also looks at the correlation between L_{AGN} vs $\mathrm{M}_\odot$, as in Figure 3.9. Best et al. (2005a) found that the probability of a galaxy becoming a radio source is a very strong function of mass, but the luminosity of the radio sources that results is independent of mass (except at the very highest masses).

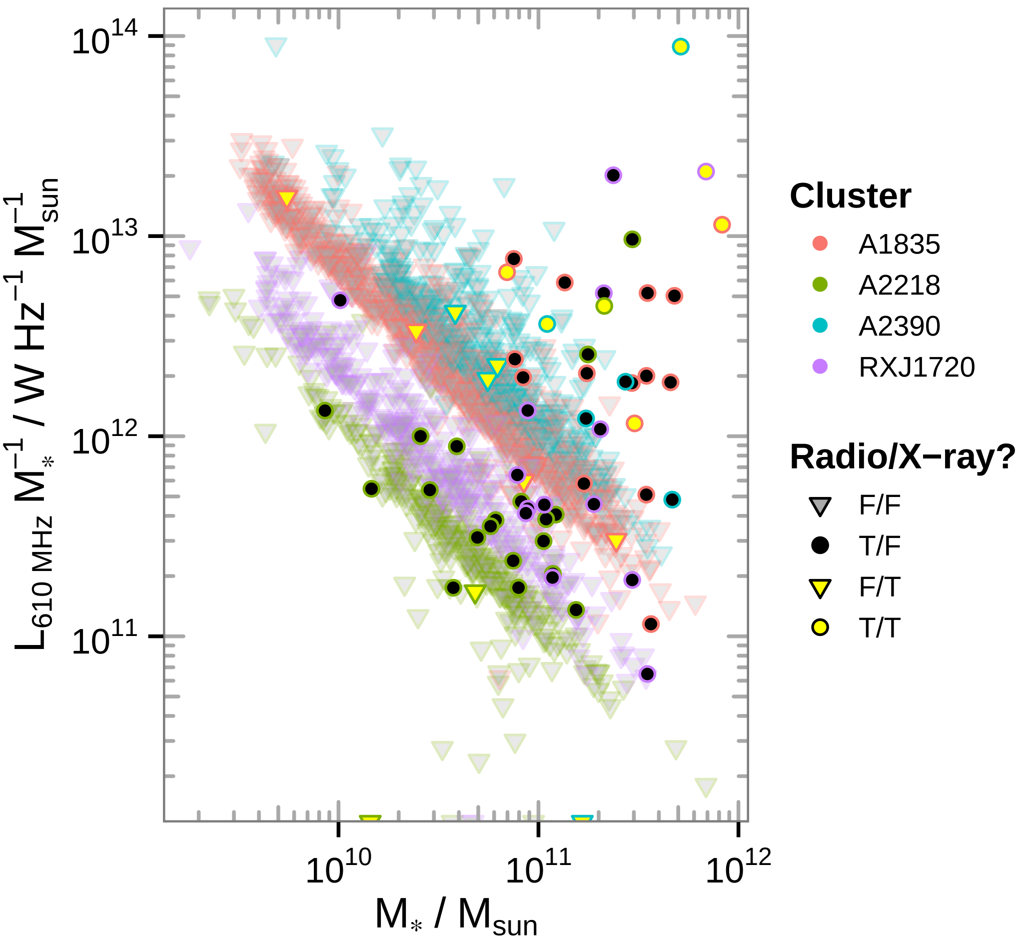

Figure 3.11: This graph plots the ratio of radio luminosity (SF subtracted) and stellar mass against $M_\star$. X-ray bright sources are plotted in yellow. T and F in the legend correspond to true and false.

Table 3.4: A table of correlation tests between different variables in the data. −BCG shows the correlations with the BCGs excluded.

Test	L_{AGN} vs $\mathrm{M}_{\odot}$	−BCG	$\frac{L_{\mathrm{AGN}}}{\mathrm{M}_{\odot}}$ vs $\mathrm{M}_{\odot}$	−BCG
Pearson r	0.70	0.63	0.27	0.10
(p–value)	3×10^{-9}	4×10^{-7}	0.044	0.50
Spearman ρ	0.71	0.65	0.29	0.16
(p–value)	4×10^{-9}	4×10^{-7}	0.035	0.27
Kendall τ	0.53	0.48	0.19	0.10
(p–value)	1×10^{-8}	7×10^{-7}	0.041	0.31

Radio–optical luminosities

The relationship between the radio luminosity of an AGN and the stellar mass of the host galaxy has previously been found to be independent. Best et al. (2006) on their previous work in Best et al. (2005a): 'The distribution of radio luminosities was found to be independent of black hole mass.' Figures 3.8, 3.9 and Table 3.4 show that our data find a positive correlation between these two quantities. The figures show M_K as the proxy for stellar mass. Table 3.4 shows the significance of the correlation, $p \sim 1 \times 10^{-8}$.

(Best and Heckman, 2012, Figure 7) found a difference between the masses of high and low excitation radio AGN, with high-excitation radio AGN preferring low mass hosts. They do not appear to comment on a relationship between radio luminosity and stellar mass.

There are some differences between this work and Best et al. (2005a). Their sample had a large number of galaxies at low redshift, using the NVSS/FIRST surveys to achieve a shallow depth of 10^{24} W Hz^{-1}. They had 2712 radio-loud galaxies in their sample. Ours has an equivalent depth of 10^{23} W Hz^{-1}, with 56 radio-loud galaxies.

Figure 3.12 shows the fraction of galaxies that are brighter than a given radio luminosity, as a function of the radio luminosity. This is calculated for four separate mass bins, and as above shows clearly the increased probability of a high mass galaxy being radio-loud. The shape of the distributions are also similar for each mass range, and a Kolmogorov-Smirnov (K-S) test finds no significant difference between the data, once centred and rescaled.

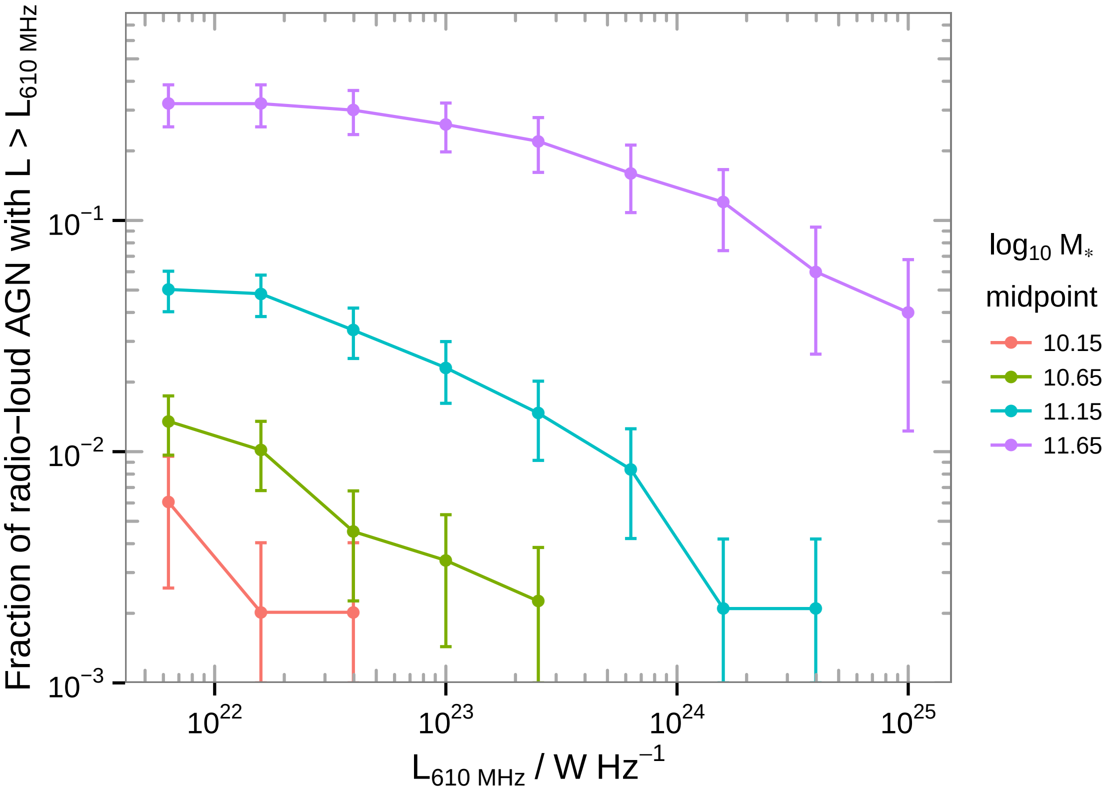

Figure 3.12: The fraction of radio-loud AGN brighter than a given radio luminosity (as shown on the x-axis), as a function of stellar mass.

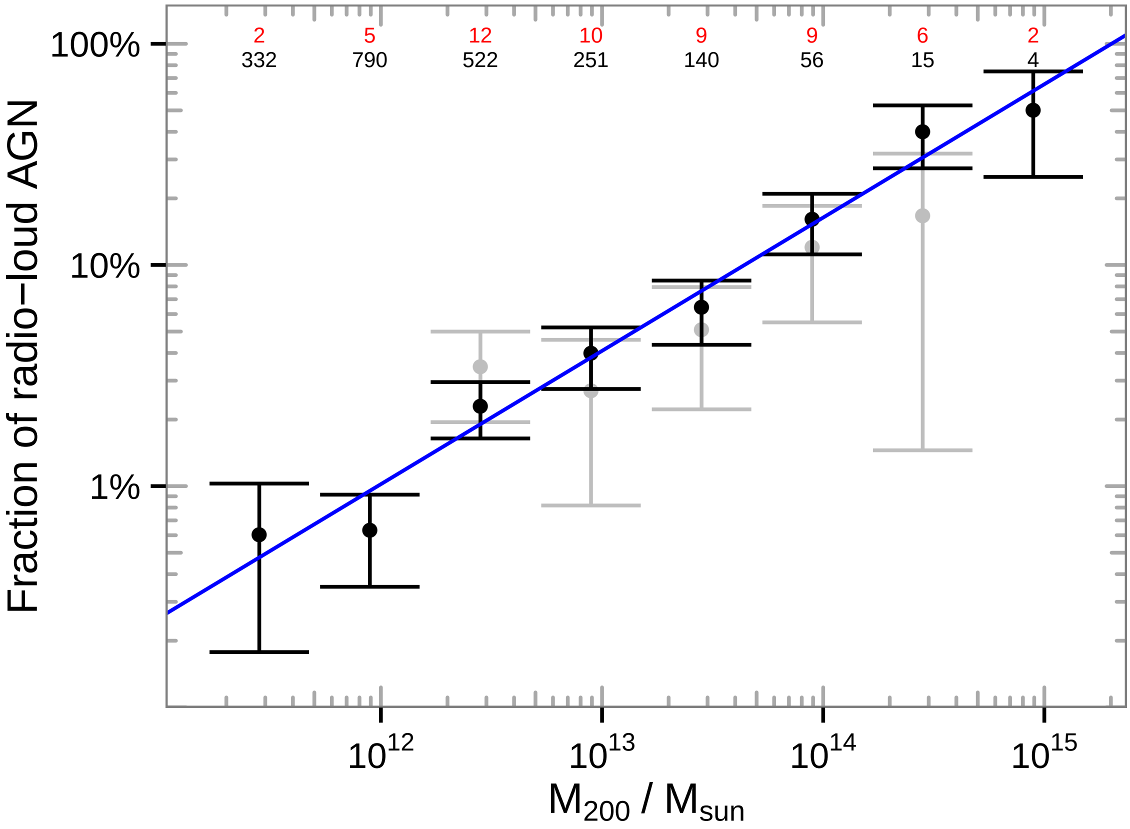

Figure 3.13: Fraction of radio-loud AGN as a function of halo mass, M_{200}, using Moster et al. (2010). The black points and errorbars are from our cluster sample, the grey points are the field galaxies only. The black values above are the number of galaxies in that mass bin, with the red values counting the subset that are radio-loud.

Figure 3.13 shows the fraction of radio-loud AGN plotted as a function of M_{200}, with the equation of best fit given in Equation 3.9. A linear relationship fits the data better than with stellar mass, although naturally the trend will have to plateau before it hits 100%. This takes into account all cluster members and uses our earlier definition of radio-loud ($L_{610} \geq 10^{22}$ W Hz^{-1} excluding star formation).

$$\log\left(f_{\text{radio-loud}}\right) = (0.60 \pm 0.04)\log\left(\frac{M_{200}}{\mathrm{M}_{\odot}}\right) - (9.22 \pm 0.54) \tag{3.9}$$

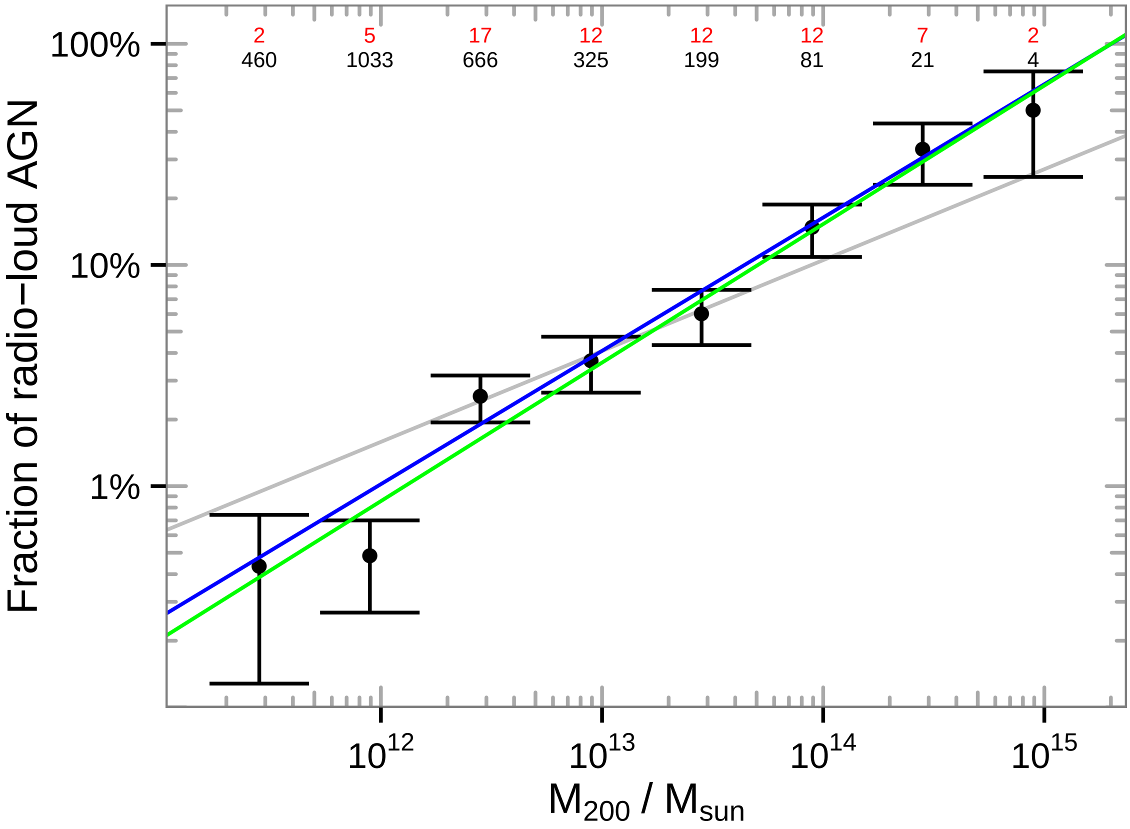

Figure 3.14: Fraction of radio-loud AGN as a function of halo mass, M_{200}. The black values above are the number of galaxies in that mass bin, with the red values counting the subset that are radio-loud. The blue, grey and green lines show the lines of best fit for the cluster, field and combined samples. The data points in this instance are from the cluster+field sample.

Inclusion of field galaxies

In §3.4.8, we created a sample of field galaxies selected to have similar completeness and multi-wavelength coverage. From this, we can repeat our analysis and add this field galaxy sample to improve our statistics. Figure 3.14 plots the radio AGN fraction against halo mass for this combined sample, with the trend ultimately unchanged from the cluster-only sample.

3.5.2 The heating power of AGN

AGN feedback in the form of radio-loud AGNs has been accepted to be an important process in heating their local environments. We wish to know how much of an impact the radio-loud AGNs in our sample have on their host galaxies, and to compare this across a range of mass bins. To determine whether the energy from our sample of radio AGN is large enough to suppress cooling of the gas, and hence star formation, we first need to calculate an estimate of the mechanical power of the jets and lobes of the AGN. One method is to infer this from the $p\mathrm{d}V$ work that these jets and lobes do on their surroundings. The mechanical energy contribution can then be estimated by $E_{\mathrm{mech}} = P_{\mathrm{mech}} \times \tau$, where the timescale τ we assume to be 10^8 yr (see §3.5.4). This will be a lower limit to the energy involved as it neglects potentially important factors such as the energy dissipated in shocks (Gitti et al., 2012).

Our observable here is the monochromatic radio luminosity from the AGN outburst. This gives only a small fraction of the total energetic output of the AGN, and so a relationship is needed to estimate P_{mech}. We use Equation 3.10, the relationship given in O'Sullivan et al. (2011), which improves on work done previously (by e.g. Bîrzan et al., 2004, 2008; Cavagnolo et al., 2010). It must be noted that these are empirical relationships taken from observations of the radio luminosity of the bubbles and X-ray measurements of the cavities that they inflate. We assume the same relation for all galaxy masses.

$$\log P_{\mathrm{cav}} = (0.71 \pm 0.11) \log L_{\mathrm{radio}} + (2.54 \pm 0.21) \tag{3.10}$$

where P_{cav} and L_{radio} are in units of $10^{42}\,\mathrm{erg\,s^{-1}}$.

To get L_{radio}, one needs to integrate under the curve $S = k\nu^{\alpha}$, for the frequency range of 10 MHz–10 GHz. This frequency range is the standard range of radio observations from the Earth, and is typically used to determine the total integrated radio luminosity.

$$\int S(\nu)\, d\nu = \int k\, \nu^{\alpha}\, d\nu = \begin{cases} \dfrac{k}{\alpha+1}\, \nu^{\alpha+1} & \text{if } \alpha \neq -1 \\ k \log \nu & \text{if } \alpha = -1 \end{cases} \tag{3.11}$$

where $k = S_\nu \, \nu^{-\alpha}$. Using the integrated radio luminosity means we should have a stronger relationship between L_{radio} and P_{mech}, as we use more than one radio frequency when available. From this, values of E_{mech} can be calculated.

Note, it is normally assumed that the energy of a cavity is equal to its enthalpy H, given by

$$E_{\mathrm{mech}} = H = \frac{\gamma}{\gamma - 1} pV \tag{3.12}$$

where p is the pressure of the gas surrounding the cavity, V is the volume of the cavity, and γ is the ratio of the specific heats of the gas inside the cavity. For a relativistic plasma, $\gamma = 4/3$, and so $E_{\mathrm{mech}} = 4pV$. If the lobes are dominated by non-relativistic gas or by magnetic fields, this coefficient could be altered by a factor of 2. It is also worth noting that the volume is normally estimated from an observer's estimate with possible differing assumptions of the geometry involved.

3.5.3 cosmo-OWLS simulations

To investigate how our observations compare to our current understanding as implemented in simulations, we use the results of the cosmo-OWLS simulation. cosmo-OWLS is a continuation of the OverWhelmingly Large Simulations project (OWLS; Schaye et al., 2010). It is a suite of cosmological hydrodynamical simulations, aimed at cluster cosmology and large-scale structure surveys. The simulations are of large volume $(400\,\mathrm{h}^{-1}\,\mathrm{Mpc})^3$, with the periodic box hydrodynamical simulations having 1024^3 baryon and dark matter particles each (McCarthy et al., 2014). The initial conditions are based on WMAP7 or *Planck* data. Further details can be found in Le Brun et al. (2014).

For this work, a smaller box of $(200\,\mathrm{h}^{-1}\,\mathrm{Mpc})^3$ was used to increase the resolution by a factor of eight. In order to try and match the process that we have used observationally, we first select clusters with $M_{200} > 10^{14}\,\mathrm{M}_\odot$. All galaxies within a projected aperture of $3\,\mathrm{r}_{200}$ and have a line-of-sight distance of <15 Mpc from the centre of the cluster are selected. Central and satellite galaxies can then be determined using the SUBFIND routine.

In our sample of simulated galaxies, we calculate the fraction of galaxies that have $E_{\mathrm{mech}} > 5 \times 10^{57}$ erg, this corresponds approximately to our most sensitive radio luminosity cutoff of $\sim 10^{22}\,\mathrm{W\,Hz^{-1}}$. The mechanical energy is calculated using,

$$E_{\mathrm{mech}} = \epsilon_f \, \epsilon_r \, \dot{M}_{BH} \, c^2 \, \mathrm{d}t \tag{3.13}$$

where $\epsilon_r = 0.1$ is the standard radiative efficiency (e.g. Marconi et al., 2004; Merloni, 2004), and $\epsilon_f = 0.15$ is the feedback coupling that we use in the model (e.g. Taylor and Kobayashi, 2015). This has been tuned to match the normalisation of the black hole scaling relations. We use a timescale of 10^8 yr to compute an energy.

This bolometric-loud fraction is as close as we can get to a radio-loud fraction, and it is plotted as a function of halo mass in Figure 3.15. We find that the overall trend is similar, with the fraction increasing towards higher masses. On the whole, our simulated data tend to have a significantly higher radio-loud fraction than our observations. There are a few caveats to consider when comparing our simulated data with observations. Firstly, the bolometric-loud fraction is very sensitive to the luminosity cut in the models. If we adopt a cut of $E_{\mathrm{mech}} > 5 \times 10^{58}\,\mathrm{erg\,s^{-1}}$, the resultant peak fraction drops to ∼30%. This cut is more in line with the sensitivity levels of two of our clusters (A1835 & A2390).

The simulations cannot distinguish the energy inside and outside the cavity, only the total mechanical output. As noted previously, for our observed data we are ignoring the energetics of shocks and so the energy from creating cavities is only a lower limit to the total mechanical energy output. In this context, the radio-loud fraction that we observe would also be a lower limit, if we were to match it to the simulation definition of the radio-loud fraction. As we use an empirical scaling relation with large scatter to go from radio luminosity to mechanical power, and our sensitivity to the radio luminosity cut is high, it is difficult to draw further conclusions.

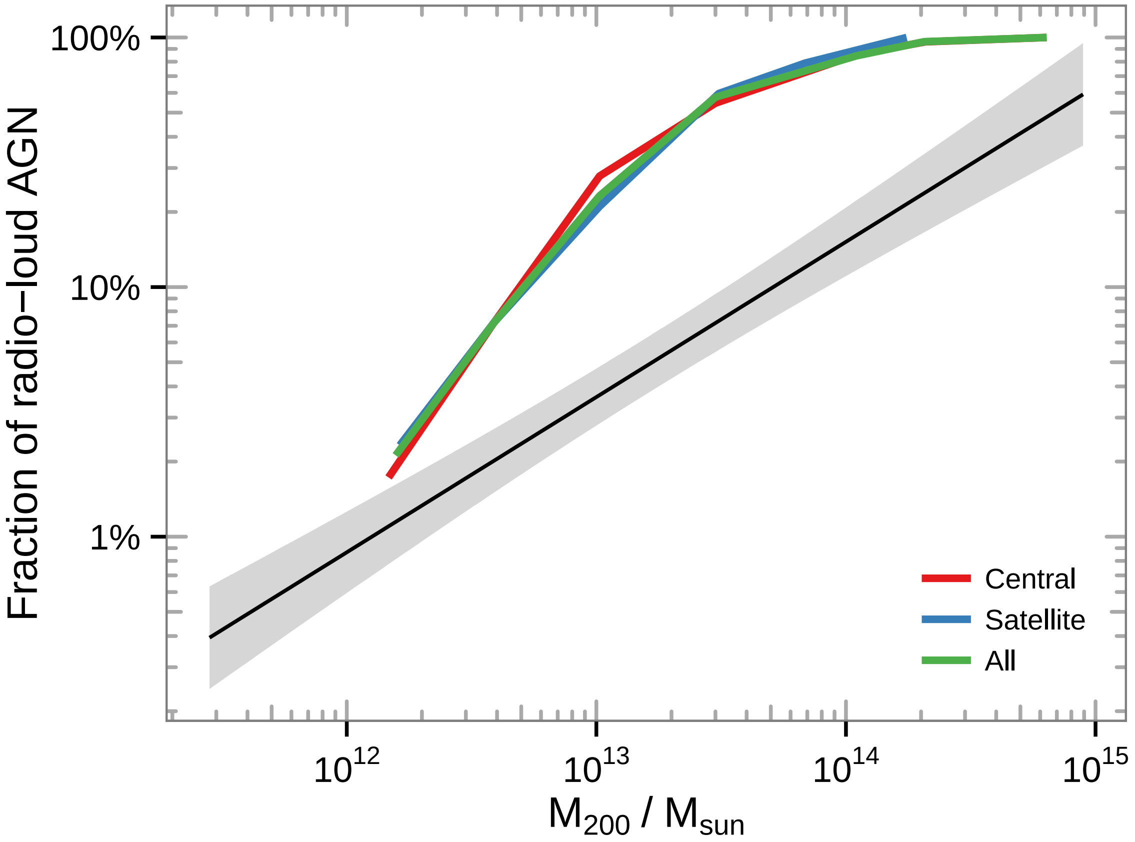

Figure 3.15: The fraction of radio-loud AGN as a function of halo mass, using simulated data from cosmo-OWLS. All galaxies here have $E_{\mathrm{mech}} > 5 \times 10^{57}$ erg and an Eddington ratio < 1. The observed trend from §3.5.1 is shown in black with its 95% confidence interval.

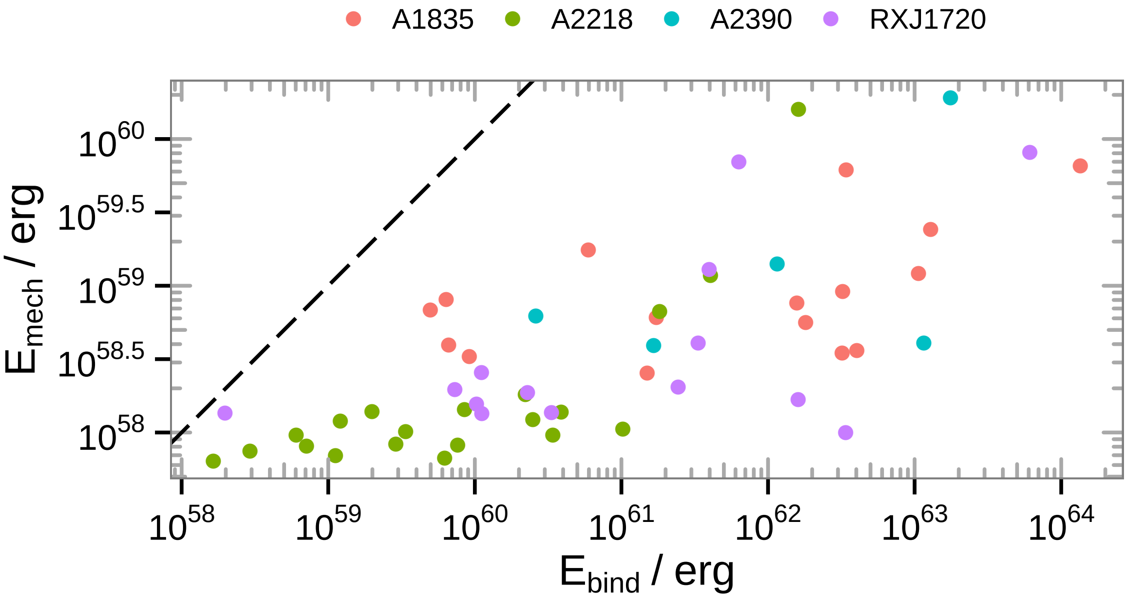

Figure 3.16: Estimated mechanical power from the radio AGN as a function of the binding energy of the hot gas. The dashed line is equality, assuming a timescale of 10^8 yr.

3.5.4 Gas ejection by radio galaxies

Using our estimates for the binding energy in §3.4.5, and the mechanical energy estimated from §3.5.2, we plot Figure 3.16 for our sample. The mechanical energy is spread over a range of three orders of magnitude, but is exceeded by the binding energy for all galaxies. Figure 3.17 plots the ratio of these energies as a function of M_{200}, where we find a best-fit relation of:

$$\log \frac{E_{\mathrm{mech}}}{E_{\mathrm{bind}}} = (-1.28 \pm 0.08) \log \frac{M_{200}}{10^{12}\,\mathrm{M}_\odot} - (0.76 \pm 0.13) \tag{3.14}$$

Figure 3.17 shows that the energy from one 10^8 yr radio outburst is not enough to unbind the

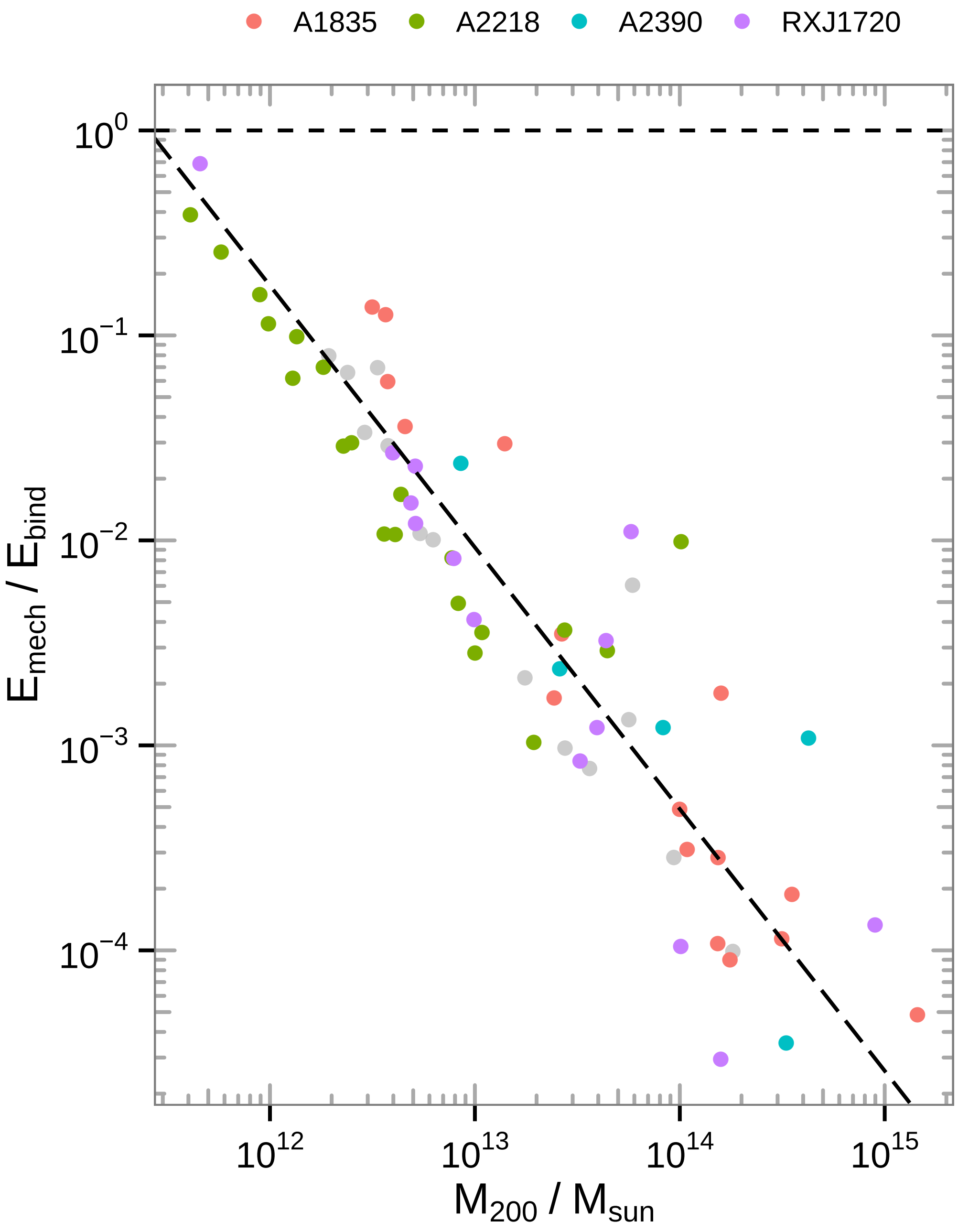

Figure 3.17: The ratio of cavity energy to binding energy for each galaxy is plotted against halo mass (M_{200}). The horizontal line is where $E_{\mathrm{mech}} = E_{\mathrm{bind}}$. Grey points are from the field galaxy sample. The dashed line is the line of best fit as given in Equation 3.14.

gas from its galaxy. We find that the ratio $\frac{E_{\rm mech}}{E_{\rm bind}} \propto {M_{200}}^{-1.28}$, so the ratio decreases as a function of halo mass. Towards Milky Way size ($\sim 10^{12}$ M$_\odot$) galaxies, the ratio approaches unity.

Figure 3.18 uses data from the cosmo-OWLS simulation, and shows the ratio of mechanical and binding energies as a function of halo mass.

There are several thousands of galaxies in the simulation, the majority of which are not radio-loud. In order to compare with our observations, we select simulated systems that we would detect as being radio-loud. In Figure 3.18, we plot shaded regions to mimic our differing GMRT depths. These enclose the central 50% of the simulated cluster population above a certain mechanical power. The blue area selects galaxies with a mechanical power of $E_{\rm mech} \gtrsim 5 \times 10^{57}$ erg, and an Eddington ratio cut of $\log\left(\frac{L_{\rm bol}}{L_{\rm Edd}}\right) < 0$ is also used to eliminate any radio-loud quasar mode objects, which are very rare in the local universe.

The red region takes all simulated galaxies with no luminosity cut applied. The overlaid black line is our best-fitting relation from our observations, from Figure 3.17, along with an estimate of the scatter.

We find that the observed and simulated results match well when considering only simulated data with a threshold meaning that it would be detected in our GMRT observations (in blue). It is not only the gradient of our results that match, but the normalisation also. This is not a trivial result to match, as there are many factors in the simulation that will affect this, such as the accretion rate.

We can draw two main conclusions from this result. Firstly, this is an encouraging result for our models, with a good correlation to the observed data once a realistic cut has been taken to match the galaxies that we can observe. Secondly, if the simulations are accurate, we see that our observed relationship between the ratio of mechanical and binding energies with halo mass appears to be largely a consequence of our radio sensitivity thresholds. What we observe appears to be only a relatively small and biased fraction of the galaxies that are there, especially in the case of the lower mass galaxies. If we take the unfiltered simulated galaxies, we see that the energy ratio is relatively constant around a magnitude on the order of 10^{-4}, and does not

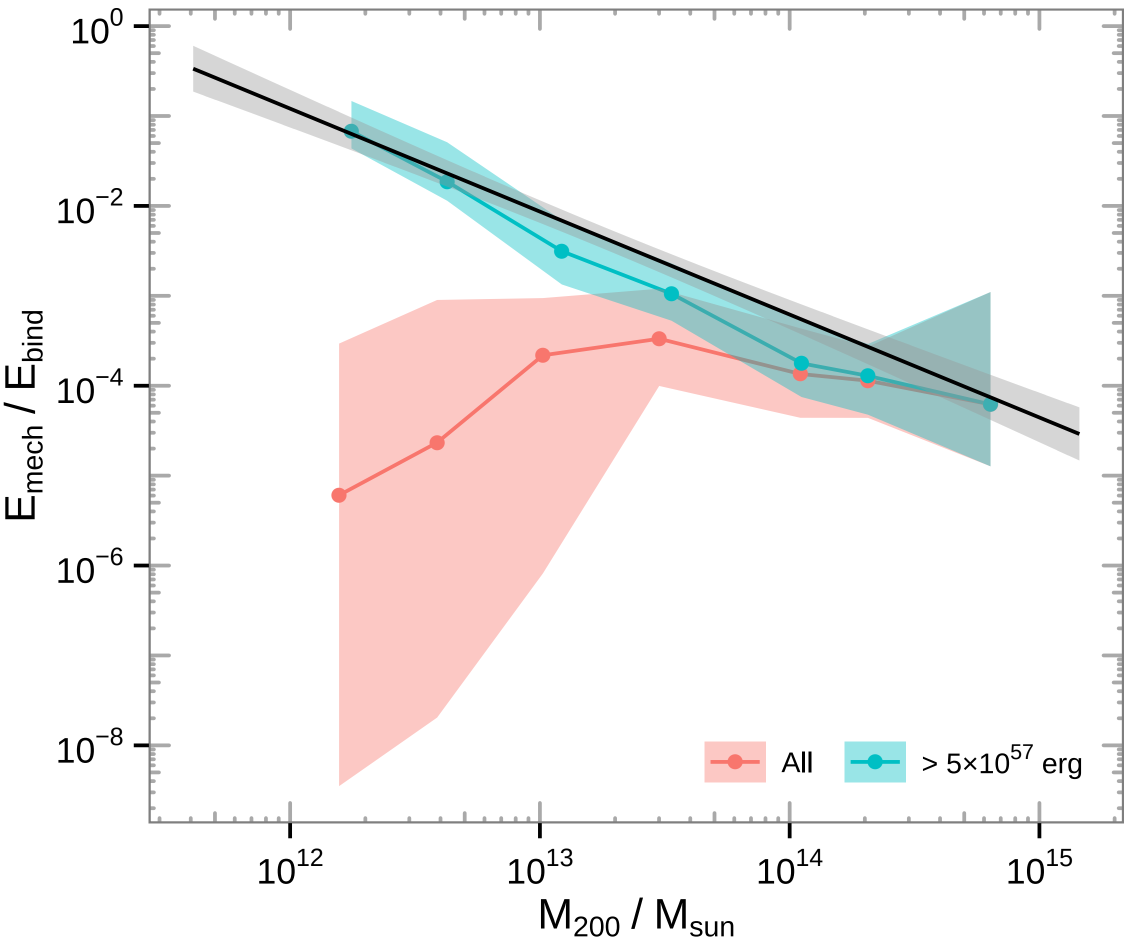

Figure 3.18: The ratio of mechanical to binding energies are plotted against M_{200}. This uses simulated data from cosmo-OWLS. The median energy ratio is plotted in bins of halo mass, and uses two mechanical power cuts. The first shows all galaxies in the simulation sample as defined in §3.5.3. In blue are all galaxies with $E_{\mathrm{mech}} > 5 \times 10^{57}$ erg, which is comparable to the lowest that we can observe with our data. An Eddington ratio cut is also imposed for the two subsets, of $\log\left(\frac{L_{\mathrm{bol}}}{L_{\mathrm{Edd}}}\right) < 0$. The shaded region encloses the first and third quartiles of the data. The black line is our relationship shown in Equation 3.14.

vary greatly with halo mass. The slight drop at the low mass end is most likely a stochastic variation due to low particle numbers in that mass range.

Of course, it is important to note that this cannot be confirmed currently, as these are only simulated results and we do not have the capabilities to look at the much lower radio powers needed to inspect the bottom-left quadrant of that plot. However, our observations do not detect any systems in the top-right quadrant, with a high ratio and high mass, which we are more than capable of observing. Moreover, the width of the distribution of the filtered population in the simulations is relatively low, which is promising as otherwise there would be a discrepancy between our observations and the simulated data.

As we noted in §3.5.1, the radio-loud fraction is a function of mass. At the high mass end, there is a relatively high proportion of radio-loud galaxies, therefore selection effects are reduced and the simulations agree more with our observed trend. At the lower end, the radio-loud fraction is much smaller, and so only a few galaxies would reach the energy levels associated with the radio jets. When they are radio-loud however, the amount of energy released is high, and is approaching the amount needed to eject gas from the galaxy.

Timescales

Our choice of 10^8 yr as the length of an AGN outburst is motivated from timescales estimated from observing X-ray cavities. There are typically three methods that are used in the literature, the sound-speed expansion time, the buoyancy rise time and the cavity refill time (e.g. Shurkin et al., 2008; Gitti et al., 2012). The first estimates the time required for the cavity to expand to the size that is observed, using the speed of sound of its current environment, $v_{c_s} = \sqrt{\gamma kT/\mu m_p}$. The second method estimates the time needed for the low density plasma of the cavity to buoyantly rise to its current position, $t_{\mathrm{buoy}} = R/v_{\mathrm{buoy}} = R\sqrt{SC/2gV}$, where R is the projected distance from the cluster centre, $S = \pi r_w^2$ is the cross-sectional area of the cavity, $C_D \sim 0.75$ is the drag coefficient (Churazov et al., 2001) and $g = GM_{<R}/R^2$. The latter method considers the time required to refill the displaced volume of the cavity, and is estimated to be $t_{\mathrm{refill}} = 2\sqrt{r/g}$, where r is the radius of the cavity.

There are few examples of galaxies that have clear evidence for multiple radio AGN outbursts. High quality low frequency radio data is needed for that. Previously, multiple X-ray cavities, such as the 'ghost cavities' in Abell 2597, suggested radio cycling every 10^8 yr (McNamara et al., 2001). Sternberg and Soker (2009) used an outburst timescale of 10^8 yr for their model of the AGN in the MS0735 cluster, although this is one of the largest radio outbursts ever observed.

An alternative approach uses the duty cycle of the AGNs to estimate the timescales for which they are radio-loud. Assuming a typical galaxy age of 10^{10} yr (assuming most galaxies formed at high redshift $z \sim 6$), the fraction of AGNs that we detect for a given mass will give us an alternative to using a single outburst timescale.

A typical $L_\star$ (Milky Way size) galaxy is radio-loud ∼1% of the time (see Figure 3.13), corresponding to 10^8 yr. For comparison, a 10 $L_\star$ galaxy is estimated to be radio-loud ∼5%, for a total time of 5×10^8 yr. The outcome of using the duty cycle as opposed to a fixed timescale would be an increase to the energies of more massive galaxies, and a reduction to lower mass galaxies. This is making the assumption that the duty cycle can be estimated from the fraction of radio-loud galaxies observed. It is not known if all AGNs go through a radio-loud stage, or if there are some galaxies whose preferred state is radio-loud. This is the case for the central galaxies in clusters, they have a higher probability of being radio-loud (Best et al., 2007). It is also possible that low mass galaxies might very rarely switch on – but when they do they are on for a long period of time.

Figure 3.19 shows how the gradient flattens when the duty cycle of the galaxies is taken into account. This shows the amount of energy that would be available to be input into the surrounding environment over the lifetime of the galaxy, instead of just in one outburst. In the case of multiple outbursts, the cumulative input energy would need to be larger than the quoted binding energy, as in between outbursts there would be enough time for further material to fall into the cluster.

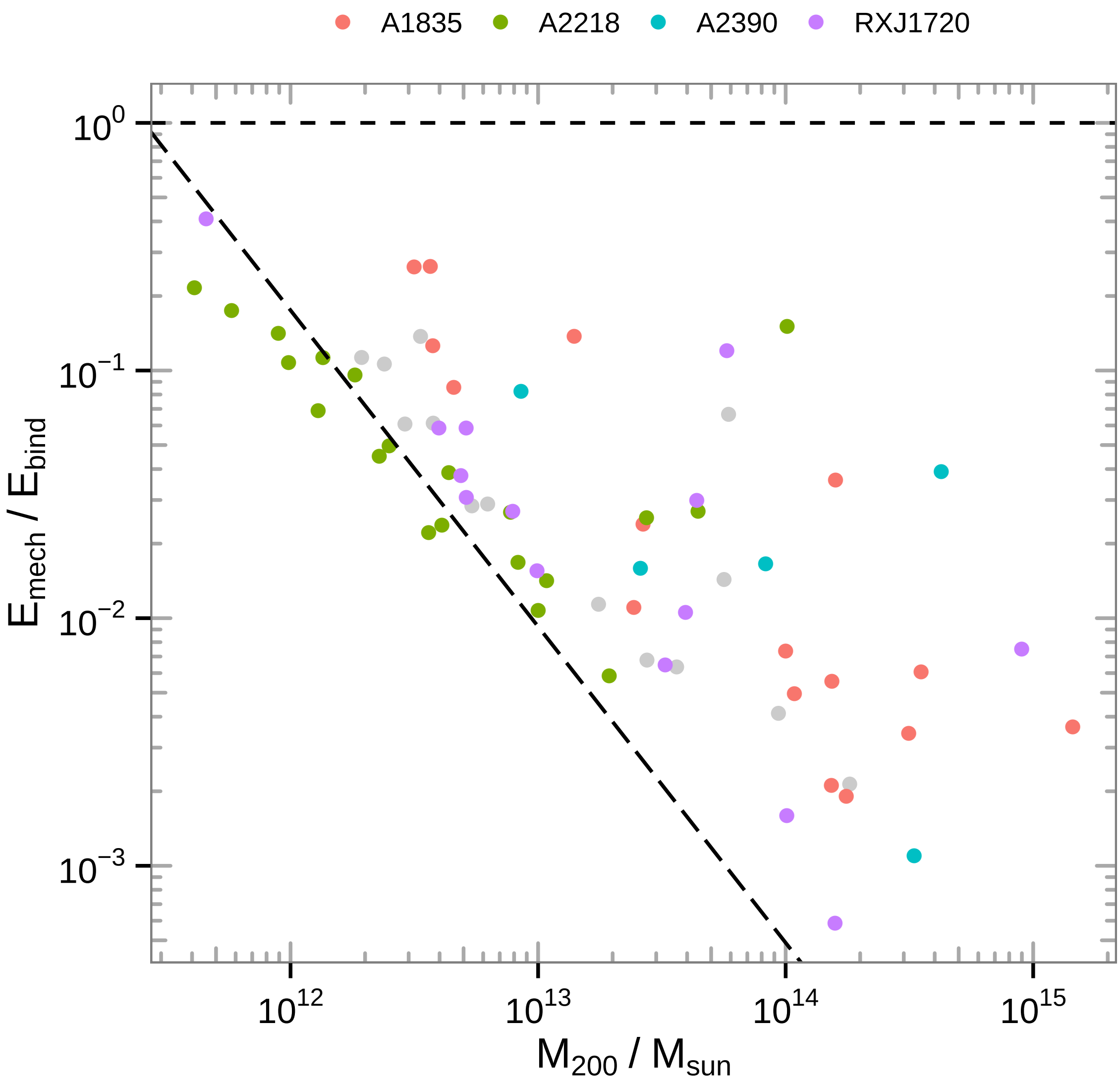

Figure 3.19: The ratio of cavity energy to binding energy for each galaxy is plotted against halo mass (M_{200}). Here, we use Figure 3.13 to estimate the duty cycle, and use that to approximate how the timescale of the radio AGN outburst. The dashed line is the previously shown best-fit line using a constant outburst timescale, instead of one related to the duty cycle.

3.5.5 Heating vs cooling for galaxies

The amount of power from these radio outbursts can also be measured against the rate of cooling that we would infer from X-ray observations. We can use scaling relations in order to estimate the bolometric X-ray luminosity, L_X, from the K-band magnitudes in our source catalogue. Initially, we used Equation 3.15 from Boroson et al. (2011) to estimate L_X from L_K for ellipticals (hot gas component only), and Equation 3.16 from Li and Wang (2013) for discs.

$$L_X/L_K = 4.4^{+1.5}_{-0.9} \times 10^{27}\ \mathrm{erg\ s^{-1}}\ L_{K_\odot} \quad \text{in } 0.5 - 2 \text{ keV} \tag{3.15}$$

$$L_X\,(10^{38}\ \mathrm{erg\ s^{-1}}) = 10^{1.14^{+0.26}_{-0.37}}\ \mathrm{SFR}\,(\mathrm{M_\odot\ yr^{-1}}) \quad \text{in } 0.5 - 2 \text{ keV} \tag{3.16}$$

These relationships are suitable for normal elliptical and disc galaxies respectively, but do not hold for larger galaxies such as BCGs. This is because the gas associated with the haloes of BCGs would be inferred from the clusters' L_X, and therefore the previous equations would not be suitable for this case. We used the cluster L_X to be the same as that of the BCG, this is most likely an overestimate though.

To take this into account, we want to compare how L_X/L_K varies as a function of galaxy halo mass. We use the ASCA cluster catalogue (ACC; Horner, 2001) for a source of cluster bolometric X-ray luminosities, and cross-correlate that with the Lin and Mohr (2004) catalogue for K-band magnitudes of 93 BCGs.

Mathews et al. (2006) investigate the correlation and scatter between X-ray emission and halo mass for elliptical galaxies. They use the catalogue of Ellis and O'Sullivan (2006) to find correlations between M_{vir}, L_X and L_K. We combine these equations to derive the following equation to estimate L_X from L_K.

$$\log\left(\frac{L_X}{L_K}\right) = 1.63\ \log M_{200} + 8.69 \tag{3.17}$$

where L_X is in units of $\mathrm{erg\,s^{-1}}$, L_K is in solar luminosities and M_{200} is in solar masses. All of these relationships are plotted in Figure 3.20, and thus we decide to use the Mathews et al.

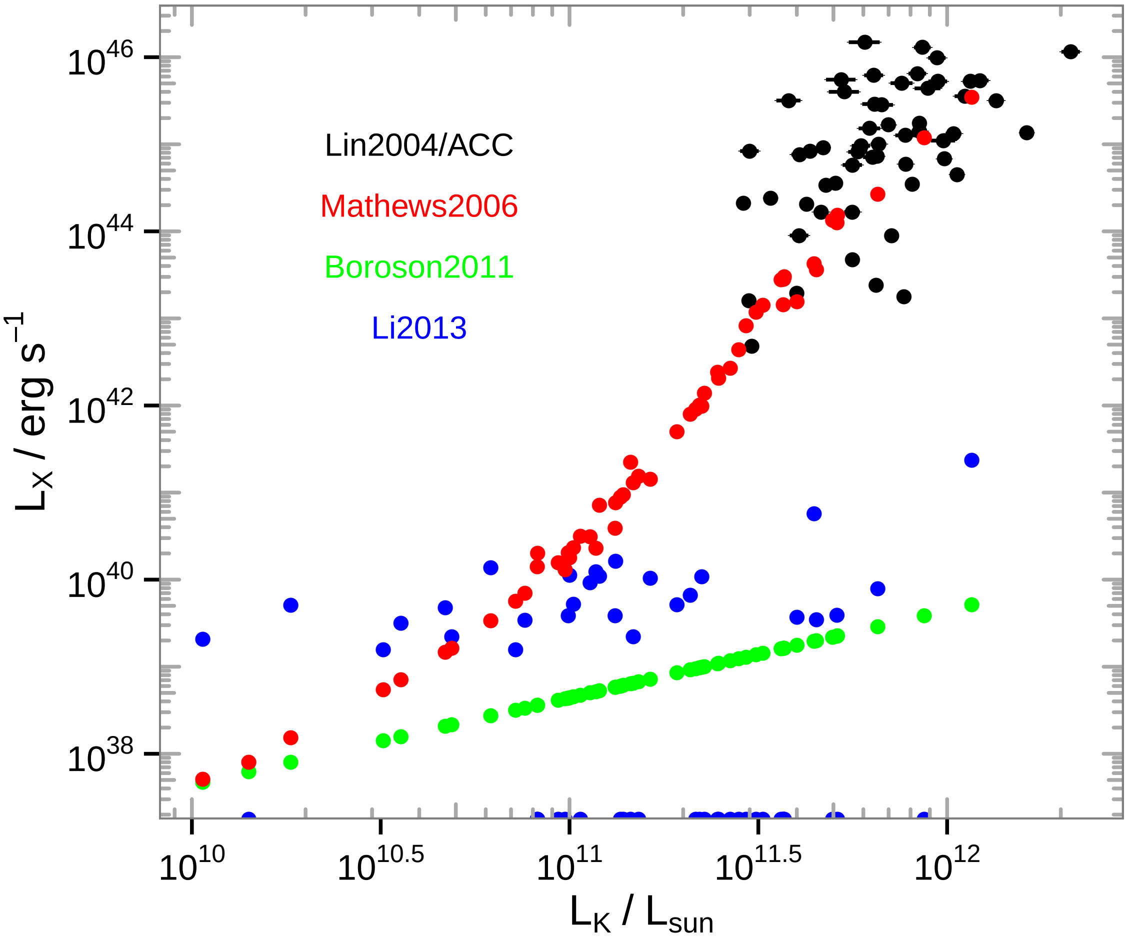

Figure 3.20: L_X is plotted as a function of L_K using different relationships. These are bolometric L_X, except for Boroson et al. (2011) & Li and Wang (2013), which use 0.5−2 keV. A conversion would increase their values slightly, but we have not done so because we are not making use of them. We choose to use Mathews et al. (2006) as it gives a good coverage for our mass range. These scaling relations are quite different from each other because they are applicable to different kinds of galaxies – with a variety of assumptions.

(2006) equation given in Equation 3.17, as it gives sensible coverage of the mass ranges in our sample.

Figure 3.21 compares the heating from the mechanical power inferred from the observed radio luminosity, to the cooling estimated from the derived X-ray luminosities. As our L_X is related monotonically to the halo mass of the galaxy (Equation 3.17), we find a similar relationship to our previous plots, where smaller mass galaxies are significantly impacted by the effects of hosting a radio-loud AGN.

If we again take the case of a typical Milky Way size galaxy with a halo mass of $\sim 10^{12}\,\mathrm{M}_\odot$, we can see that a radio outburst would have enough power to easily overcome cooling by several orders of magnitude. Even if the efficiency of the coupling between the energy output and the surrounding gas was as low as 1%, there would be no difficulty in heating the gas. We see that a radio AGN in a galaxy with a halo mass of $10^{14}\,\mathrm{M}_\odot$ has an amount of energy available similar to the amount needed to stop cooling. This is similar to what Ma et al. (2011) found, using a serendipitous survey of X-ray bright clusters. They found that a system with $L_X \sim 10^{44}\,\mathrm{erg\,s^{-1}}$ has a radio jet power roughly equal to that, and that the average jet power is independent of the X-ray luminosity of the cluster.

3.6 Conclusions and further work

In this work we have used our low frequency GMRT observations of four clusters consisting of 2110 member galaxies, as well as 679 surrounding field galaxies, to investigate radio AGN in a population of galaxies. We derived mechanical powers from the observed radio jets, from an empirical relationship between the integrated radio luminosity of the source and the observed X-ray cavity power. For our radio-loud sources, we found a relatively tight relationship between the ratio of mechanical to binding energies of galaxies to those galaxies' halo masses. The low mass end of our sample shows that Milky Way size galaxies with a radio AGN would have enough energy to eject the gas from their system.

These results were compared to recent simulations from cosmo-OWLS to see if the models present in the simulations gave similar results to our observations. The simulated galaxies were

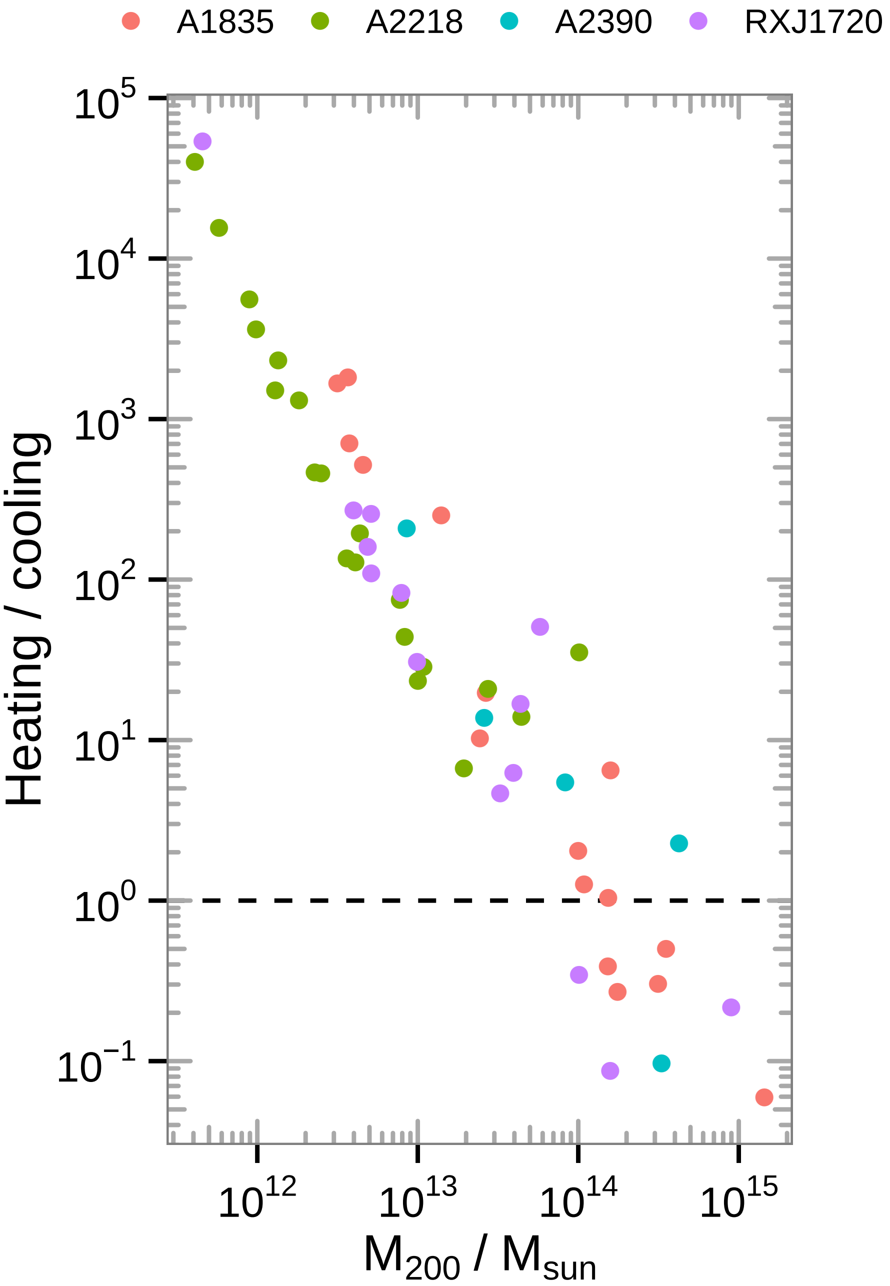

Figure 3.21: Mechanical power of the galaxy divided by the galaxy X-ray luminosity from Equation 3.17, as a function of halo mass.

filtered to include only galaxies above a fixed radio luminosity cut-off, designed to roughly match the depth of our observations. This resulted in very good agreement between the simulated and observed galaxies, suggesting that the model parameters are functioning well. It is also clear that one outburst releases a large quantity of energy into the galaxy. This significantly overheats the gas in lower mass systems and would quench star formation, and could even eject the gas from the system. This assumes that the AGN input at the time of quenching is at least as large as we observe now. As shown by the heating/cooling plot in Figure 3.21, AGN in $L_\star$ galaxies have more than enough energy to balance cooling in galaxies, even if their efficiency is as low as 1%. The AGN in more massive galaxies can help to regulate gas cooling, although they do not have enough energy to eject the gas, they fall into more of a maintenance mode.

However, when no subsets are used and all simulated galaxies are plotted, we find that the energy ratio remains near constant with mass. This shows the large difference that selection effects can have, and that it is important to take them into account. Self-regulation is a plausible explanation to this relatively unchanging ratio with mass, where the AGN only needs to heat and eject a certain fraction of gas.

We also looked at the radio-loud AGN fraction as a function of mass for different radio luminosities. We found that the radio-loud fraction increases with the stellar mass of a galaxy, with a slope of $\beta \sim 1.3$. This is a much flatter slope than previously found in e.g. Best et al. (2005a), and implies that there are a greater number of radio-loud AGN at lower masses than expected from extrapolating the higher mass slope. With the current standard definition of defining a galaxy as radio-loud if it has $L_{1.4\,\mathrm{GHz}} > 10^{24}\,\mathrm{W\,Hz^{-1}}$, it is difficult to probe much below galaxies of mass $10^{11}\,\mathrm{M_\odot}$.

Our sample concentrated on galaxies at a redshift of $z \sim 0.2$, so we were looking at more distant galaxies than the local survey undertaken by Best et al. (2005a). For typical extragalactic radio sources, a source is twice as bright at 610 MHz than at 1.4 GHz. Coupled with our long integrated time on source for our observations means we could take a deeper look at radio galaxies than possible with snapshot surveys, and explore their energetics across a range of masses.

In future work, we would like to investigate the differences between satellite and central galaxies with respect to their fractions and energetics. Our sample would have to be split carefully between the two, but at first order we could assume that cluster galaxies would be satellite galaxies, and the nearby field galaxies would be central galaxies (due to having their own dark matter halo and not being in another group or cluster).

We present now some supplementary work on the effect of radio AGN on the cluster. This work is separate to the above, which is intended to be submitted as a standalone paper, and would ideally be developed further.

3.7 Radio AGN and their environment

In addition to taking the galaxies in our sample as individuals, all of the galaxies in our sample are found in clusters. Therefore, we can also look at both the influence of the cluster environment on these galaxies, and what the galaxies will be doing to their surrounding environments. If we assume the energy escapes into the cluster, we can investigate what impact this will have.

Cluster properties

Our sample of four clusters consist of three strong cool-core clusters, and the non cool-core cluster is Abell 2218. More information on these clusters can be found in §5.

3.7.1 Radio fraction as a function of its environment

An interesting question to answer is does the radio-loud fraction change as a function of its environment? Does the denser environment provoke radio AGN activity? Figure 3.22 presents the radio fraction as a function of radius. This radius has been scaled by r_{200} and all cluster members are stacked together. The BCGs are given their own separate bin as they are considered to be a special case. We also plot the field galaxies, described earlier, as a separate comparison sample.

Table 3.5: List of offsets between BCG and X-ray centres.

Name	Offset (r/r_{500})
A1835	0.004
A2218	0.034
A2390	0.002
RXJ1720	0.005

We define the centre of the cluster as the position of the BCG. The X-ray profiles use the X-ray centre. The difference between them is negligible in all but one cluster, where the merging cluster A2218 has a slightly larger offset. Table 3.5 shows the offsets between them in terms of r_{500}, and none are significant enough to take note of.

Figure 3.23 shows how the fractions of radio-loud galaxies with stellar masses, $M_\star \gtrless 10^{11} M_\odot$, decrease as a function of intracluster radius. The less massive, fainter galaxies drop off much quicker than the larger galaxies, suggesting that it is the low mass group having the affect on the decreasing overall fraction.

For the cluster galaxies, this is perhaps what you would expect. The larger galaxies are more likely to be passive and less susceptible to environmental processes. If we assume that radio-loud AGN prefer to be hosted by ellipticals, we would recover this flat trend.

It is important to consider the loss of sensitivity with increasing distance from the centre. Figure 3.24 shows the observed 610 MHz radio luminosity of our clusters as a function of radius. We can see that the upper limits gradually increase as the source gets further away from the centre. For both the cluster and field sample we see some evidence of a negative trend with radius is observed. There should be no physical reason why the fraction of radio-loud AGN decrease for the field sample, as this should be mostly uniform across the sky. We must assume that we are missing some of the fainter galaxies towards the outskirts of the field of view.

3.7.2 Heating vs cooling for clusters

Thermal energy

We estimate the amount of energy input from a radio AGN into its surroundings by taking the calculated mechanical powers from §3.5.2, and assuming a typical outburst timescale of 10^8 yr.

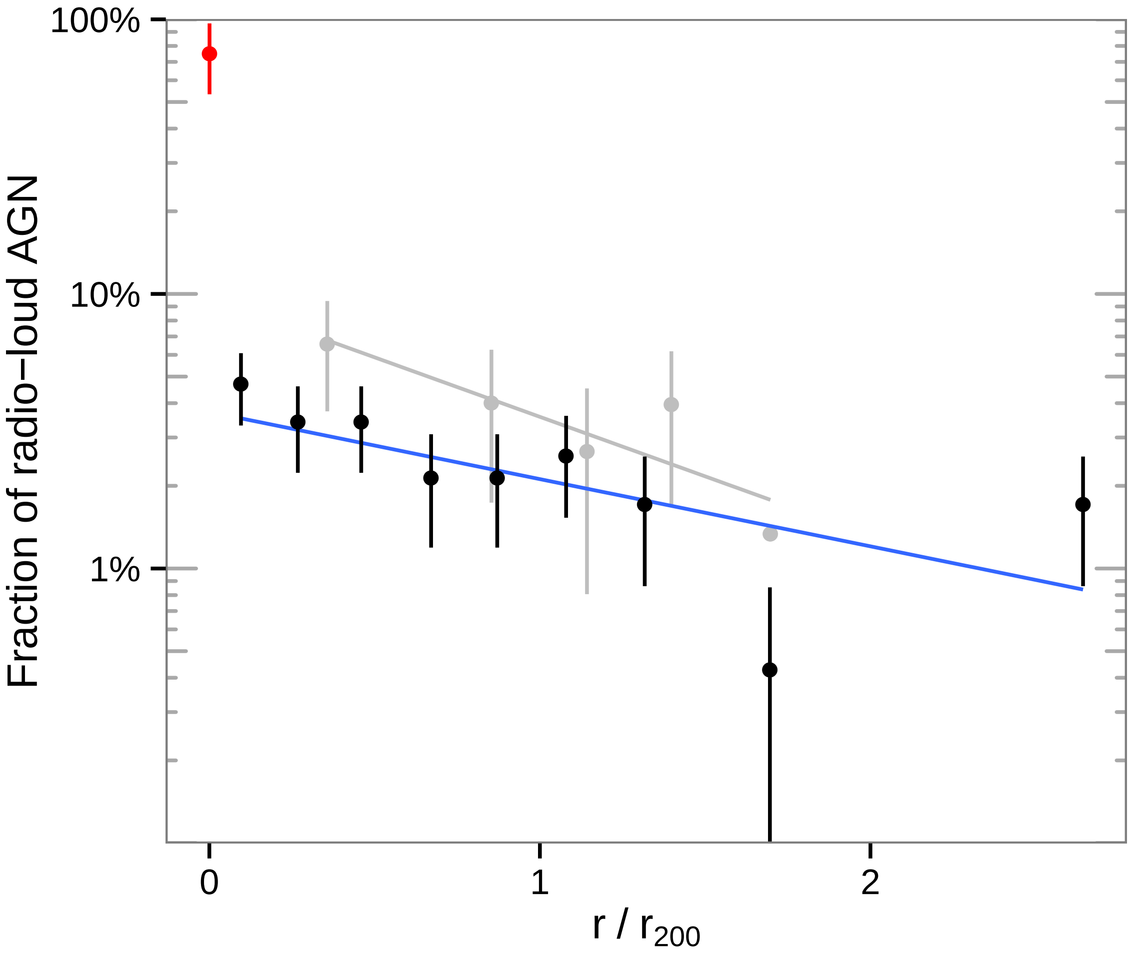

Figure 3.22: The radio fraction as a function of r/r_{200}. Each bin has an equal number of galaxies in, and its position on the x-axis is the midpoint of the range of the bin.

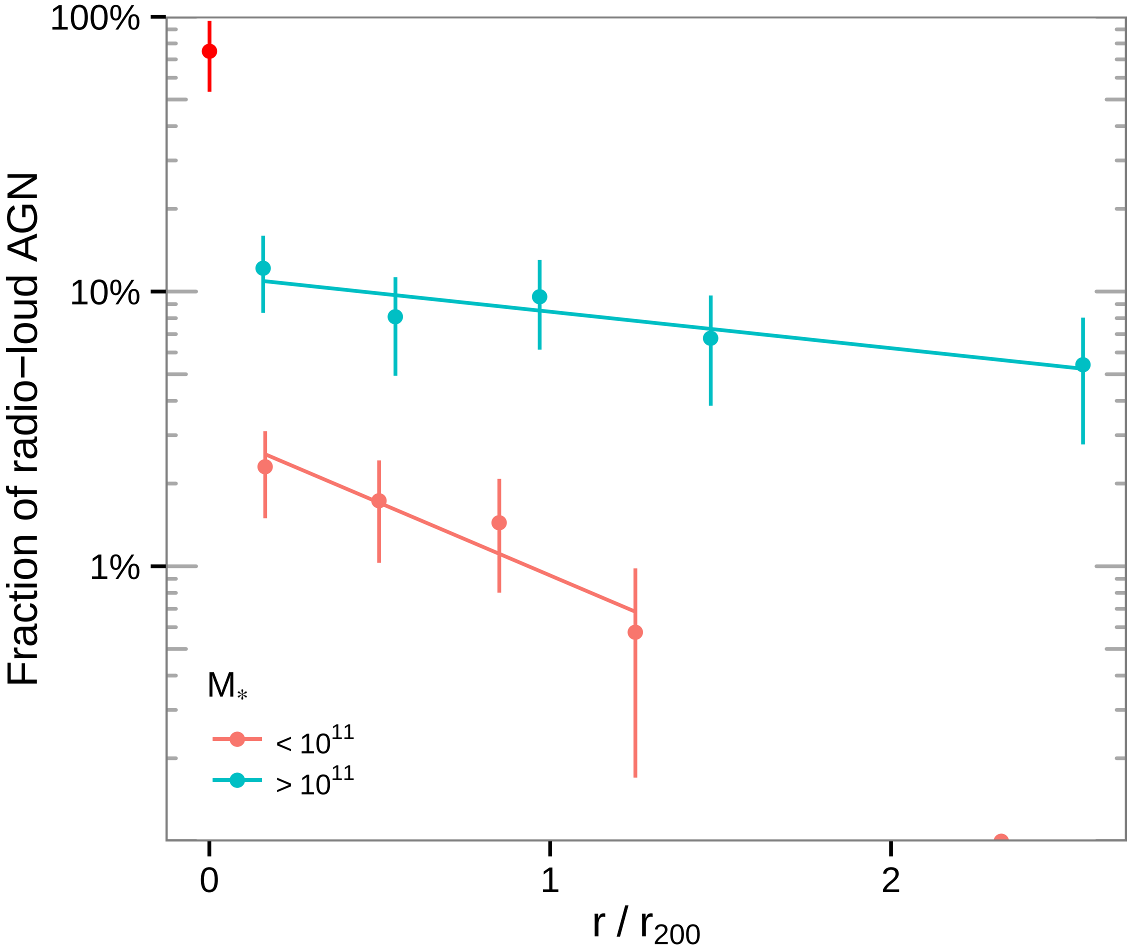

Figure 3.23: The radio fraction as a function of $\frac{r}{r_{200}}$, split by $M_\star \gtrless 10^{11}\ M_\odot$. Each bin has an equal number of galaxies in, and its position on the x-axis is the *midpoint* of the range of the bin. The upper-left point at zero radius are the cluster BCGs.

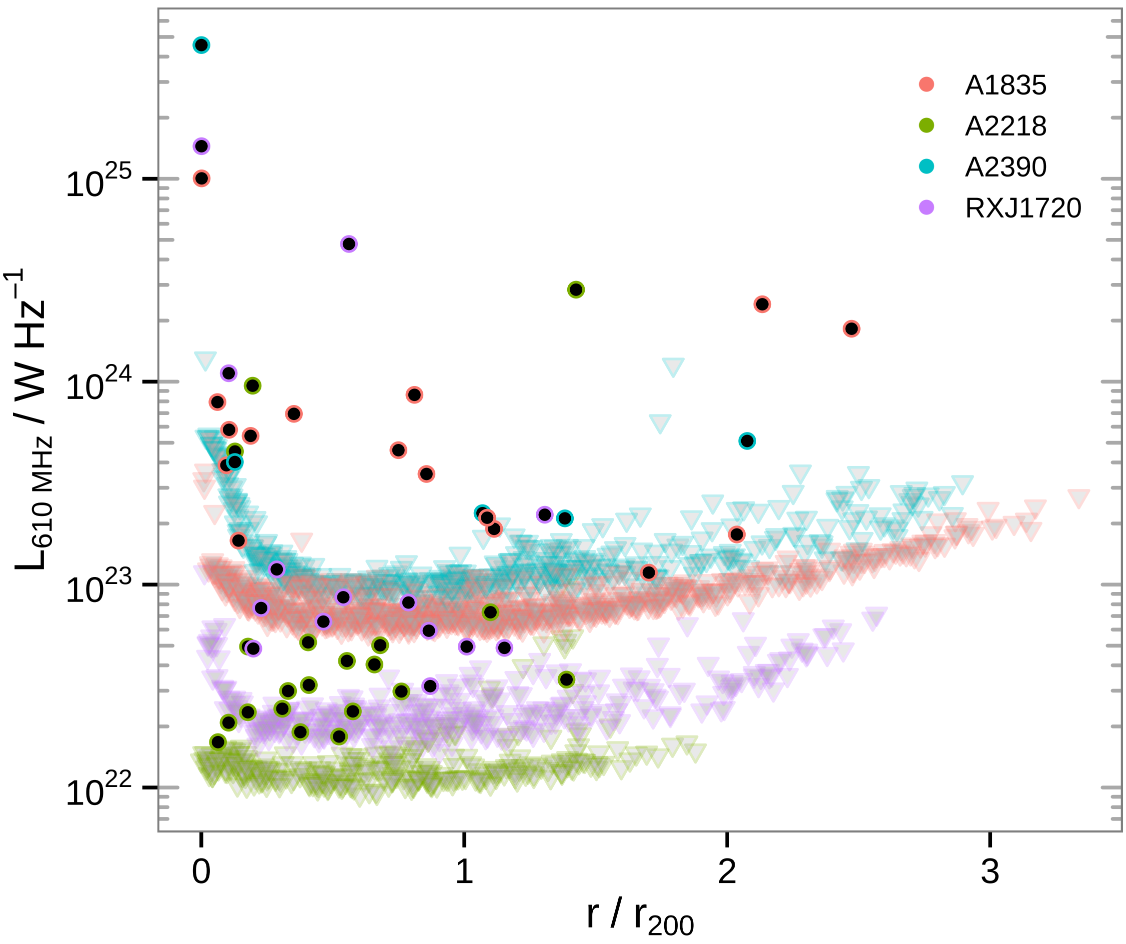

Figure 3.24: The observed 610 MHz radio luminosity as a function of r/r_{200}. Filled point are radio detections, shaded triangles are upper limits.

In this instance, we are only considering one outburst. We then consider within what volume an AGN would have a significant influence on its surroundings. We determine significant to be when the mechanical energy input is equal to the thermal energy. For this section, to simplify things we assume that the efficiency of converting the mechanical energy from the radio AGN to thermal is unity, and that all of the mechanical energy is released outside of the galaxy. In reality though the efficiency will be less than unity, which would then be factored into our calculations. At the resolution of our observations, the maximum size to the jets of our point source radio AGN are ∼15 kpc.

The thermal energy of the gas in the cluster, U, is calculated from X-ray observations, using Equation 3.18,

$$U = \frac{3}{2} \int_0^r \epsilon \, n_e(r) \, kT(r) \, 4\pi r^2 \, dr \tag{3.18}$$

where $\epsilon \, n_e(r)$ and $kT(r)$ are the particle density and temperature at a radius r from the centre of the cluster. Following Sanderson et al. (2013), we assume the ICM is a fully ionised plasma with a mean metallicity of 0.5 solar, with a ratio of electron to hydrogen number density of 1.157. From this, we take $n = n_e + n_H$ and therefore $\epsilon = 1.86$.

To find the local thermal energy inside a spherical volume with radius, r_{loc}, we use Equation 3.19.

$$U = \frac{3}{2} \epsilon \, n_e(r) \, kT(r) \, \frac{4}{3} \pi r_{\mathrm{loc}}^3 \tag{3.19}$$

This assumes that the local gas density and temperature are good approximations for the local volume as a whole, and that the galaxy does not move significantly with respect to the cluster in the timescale given. The latter is probably not a very good assumption, because a typical velocity dispersion of a cluster galaxy is on the order of ∼1000 km/ sec, which would result in a distance of ∼1 Mpc travelled over this timescale. However, the conclusions should not change significantly. For each galaxy, we calculate the radius of a sphere needed to balance the thermal energy to the mechanical energy provided by the radio AGN. This sphere of influence is presented in Figure 3.25. A galaxy on the outskirts of a cluster is able to have a bigger local effect due to the decreased gas density.

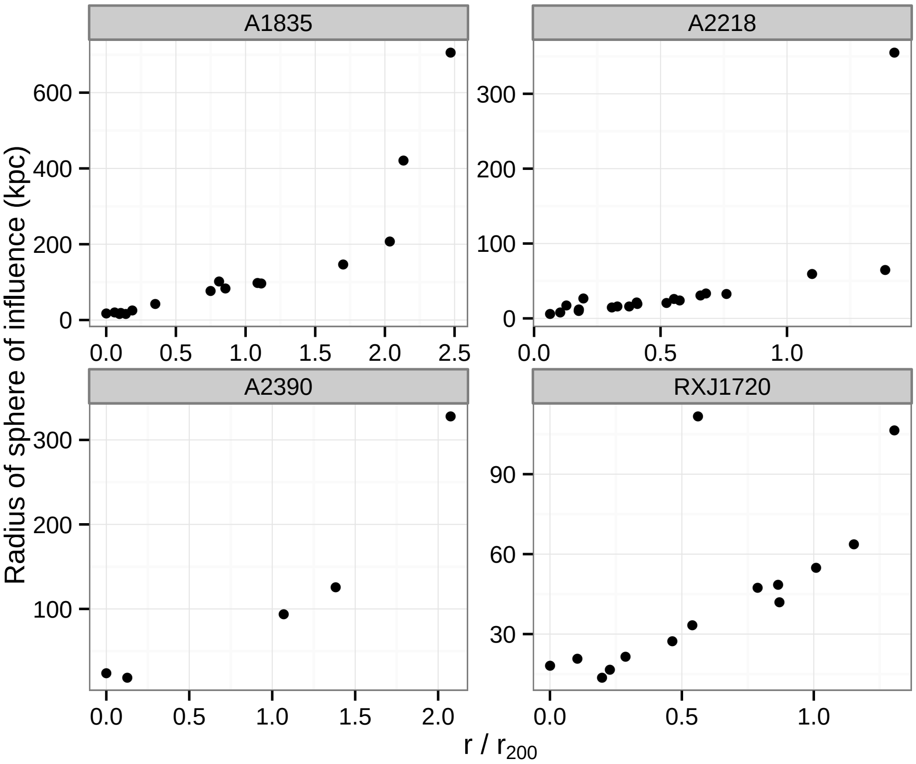

Figure 3.25: The localised influence of each radio AGN in their clusters, as a function of radius from the cluster.

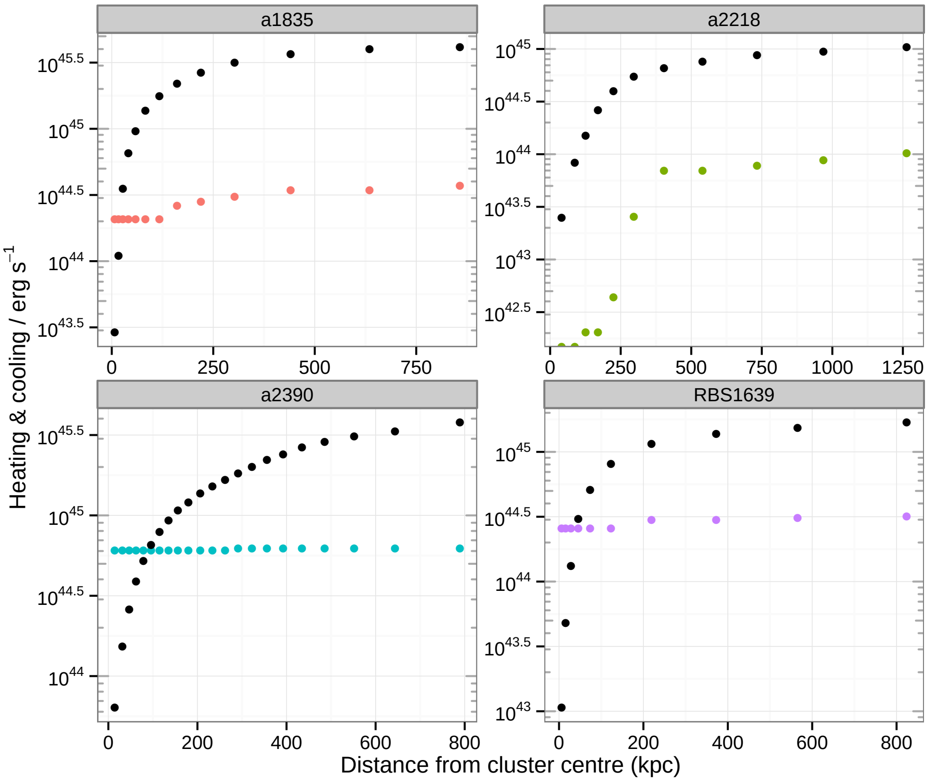

Figure 3.26: Shows the raw values of the **cumulative** mechanical power and X-ray luminosity, as a function of radius. Radio power are the coloured points, L_X are the black points.

Using X-ray luminosities

Another estimate of the effect on the cluster can be found by using bolometric X-ray luminosities (0.001–100 keV) for the 3D shells of each cluster (note: not projected annuli). For the same radial bins as used above, we find the amount of mechanical power estimated from the radio luminosity inside each bin, giving both an energy input from the AGN (heating), and energy losses from L_X (cooling) as a function of radius.

Figure 3.27 shows the ratio of the cumulative radio power and L_X. The central radio AGN power is more than enough to heat the core, but at larger radii the cooling increases considerably due to acting over a much larger volume than the radio AGN can cover. The bins can also be looked at individually, as in Figures 3.26 & 3.28. Some bins are zero because there are no radio AGN in that radial section, and also there are more radio AGN towards the outskirts of the cluster, but the X-ray radial profiles do not extend as far.

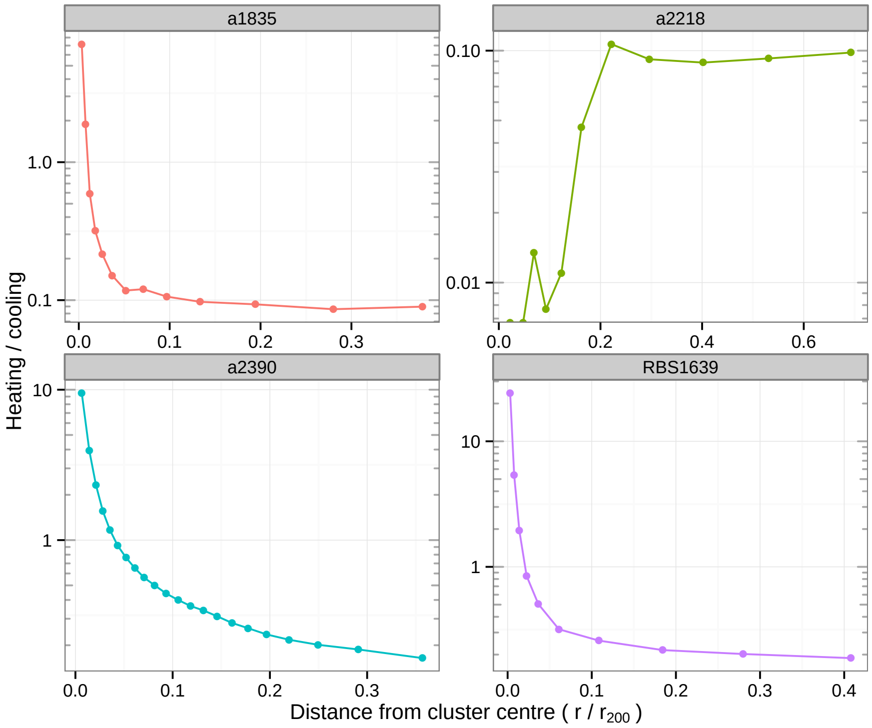

Figure 3.27: Shows the ratio of the **cumulative** mechanical power and X-ray luminosity, as a function of radius. As in Figure 3.26.

Figure 3.29 has tickmarks showing the positions of the radio AGN, and splits the contribution from the BCG and other radio AGN. If the AGN activity observed is a typical snapshot of the activity of a cluster, this shows that the non-central radio AGN do provide up to $\sim$ 10% of the energy needed to balance cooling at any given time. This assumes that current snapshot will on average remain constant, with this fraction of AGN each powering on for 10^8 yr.

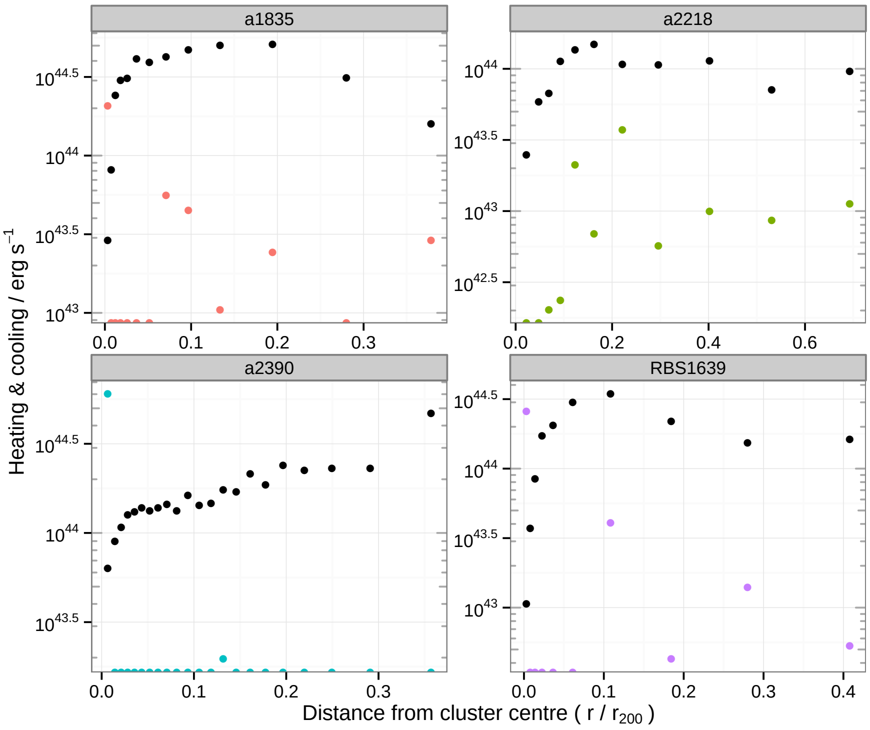

Figure 3.28: This is the power **inside each radial bin**. Radio power are the coloured points, L_X are the black points.

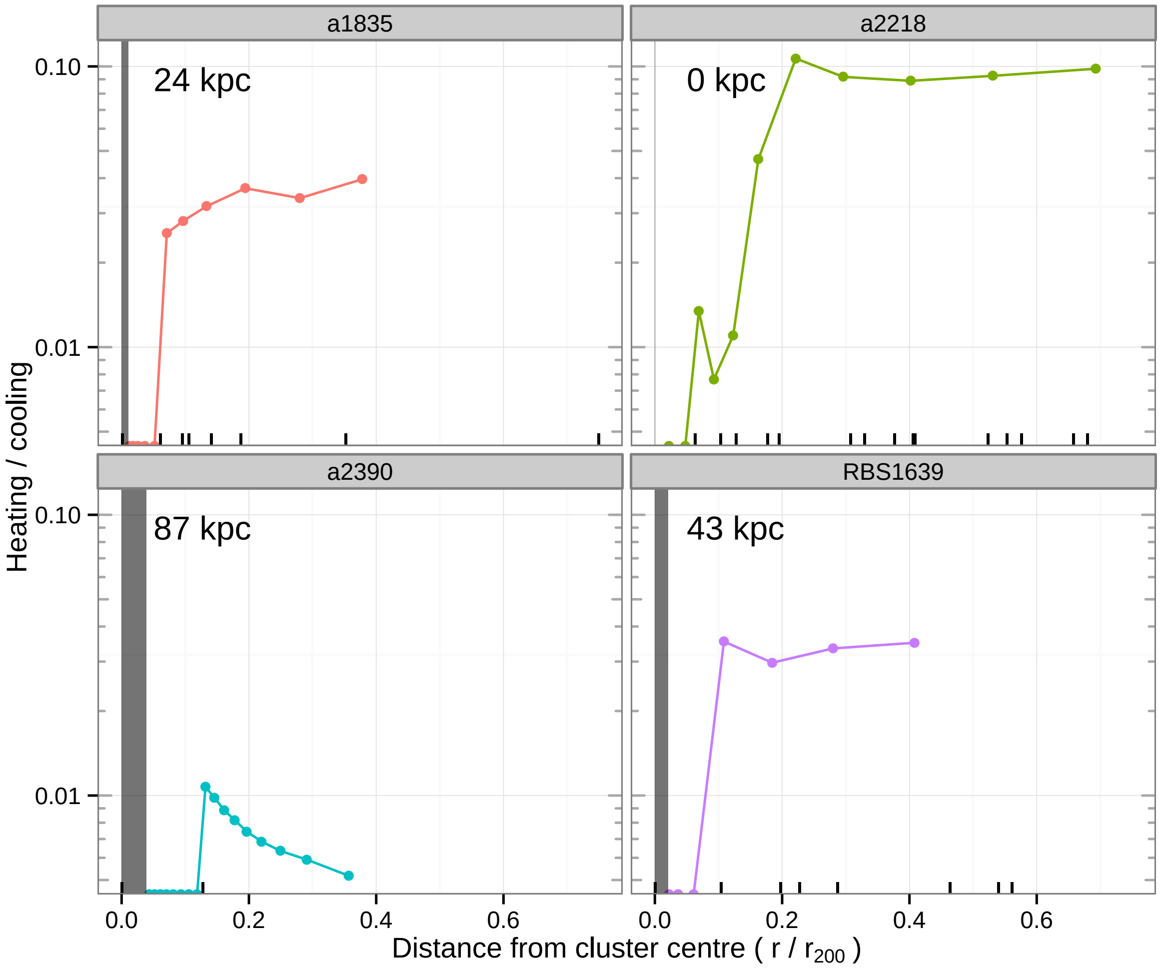

Figure 3.29: Ratio of **cumulative** powers. The shaded area is the radius at which the BCG alone can balance cooling, with the radius quoted in kpc. The coloured points are for the cumulative non-BCG radio AGN. The black ticks along the x-axis show the position of each radio-loud AGN, for $r/r_{200} < 0.75$.

Chapter 4

The interaction between AGN and the intracluster medium

Extragalactic radio jets seen in active galactic nuclei are likely an important source of energy to explain a number of conflicts between observations and theory. Their composition and power, however, is still uncertain. In this chapter, we will use a sample of radio-loud galaxies with discovered X-ray cavities to explore these radio properties. Low frequency observations are key to ascertaining and placing constraints on these different variables, as it is only at these frequencies that we can see the faint, but energetically important population of electrons. We use the GMRT to observe our sample with at least two of the 150, 235 and 610 MHz frequencies available with that array. Previous investigations of the jet radio spectrum used higher frequency data, which were then extrapolated to the lower frequencies, yielding large error values. With low frequencies, it is possible to cover more of the synchrotron spectrum, and thus place limits to its shape in the frequency plane. This, along with X-ray estimates of the age of the source, will allow us to place constraints on k, the ratio of energies carried by heavy particles to electrons, for our entire sample. Our estimates of the synchrotron ages of our sources can be compared to the X-ray deduced buoyancy timescales.

Our second motivation is to investigate the correlation between the synchrotron power we observe at low frequencies with the mechanical power of the jets. The surface depressions in the X-ray luminosity are a good proxy for the amount of energy the jets impart onto the gas. Finding a relationship between the two can allow good estimates of jet power when X-ray

Table 4.1: List of galaxy clusters observed by the GMRT (sample selection described in §1.5) The radio emission is the measured extended emission of the central AGN. Scale is the linear scale on the sky, given the redshift.

Cluster Name	RA$_{J2000}$ ($^{\mathrm{h\ m\ s}}$)	Dec$_{J2000}$ ($^{\circ}$,$'$,$''$)	z	$S_{1.4\ \mathrm{GHz}}$ (mJy)	log $P_{1.4\ \mathrm{GHz}}$ (W Hz^{-1})	Scale (kpc arcsec^{-1})
2A0335	03:38:35.3	09:57:54.7	0.0349	36.7	23.00	0.688
A478	04:13:20.7	10:28:35.0	0.0881	36.9	23.84	1.628
MS0735	07:41:44.5	74:14:39.5	0.2160	21.9	24.47	3.474
Hydra A	09:18:05.7	-12:05:44.0	0.0549	40800.0	26.45	1.054
RBS797	09:47:12.9	76:23:12.8	0.3540	21.7	24.98	4.949
A1795	13:49:00.5	26:35:06.7	0.0625	925.0	24.93	1.190
A1835	14:01:02.1	02:52:41.9	0.2532	32.2	24.79	3.913
A2029	15:10:56.0	05:44:40.9	0.0773	480.0	24.84	1.447
A2052	15:16:45.5	07:00:01.1	0.0355	5500	25.19	0.697
A2218	16:35:54.0	66:13:00.1	0.1756	4.7	23.60	2.949
Hercules A	16:51:08.1	04:59:33.3	0.1540	44870.0	27.45	2.647
RXJ1720	17:20:08.9	26:38:06.0	0.1640	89.0	24.81	2.789
A2390	21:53:34.6	17:40:10.9	0.2280	63.0	24.98	3.621
A2597	23:25:18.0	-12:06:29.9	0.0852	1875.0	25.52	1.580
A2670	23:54:13.7	-10:25:08.0	0.0762	6.6	22.96	1.428

data is not available or deep enough to find cavities. As stated previously, low frequencies can observe the older and fainter electron population, and see the radio emission that fill what were previously defined as 'ghost cavities'. These formed the basis for our proposals to gaining time with the GMRT. We were awarded observation time in observing cycles 17–20. Our sample of galaxy clusters is shown in Table 4.1. In Chapter 5, we present our GMRT radio images for our sample, and also take a more in-depth look at several selected clusters.

4.1 Cluster energetics

Our sample consists almost exclusively of cool-core clusters, with Abell 2218 being the sole non-cool-core cluster. We determined this by using the Archive of Chandra Cluster Entropy Profile Tables (*ACCEPT*) [1] (Cavagnolo et al., 2009). We plotted this X-ray data in Figure 4.1, where one cluster is clearly separate from the others. Indeed, as stated in §1.5, this cluster was observed for alternative reasons.

---

[1] `http://www.pa.msu.edu/astro/MC2/accept/`

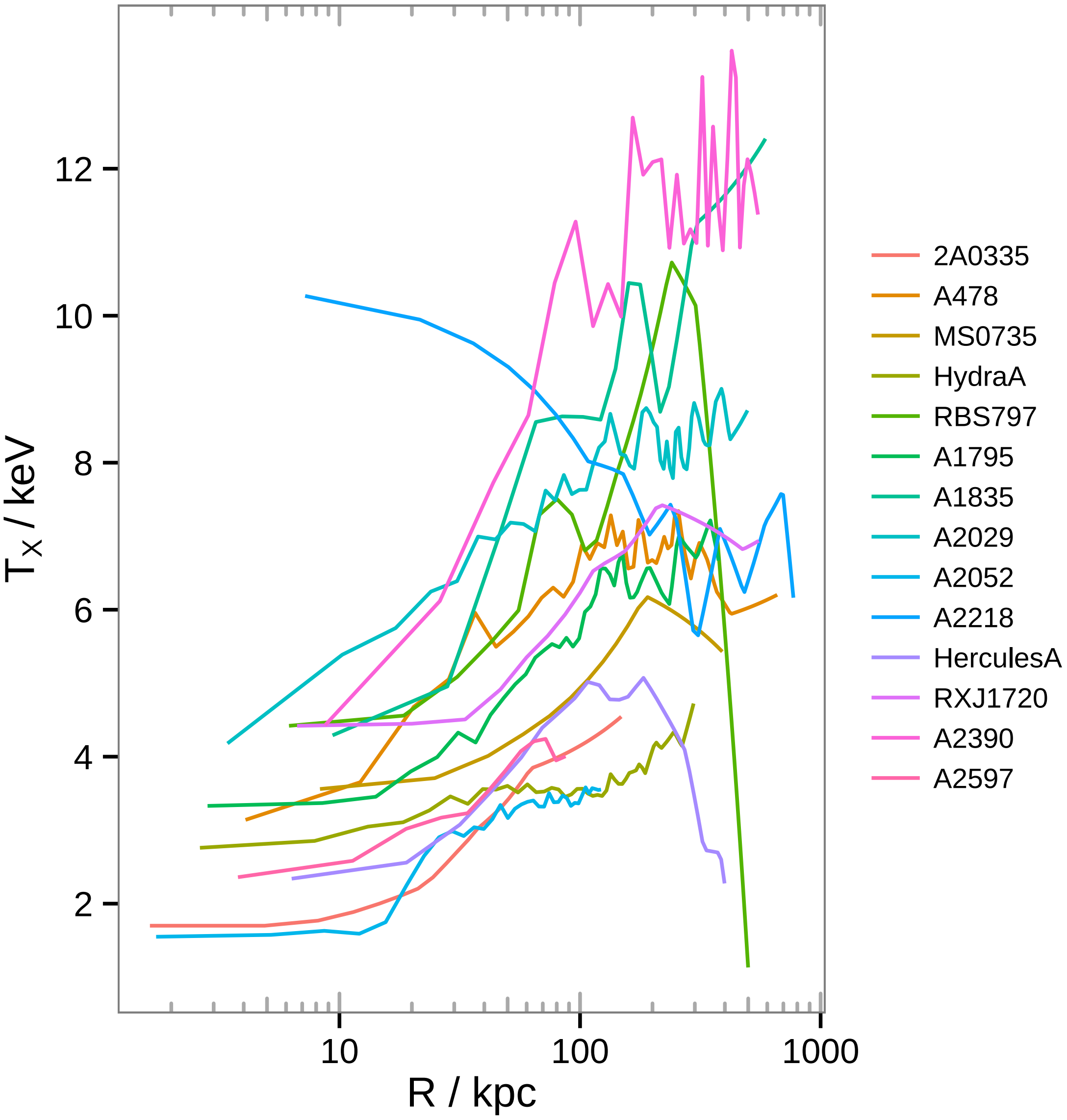

Figure 4.1: The X-ray temperature is plotted as a function of radius for all of the clusters in our sample. The data have been acquired from the ACCEPT database (Cavagnolo et al., 2009).

Table 4.2: The flux densities for all the central AGN of our sample.

Cluster Name	S_{610} (mJy)	S_{235} (mJy)	S_{150} (mJy)	α	L_{radio} (10^{42} erg s^{-1})	P_{cav} (10^{42} erg s^{-1})
2A0335	54.5		952	−1.6	0.0251	24
A478	89.6	182	274	−0.74	0.0730	100
MS0735	172	1550	4520	−2.3	20.5	6900
Hydra A	82 400	184 000		−0.84	23.2	430
RBS797	50.8	126	218	−0.95	0.893	1200
A1795	2060				0.765	160
A1835	59.5	106		−0.61	0.545	1800
A2029	1660	4300		−1.0	1.00	87
A2052	15 700	40 000			1.86	150
A2218	18.8	52			0.0697	
Hercules A	79 500	170 000		−0.80	207	310
RXJ1720	219	425		−0.70	0.686	
A2390	341	624		−0.63	2.38	
A2597	4960				3.55	67

We calculate integrated flux densities at multiple frequencies for each of the radio sources in our sample. These are shown in Table 4.2. We show these flux densities as a function of frequency in Figure 4.2. Fluxes from our radio maps are marked as red points, other literature values have been taken from Bîrzan et al. (2008). Hercules A literature flux density values are from Gizani and Leahy (2003); Gizani et al. (2005).

Figure 4.3 plots luminosity as a function of frequency, using the k-corrected formula

$$P_\nu = 4\pi\, D_L^2\, (1+z)^{-(\alpha+1)}\, S_\nu \tag{4.1}$$

where D_L is the luminosity distance to the source, z is the redshift, α is the spectral index and S_ν is the flux density of the source at the frequency ν.

Rafferty et al. (2006) used the *Chandra* X-ray telescope to observe a sample of systems with known or suspected X-ray cavities. From this data, they can calculate the energy needed to create a cavity. This is equal to the work done by the AGN jet against the surrounding intracluster medium, $E_{\mathrm{cav}} = 4pV$. To convert this into a power, one simply needs to divide by the age of the outburst. This is typically assumed to be the buoyancy timescale.

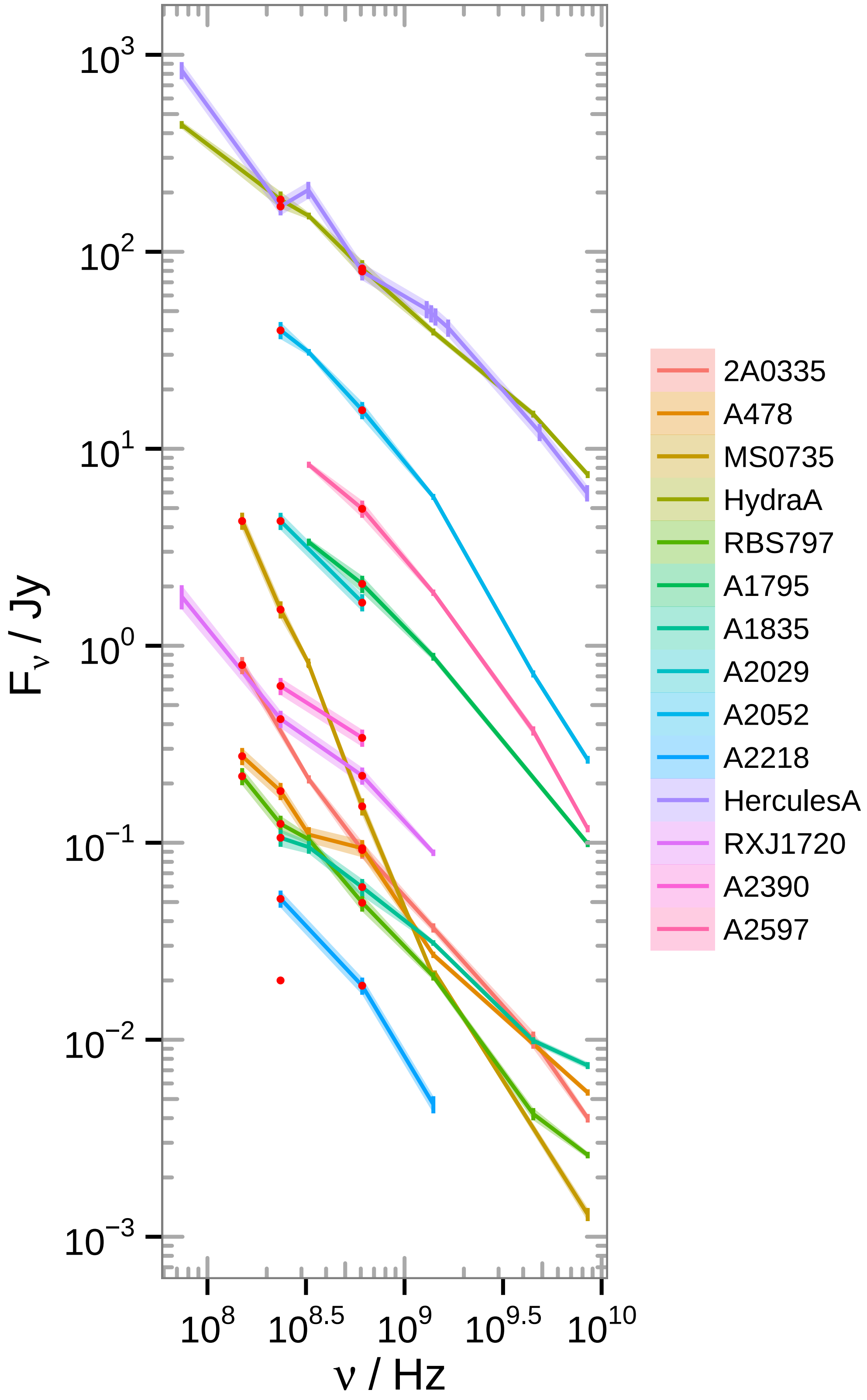

Figure 4.2: The radio *flux* for each cluster is shown here at each of the frequencies it is detected in. This gives an idea to how sensitive our observations were. Each connected line is a single cluster. Red points are from our GMRT data, the rest are from Bîrzan et al. (2008) unless stated in the text. Note, no radio emission is found associated with the BCG for Abell 2218, plotted for this cluster is the diffuse emission of the radio halo (see §5.5).

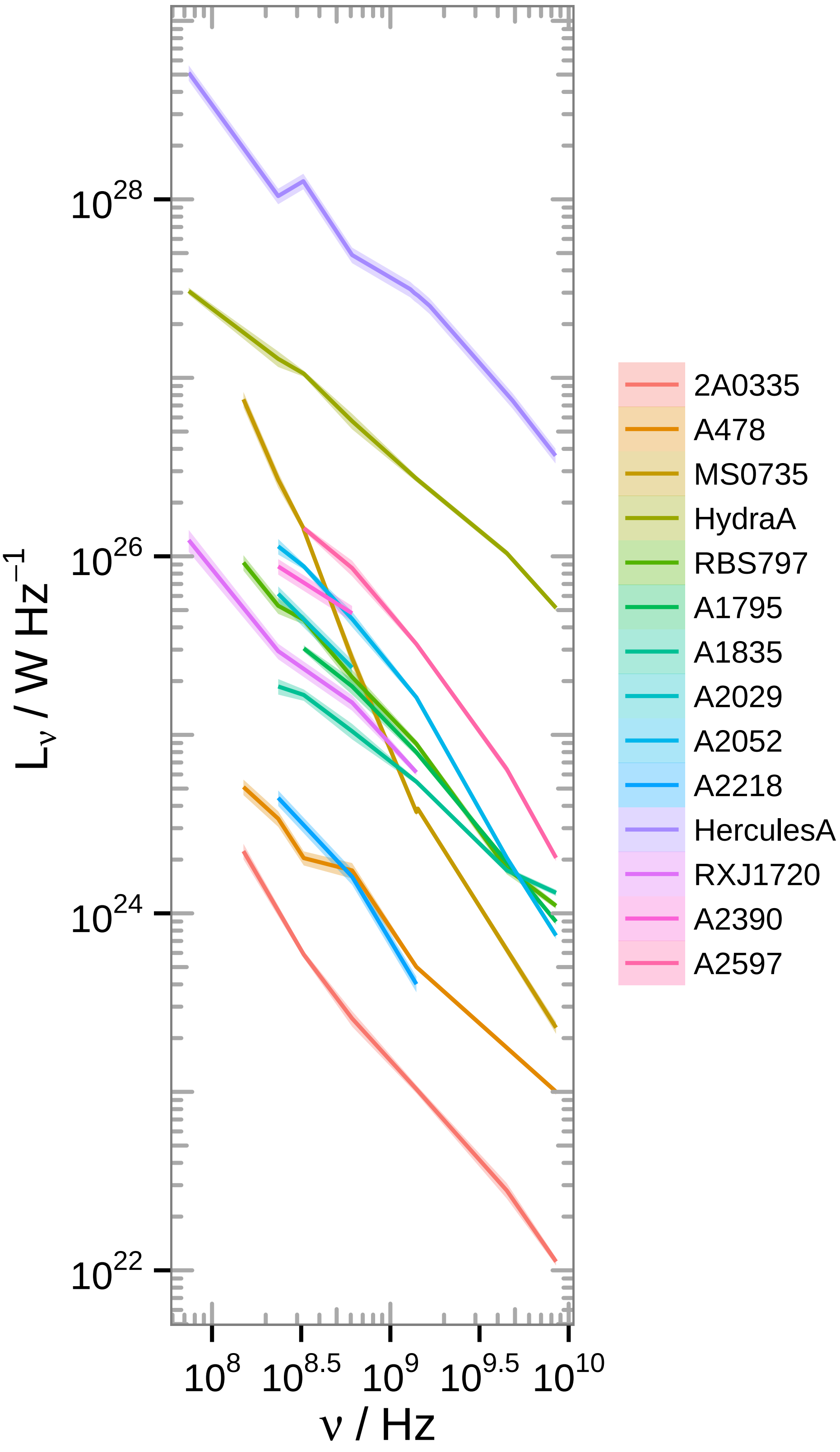

Figure 4.3: Radio *luminosity* is shown here as a function of frequency.

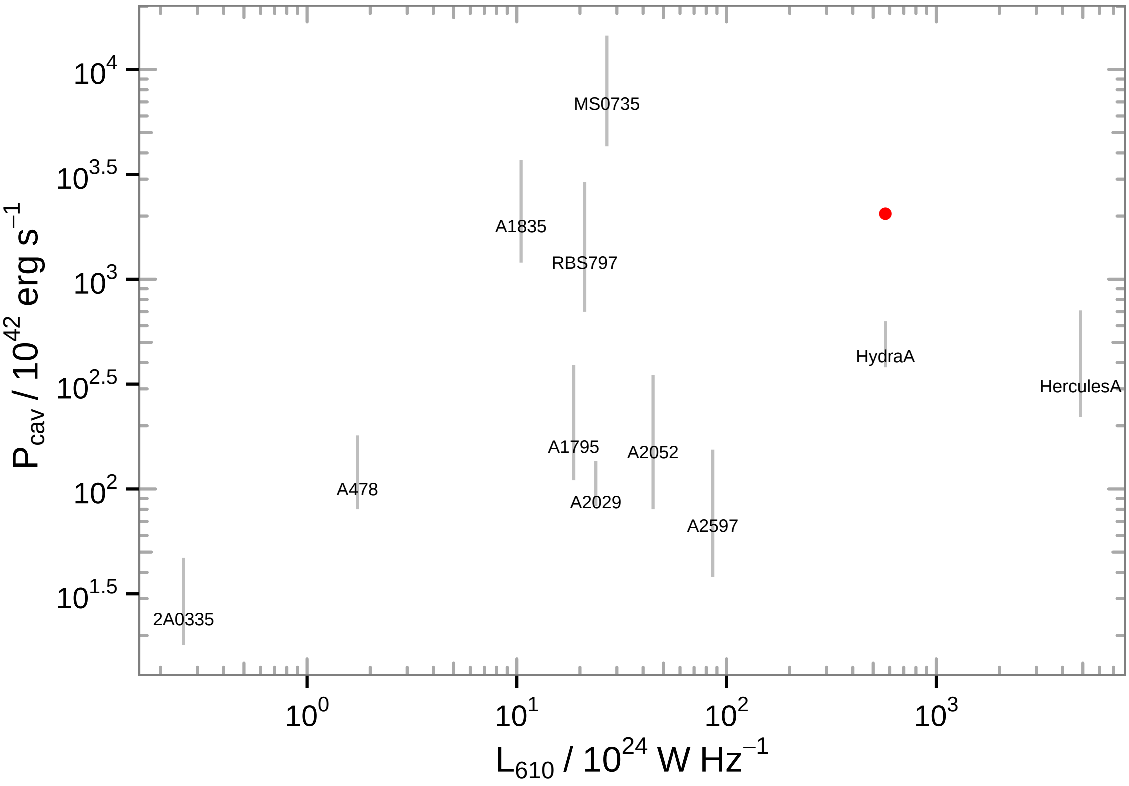

Figure 4.4: Radio luminosity vs cavity power for each of our cluster sample. This is for our 610 MHz data, the cavity powers are from Rafferty et al. (2006). The red dot shows the totalled cavity power of Hydra A from Wise et al. (2007).

11 systems in our galaxy cluster sample are also part of the study by Rafferty et al. (2006). We can thus use their cavity powers and compare them to the radio luminosities of the cluster BCGs that we observe. These results are plotted in Figure 4.4.

Previously, higher frequency data has been used to try and link jet power with radio luminosity. Higher frequencies show more of an instantaneous jet power, so will significantly underestimate the powers involved in older outbursts. Our 610 MHz observations are of high quality, so will be able to detect the less luminous and older outburst. A good example of this is in Hydra A, where deep X-ray data discovered a pair of outer cavities (Wise et al., 2007). These were undetected at 1.4 GHz, but are observable with the GMRT.

We find a weak positive correlation between jet and cavity powers (for the 610MHz values: we find a correlation coefficient of 0.31, with a p-value = 0.35). Figure 4.5 shows the same relationship, but this time using only our 235 MHz observations. As this is an even lower

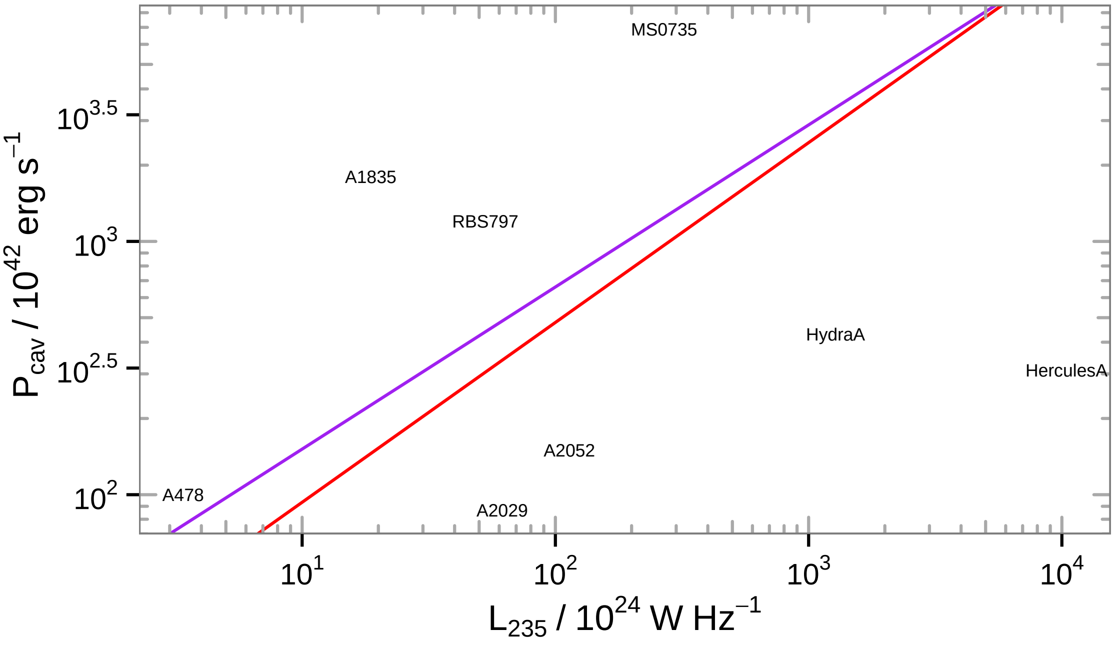

Figure 4.5: Radio luminosity vs cavity power for each of our cluster sample. This is for our 235 MHz data, the cavity powers are from Rafferty et al. (2006). The red line is from the relationship given by O'Sullivan et al. (2011), and the purple line is from Cavagnolo et al. (2010).

frequency, we should be less affected by synchrotron losses from spectral ageing. The red line is from the best-fit relationship of O'Sullivan et al. (2011) for their group sample, and is given in Equation 4.2. The purple line is from Cavagnolo et al. (2010), and is Equation 4.3. With this fewer number of clusters, the trend is not as strong as we would prefer to observe. These results are for monochromatic data though, the situation improves if we combine our data together.

$$\log P_{\rm cav} = (0.71 \pm 0.11) \log L_{235} + (1.26 \pm 0.21) \tag{4.2}$$

$$\log P_{\rm cav} = (0.64 \pm 0.09) \log L_{200--400} + (1.54 \pm 0.12) \tag{4.3}$$

where $P_{\rm cav}$ and $L_{\rm radio}$ are in units of 10^{42} erg s^{-1}.

To try and improve our estimates of radio luminosity further, we calculate the integrated radio luminosity for each of our clusters. We follow O'Sullivan et al. (2011) and assume a power-law spectrum based on the spectral indices that we calculate from our data. These spectral indices vary for each cluster, so this should provide a better measure for the radiative

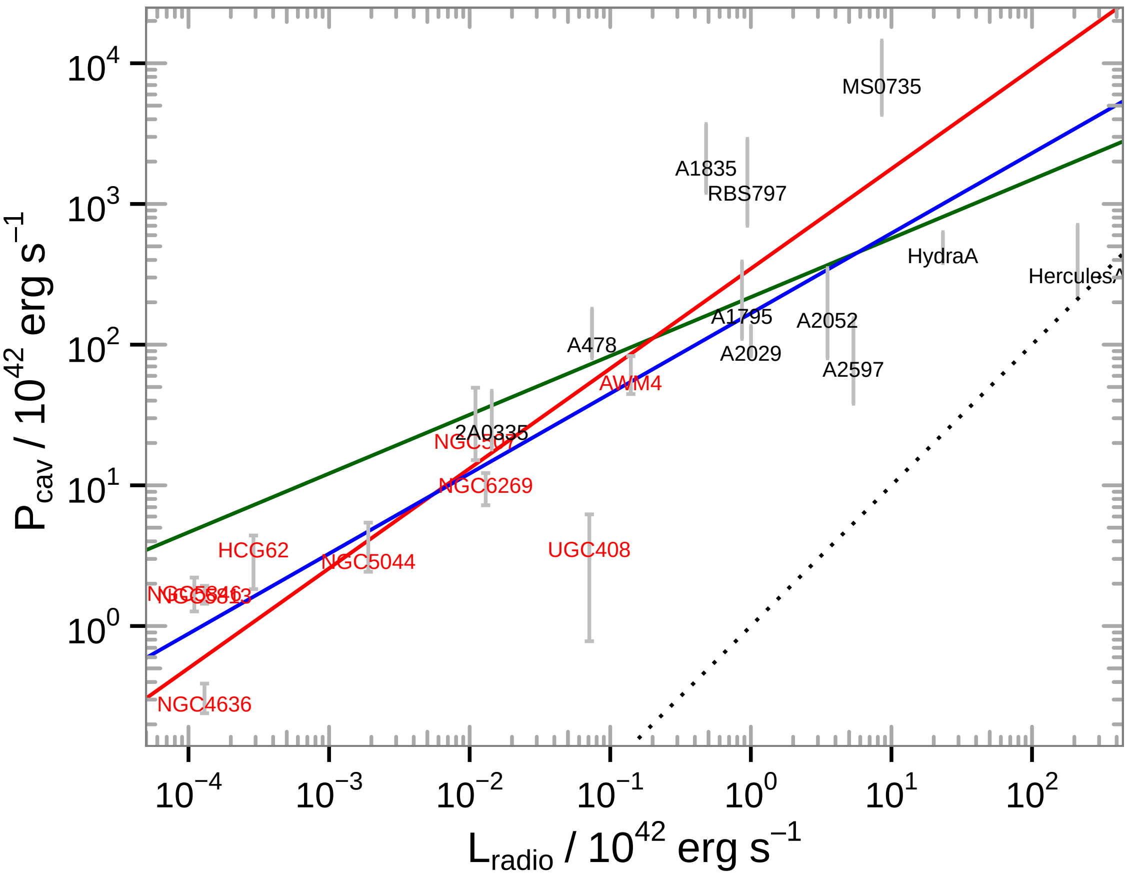

Figure 4.6: Integrated radio luminosity (10 MHz–10 GHz) is plotted against cavity power. Luminosities are calculated from all available data points, including those from literature. The red line is from the relationship given by O'Sullivan et al. (2011). The blue line is from an orthogonal BCES regression line, the green from using our cluster GMRT observations only. The red points are also from GMRT observations of groups by O'Sullivan et al. (2011). The dotted black line is equality.

power. We only include our GMRT data in the calculation of the spectral index because we have been using dual-frequency data, which has then been resolution matched and the same uv–range has been used, this should mean our spectral indices are reliable. We use a frequency range of 10 MHz–10 GHz as the limits to our integral.

$$\int S(\nu)\,d\nu = \int \kappa\,\nu^{\alpha}\,d\nu = \begin{cases} \dfrac{\kappa}{\alpha+1}\,\nu^{\alpha+1} & \text{if } \alpha \neq -1 \\ \kappa \log \nu & \text{if } \alpha = -1 \end{cases} \tag{4.4}$$

where $\kappa = S_{\nu}\,\nu^{-\alpha}$.

Figure 4.6 shows the cavity power as a function of integrated radio luminosity (10 MHz−10 GHz). Equation 4.5 shows the best fit using the bivariate correlated error and intrinsic scatter (BCES) algorithm (Akritas and Bershady, 1996). This was used to perform linear regression fits to the data, and we chose the orthogonal BCES regression to fit the parameters in log space.

$$\log P_{\mathrm{mech}} = (0.42 \pm 0.34) \log L_{\mathrm{radio}} + (2.46 \pm 0.22) \tag{4.5}$$

We find a relatively shallow slope with a significant uncertainty (comparable to the original value). To extend the range of our powers and gain a better sense of the trend, we can add our results to the observations of groups by O'Sullivan et al. (2011). They looked at 9 galaxy groups also with the GMRT, as well as *Chandra* and *XMM-Newton* for the X-ray data. Their sample was designed in a similar way to ours, their groups chosen to have evidence for interaction between the AGN and intergroup medium. We use the same radio array and so will have a similar quality of image, along with the same low frequencies. These lower frequencies are especially important when observing the radio synchrotron bubbles that leave cavities in the X-ray emitting gas. That we use the same telescope array is important when comparing radio sources over a wide luminosity range. We should have similar values for sensitivity and dynamic range, as well as being at the same frequencies and resolutions. Equation 4.6 has the parameters for the best fitting orthogonal regression line to the combined sample of our clusters and the groups of O'Sullivan et al. (2011).

$$\log P_{\mathrm{mech}} = (0.57 \pm 0.10) \log L_{\mathrm{radio}} + (2.22 \pm 0.22) \tag{4.6}$$

There is still a sizeable amount of scatter in this relationship, but we do see that the gradient is a little flatter than found in O'Sullivan et al. (2011). In that paper, they compared their results with a sample of elliptical galaxies found in Cavagnolo et al. (2010). Cavagnolo et al. (2010) primarily used 1.4 GHz VLA data, along with low frequency flux densities from heterogeneous archival sources.

4.2 Spectral ageing

From purely radio data, it is possible to determine the synchrotron age of a radio source, t_{syn}. If we make the assumption that the only radiative losses happen via synchrotron emission and inverse Compton scattering, we can use the following equation for the KP model (Feretti and Giovannini, 2007),

$$t_{\text{syn}} = 1060 \frac{B^{1/2}}{B^2 + (2/3)B_{CMB}^2} \left[\nu_c(1+z)\right]^{-1/2} \text{ Myr} \tag{4.7}$$

where the magnetic field B is in μG and the break frequency ν_c is in GHz. The magnetic field equivalent of the cosmic microwave background, B_{CMB}, accounts for inverse Compton losses, with $B_{CMB} = 3.25(1+z)^2$ μG. This formula assumes an anisotropic pitch angle distribution. We will need to estimate B and ν_c.

For each of our galaxy clusters we can calculate an estimate of the magnetic field strength of the radio source. The minimum energy condition in a plasma as used in the context of radio galaxies leads to the equipartition condition, i.e. equal amounts of energy in the three important components, namely negatively charged particles (electrons), positively charged particles (protons) and the magnetic field (e.g. Kellermann and Verschuur, 1988). This is a common assumption in estimates of the interstellar or intergalactic magnetic field, though there are several conditions where this assumption might not be strictly true (e.g. Lacki and Beck, 2013). We will assume equipartition arguments for the magnetic field, and use the following (e.g. Pacholczyk, 1970; Beck and Krause, 2005),

$$B_{\text{eq}} = \left(6\pi(1+k)\,\Phi^{-1}\,c_{12}(\alpha,\nu_1,\nu_2)\,V^{-1}\,L_{\text{radio}}\right)^{2/7} \tag{4.8}$$

where k is the ratio of energies carried by heavy particles to electrons, $\Phi = 1$ is the filling factor (the fraction of the volume that is filled by relativistic particles and magnetic field), V is the volume of the radio lobes and L_{radio} is the radio luminosity of the source. Our choice of $\Phi = 1$ is motivated by X-ray observations of cavities and shocks. If the radio-emitting plasma did not displace the cavity of most of the thermal gas, there would be no cavity by definition, as there would be no detectable surface brightness deficit (McNamara et al., 2000). This causes Φ to be near unity. McNamara and Nulsen (2007) also require radio lobes to fill the volume due to the energy seen in shocks. c_{12} is a coefficient defined in Pacholczyk (1970), computed in cgs units below. α is the spectral index of the source and ν_1 and ν_2 are the lower and upper frequency cutoffs, we use 10 MHz–10 GHz as our range.

$$c_{12} = 1.06 \times 10^{12} \left(\frac{2\alpha + 2}{2\alpha + 1} \right) \left(\frac{\nu_1^{(1+2\alpha)/2} - \nu_2^{(1+2\alpha)/2}}{\nu_1^{1+\alpha} - \nu_2^{1+\alpha}} \right) \tag{4.9}$$

Using our radio maps, we make use of DS9 (Joye and Mandel, 2003) and FUNTOOLS (Mandel et al., 2011) to estimate the volumes of our sources. Thus, we calculate B_{eq} for the majority of the clusters in our sample, shown in Table 4.3, where we assume that the plasma consists of relativistic electrons and positrons, i.e. $k = 0$. We find that the magnetic field strengths range from ∼3–12 μG.

To calculate a synchrotron age estimate we still need some knowledge of the break frequency. Our methodology is as follows. We use Figure 4.3 to visually identify any obvious breaks in the synchrotron spectrum, so we can initially constrain the break frequency. For sources with enough published flux densities, we fit a KP model (Kardashev, 1962; Pacholczyk, 1970) to the integrated fluxes and frequencies from our observations and from the literature using the Broadband Radio Astronomy ToolS[1] (BRATS; Harwood et al., 2013) software package.

We decide to use the KP model because it tends to give better fits to the data than the JP model (Jaffe and Perola, 1973). This is found in Cygnus A for example (Carilli et al., 1991). The main difference between the two models is the pitch angle of the particles, for the KP model this is constant, whereas in the JP model it is rapidly isotropised. Tribble (1993) used a more complicated model involving a variable magnetic field, this is more computationally expensive, but results show this gives a result similar to the KP model.

We use the magnetic field strength that we calculate earlier, and vary the injection index α_{inj}, until we get the best fit. Figure 4.7 shows our fitted spectra, and returns estimates of the

---

[1] `http://www.askanastronomer.co.uk/brats/` – many thanks to Jeremy Harwood for providing the software.

Table 4.3: The radio lobe properties for our sample. (1) Name of the cluster; (2) The magnetic field strength of the radio lobes assuming equipartition and $k = 0$; (3) The break frequency of the source from Equation 4.7; (4) The radio source age found using the best fit KP model; (5) The buoyancy age from X-ray observations (Rafferty et al., 2006); (6) The pressure of the radio lobe using Equation 4.10 and assuming $k = 0$; (7) The thermal pressure derived from X-ray data (pV); (8) The heavy particle to electron ratio needed for the equipartition magnetic field to be equal to the magnetic field required for pressure equilibrium.

Name	B_{eq} (μG)	ν_{br} (GHz)	t_{syn} (Myr)	t_{buoy} (Myr)	p_{eq} (dyne cm^{-2})	p_{th} (dyne cm^{-2})	$1 + k_{\mathrm{eq}}$
2A0335	2.9			58	0.60	210	1100
A478	4.4	17	18	19	1.4	950	4800
MS0735	5.4	0.094	160	290	1.6	70	610
Hydra A	3.4	9.3	31	190	0.84	120	120 [a]
RBS797	2.8	63	6.1	40	0.56	1700	8100
A1795	9.6	6.5	12	37	6.7	390	650
A1835	3.3	18	15	33	0.87	1100	29 000
A2029	8.7			70	5.4	580	490
A2052	8.6	3.7	19	14	5.4	150	34
Hercules A	6.3	33	8.3	130	2.9	89	5.4
A2597	12.4	3.4	12	68	11	340	97

[a] Using data from Wise et al. (2007), we find $k = 250$.

spectral age. We can use this and Equation 4.7 to estimate a break frequency to compare with the literature.

One example is the model fitting is shown for Hydra A, where we use literature values from NED[1] for a range of frequencies. This is shown in Figure A.4, where an age of 17 Myr was estimated using $\alpha = 0.74$ and $B = 3.4$ μG. This gives a value for the break frequency of ~30 GHz. Bîrzan et al. (2008) estimated a break frequency of >8.6 GHz, so this is consistent with our model. For MS0735, we differ with Bîrzan et al. (2008) in our estimation of the break frequency. Our additional low frequencies at 150 and 235 MHz show that the break frequency must be below that of their 490 MHz estimate. Using our integrated fluxes and the magnetic field strength we found earlier, we estimate a break frequency of only 67 MHz. This shows the importance of the constraints that the low frequency data provides.

---

[1] This research has made use of the NASA/IPAC Extragalactic Database (NED) which is operated by the Jet Propulsion Laboratory, California Institute of Technology, under contract with the National Aeronautics and Space Administration.

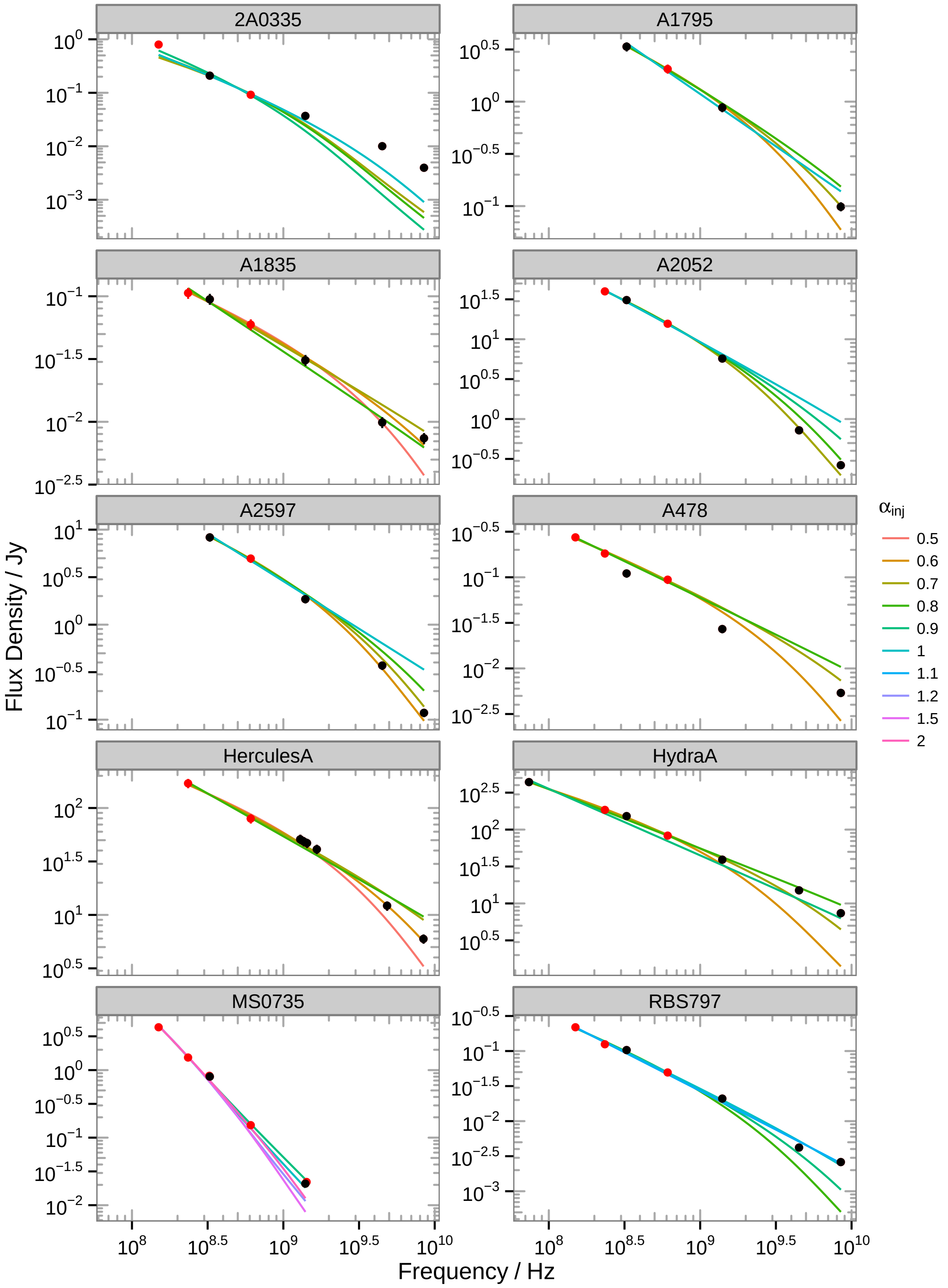

Figure 4.7: We have used the KP model to model the synchrotron spectrum for each cluster that we have sufficient data for. The magnetic field strengths used are the ones that we have calculated from flux density and area measurements, assuming $k = 0$. Different injection indices are shown here, each resulting in an estimate for the synchrotron age. We take the results that have the best fit to the data. Red points are from our GMRT observations, black are from the literature.

We must give a word of warning when using fluxes integrated over the entire radio source. This integrates the superposition of many electron spectra, which could have a range of ages. This leads to a less reliable estimate of the spectral age of the source (Harwood et al., 2013).

Our calculated synchrotron ages for each of the sources are found in Table 4.3, along with the buoyancy timescales from Rafferty et al. (2006). They are plotted against each other in Figure 4.8. There is a significant discrepancy between the two ages, with the buoyancy time usually much longer than the synchrotron ages. There are a couple of ways of interpreting this. Firstly, we can assume the buoyancy timescale is the true age of the system. In this case we see that the synchrotron timescales can significantly underestimate the age by up to a factor of 10. One assumption is that reacceleration is not taking place in the radio lobes. If this is occurring at significant levels then the synchrotron age we infer would be from the time since the previous reacceleration rather than when the particles were originally injected. We also make the assumption that the magnetic field is constant throughout the radio lobes. Although if the magnetic field strength decreases as it expands, this would actually lead to an overestimate of the radiative electron ages.

The other case is that the synchrotron age is correct and it is the buoyancy timescales that are overestimated. If this scenario were true then it would mean that the cavities either would have to form close to their observed location, or that they are driven in some way in order to be moving at an increased velocity. For this to be the case, they would in the majority of cases have to be moving supersonically, so shocks would be observed. This is seen in some sources (e.g. A2052; Blanton et al., 2011).

4.3 Radio lobe composition

Up to now, we have assumed a cosmic ray nuclei to electron/positron energy ratio of $k = 0$. We can use some X-ray observations of our sample in combination with our radio data to try and narrow down the lobe composition. To start, we can explore what magnetic field strength would be needed if we assumed the age of the source was equal to the age suggested from buoyancy timescales. We use Equation 4.7, and assume the break frequency that we found

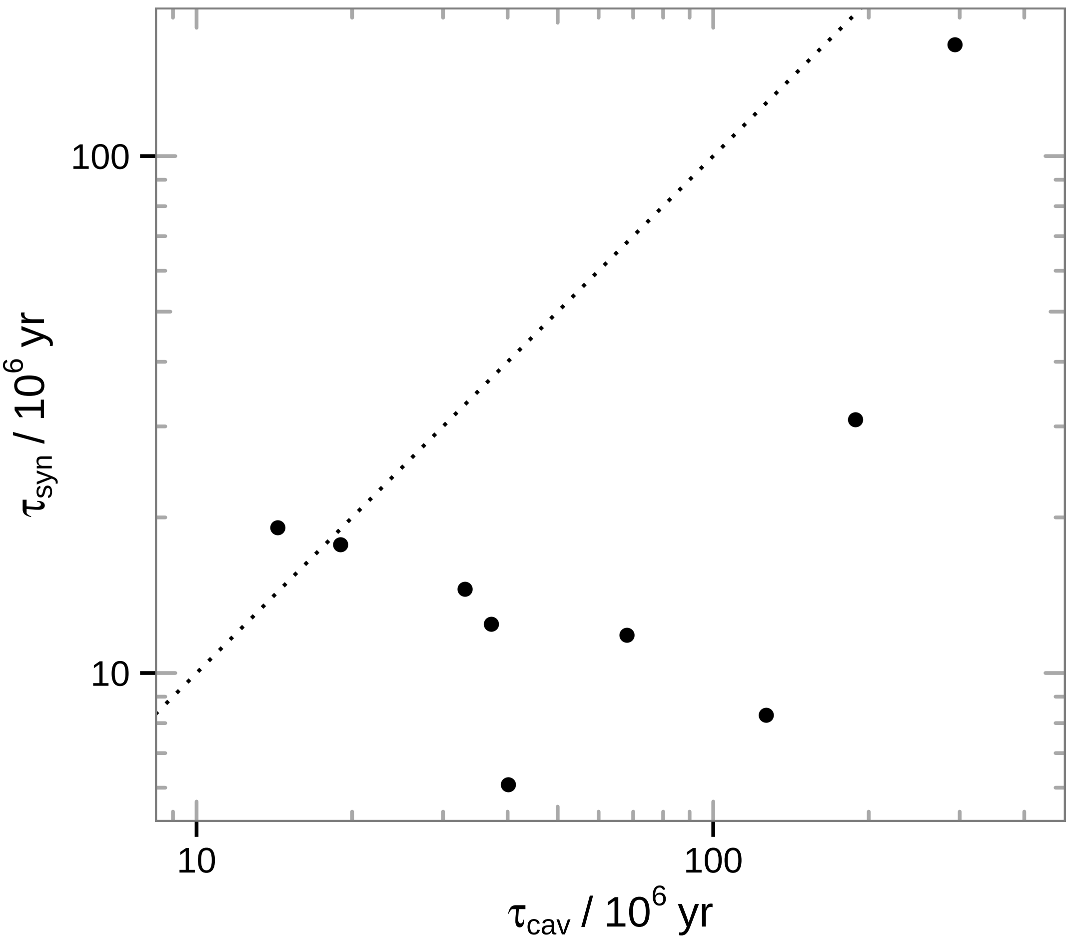

Figure 4.8: The ages from synchrotron and buoyancy timescales are plotted against each other. We see that the buoyancy timescale is significantly longer than the synchrotron age estimate.

earlier for each cluster. For A2052, a magnetic field strength of $B_{\mathrm{eq}} = 10.7\,\mu\mathrm{G}$ would allow the spectral age to be equal to the buoyancy timescale. However, no solution could be found for any of the other clusters. Instead, we can look at the pressures derived from both radio and X-ray observations. The X-ray cavities are assumed to be in pressure equilibrium with the surrounding gas, and we compare these to the radio lobe pressure, which is the sum of the particle and magnetic pressures. Our galaxy cluster sample overlaps with Rafferty et al. (2006), who have pV estimates for the cavities in each of their clusters. We estimate the pressures from particles and magnetic fields in the radio lobes using the following equation.

$$p_p + p_B = \frac{(1+k)E_e}{3V\Phi} + \frac{E_B}{V\Phi} \tag{4.10}$$

where $E_e = B^{-3/2}\,L_{\mathrm{radio}}\,c_{12}(\alpha, \nu_1, \nu_2)$, and $E_B = \left(\frac{B^2}{8\pi}\right)\Phi V$. This assumes that the magnetic field pressure is $p_B = \frac{B^2}{8\pi}$. The radio lobe pressures are found to be a few orders of magnitude smaller than the surrounding gas pressure. There are a few possibilities that could account for this difference. Taking the filling factor Φ to be less than unity is one way of achieving this, although this has been ruled out by X-ray observations of shocks and cavities as stated previously (McNamara and Nulsen, 2007). Secondly, the radiating plasma of the radio source could quite possibly not be in equipartition, so the total internal pressure of the lobes would not be constrained. There may be other sources of pressure from within the radio lobes, such as cosmic ray pressure and from hot thermal material that has been entrained (Croston and Hardcastle, 2014). Alternatively, the content of the lobes could predominantly consist of heavy particles such as protons, implying a high k value. De Young (2006) suggests that these cold, heavy particles would not contribute much to the pressure of the jets, but would carry most of the energy and stop the jets from decollimating.

We can explore this further by rearranging the previous equations to be a function of B, and thus we can determine what k is needed to make this equal to the equipartition magnetic field strength (e.g. Bîrzan et al., 2008).

$$\frac{1+k}{\Phi} = \frac{V}{6\pi\, L_{\mathrm{radio}}\, c_{12}(\alpha, \nu_1, \nu_2)} \left(\frac{72\pi}{13} p_{\mathrm{th}} \right)^{7/4} \tag{4.11}$$

Our k values are shown in Table 4.3. We find a large range, from $k \sim$5–29 000. The majority of the results suggest that there is a high proton-to-electron (or similar) ratio in the make-up of this sample of radio sources, if equipartition is assumed. This is similar to the results of Dunn and Fabian (2004); Dunn et al. (2005); Bîrzan et al. (2008).

We have three clusters in common with Bîrzan et al. (2008): MS0735, Hydra A and Abell 2052. With our additional lower frequency data, we should be able to find a better estimate for k. For MS0735, Hydra A and Abell 2052, we find values of k of 610, 120 and 33 compared to the Bîrzan et al. (2008) values of 1100 ± 300, 1300 and 100 ± 10 respectively. We use the X-ray measurements of the volume from Rafferty et al. (2006) in order to be consistent with Bîrzan et al. (2008). Our calculated values are at least a factor of 2 less than theirs. As our volumes are the same, and $k \propto L_{\mathrm{radio}}^{-1}$, our lower k values suggest that we are detecting significantly more flux from the older population. It is therefore important to have lower frequency data as part of a good range of frequencies, in order to better constrain the composition of the radio lobes.

4.4 Conclusions and further work

In this chapter we have taken a sample of cool-core clusters and used high quality low frequency radio observations to ascertain a selection of radio properties. These have enabled us to probe the vast number of lower energy electrons that make up a significant amount of the radio power. This suggests that low frequency broadband measurements are a better proxy of cavity power than simple monochromatic high frequency measurements.

We find a higher L_{radio} than Bîrzan et al. (2008) for nearly all of our clusters, which should lead to a flatter relationship between cavity power and radio luminosity. They find a slope of 0.49 ± 0.07, which is actually flatter than our 0.57 ± 0.10. However, they used an ordinary least squares regression, minimising the difference in the P_{cav} axis only, leading to a flatter gradient.

When refit to the BCES orthogonal regression that we use, their gradient and errors increase to 0.68 ± 0.19.

Our gradient is also flatter than the O'Sullivan et al. (2011) relation for groups. This may be due to the difficulty of accurately measuring the cavity properties in groups, as they are significantly smaller and fainter. We find our systems have a cavity power to radio luminosity ratio of between 1 and ~ 4000, with a median of 185. These cavities powers theoretically are a lower limit to the jet powers, as contributions from shocks are not included.

Using synchrotron models, we estimated the ratio of energy in heavy particles to electrons, k, for each of our clusters. We found a large range for k for our sample, but in the clusters that we have in common with Bîrzan et al. (2008), we find values of k that are at least a factor of two smaller. We have found that a relativistic electron/positron plasma (i.e. $k = 0$) is not supported by our observations, but more work needs to be done on this in order to attempt to constrain these values further.

In future work, we will use our own, deeper, X-ray data in order to determine more accurate estimates for pV and $t_{\rm buoy}$. We would also like to include further low frequency measurements of these clusters, and other clusters with suspected X-ray cavities. Building up a range of data for a range of systems is important in understanding the injection of energy into galaxy clusters, and AGN feedback in general.

Chapter 5

Low-frequency observations of radio galaxies in rich clusters

In this chapter, we take a more detailed look at the individual radio galaxies in our cluster sample. Here, we can provide more in-depth analyses for clusters with additional data, and investigate the spectral properties of the radio sources. We also present our GMRT radio images for the extended emission seen in the observations of the clusters in our sample, listed previously in Table 4.1. Of these, a detailed description has been given of some of the interesting features found in some of the clusters.

5.1 2A0335+096

2A 0335+096 (also known as Zw 0335.1+0956; hereafter 2A0335) is an X-ray bright galaxy cluster situated at a redshift of $z = 0.0349$ (Wilman et al., 2011). It is an interesting cluster, known to have a cool core with a central radiative cooling time shorter than a Hubble time (Donahue et al., 2007). 2A0335 is a complex source at X-ray wavelengths, Mazzotta et al. (2003) observed it to have intricate structure consisting of eight cool dense blobs around 4 kpc in radius, along with two cavities. There are also many temperature differences radially, as well as a cold front 40 kpc south of the centre of the cluster.

Using the William Herschel Telescope (not to be confused with the *Herschel Space Observatory*), Hatch et al. (2007) observed two separate Hα + [N II] central knots less than ~2 arcsec to the north-west and south-east of the central source. Further diffuse emission is seen extending towards a galaxy in the north-east, which is only ~4 kpc away from the nucleus. This companion galaxy appears to be interacting with the central one, and may be in the process of merging (Donahue et al., 2007). As well as the emission bar between them, X-ray observations show the cool X-ray peak to be in-between the central galaxy and its companion, a typical signature of a merger. They also suggest that this interaction between the two galaxies could be responsible for the reignition of the radio source in the central galaxy.

The BCG hosts a radio-loud AGN with two radio lobes that extend ~12 arcsec from the compact central source (Sarazin et al., 1995). Sanders et al. (2009) used the Very Large Array (VLA) at 5 GHz to compare how the radio emission at that frequency correlates with their *Chandra* X-ray observations. They detected five cavities surrounding the core, but the 5 GHz data did not appear to correlate with these. The archival 1.5 GHz observations show some extended emission and evidence for a mini-halo, elongated in the ENE–WSW direction.

GMRT observations

2A0335 was observed at 610 MHz and 150 MHz with the GMRT on the 20th & 23rd December 2009. They were observed with the GMRT Software Backend (GSB; Roy et al., 2010) and at both RR & LL polarisations. The aggregate time on source for these observations totalled up to be over six hours, resulting in high quality deep data with rms noise levels of 0.060 and 3.1 mJy beam^{-1} for the 610 MHz and 150 MHz observations respectively. Our 150 MHz data was taken with 2 s integration time period for each visibility, as opposed to the standard 16.9 s, resulting in better calibration in exchange for larger data files.

Results

Our 610 MHz image is shown in Figure 5.1. It is taken using the full-resolution of the GMRT. The two radio lobes can be clearly seen in a ENE–WSW direction as previously found, each of length ~16 arcsec, which using our chosen cosmology correspond to a length of ~11 kpc. A small bright extension also appears to the north-west, matching the location of the companion

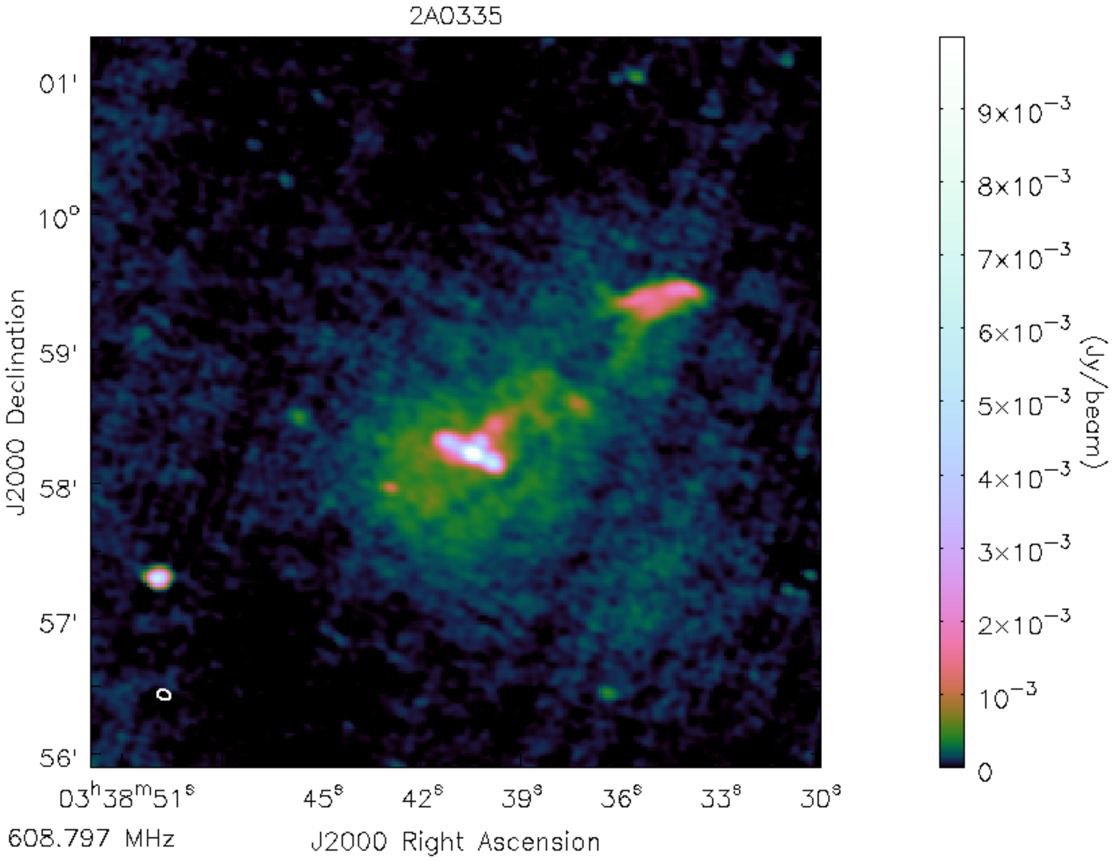

Figure 5.1: The full resolution 610 MHz map for 2A0335. The beamsize of 5.93″ × 4.21″ (PA: −68.25°) is shown in the bottom-left corner.

galaxy. Slightly fainter diffuse radio emission is detected in the form of a mini-halo around the central galaxy. We measure a flux density of 89.4 mJy for this mini-halo.

The 150 MHz image has a very large ∼2.5° × 2.5° field of view. Interestingly, the lower frequency radio emission is aligned in a perpendicular to the high frequency radio jets, and more in line with the Hα emission.

We present the spectral index map for 2A0335 in Figure 5.2. The map has been clipped to show only values above the first contour level. We see that the central source has a spectral index $\alpha \sim -1.2$ along the axis of the main radio lobes. The diffuse emission surrounding it has a steeper index.

Figure 5.3 shows a false-colour image of the wider field, including some other interesting sources. They have been labelled with letters in the figure. Immediately striking is object C, which is a large structure defined as a narrow angle tail (NAT) radio galaxy in Sarazin

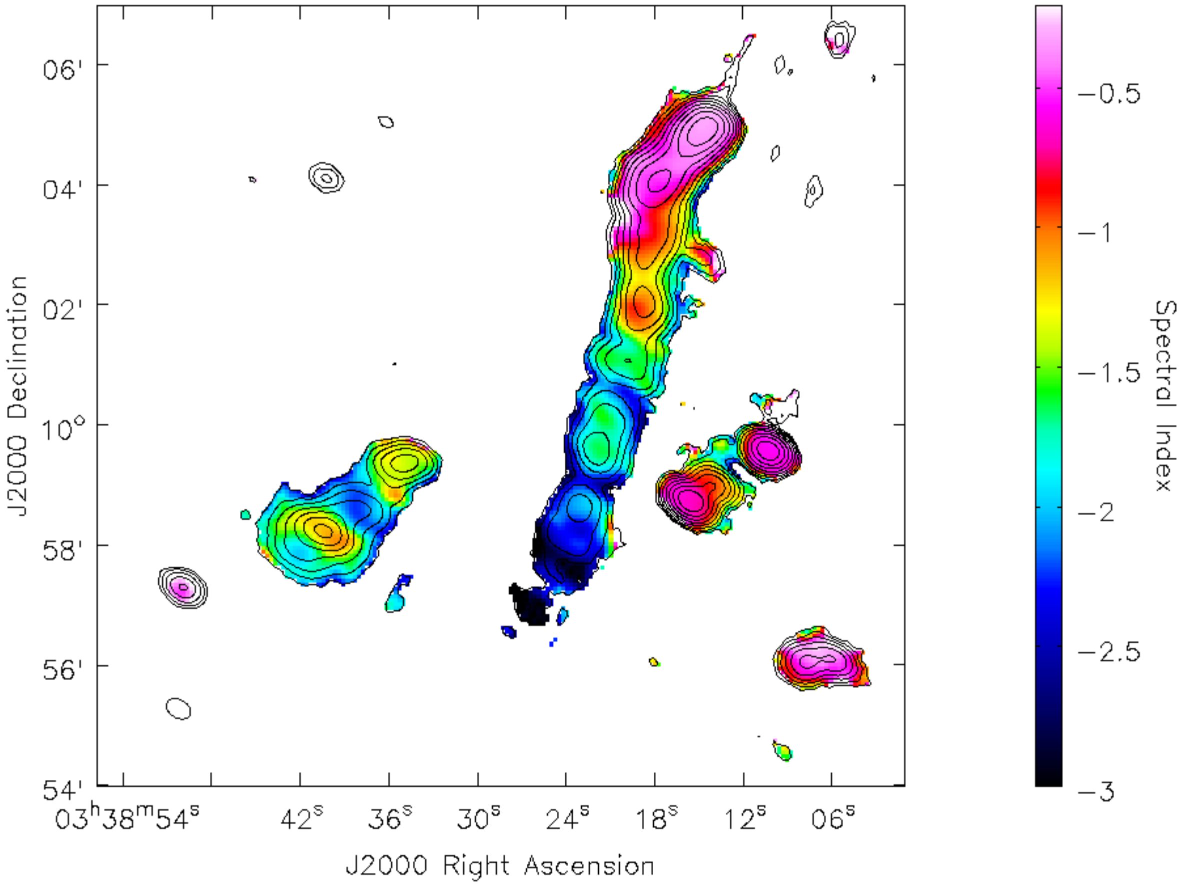

Figure 5.2: The 610−150 MHz spectral index map for 2A0335. Contours are from the low resolution 610 MHz map starting from 0.5 mJy beam^{-1} and increasing by factors of 2. The beamsize of 26″ × 18″ (PA: −60°) is shown in the bottom-left corner.

et al. (1995). This galaxy is the second brightest (optical) cluster galaxy in 2A0335, and it is an excellent example of how radiative losses steepen the radio spectrum of the source. As seen in the false-colour image, the 150 MHz emission extends much farther than the higher frequency emission. At 4.8 GHz, only the head of the source is visible. There is a clear bend in the NAT of $\sim 30°$, theorised to be due to the tail being deflected away from denser gas seen in X-ray observations. The spectral index map displays the quite flat spectrum of the head of the source, and the gradual steepening of the spectrum towards the tail. There are also a couple of flatter index knots where the tail brightens in intensity, these could be due to regions of reaccelerating particles, or other variations in the tail consistency. At the tail end, the spectral index drops to as low as $\alpha < -3$, before becoming too faint to be seen at our higher frequency. It also starts to slowly curve in the opposite direction, most likely due to it just following the areas of least density. By taking a selection of regions along the tail, and calculating their flux densities for both frequencies, we estimate a relatively constant magnetic field strength of 5 μG. We use this to calculate an approximate synchrotron age of the radio source (see §4.2), of on the order of 30 Myr. This is consistent with the estimate of Sarazin et al. (1995), who only had higher frequencies at their disposal. This is also similar to the age of the central radio source (Donahue et al., 2007).

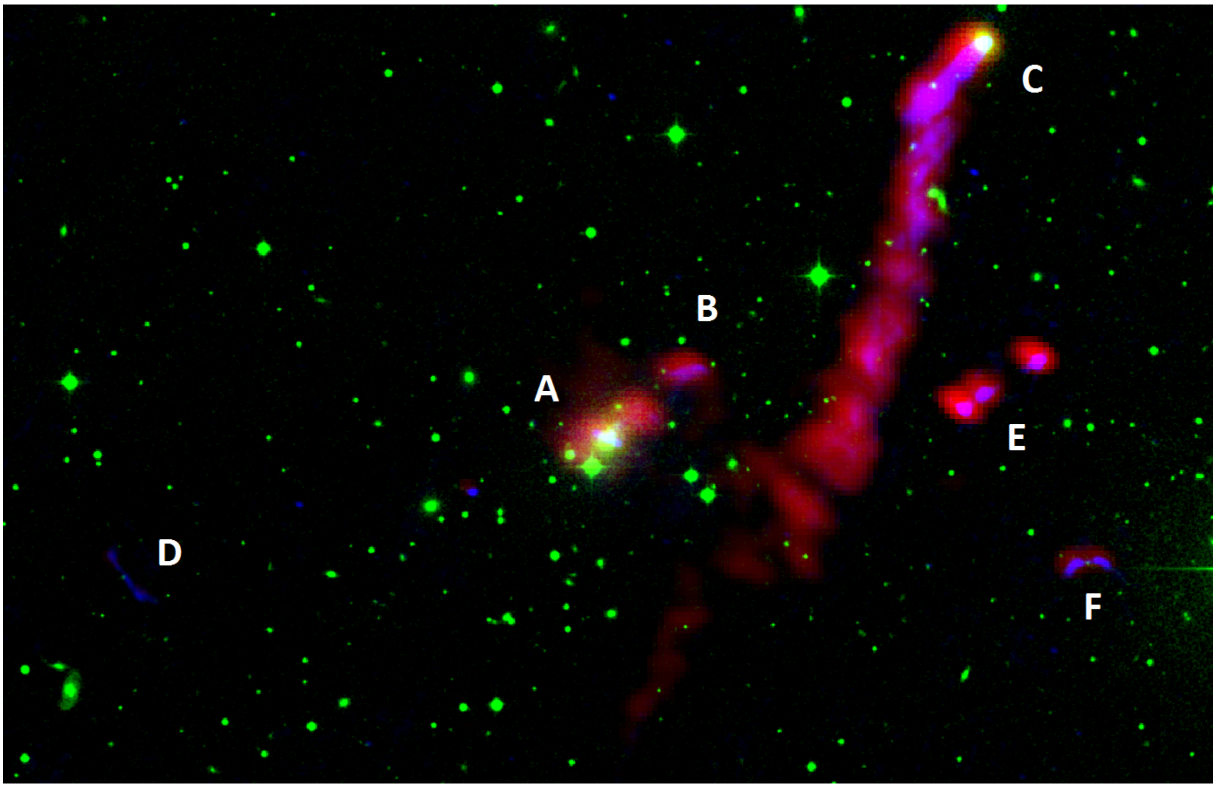

Figure 5.3: RGB false-colour image of the 2A0335 cluster. Red is 150 MHz emission, green is DSS optical, and blue is 610 MHz emission.

5.2 MS0735.6+7421

MS0735.6+7421 (also known as ZwCl 0735.7+7421, hereafter MS0735) is a galaxy cluster hosting the most powerful radio outburst observed. The cluster, located at a redshift of $z = 0.216$, has been studied extensively at X-ray wavelengths with both the *Chandra* and *XMM-Newton* X-ray space telescopes. The interaction between the powerful central engine of the supermassive black hole and the surrounding hot gas of the ICM has led to extremely large cavities, each 200 kpc in diameter (McNamara et al., 2005). These cavities are filled with emission from the radio lobes, although these become evident only at lower frequencies.

The radio source (also known as 4C+74.13) is observed to have an extremely steep spectral index. Cohen et al. (2005) measure $\alpha_{325}^{1425} = -2.45 \pm 0.04$ for the whole source, using the VLA in the B and C configurations. They find a significant extension to the radio emission to the southwest, suggesting this to be the result of either the radio jet interacting with the ICM, or an inner lobe due to a new outburst. We use archival VLA data at 325 and 1400 MHz to make full resolution images and measure the flux densities at these frequencies. Multiple configurations of the VLA were used to take these observations. The VLA has four main dish arrangements, ranging from all antennae within 0.6 km in the D config, to being spread out over 36 km in the A configuration.

GMRT observations

Three low frequencies were observed with the GMRT on December 2009. The 610 and 235 MHz frequencies were observed simultaneously using the dual-frequency mode of the GSB. Full resolution images were made using a Briggs robust value of 0 (Briggs, 1995) and no tapering of the uv–range. The 610 MHz image is shown in Figure 5.4. We use the ‘cubehelix’[1] colour scheme for a more appropriate representation of intensities (Green, 2011).

We can clearly see the powerful radio lobes emanating from the core of the galaxy. The northern lobe stretches ~79 arcsec, which equates to a physical distance of ~274 kpc. While

---

[1] http://www.mrao.cam.ac.uk/~dag/CUBEHELIX/

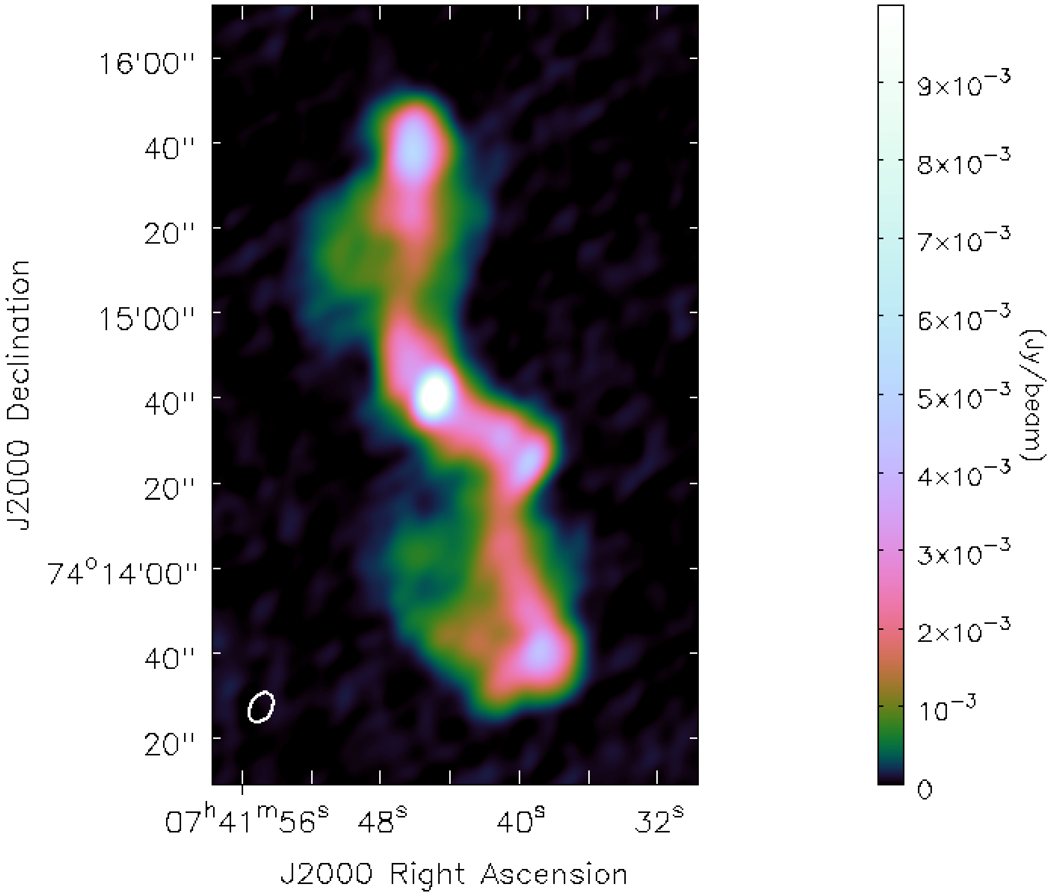

Figure 5.4: The full resolution 610 MHz map for MS0735. The beamsize of 7.54″ × 4.93″ (PA: −30.08°) is shown in the bottom-left corner.

these large radio lobes are orientated roughly north-south, closer to the core the emission is seen to be orientated 60° to this.

The radio jets fades in intensity as you look farther from the core, before brightening towards the ends of the radio lobes. It is interesting to note the backflow, the fainter diffuse emission to the east of both sets of lobes. In the southern lobe it extends from the kink noted above to the end of the radio lobe. In the northern lobe, it does not quite reach the hotspot at the end, suggesting that the jet begins to lose integrity in the middle part of the lobe, where it also becomes less luminous. As it is mostly appearing towards the eastern side it seems likely that there are some interactions between the radio source and the ICM. We find that at 610 MHz, the core is still slightly brighter than the radio lobes, this is not the case at 235 and 150 MHz, as seen in Figure 5.5. In fact, the 235 MHz map shows the unusual nature of the centre of the source, with the south-west extension of the core distinct from the core itself.

We see the X-ray emission from the cluster in Figure 5.6. The energy required to inflate these cavities is on the order of 10^{62} erg, the most powerful outburst known, and enough to quench star formation for several Gyr (McNamara et al., 2005). In order to power this outburst, either the black hole mass must be exceptionally large (10^{11} $M_\odot$), or it is powered by the angular momentum released from a spinning black hole (McNamara et al., 2009). The flaring of the jets in our low frequency radio images, coupled with the X-ray data, show how the radio plasma fills the cavities more completely than the original VLA data in McNamara et al. (2005).

In order to compare the different frequencies we have observed, we need to re-image our data with the same resolution and uv−range. We set a minimum uv−range of 0.075 kλ when imaging. This is to ensure the uv coverage is matched, so the maps will not be missing flux due to the fewer short spacings at the high frequency. §2.3 has more details on uv−coverage.

Figure 5.7 shows the 610−235 MHz spectral index map for MS0735. We can see the steep spectral index is fully evident here, with $\alpha = -1.54$ in the core, and steepening to $\alpha \sim -2.75$ in the lobes. At 610 MHz, the core is slightly more luminous than the lobes. The map shows the extent of the lobes, the northern lobe stretches ∼69 arcsec across the sky, equating to ∼240 kpc. We can also see the difference between the spectral index in the core and the south-west

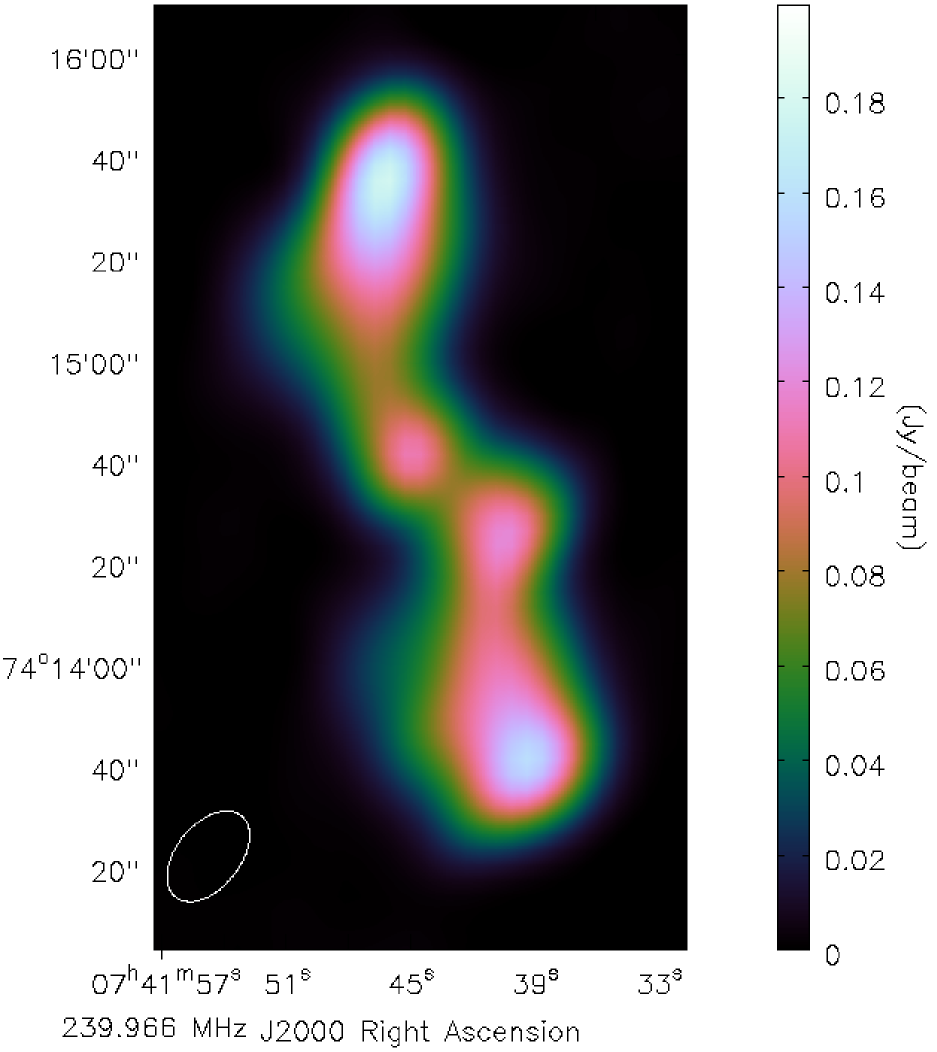

Figure 5.5: The full resolution 235 MHz map for MS0735. The beamsize of 20.66″ × 12.58″ (PA: −39.13°) is shown in the bottom-left corner.

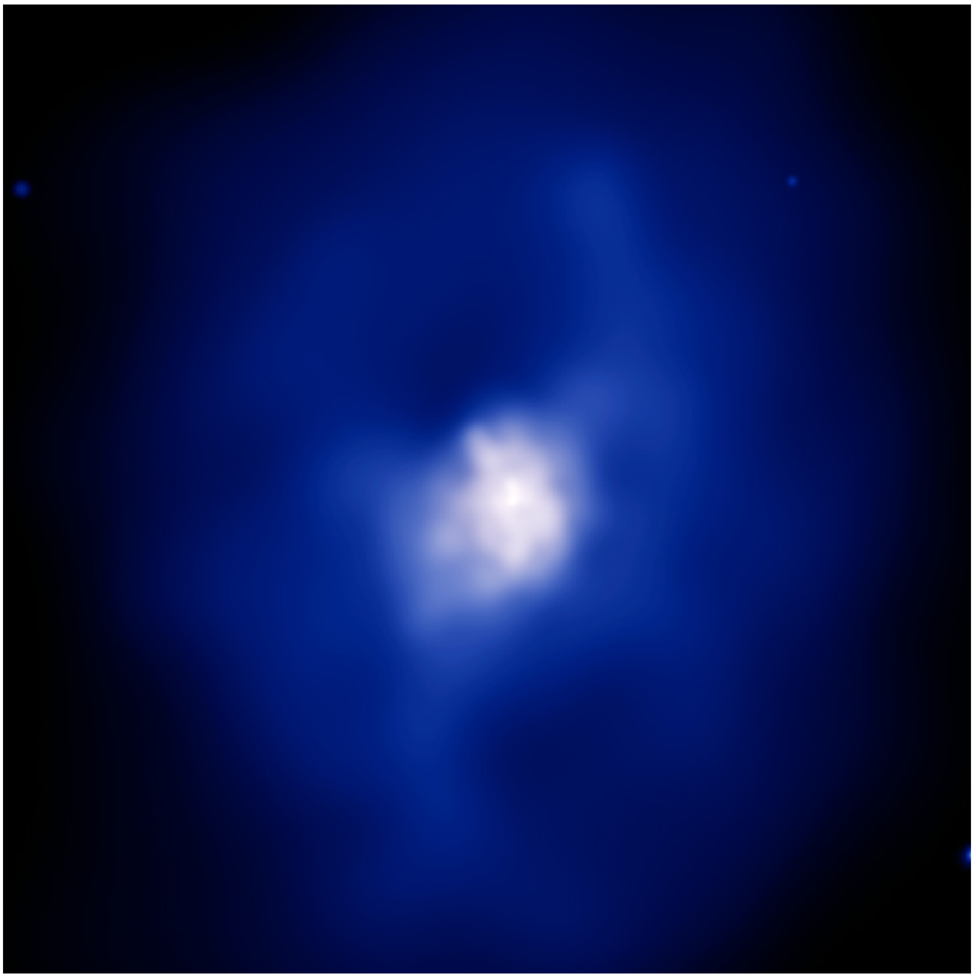

Figure 5.6: The *Chandra* X-ray image for MS0735. Cavities are clearly visible to the north and south, and our observations of the radio lobes show these being filled. Image from McNamara et al. (2005).

Table 5.1: Our GMRT observed MS0735 integrated fluxes. A minimum uv–range of 0.2 kλ was used.

Frequency (MHz)	Flux (Jy)
150	4.30
235	1.53
327	0.787
610	0.153
1400	0.0226

Table 5.2: MS0735 radio properties by region.

d (″)	S_{610} (mJy)	S_{235} (mJy)	α	B_{eq} (μG)
−62.4	24.7	290.4	−2.59	8.2
−29.6	22.9	245.2	−2.48	7.3
0.0	37.3	180.2	−1.65	3.7
30.6	19.2	253.0	−2.71	8.4
63.0	20.5	238.2	−2.57	7.7

extension, which has a clearly defined region of $\alpha \sim -2.3$ emission. The faint diffuse areas towards the eastern outskirts of the radio lobes described earlier also have a very steep spectral index of $\alpha \sim -3.1$.

Our GMRT data at three frequencies gives us an opportunity to investigate how the spectral age varies over the radio lobes. We start by splitting the source into different regions, and look how the spectral index and magnetic field changes as a function of distance from the centre. This is shown in Table 5.2, where our magnetic field strengths assume equipartition, see §4.2 for more details. Figure 5.8 shows the regions that were selected, and Figure 5.9 plot spectral index as a function of distance. This is also done for smaller regions and is shown in the same figure. A simple line is used to connect the points, but it shows the gradual steepening of the spectral index from the core to the lobes.

We explore further by using the Broadband Radio Astronomy ToolS (BRATS; Harwood et al., 2013) software package. With this, a model is fit to the data for each pixel above a specified signal-to-noise threshold. We set $\alpha_{\mathrm{inj}} = -0.9$ and a magnetic field strength of 5.4 μG (more details found in §4.2.

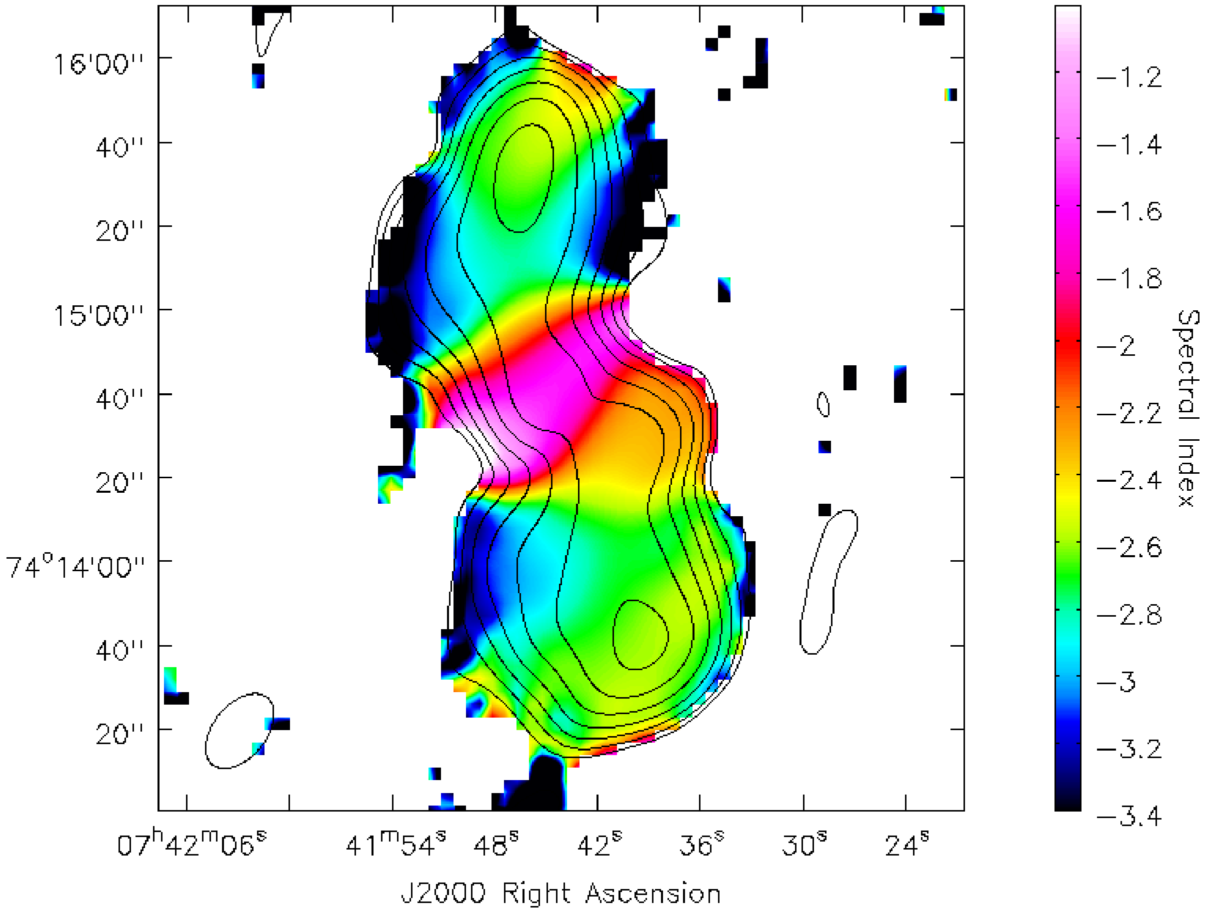

Figure 5.7: The 610–235 MHz spectral index map for MS0735. Contours for the 235 MHz map are shown in black, starting from 2 mJy and increasing by factors of 2. The beam size of 20.66″ × 12.58″ (PA: −39.13°) is shown in the bottom-left corner.

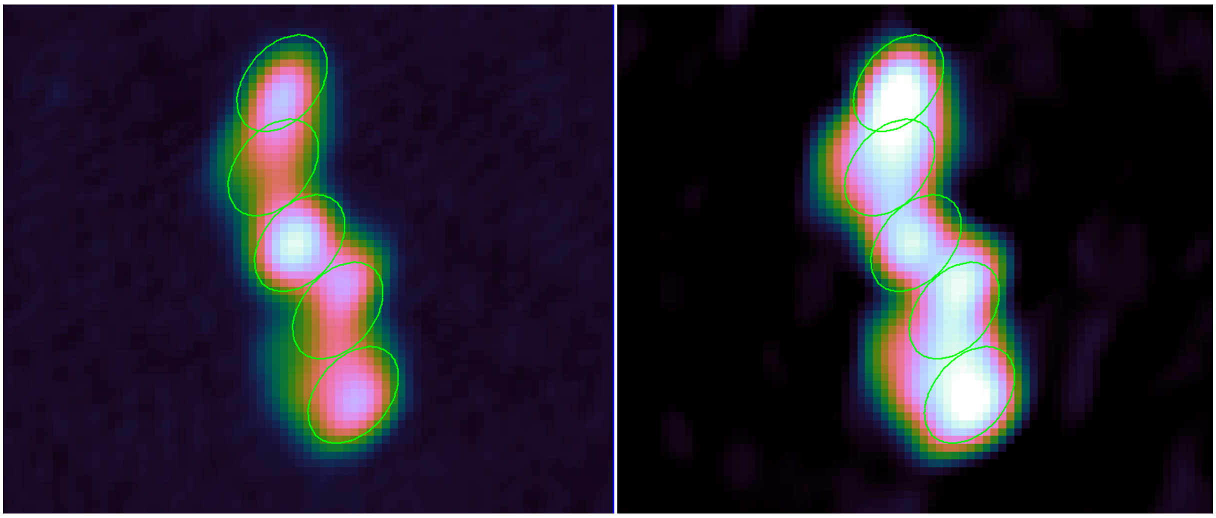

Figure 5.8: MS0735 is displayed here at 610 and 235 MHz from left to right, where both maps have been imaged at the lower frequency resolution (21″ × 14″). Five regions are overlaid on the images, which approximate the beam size and shape. The flux density is calculated within each of these regions, so the radio properties can be seen for the different areas of the extended emission, this is shown in Table 5.2.

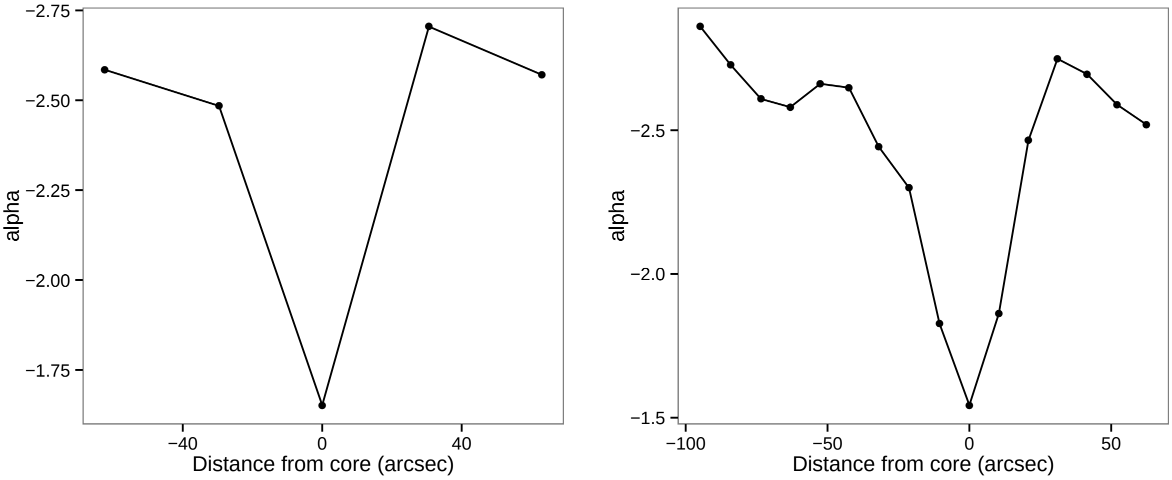

Figure 5.9: Spectral index is plotted as a function of distance from the core of MS0735.

Figure 5.10 presents the spectral age as a function of position. There are two points on the plot, marked A & B. A is in the south-west extension and is found to be younger than the main radio lobe to its south. This is different to what is seen in the north lobe, where the spectral age increases from the edge of the radio lobe back towards the central regions.

The spectral age that we calculate is highly dependent on our choice of injection index. Setting $\alpha_{\text{inj}} = -2.0$ gives a radio lobe age of 50 Myr; whilst giving a reasonable fit to our 150–610 MHz range, this is an extremely high index and would not be theoretically consistent. We can safely assume that our observational frequencies are above the break frequencies for this source, and the KP model gives a post-steepening spectral index of $\alpha = 4/3(\alpha_{\text{inj}} - 1)$ (e.g. Stroe et al., 2013). Using $\alpha_{\text{inj}} = -0.9$ would give an observed spectral index of $\alpha \sim -2.2$, which is not too far from what we find (see Figure 5.7). We also use the Tribble model (Tribble, 1993) to find the synchrotron ages, this is shown for comparison in Figure 5.11. It gives a similar result to the KP model, but with a lower overall χ^2.

A lobe speed of 0.01 c is determined simply by using the difference in spectral ages between the core and lobe and the distance between them. In the model of Sternberg and Soker (2009), the energetic phase of the AGN lasted for $\sim 10^8$ yr, and ended a few 10^7 yr ago. The inflating jets in their model were slow and massive, with $v \simeq 0.1c$. With both of the spectral age maps, the difference in age between the end of the lobes and the core is striking, with the lobes being on the order of 130 Myr old. With our chosen input parameters, we see that no new injection of electrons has taken place, even in the core, for over 50 Myr. This is consistent with the age calculated from shock models of $\sim$110 Myr from McNamara et al. (2009).

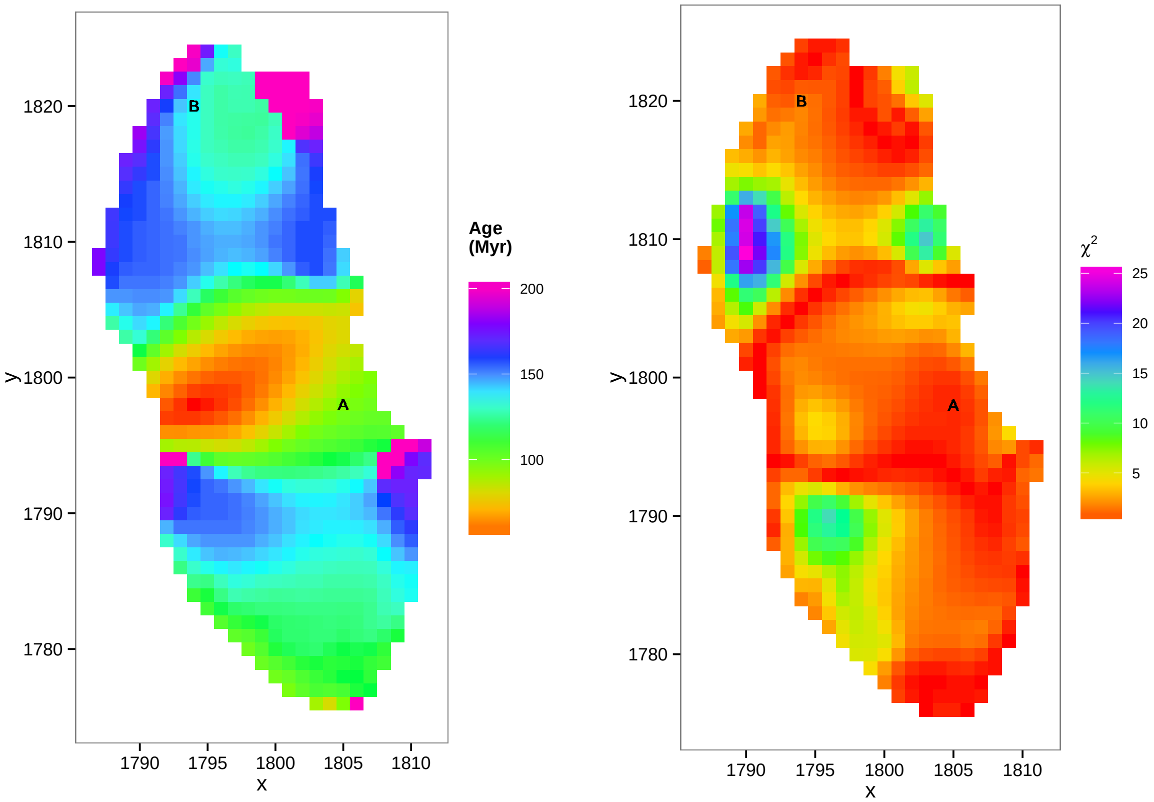

Figure 5.10: Left: The spectral age map for MS0735. We use $\alpha_{\mathrm{inj}} = -0.9$, $B = 5.4\,\mu\mathrm{G}$, and the KP model. The scale is 4″/pixel. Right: The correspond χ^2 value to give an indication in the confidence level that the model matches the data. The points marked A & B are discussed in the text.

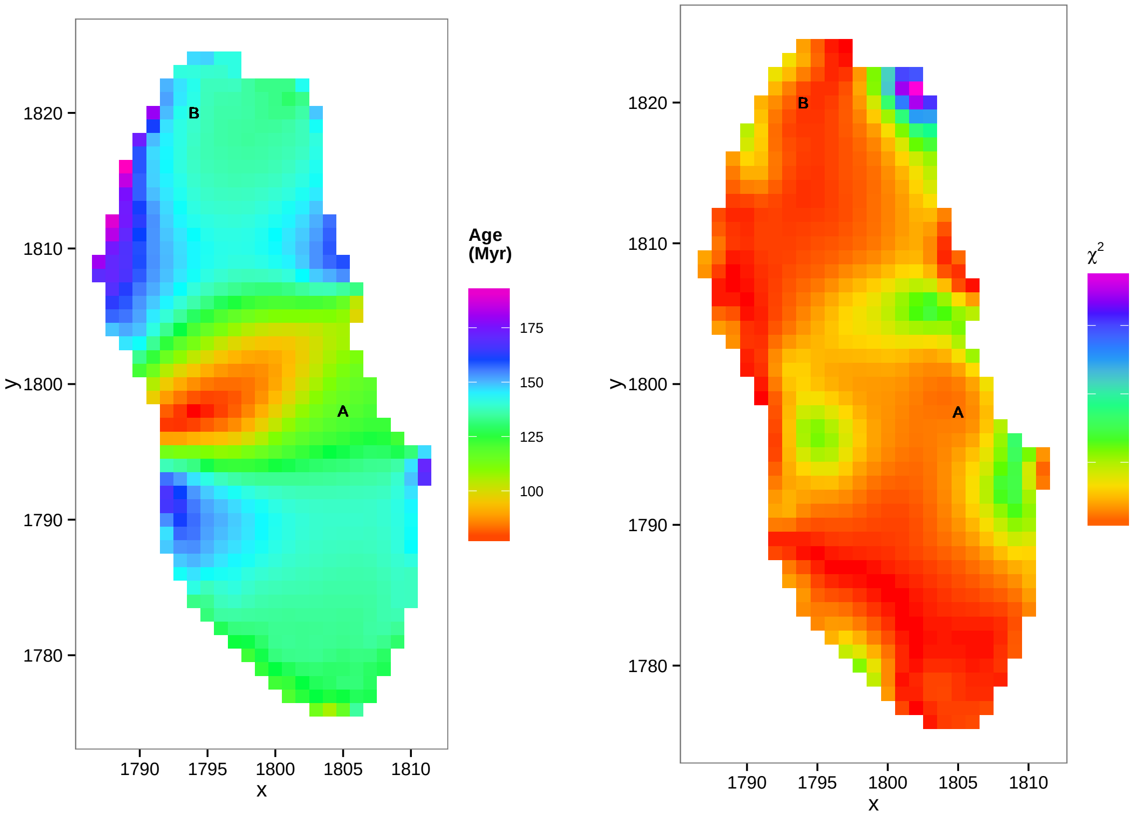

Figure 5.11: Left: The spectral age map for MS0735. We use $\alpha_{\mathrm{inj}} = -0.9$, $B = 5.4\,\mu\mathrm{G}$, and the Tribble (1993) model. The scale is 4″/pixel. Right: The correspond χ^2 value to give an indication in the confidence level that the model matches the data. The points marked A & B are discussed in the text.

5.3 Hydra A

Hydra A (also known as 3C218) is a bright radio galaxy at the centre of the poor cluster Abell 780, more commonly referred to as the Hydra A cluster. It is at a redshift of $z = 0.0549$, this means that with our chosen cosmology $1'' = 1.054$ kpc. It is another one of our sample that possesses X-ray cavities (McNamara et al., 2000; Nulsen et al., 2002), as seen using *Chandra*.

GMRT observations

We observed Hydra A on the 2nd December 2009, for just over five hours with the dual frequency mode. In order to image the northern emission at 610 MHz, we had to make a low resolution map in order to not resolve out the fainter diffuse lobe. Figure 5.12 shows the lower resolution 610 MHz image with the higher resolution contours overlaid. With these contours the two jets can be seen, with an 'S' shape suggested to be due to precession of the central AGN (Taylor et al., 1990).

The spectral index map for Hydra A can be seen in Figure 5.14. We find $\alpha \sim 0.64$ for the core, and it gradually steepens to $\alpha \sim -1.5$ along the jets. These jets extend ~60 kpc in either direction. The northern lobe has $\alpha \sim -2.2$, but has moderate variations across the lobe due to low-level deconvolution artefacts. Our spectral indices are comparable to those of Lane et al. (2004), and the location of our lobes matches the X-ray cavities seen in Figure 5.13 (Wise et al., 2007).

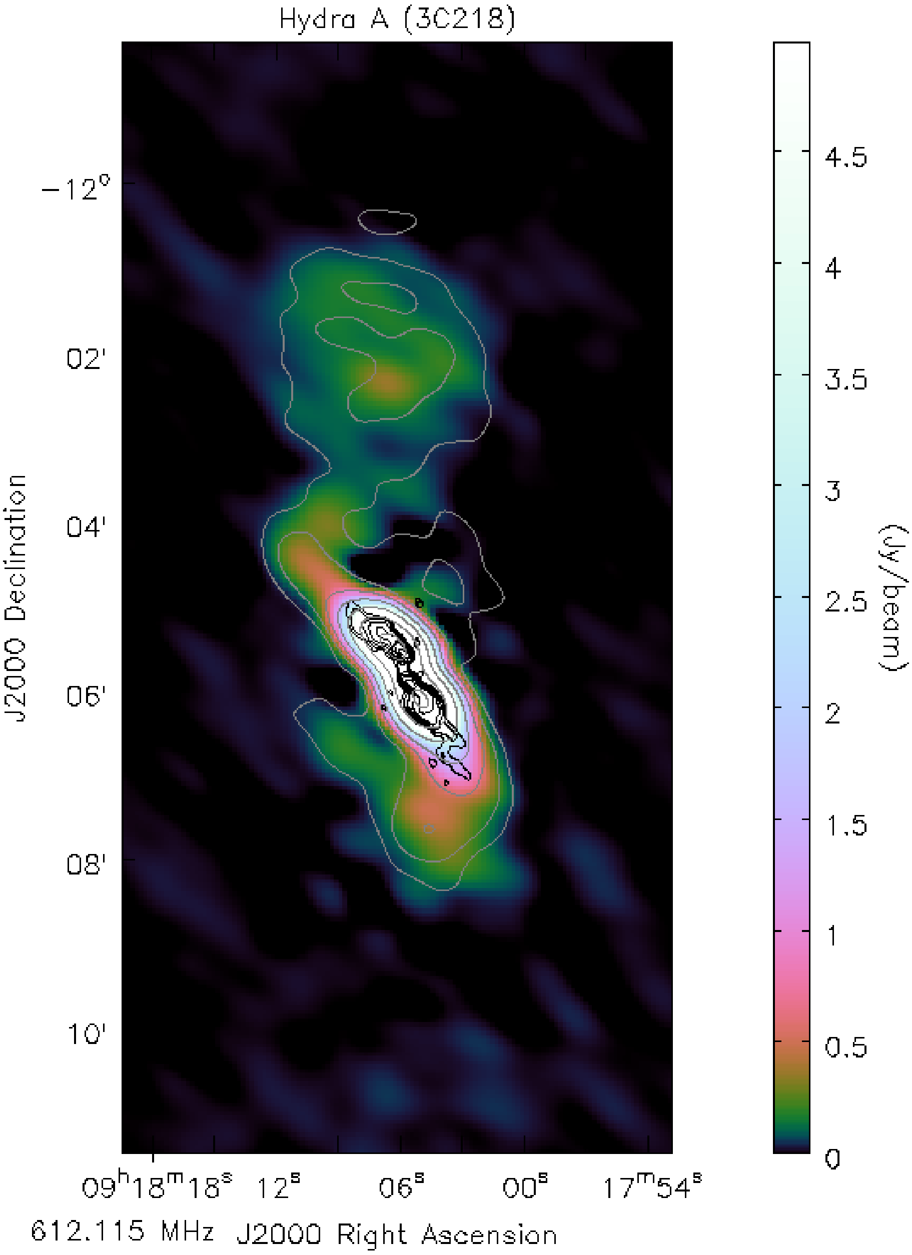

Figure 5.12: The GMRT 610 MHz map for Hydra A. Black contours are the 610 MHz high resolution image and start at 0.1 Jy and increase by factors of 2. The grey contours are for the 235 MHz emission and start at 0.6 Jy. The beamsize for the image is 30″ × 24″ (PA: 55°).

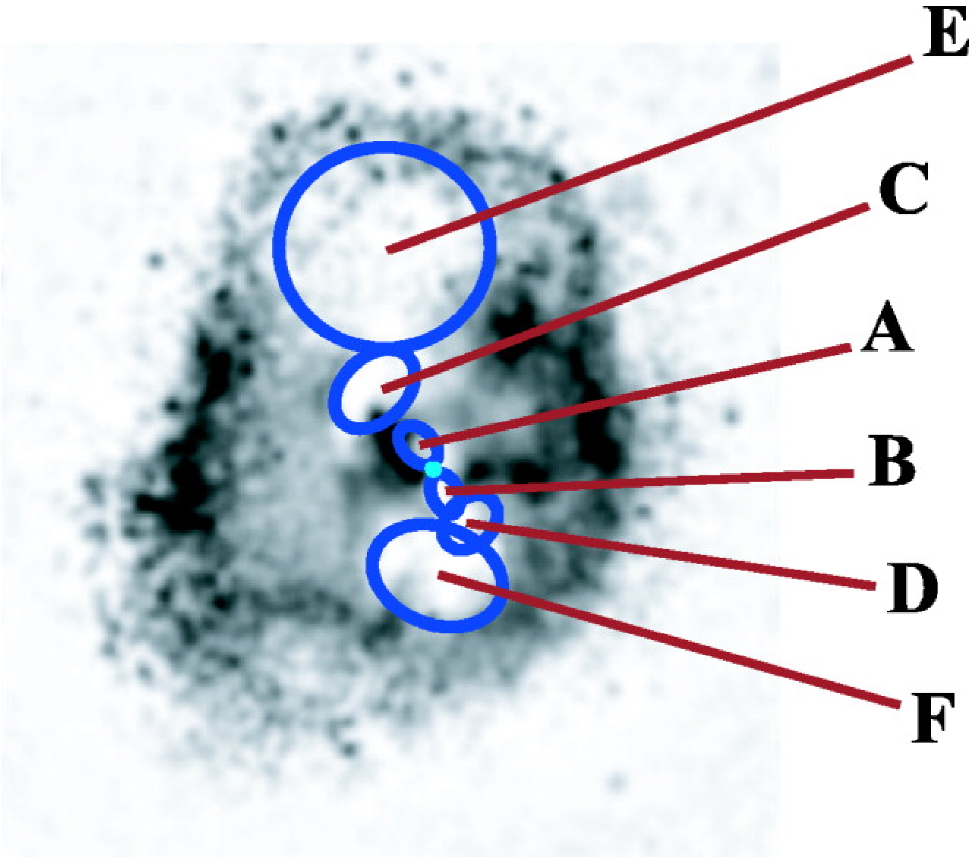

Figure 5.13: The residual X-ray map for Hydra A using *Chandra* data. The positions of the cavities are indicated. Image taken from Wise et al. (2007).

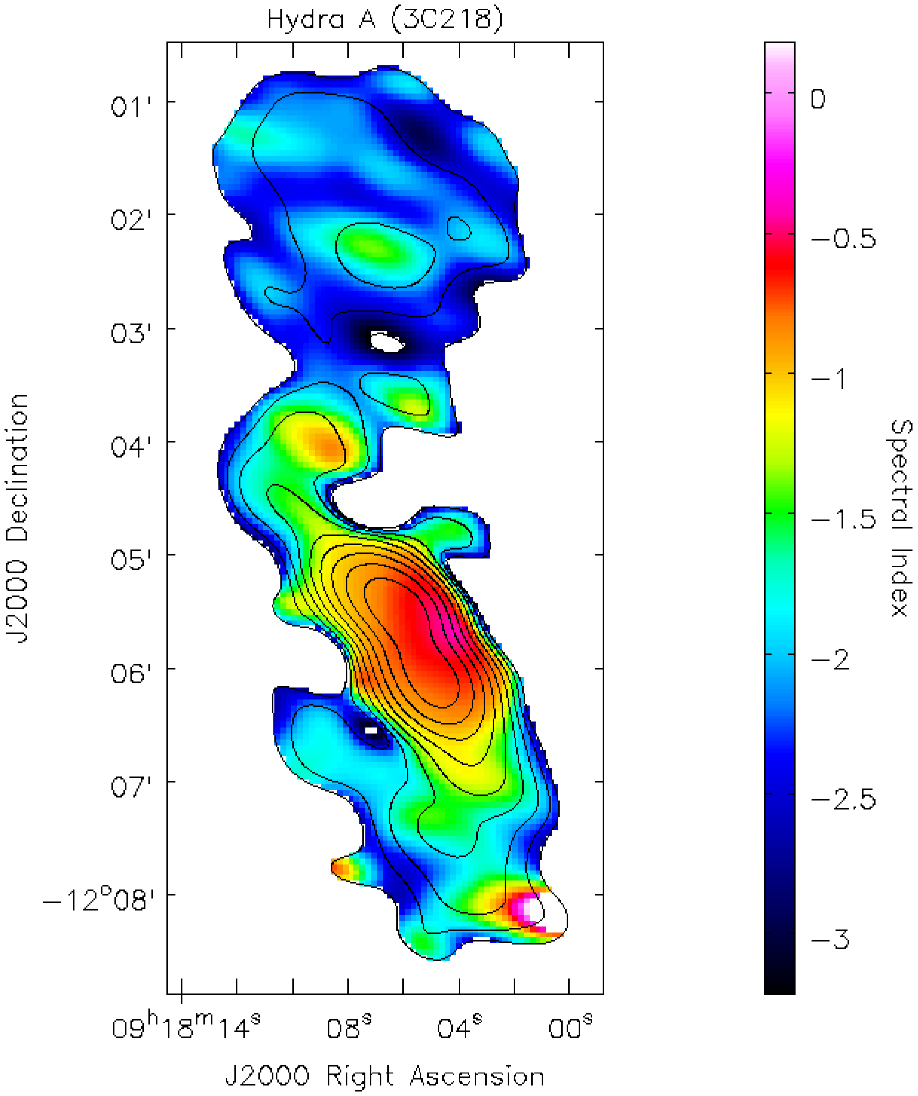

Figure 5.14: The 610–235 MHz spectral index map for Hydra A. Black contours are for the matched resolution of 30″ × 24″ (PA: 55°) and start at 0.05 Jy and increase by factors of 2. The spectral image has been clipped to only show emission above the first contour level.

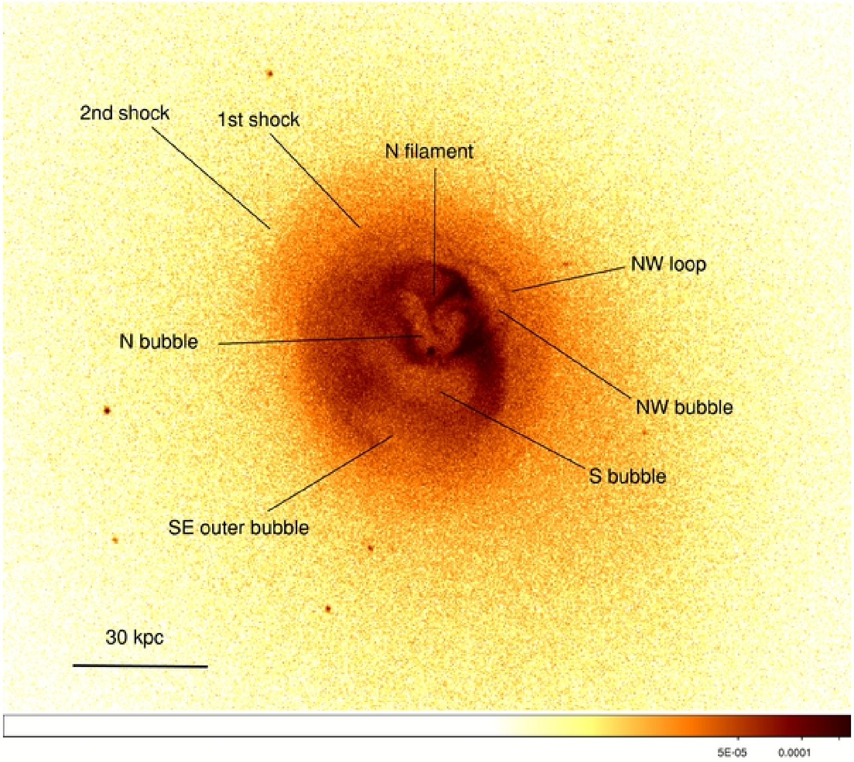

Figure 5.15: A *Chandra* image of Abell 2052 in the 0.3–2.0 keV band. This image is from Blanton et al. (2011).

5.4 Abell 2052

Abell 2052 is a well known cool core galaxy cluster at a redshift of $z = 0.0355$. With our chosen cosmology, this equates to a luminosity distance of 154 Mpc and a scale of $1'' = 0.697$ kpc. A2052 has been extensively studied at X-ray wavelengths, most recently with *Chandra* by Blanton et al. (2011). Figure 5.15 shows the unsmoothed 0.3–2.0 keV band *Chandra* image from Blanton et al. (2011). There are many different features that show the interactions between the ICM and the AGN.

The radio source in A2052 is also known as 3C 317, and is associated with the cD galaxy of UGC 09799. As it is at a relatively close distance, the flux densities are high. For example, a flux density of 5.5 Jy at 1.4 GHz was found using the VLA (Zhao et al., 1993; Bîrzan et al., 2004). Venturi et al. (2004) used VLBA to look at the core region, and they found a compact double source on the scale of a few milliarcseconds. They estimate a young age for the nucleus, and suggest that the radio emission has just been restarted.

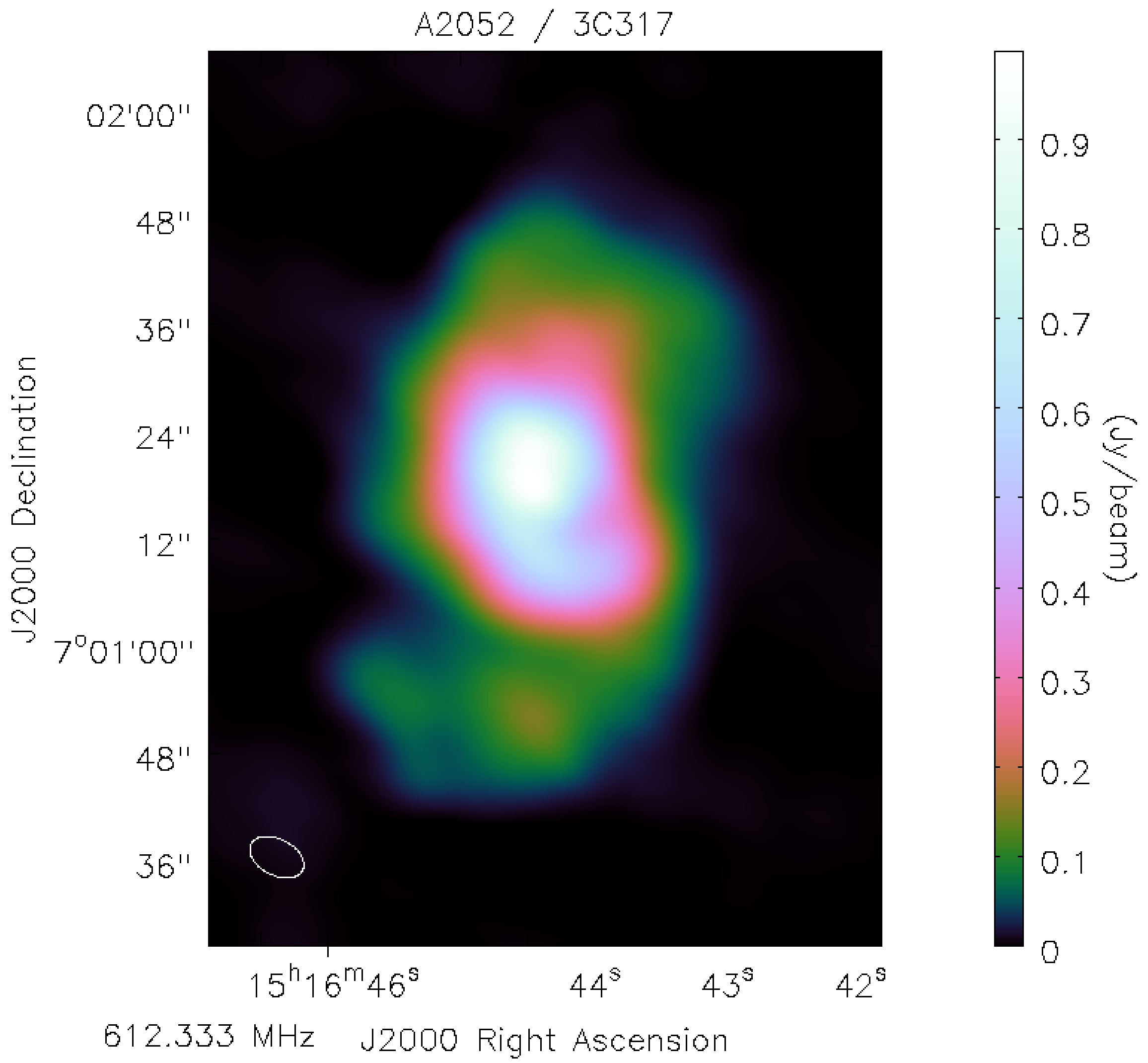

Figure 5.16: The GMRT 610 MHz map for Abell 2052.

GMRT observations

We observed Abell 2052 with the GMRT on the 22nd July 2011. The observations were again taken in dual-frequency mode with the GSB, and our time on source was almost six hours. Our full resolution 610 MHz map is shown in Figure 5.16. Dynamic range could become an issue with such a bright source, but not in this case as we are concentrating on the central galaxy and the flux density is high throughout the source.

We find a flux density of 15.18 Jy at 610 MHz and 37.2 Jy at 235 MHz. This gives a spectral index of $\alpha = -1.05$. We can see the correlation between the south and south-east outer bubbles

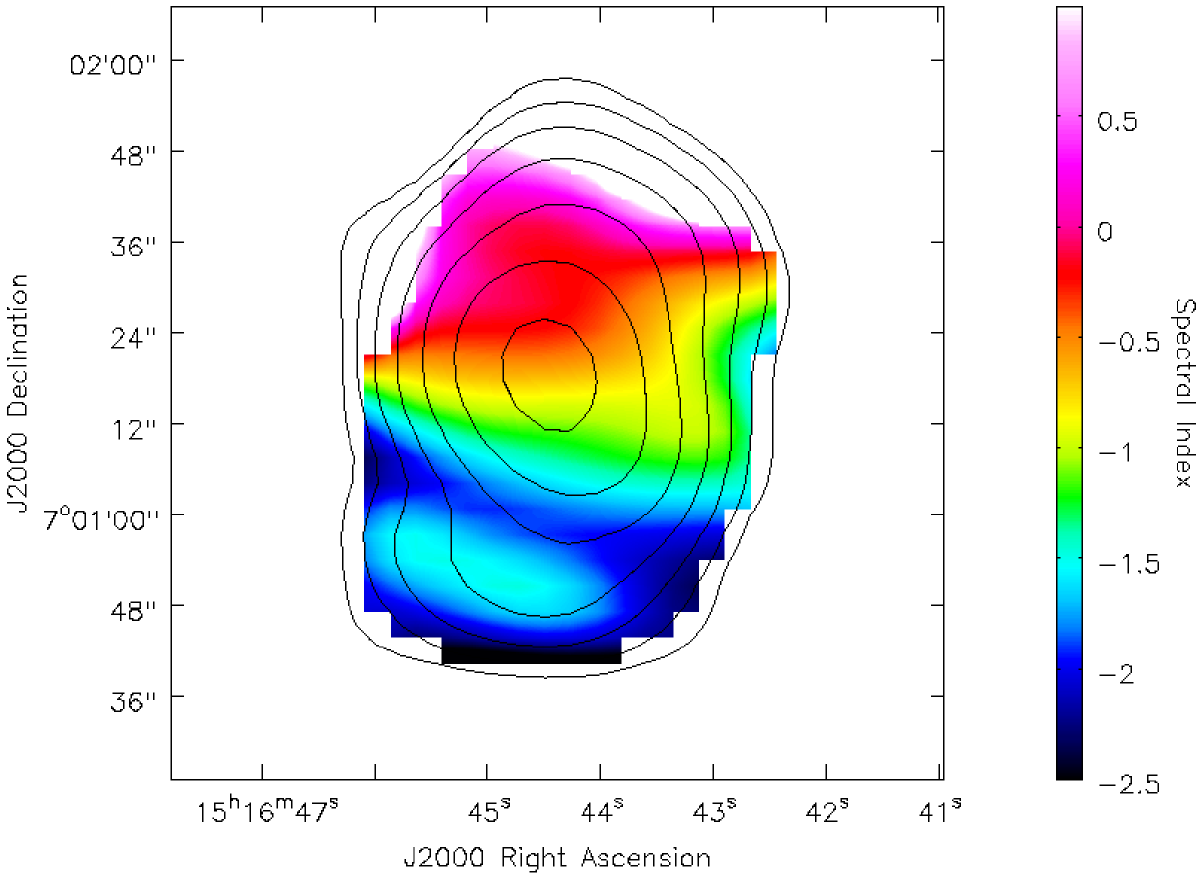

Figure 5.17: The 610–235 MHz spectral index map for Abell 2052. 610 MHz contours are overlaid, with the resolution of the 235 MHz map. Contours starts at 50 mJy and increase by factors of 2.

shown in the X-ray and the shape of the radio emission in the full resolution map. This gets washed out at lower resolutions, although there is still a definite gradient shown in our spectral index map of Figure 5.17.

5.5 Abell 2218

Abell 2218 is a famous gravitational lensing cluster at a redshift of $z = 0.1756$ (Kneib et al., 1996; Smith et al., 2005). The cluster is currently observed to be undergoing a merger, with evidence including the significant difference between the lensing and X-ray mass estimates (e.g. Pratt et al., 2005).

Radio haloes

Birkinshaw (1986) discovered evidence for a faint radio halo with the Cambridge One-Mile radio telescope, incidentally the first telescope to use aperture synthesis (Ryle, 1962). This was confirmed by Giovannini and Feretti (2000) using the VLA, but no radio observations of it have been published since. Radio haloes are diffuse radio sources that found near some centres of clusters. They can extend to megaparsecs in size and usually have a low surface brightness. The halo observed in A2218 is one of the smaller haloes to be discovered.

As the haloes are faint, they are normally detected at low frequencies where their flux density is higher. This does to lead to problems when fitting a model to the emission processes, as a wide range of frequencies is necessary to constrain this. It is argued that the acceleration of the particles must be undergone *in situ*, as they would not have enough time to diffuse throughout the cluster volume. In all known cases of radio haloes, the host systems are undergoing a merger, Abell 2218 is no different in that respect. Further information can be found in a review by Feretti et al. (2012).

GMRT observations

We observed Abell 2218 with the GMRT on the 19th May 2010. Dual-frequency observations were taken and high quality maps were made, with local rms values of 0.027 and 0.39 mJy beam^{-1} for the full resolution 610 and 235 MHz maps respectively. Our 610 MHz map is shown in Figure 5.18, with the large field of view shown. This was especially important for our work in Chapter 3.

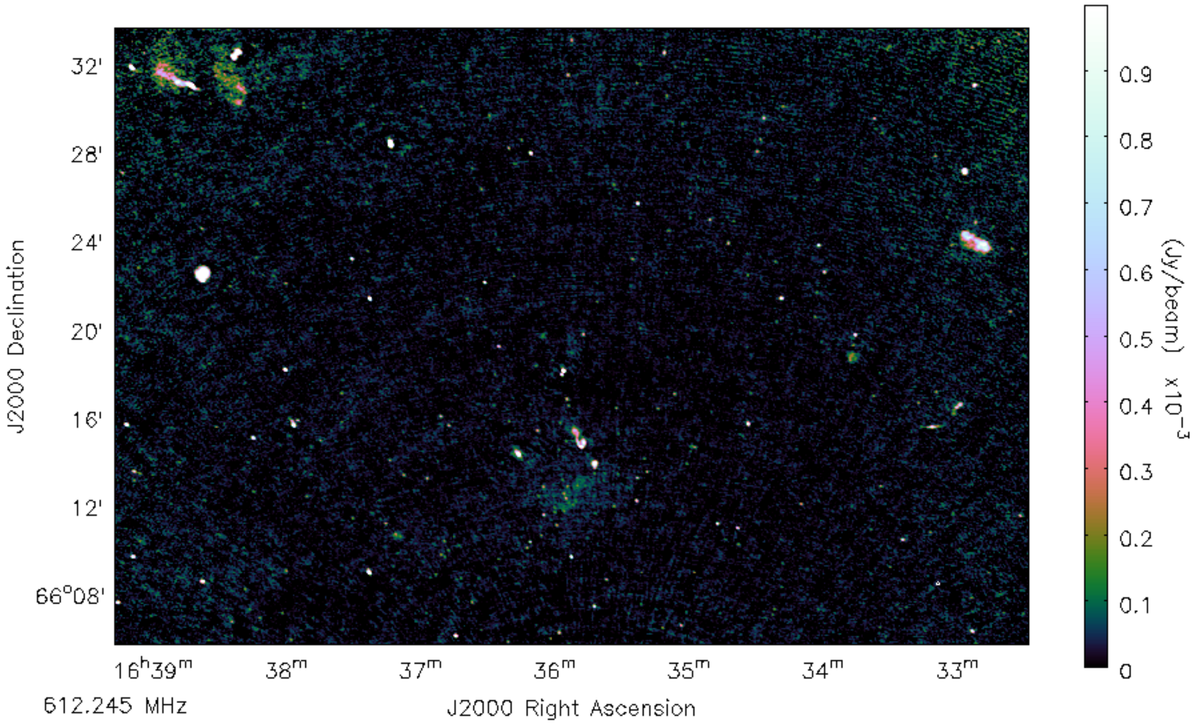

Figure 5.18: The high resolution 610 MHz image of A2218.

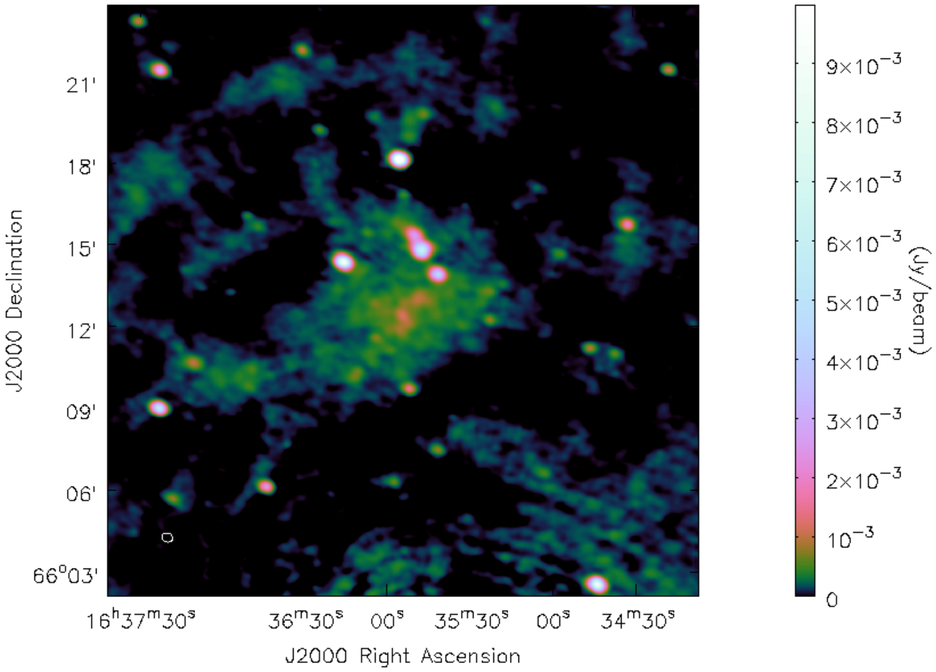

Figure 5.19: The radio halo of A2218 is shown here using the low resolution map at 610 MHz.

The result of our low frequency observations of the radio halo in Abell 2218 is seen in Figure 5.19. With a total integrated flux density of only ∼18 mJy at 610 MHz, the radio halo is difficult to image clearly. Despite this, our high resolution map still sees an excess of flux around the halo region, even though there it is potentially being resolved out. For both frequencies, we make an image with resolution of $38.65'' \times 33.12''$ (PA: 59°), and a uv−range of 0.1−15 kλ and a uv−taper of 8 kλ. We choose a Briggs robust weighting of 2, which is more towards natural than uniform weighting. This enables us to make a spectral index map, which we show in Figure 5.21. Giovannini and Feretti (2000) find a spectral index of $\alpha_{1.4}^{5.0} = 1.6$, but no spectral index map of the radio halo of A2218 has been published before. Our image shows the halo is similar in shape, size and spectral index to that seen by Giovannini and Feretti (2000). Variances in the spectral index could have multiple explanations. The first is that there are some contaminating point sources that have a significant contribution that needs to be removed. Alternatively, regions with a flatter spectral index could be due to more energy being injected into the electron population from an area of merger activity (Feretti et al., 2004). It could also signify an area of more recent injection, with steeper spectrum areas showing the older emission. This deserves further attention with a larger range of frequencies in order to derive more spectral properties.

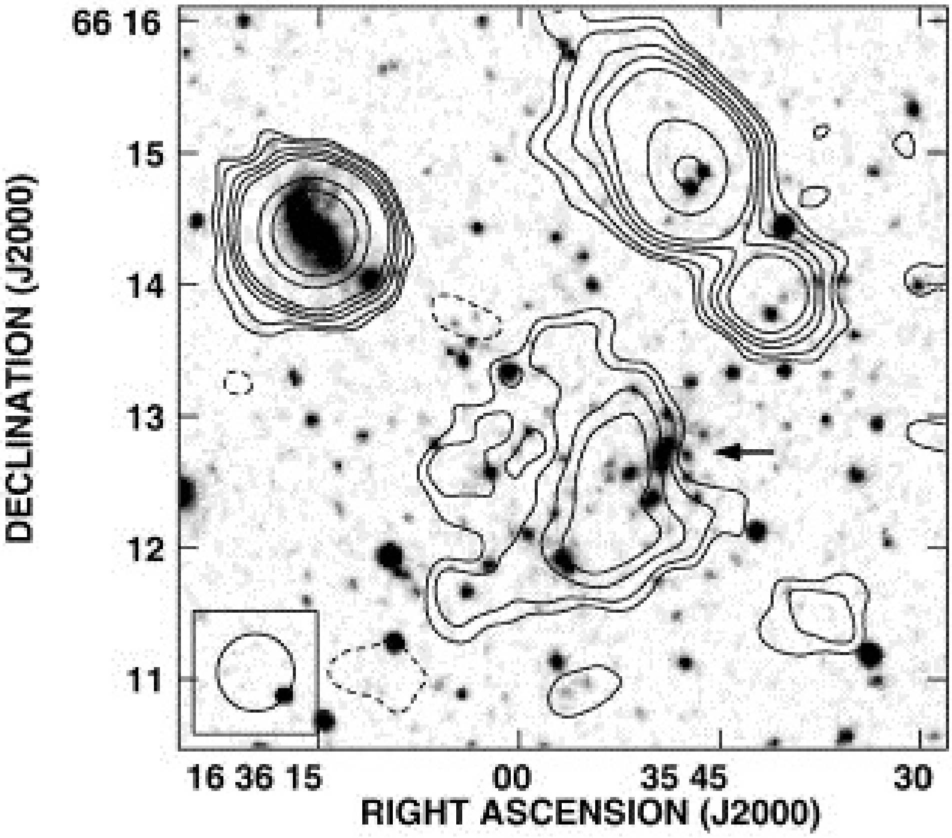

Figure 5.20: The radio halo of A2218 is shown here at 1.4 GHz. The image is from Giovannini and Feretti (2000).

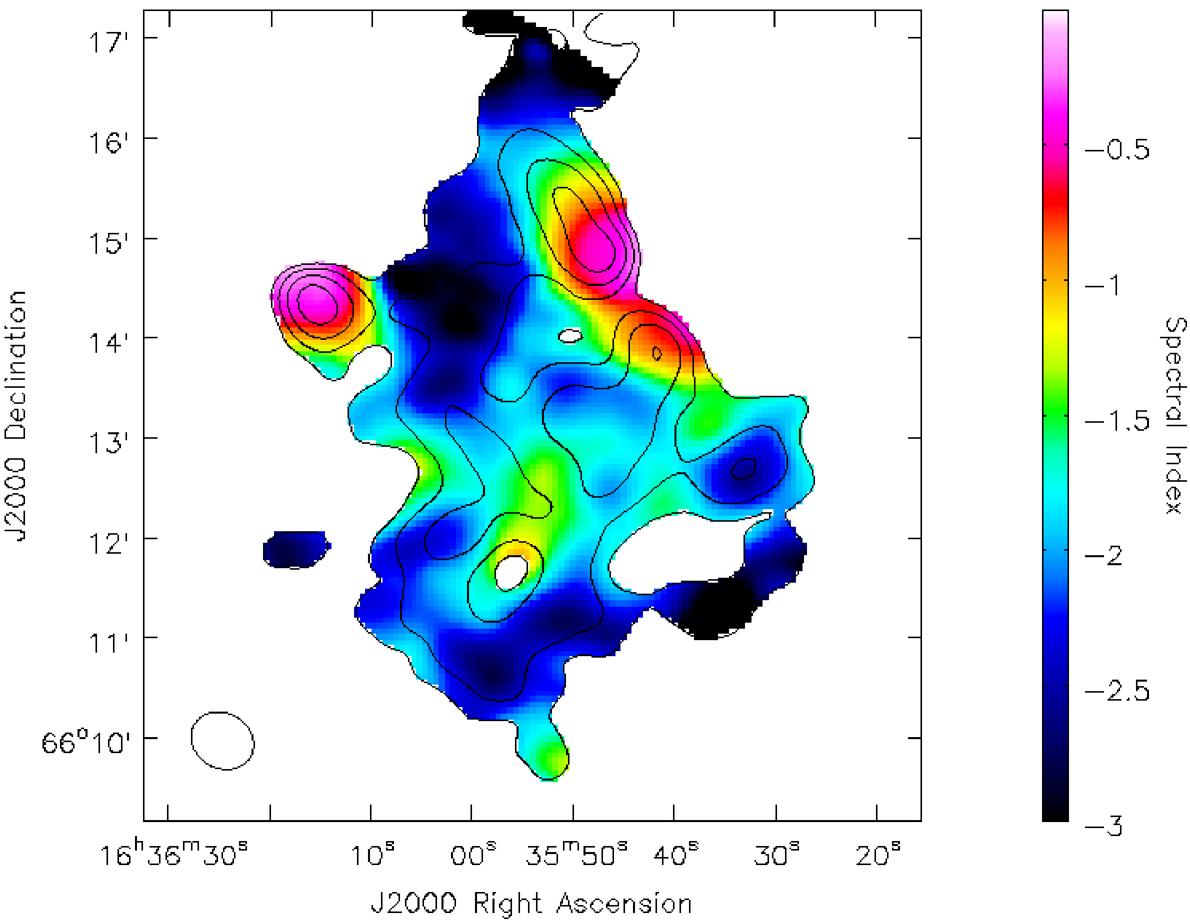

Figure 5.21: The 610–235 MHz spectral index map for Abell 2218. 235 MHz contours are overlaid, with the resolution of 38.7″ × 33.1″ (PA: 59°). Contours starts at 4 mJy and increase by factors of $\sqrt{2}$. The maps have a *uv*–range of 0.1–15 kλ and a *uv*–taper at 8 kλ. We choose a Briggs robust weighting of 2, which is more towards natural than uniform weighting.

5.6 Hercules A

Hercules A (also known as 3C348) is a very luminous radio source, located at the centre of a cooling flow cluster of galaxies at a redshift of $z = 0.154$.

Hercules A has been studied extensively over many radio wavelengths, and is known for its unusual morphology. Gizani and Leahy (2003) observed the source with the VLA at frequencies ranging from 1.3 to 8.4 GHz. They found several points of interest, with the first being that the core possesses an atypically steep spectrum ($\alpha = -1.2$), which they suggest is as a result of substantial variability of the AGN activity. There is also a difference in the morphology of the two radio jets. The western jet shows a series of ring-like features, whereas the eastern jet consists of a number of knots and twists. Unusually, Hercules A does not have any radio hotspots that are normally associated with such high luminosity radio AGN.

Chandra observations by Nulsen et al. (2005a) discovered a shock front powered by the AGN outburst. These shock fronts have been found in other sources (e.g. McNamara et al., 2005; Nulsen et al., 2005b), and are another source of heating that has to be considered when investigating the energetics and ages of AGN outbursts. Hercules A does also have some faint cavities, although strangely they are not associated with any radio emission.

GMRT observations

We observed Hercules A with the GMRT with two frequencies on the 23rd May 2010 for approximately six hours. It has the highest flux density of our sample, we find values of 79.5 and 170 Jy for 610 and 235 MHz respectively.

Each jet is approximately 100″ in length, which equates to 265 kpc. Figure 5.23 shows the 610–235 MHz spectral index map for Hercules A. We can see the difference in spectral index between the jet features and the radio lobes. The ring-like features to the west are clearly visible with a flatter spectrum, despite not being so obvious in our monochromatic image. We find a region of flat-spectrum structure at the outskirts of the eastern jet. This has a spectral index of $\alpha \sim -0.2$, which is significantly flatter than the minimum of $\alpha = 0.61$ found by Gizani

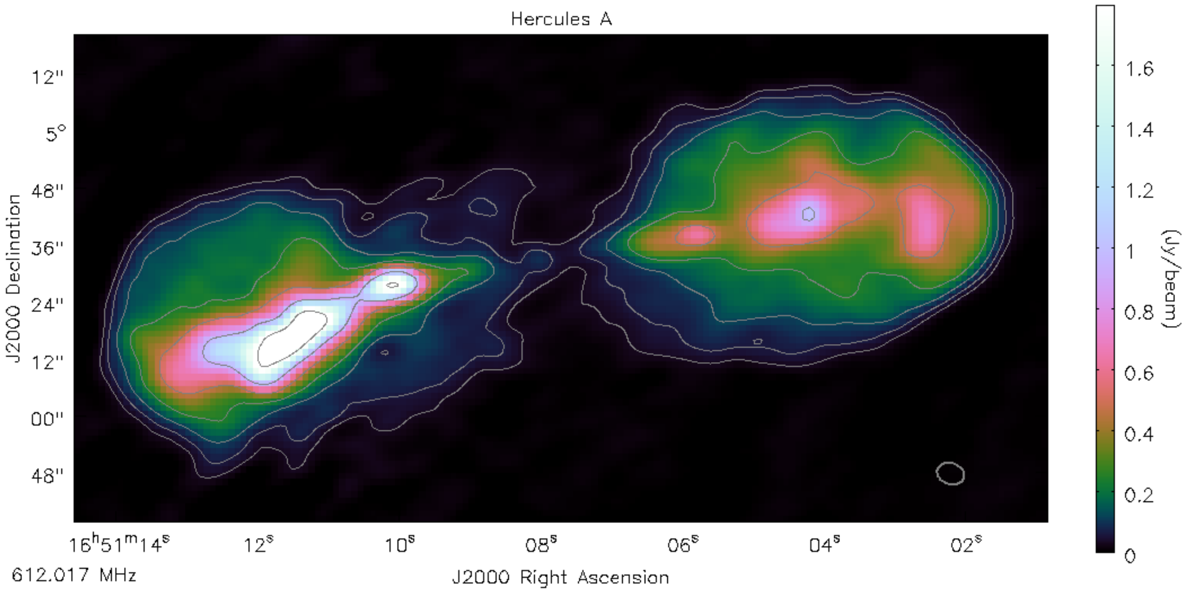

Figure 5.22: The GMRT 610 MHz map for Hercules A. Contours are 30 mJy and increase by factors of 2. The beamsize of 5.84″ × 4.41″ (PA: 72.1°) is shown in the bottom-right hand corner.

and Leahy (2003). Gizani et al. (2005) also used the VLA at lower frequencies (74 and 330 MHz), but our resolution is significantly better for our spectral index map, where the jet and lobes are more easily distinguished. The backflow towards the core has a much steeper spectral index than the rest of the radio source, this is due to the ageing of that population of electrons.

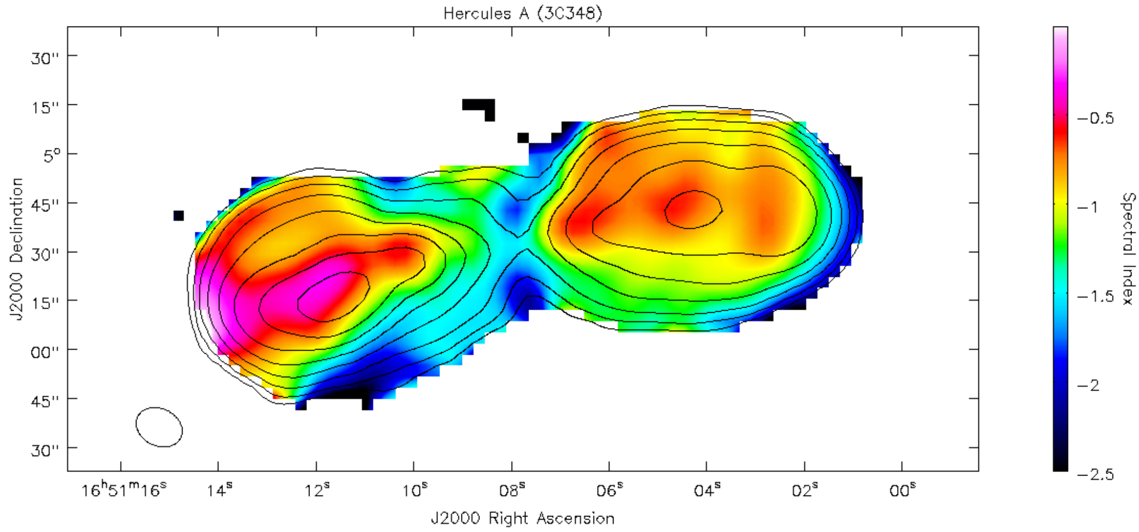

Figure 5.23: The 610–235 MHz spectral index map for Hercules A. The 610 MHz radio contours are overlaid, starting from 50 mJy beam^{-1} and increasing by factors of 2. They are resolution matched to the 235 MHz radio map, with a beamsize of 14.67″ × 11.35″ (PA: 64.07°) shown in the bottom-left corner.

5.7 RXJ1720.1+2638

RXJ1720.1+2638 (also known as SDSS-C4 3072, RBS 1639; hereafter RXJ1720) is a galaxy cluster located at a redshift of $z = 0.164$. It is X-ray bright and hosts a pair of 'cold fronts' – a sharp discontinuity in the surface brightness distribution interpreted to be the boundary between regions of gas with different entropies (for a review, see Markevitch and Vikhlinin, 2007). RXJ1720 otherwise has a regular X-ray morphology, and the main hypothesis for the formation cold fronts in relaxed clusters is due to 'sloshing' – the motion of low entropy core gas (Markevitch et al., 2001). There are a few suggestions for the cause of this motion, AGN feedback could possibly provide enough energy. Clusters with more complex morphologies hosting cold fronts are generally believed to be as a result of major mergers, which are normally confirmed with observations of other merger-related processes. Owers et al. (2011) believe that for relaxed clusters, the cold fronts observed are as a result of minor mergers. As a result, cold fronts can be used to identify clusters that have undergone a merger, and combined with X-ray morphology can be used to differentiate between minor and major mergers.

Clusters with cold fronts observed in radio frequencies are sometimes seen to host some diffuse extended emission. These radio mini-haloes are normally very faint and have steep spectral indices. The emission typically extends to outside of the central galaxy. It is hypothesised to be associated with electrons that have been re-accelerated by the sloshing of the gas. Due to their low surface brightness, radio mini-haloes are rare to observe, only a few clusters have confirmed detections (Feretti et al., 2012). RXJ1720 was one of the first galaxy clusters that was found to have a correlation between its diffuse radio emission and X-ray cold fronts (Mazzotta and Giacintucci, 2008).

GMRT observations

We will use our dual-frequency 610 and 235 MHz GMRT observations to investigate the radio emission from the galaxy cluster. RXJ1720 was observed on the 23rd July 2011 as part of GMRT observing cycle 20. Full resolution images were made at both frequencies resulting in rms noise

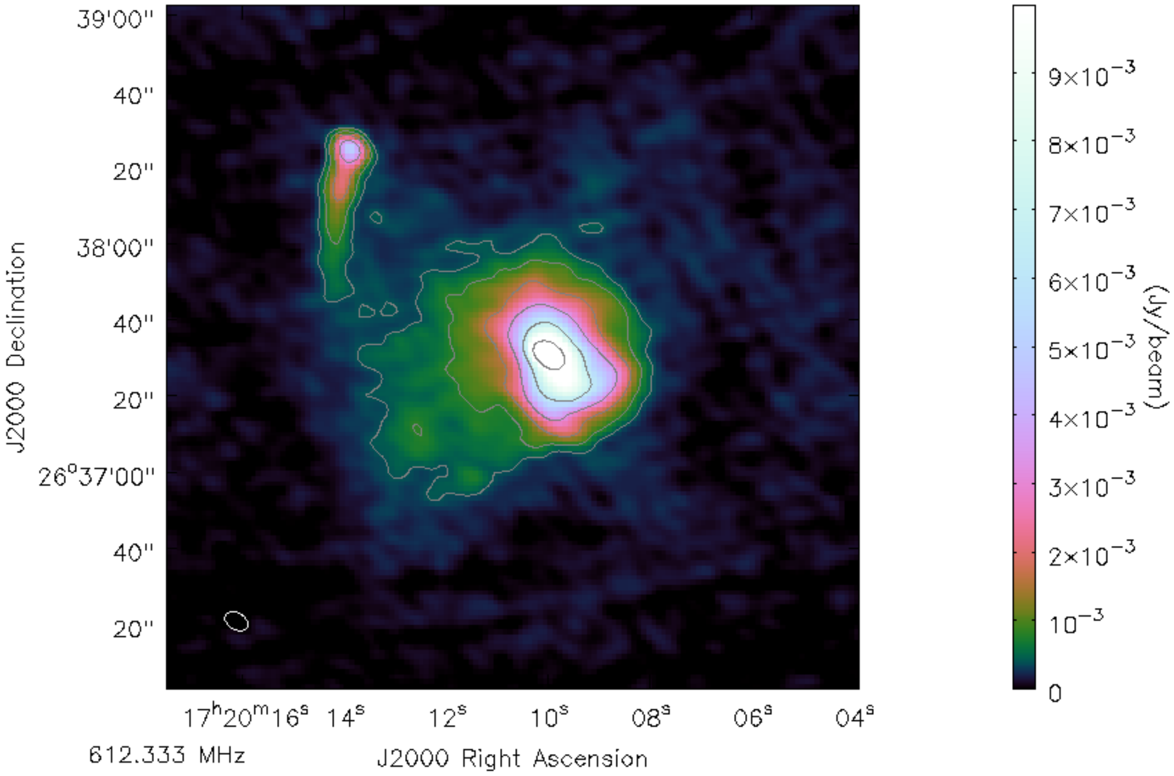

Figure 5.24: The GMRT 610 MHz map for RXJ1720. Contours are 0.4 mJy and increase by factors of 2. The beamsize of 6.60″ × 4.32″ (PA: 61.1°) is shown in the bottom-left hand corner.

levels of 0.060 and 0.450 mJy beam^{-1} for 610 and 235 MHz respectively. Our 610 MHz image is shown in Figure 5.24. We use a scale of 2.789 kpc/arcsec for our chosen cosmology.

Bright radio emission is seen from and encompassing the central galaxy. The luminosity decreases radially, but is extended towards the south-east. A head-tail source is nearby to the west, which also is a cluster member. The diffuse emission links up with the second source.

We can see how our GMRT radio emission is slightly more extended at our lower frequencies than the VLA 1.5 GHz contours shown in Figure 5.25. This emission is still constrained by the blue curves showing the cold front locations.

The spectral index map is shown in Figure 5.26. It is evident that there is a gradient either side of the central peak of the radio emission, from $\alpha \sim -0.4$ to the east, to $\alpha \sim -1$ to the west. This gives us an insight into the possible relative motions of the BCG and ICM, with the older emission having a steeper spectral index. However, our results differ from those recently

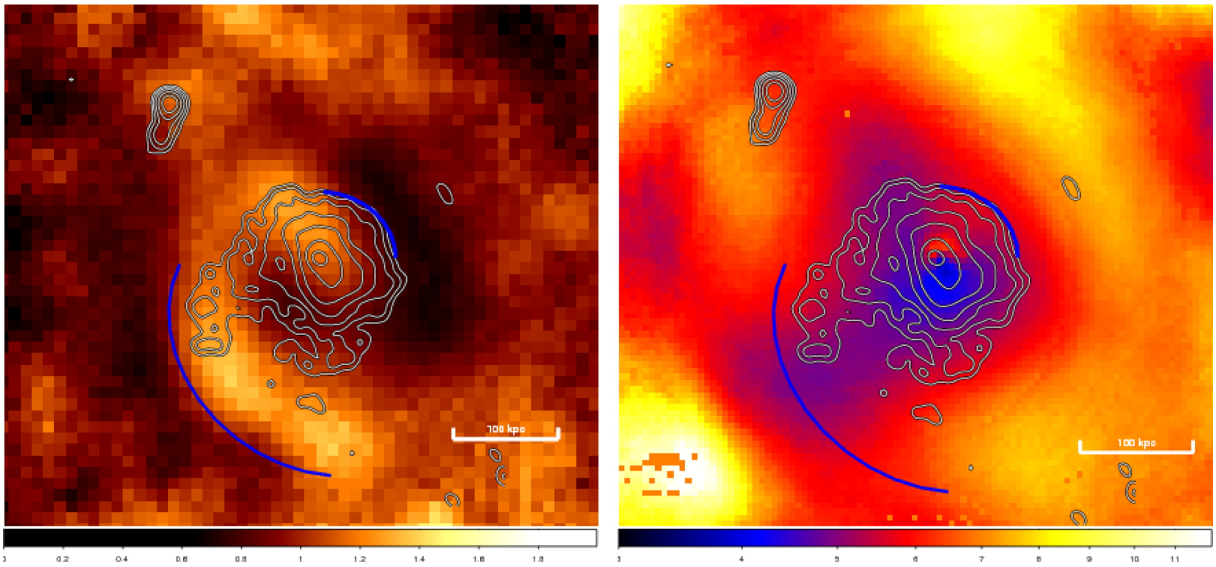

Figure 5.25: Left: *Chandra* X-ray image of RXJ1720 in the 0.5–2.5 keV band taken from Mazzotta and Giacintucci (2008). Right: Their X-ray projected temperature map. Cold fronts are marked in blue and 1.5 GHz VLA contours are overlaid.

published by Giacintucci et al. (2014); they use older GMRT data and find a steeper spectral index as a function of distance from the core. This discrepancy needs to be investigated further.

Further radio sources

In the RXJ1720 radio map, we see two more interesting sources worthy of discussion. Both are at a similar redshift to our cluster and show extended radio emission.

5.7.1 SDSS J172027.49+263158.7

SDSS J172027.49+263158.7 are the coordinates of an elliptical galaxy at $z = 0.160$ with an apparent r-band magnitude of 17.16. It appears to be in the centre of a small group of galaxies, situated 1134 kpc from the BCG. While fairly innocuous in the optical regime, some interesting emission is observed when looked at with the low frequency radio array. First of all, two radio jets are visible, with the shorter southern jet extending for ∼46 arcsec (128 kpc). Our high resolution 610 MHz image (Figure 5.27) shows that there is an isolated local maxima of radio emission corresponding to the SDSS galaxy we have attributed it to (Figure 5.28). Unusually, immediately either side of this peak are two minima in emission, before brightening up again.

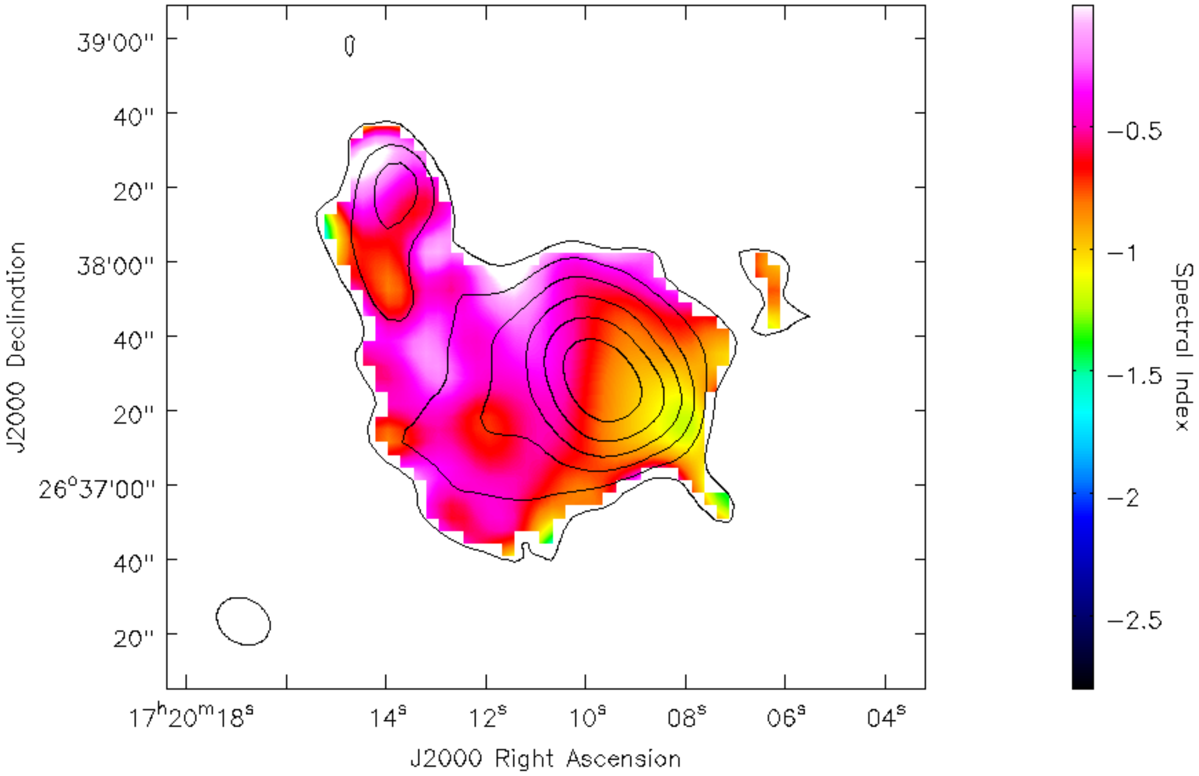

Figure 5.26: The 610–235 MHz spectral index map for RXJ1720. Contours are from the 235 MHz map and start from 2 mJy and increase by factors of 2.

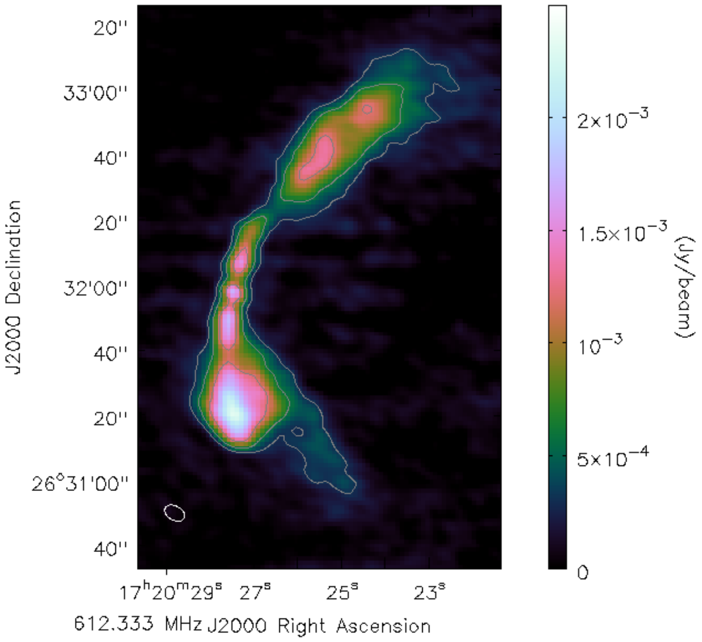

Figure 5.27: The 610 MHz radio image of SDSS J172027.49+263158.7. The first contour starts at 0.3 mJy beam^{-1} and increases by factors of 2. We can see a peak of emission correlating with the galaxy shown in Figure 5.28.

This is repeated for the northern jet, another dip in radio emission occurs approximately 75 kpc from the galaxy.

The radio jets are curved, implying that they have interacted with their surroundings, most likely due to the host galaxy moving through some high density ICM. This would result in significant ram pressure on the radio emitting material of the jet (Begelman et al., 1984). We find the radius of curvature to be ~234 kpc, by simply measuring the radius of a circle aligned with the radio jets.

Theoretically, we can find some properties of the ICM it passes through by using Euler's equation of hydrodynamics in its classical form.

$$\frac{\rho_j v_j^2}{R_{\text{bend}}} = \frac{\rho_e v_g^2}{R_p} \tag{5.1}$$

In this bending equation, ρ_j and v_j are the constant density and velocity of the jet, ρ_e is the density of the external medium, v_g is the velocity of the host galaxy with the respect to the medium, and R_{bend} and R_p are the radius of curvature of the jet and the pressure scale height

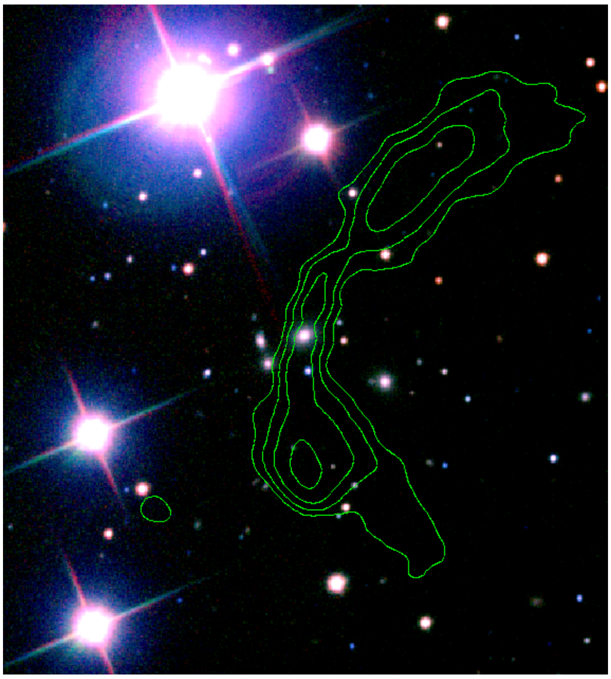

Figure 5.28: An RGB false-colour image of SDSS J172027.49+263158.7 created using the g, r and i filters from the SDSS. The 610 MHz GMRT radio contours are overlaid in green, with the first contour starting at 0.2 mJy beam^{-1} and increasing by factors of 2.

over which the ram pressure acting on the beam changes (De Young, 1991). R_p is typically taken to be equal to h, the width of the jet (Jones and Owen, 1979).

We can estimate the minimum synchrotron pressure in the jets by using the following equation (O'Dea and Owen, 1987; Freeland and Wilcots, 2011).

$$P_{\text{min}} = (2\pi)^{-3/7} \left(\frac{7}{12}\right) \left(c_{12}\, L_{\text{radio}}\, (1+k)\, (\phi V)^{-1}\right)^{4/7} \tag{5.2}$$

where $\Phi = 1$ is the filling factor, c_{12} is a constant found in Pacholczyk (1970), $k = 0$ and we estimate V from our radio observations and assuming a ellipsoidal volume. From this we find $P_{\text{min}} = 1.3 \times 10^{-13}\,\text{erg cm}^{-3}$. Rearranging Equation 5.1, we can find the external ram pressure, $\rho_e v_g^2$, by substituting in our values for R_{bend}, h and $\rho_j v_j^2 = P_{\text{min}}$. We find a value of $1.9 \times 10^{-14}\,\text{erg cm}^{-3}$. From X-ray observations (Cavagnolo et al., 2009), we can determine an electron number density of $5 \times 10^{-4}\,\text{cm}^{-3}$, and assuming $\mu_e = 1.157$ we calculate $v_g = 44.3\,\text{km s}^{-1}$.

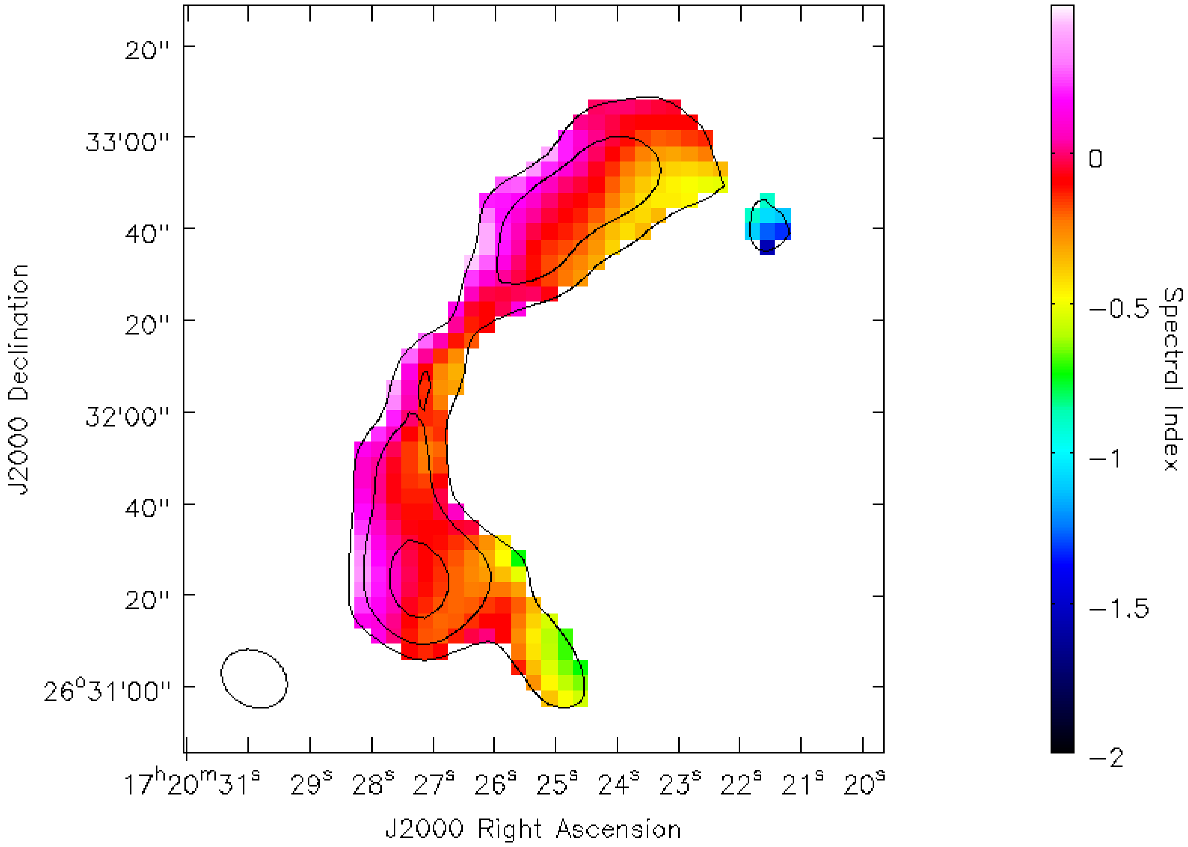

Figure 5.29: The 610–235 MHz spectral index map for SDSS J172027.49+263158.7. Contours are from the 235 MHz map and start from 2 mJy and increase by factors of 2.

Our spectral index map gives further evidence for a significant velocity for the host galaxy relative to the ICM, as we see a clear gradient between the two sides of the jets. This is shown in Figure 5.29.

5.7.2 SDSS J172107.89+262432.1

SDSS J172107.89+262432.1 is another interesting galaxy in our RXJ1720 field of view. It has a spectroscopic redshift of $z = 0.170$ and is classified as a star forming galaxy. It lies a projected distance of ∼3 Mpc from the centre of the cluster. As it is a farther redshift than the cluster, it is not classed as a cluster member. Figure 5.30 shows an RGB false-colour image of the galaxy, with 610 MHz radio contours overlaid. There appears to be some faint optical emission associated with the galaxy, as seen more clearly in Figure 5.31. Whether these are spiral arms or it is an interacting system is not so clear. The radio emission on the other hand, is very obvious. The jets extend 330 kpc in either direction and are collinear with the core. At the end of each jet are the hotspots that are typically seen in classical radio galaxies.

Interestingly, directly north of the western hotspot is another region of diffuse emission. Also seen is some fainter emission perpendicular to the core. It is worth noting that the scale width of the radio lobes compared to the length is quite large, and quite asymmetric. The spectral index for this source is found in Figure 5.32. We can see that the hotspots have a slightly steeper index as is typical for these kind of radio galaxies. The whole source though does not show much variation in spectral index, and is quite flat for an extragalactic radio source. This could be due to a fresh injection of electrons, consistent with recent interactions of the host galaxy.

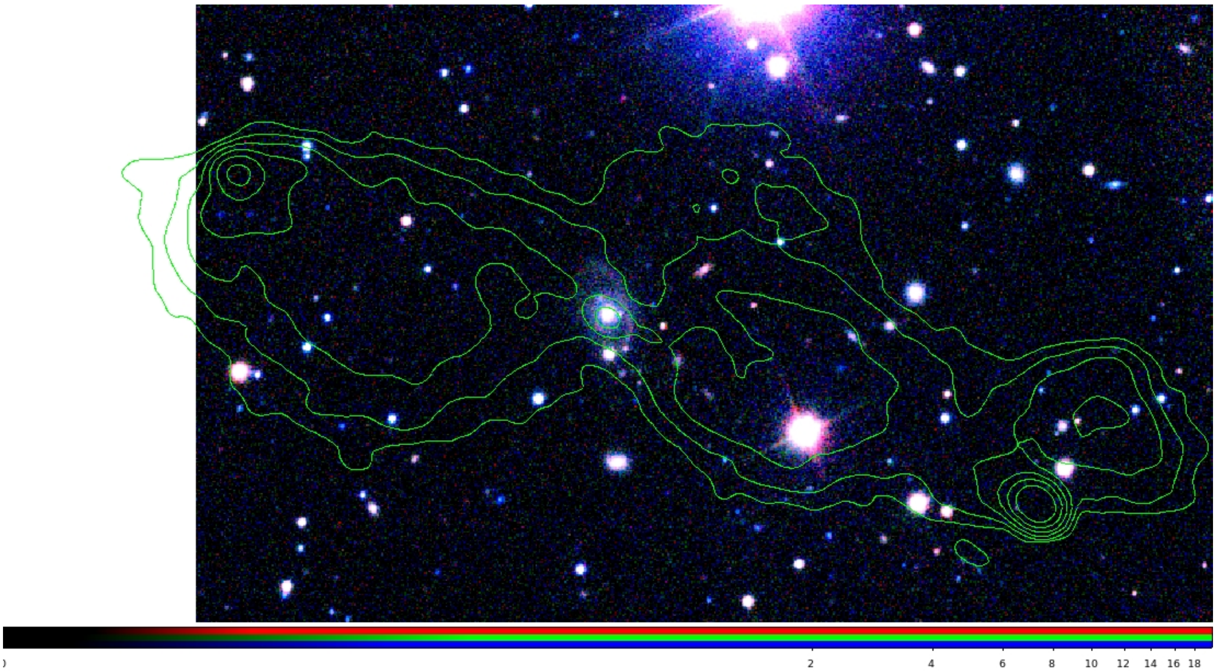

Figure 5.30: An RGB false-colour image of SDSS J172107.89+262432.1 created using the *g*, *r* and *i* filters from the SDSS. The 610 MHz GMRT radio contours are overlaid in green, with the first contour starting at 0.3 mJy beam^{-1} and increasing by factors of 2.

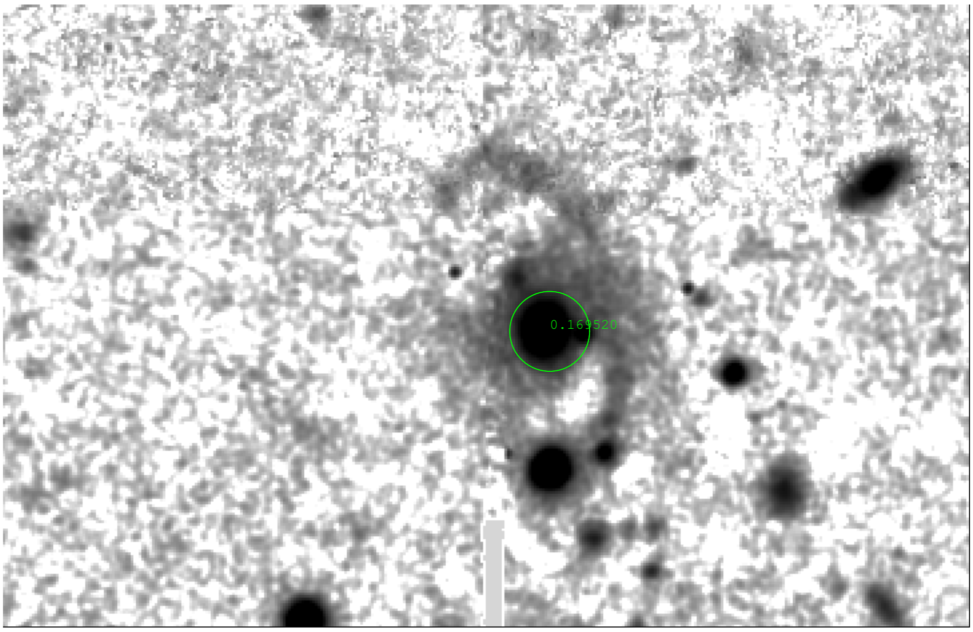

Figure 5.31: Optical *V*-band image using the 8.2 m Subaru telescope. Image from Chris Haines (private communication).

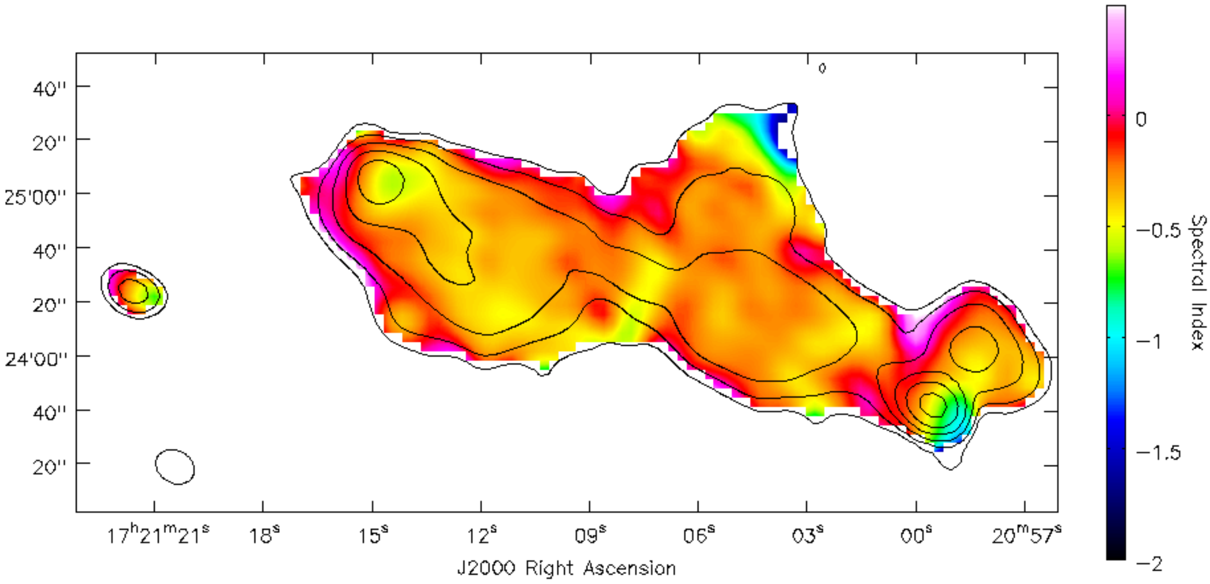

Figure 5.32: The 610−235 MHz spectral index map for SDSS J172107.89+262432.1. Contours are from the 235 MHz map and start from 2 mJy and increase by factors of 2.

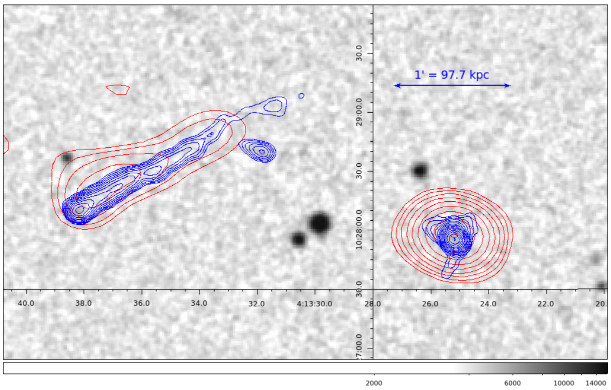

Figure 5.33: Greyscale optical image of Abell 478 with our GMRT radio contours overlaid in blue for 610 MHz and red for 150 MHz. 610 MHz contours start at 0.3 mJy and increase by a factor of $\sqrt{2}$. The 150 MHz first contour is 12 mJy and has the same spacing.

5.8 A brief description of the other cluster observations

We present further images of our results for these clusters, although the majority of these are point sources at our resolutions.

5.8.1 Abell 478

We have images at 610, 235 and 150 MHz for Abell 478. The 610 MHz image has a resolution of $5.2'' \times 4.2''$, and an rms noise near the source of $\sim$50 μJy beam^{-1}. The 150 MHz image has a resolution of $25.5'' \times 19.7''$, and an rms noise of $\sim$2.0 mJy beam^{-1}. These are both full resolution images taken with the entire *uv* range available and a robust value of 0. No significant extended emission was seen around the central radio source.

5.8.2 RBS797

We have images of RBS797 at 610, 235 and 150 MHz. They are good, large, deep images with local rms values of 0.035, 0.24 and 2 mJy beam^{-1} respectively. We do not see the radio jets seen in Gitti et al. (2006), due to the redshift and frequency of our observations.

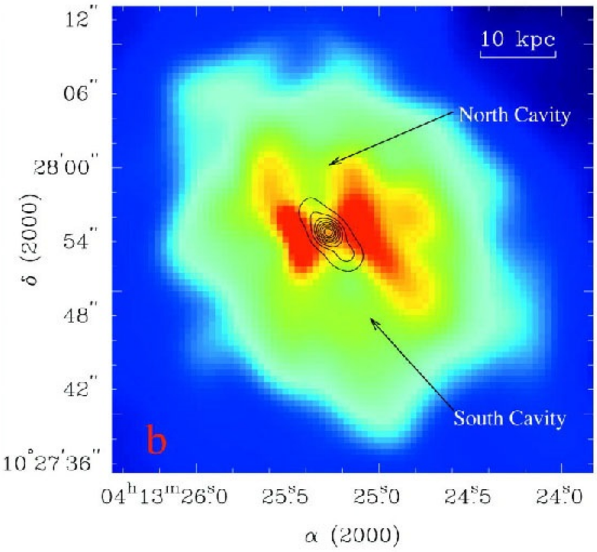

Figure 5.34: The smoothed *Chandra* 0.5–5 keV image of the central part of A478 with 1.4 GHz radio contours superposed. The two X-ray cavities are labelled, and the image is from Sun et al. (2003).

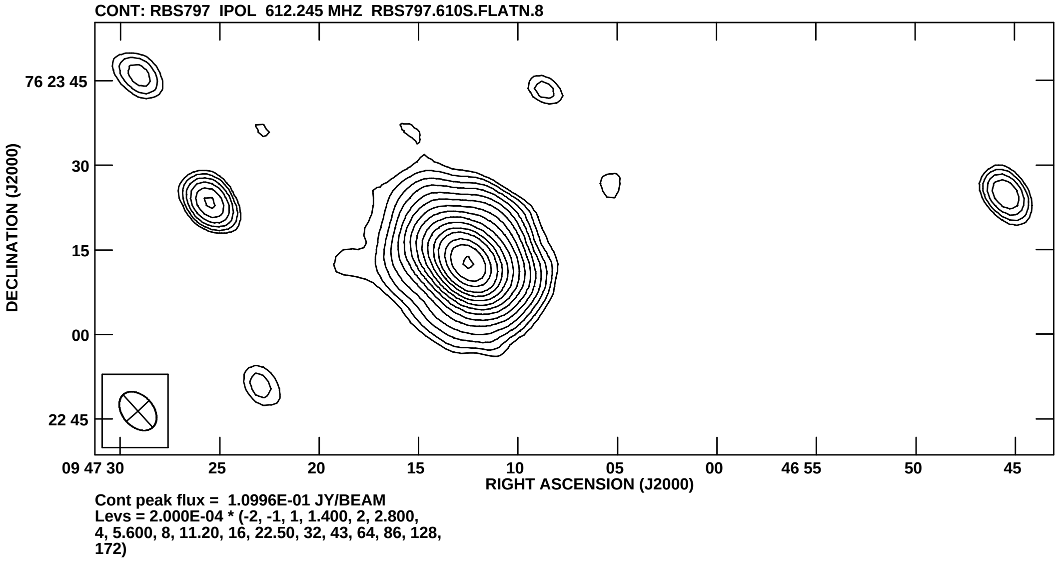

Figure 5.35: RBS797 at 610 MHz with the GMRT.

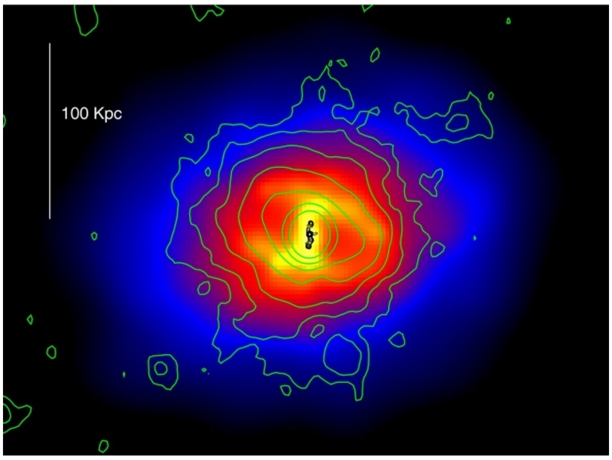

Figure 5.36: 4.8 GHz black contours from Gitti et al. (2006) and 1.4 GHz VLA radio green contours from Doria et al. (2012) are overlaid on the smoothed Chandra X-ray image of RBS797. Image from Doria et al. (2012).

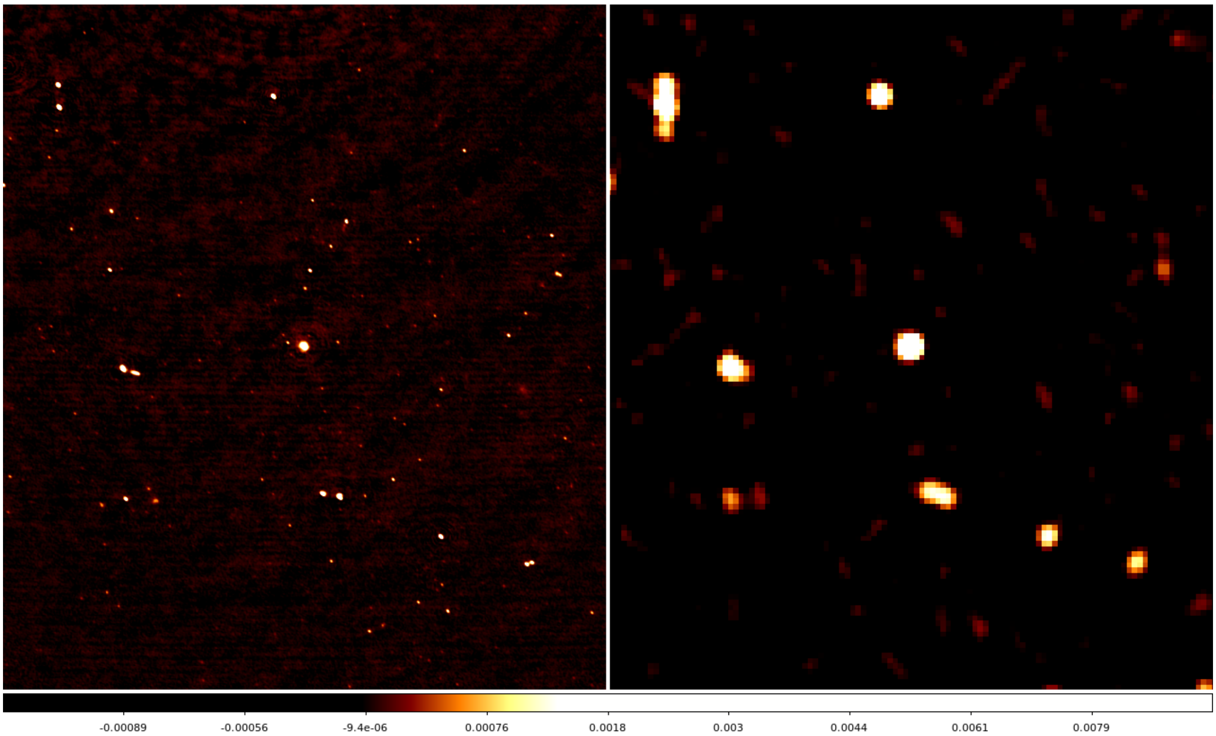

Figure 5.37: RBS797: The difference in resolution and depth between the 610 MHz GMRT map on the left, and the 1.4 GHz NVSS image on the right.

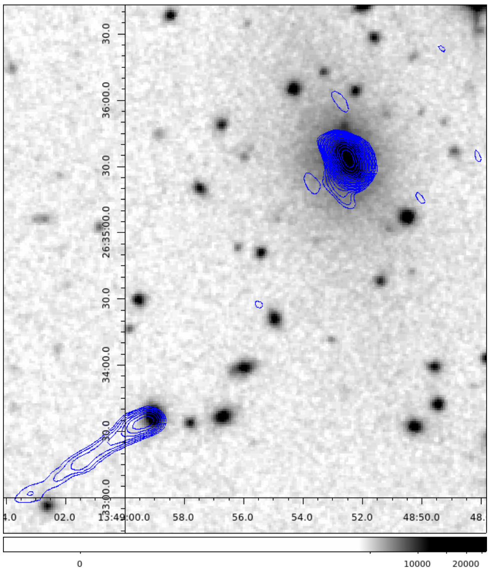

Figure 5.38: Abell 1795: Greyscale optical image with the GMRT radio contours overlaid in blue for 610 MHz. 610 MHz contours start at 0.1 mJy and increase by a factor of $\sqrt{2}$. The BCG is the bright radio source to the top-right, with a flux density of over 2 Jy. A head-tail source is observed nearby, similar to what is seen in Figure 5.33.

5.8.3 Abell 1795

For Abell 1795, we have dual-frequency observations at 610 and 235 MHz. The 610 MHz radio contours are presented below. The source is slightly extended towards the south, but at this frequency our resolution is not high enough to discern anything more.

5.8.4 Abell 1835

Abell 1835 was observed on May 2009 in dual frequency mode. Only GHB data is available but a decent image has been produced. Separate images using the lta and ltb data were produced and then averaged to create the final image. A1835 hosts a starburst in the central galaxy as well as a radio-loud AGN.

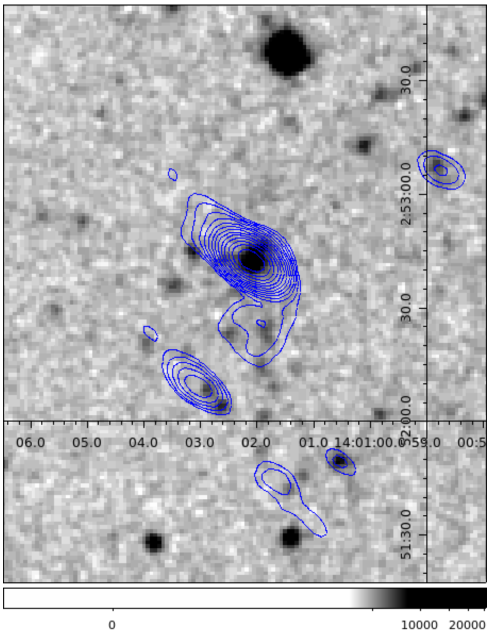

Figure 5.39: Greyscale optical image of A1835 with GMRT radio contours overlaid in blue for 610 MHz. 610 MHz contours start at 0.4 mJy and increase by a factor of $\sqrt{2}$.

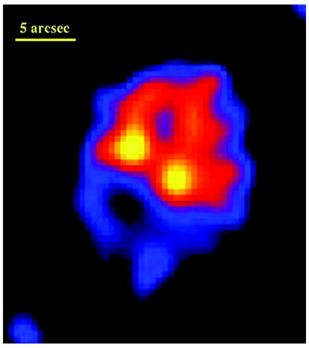

Figure 5.40: X-ray image of A1835 taken with the ACIS-I detector, showing the two cavities to the NW and SE of the nucleus. Image from McNamara et al. (2006).

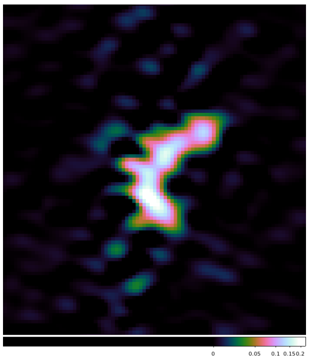

Figure 5.41: A2029 at 610 MHz with the GMRT. The source is extended in two directions, as seen in Govoni et al. (2009).

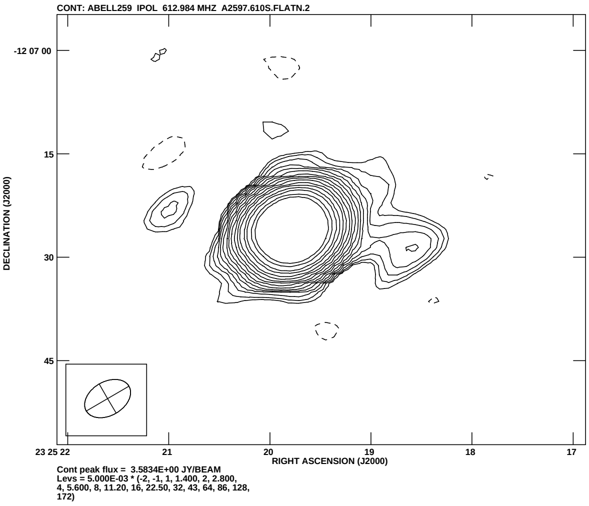

Figure 5.42: A2597 at 610 MHz with the GMRT. The E–W structure appears to match literature images, as seen in Clarke et al. (2005).

5.8.5 Abell 2029

A dual frequency observation was taken at 610 MHz and 235 MHz for Abell 2029. Comparisons with literature Govoni et al. (2009) show that the extensions to the north-west and south-west are real. The source is also very bright at 1.66 Jy at 610 MHz, the radio image is shown in Figure 5.41.

5.8.6 Abell 2597

Abell 2597 was observed at 610 and 235 MHz in dual-frequency mode. This is a bright source of ~0.5 Jy at 610 MHz, and is shown in Figure 5.42.

Chapter 6

Conclusions & further work

In this thesis, we have made use of deep radio observations using the Giant Metrewave Radio Telescope to investigate how active galactic nuclei interact with the intracluster medium.

In Chapter 3, we used multiwavelength data to investigate the radio AGN in a population of galaxies. We found that the fraction of radio-loud AGN is a function of galaxy mass, a result that has been found previously. However, we find a flatter gradient compared to earlier work with shallower survey data (NVSS/FIRST), implying that there are more low mass radio AGN than originally seen.

We derived mechanical powers from the observed radio jets, and found a relatively tight relationship between the ratio of mechanical to binding energies of galaxies to those galaxies' halo masses. Extrapolating that to lower masses would mean Milky Way size galaxies with a radio AGN would have enough energy to eject the gas from their system. These results were compared to recent simulations from cosmo-OWLS, with good agreement between the simulated and observed galaxies after a luminosity cut-off was made. It is also clear that one outburst releases a lot of energy into the galaxy. This significantly overheats the gas in lower mass systems and would quench star formation, and could even eject the gas from the system, assuming that the AGN input at the time of quenching is at least as large as we observe now. We find that AGN in $L_\star$ galaxies have more than enough energy to balance cooling in galaxies, even if their efficiency is as low as 1%. The AGN in more massive galaxies can help to regulate gas cooling, although they do not have enough energy to eject the gas, they fall into more of a maintenance mode.

Chapters 4 & 5 explored the central AGN and their interactions with the ICM in a sample of galaxy clusters. We first explored their similarities and differences as part of a sample, to try and identify overall trends in their energetics and jet composition. We found that low frequency broadband measurements are a better proxy of cavity power than simple monochromatic or high frequency measurements, as the low energy electron population is important in determining the powers involved. The gradient for our cavity–radio power relationship is flatter than the previous literature values for clusters and groups. The additional radio power that we infer will be important when attempting to compare observed values to theoretical models. The values of k that we found still have a large amount of scatter, so it seems likely that there are other processes involved that are not fully understood. We have found that a relativistic electron/positron plasma is not supported by our observations, but that more work needs to be done on this in order to attempt to constrain other models further.

In future work, we will use our own, deeper, X-ray data in order to determine more accurate estimates for the various X-ray derived parameters. Having access to the X-ray maps will allow us to combine them with the radio maps, giving us a clear picture of where the AGN/ICM interactions take place. *XMM-Newton* and *Chandra* data will be made available for us to do this.

We would also like to include further low frequency measurements of these clusters, and other clusters with suspected X-ray cavities. Building up a range of data for a range of systems is important in understanding the injection of energy into galaxy clusters, and AGN feedback in general.

For the majority of our clusters, we have two low frequencies to work with. A wider range of frequencies might enable us to model our galaxies better, perhaps including the likes of LOFAR or TGSS[1] for even lower frequencies, and the JVLA for the broadband higher frequencies. The need to match resolutions and uv–coverage is an important point to note, to ensure that the comparisons between the frequencies are valid. We would also be able to create spectral age maps for all of our interesting sources, where we would also have more data points to look

---

[1] The TIFR GMRT Sky Survey: `http://tgss.ncra.tifr.res.in`

at the difference between different synchrotron models. There are many exciting prospects for our images in Chapter 5, we found some interesting features that would be worth pursuing and would benefit from further observations.

Further work on would include looking at the differences between satellite and central galaxies with respect to their fractions and energetics. Best et al. (2007) showed that BCGs are more likely to be radio-loud than other galaxies, but how do the fraction and the energetics differ when looking at brightest groups galaxies and satellite galaxies? As part of this work, we took an initial look at relevant simulations needed to explore this area. We would like to interact more closely with simulations, so that incorporation of our observational results would result in further advances in simulations.

Our work on the non-central galaxies was for four of the galaxy clusters in our sample. A natural extension of this work would be to acquire multiwavelength data for the rest of the sample, and explore further the energetics and interactions of cluster AGN.

Appendix A

Synchrotron model fits

We show the KP model fits to the radio spectra of our sample using the BRATS software package. Fluxes and frequencies are taken from our observations as well as from the literature. This procedure is outlined in §4.2.

This work made use of R (R Core Team, 2013) and the ggplot2 (Wickham, 2009) package. We thank the staff of the GMRT that made these observations possible. GMRT is run by the National Centre for Radio Astrophysics of the Tata Institute of Fundamental Research.

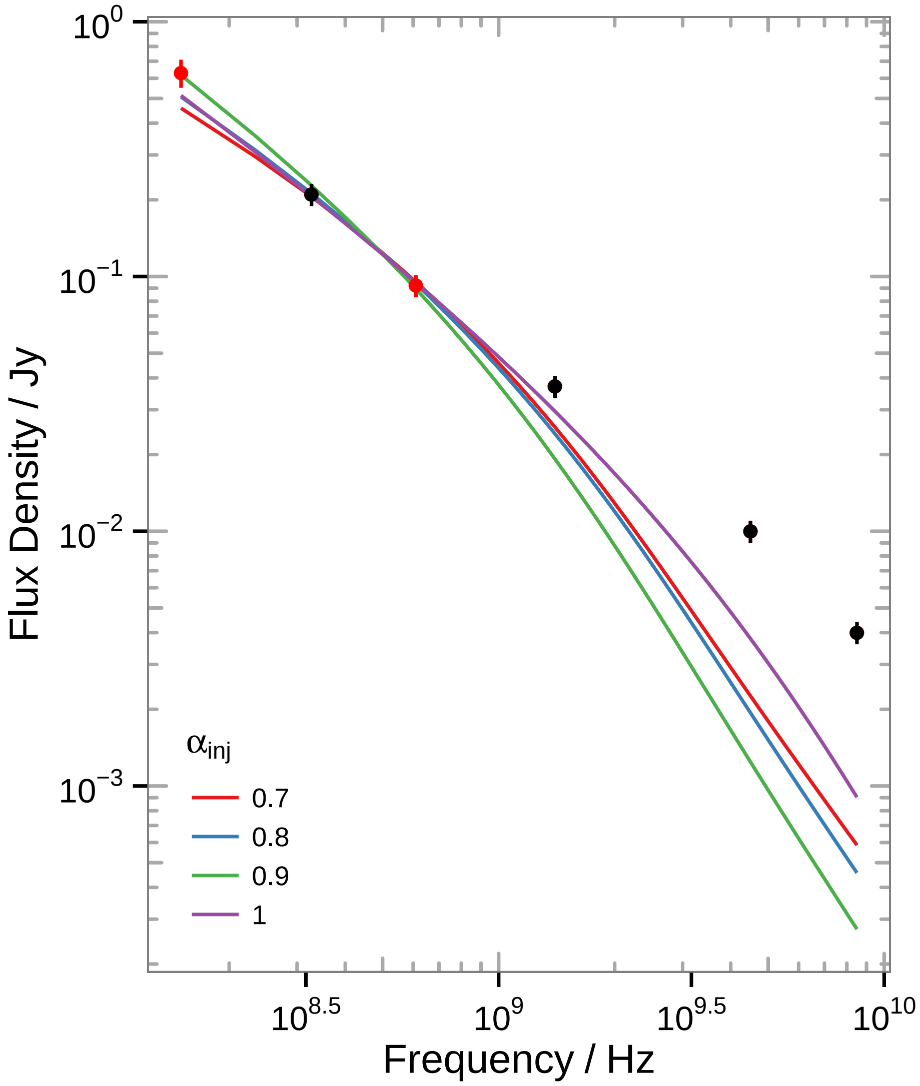

Figure A.1: 2A0335: A sample of KP models with different injection indices and $B = 2.9\,\mu$G, no acceptable solution was found due to steepening at low frequencies.

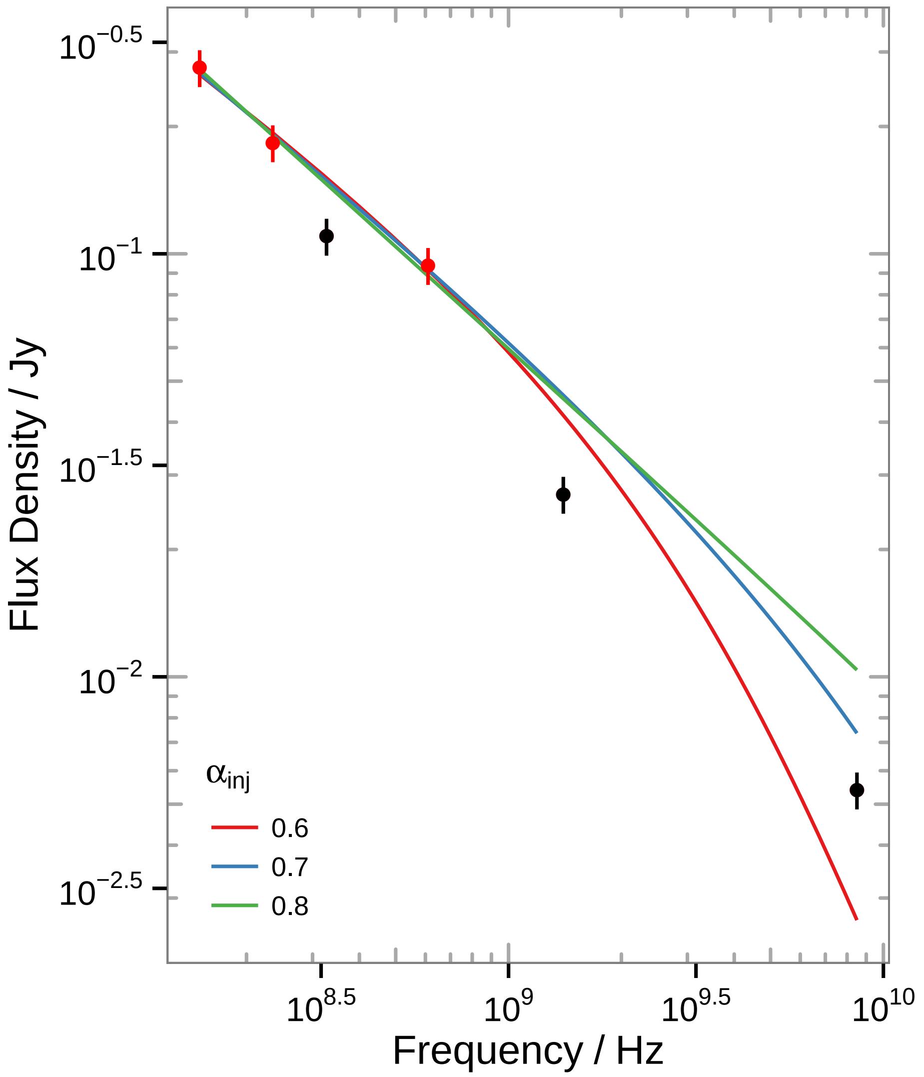

Figure A.2: A478: A sample of KP models with different injection indices and $B = 4.4\,\mu\text{G}$, this returns a result of 17.7 Myr for the synchrotron age.

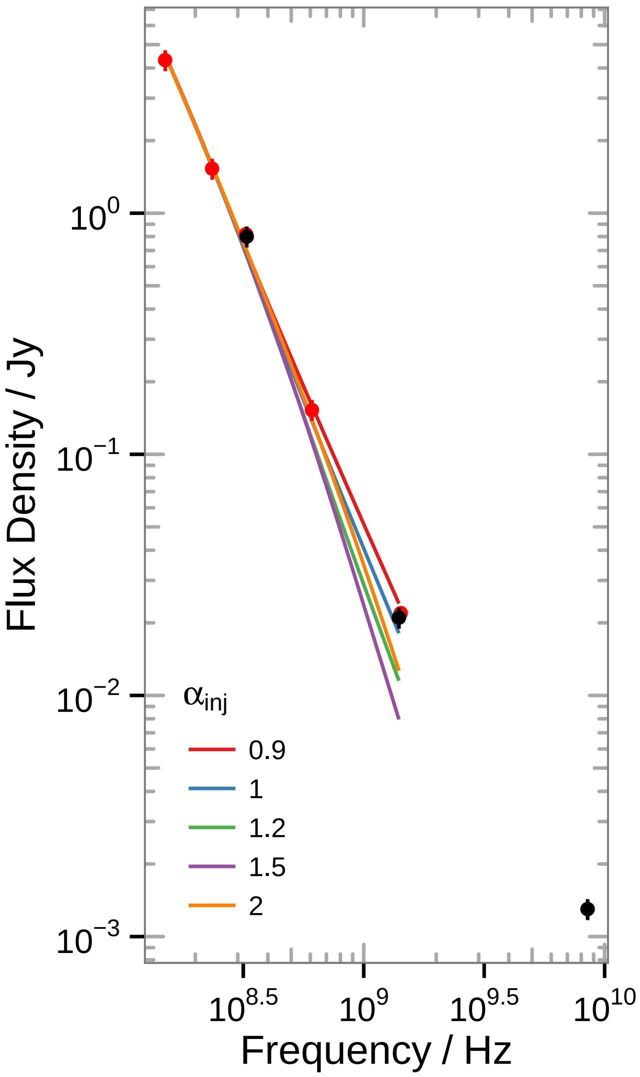

Figure A.3: MS0735: A sample of KP models with different injection indices and $B = 5.4\,\mu G$, this returns a result of 164 Myr for the synchrotron age.

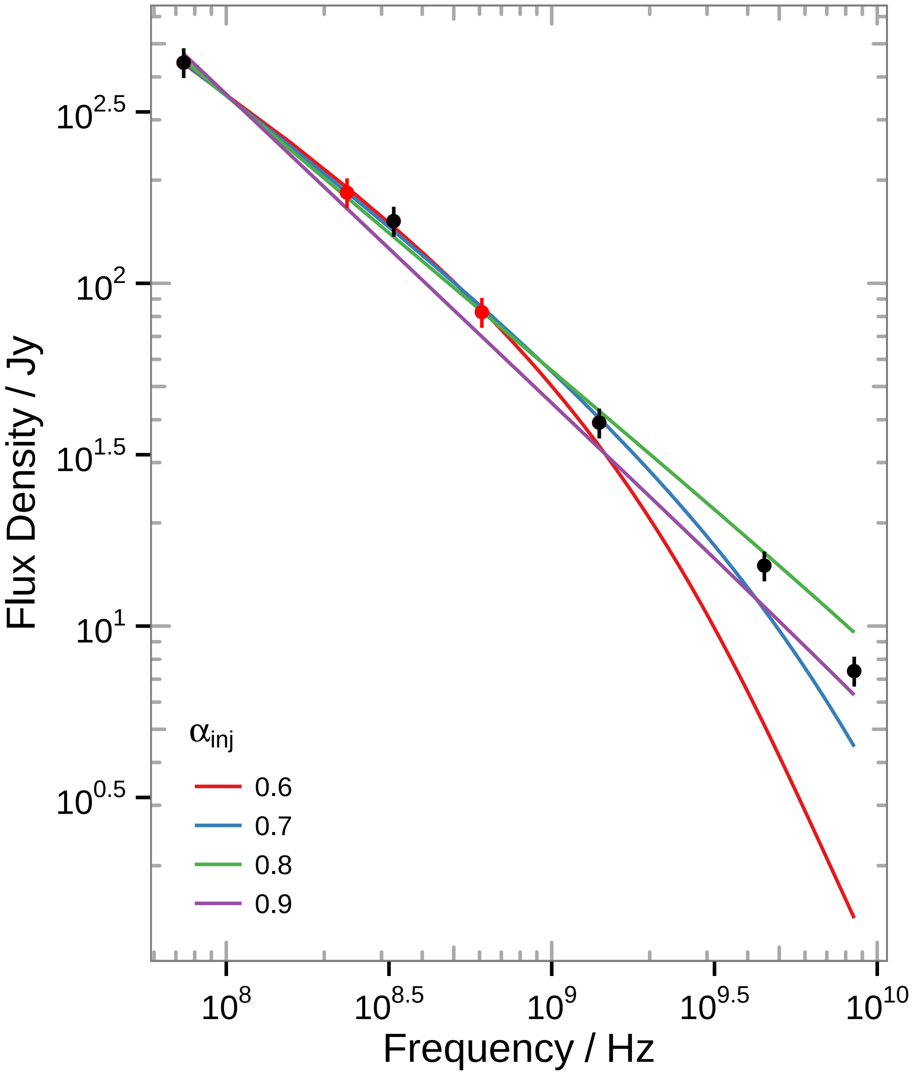

Figure A.4: Hydra A: A sample of KP models with different injection indices and $B = 3.4\,\mu$G, this returns a result of 30.9 Myr for the synchrotron age.

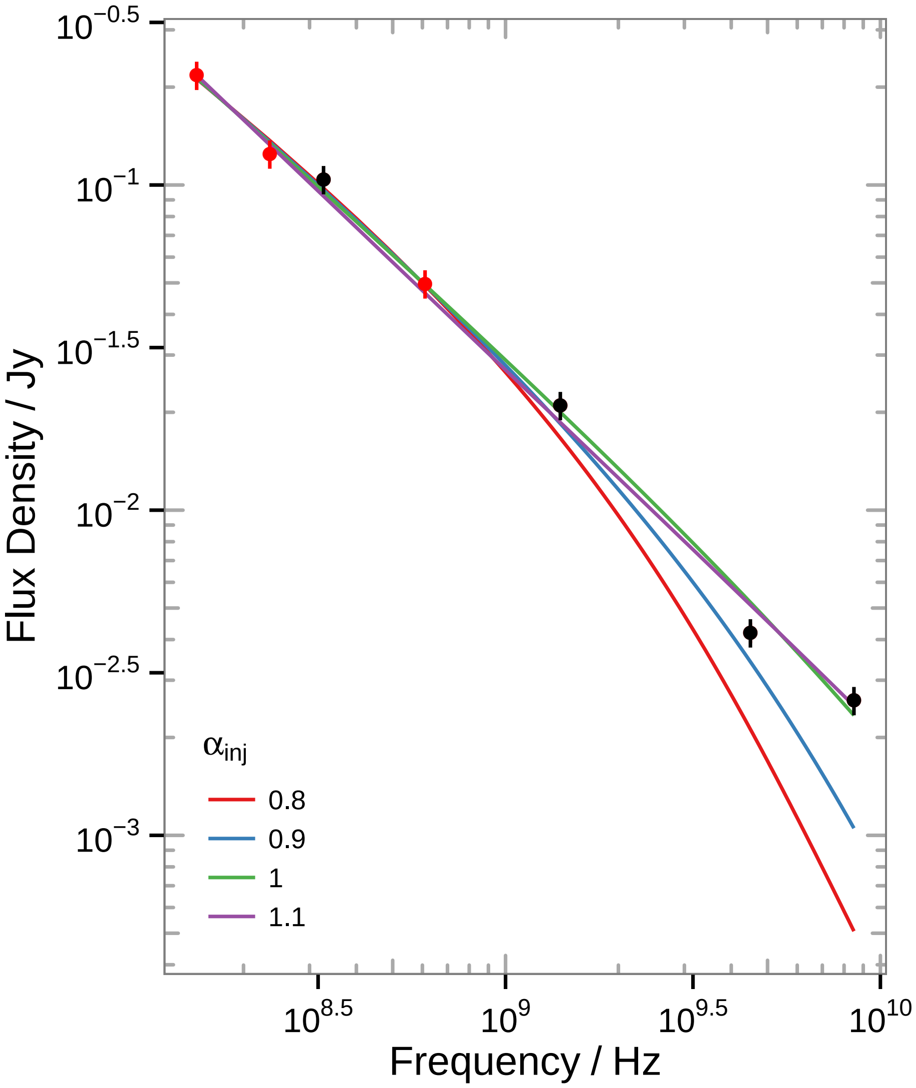

Figure A.5: RBS797: A sample of KP models with different injection indices and $B = 2.8\,\mu$G, this returns a result of 6.1 Myr for the synchrotron age.

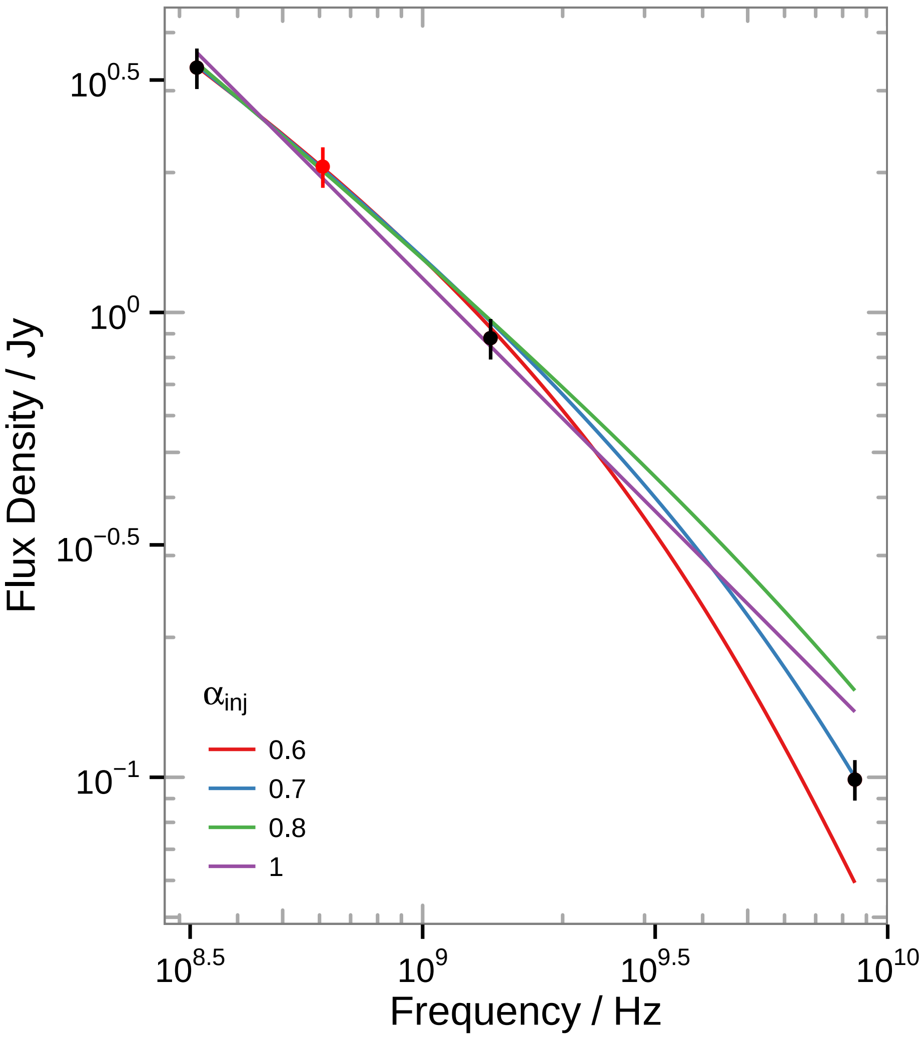

Figure A.6: A1795: A sample of KP models with different injection indices and $B = 9.6\,\mu\mathrm{G}$, this returns a result of 12.4 Myr for the synchrotron age.

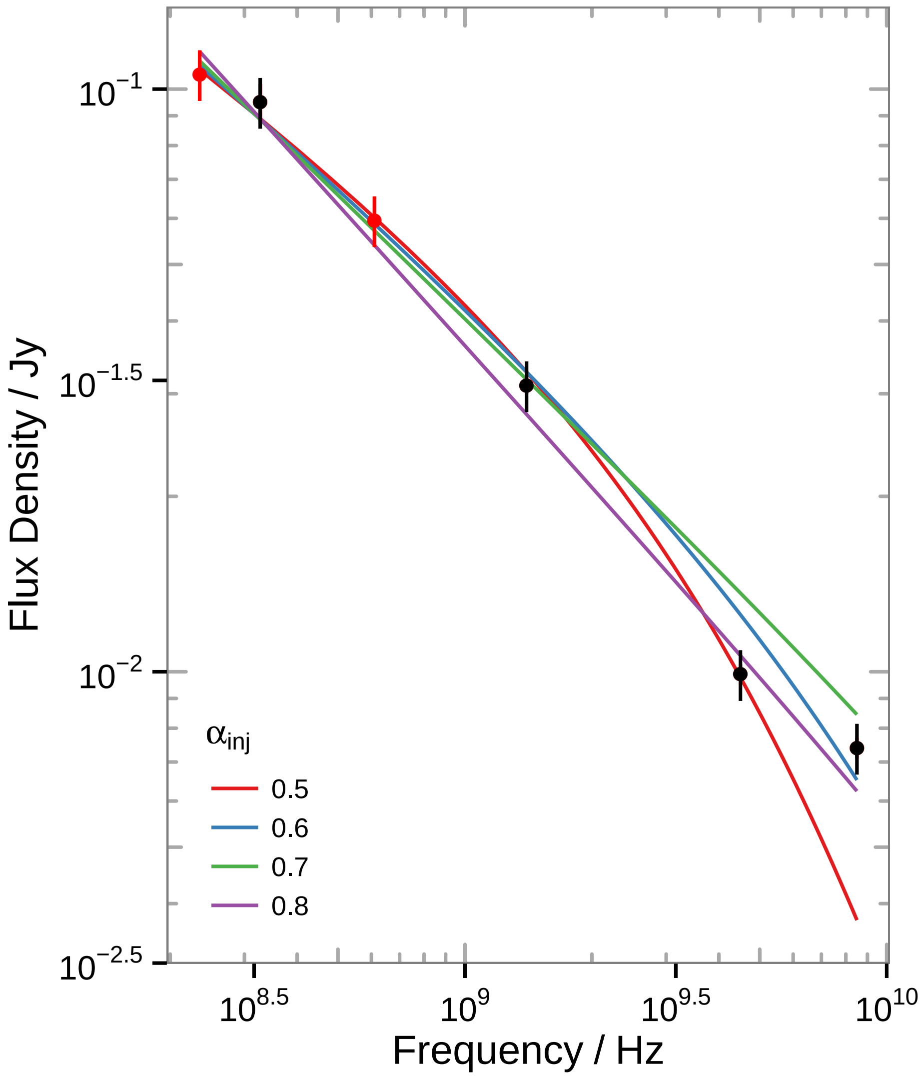

Figure A.7: A1835: A sample of KP models with different injection indices and $B = 3.3\,\mu$G, this returns a result of 14.5 Myr for the synchrotron age.

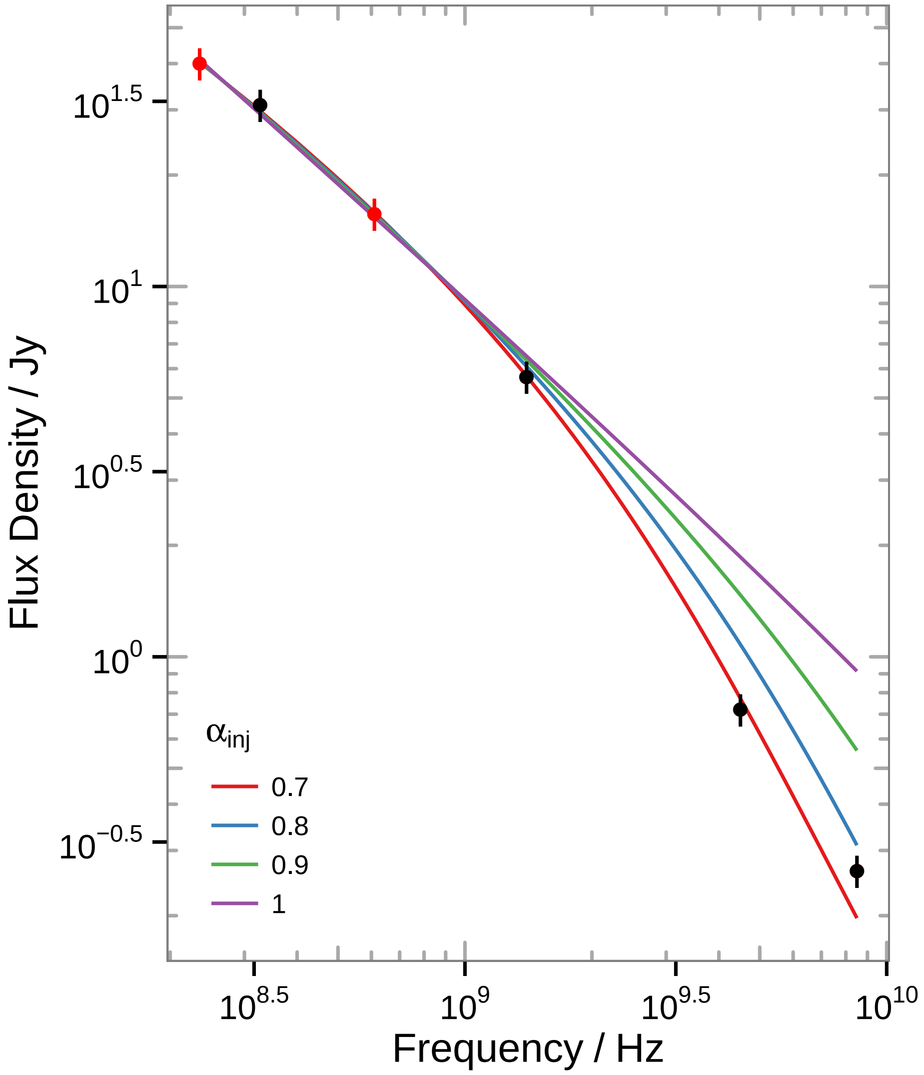

Figure A.8: A2052: A sample of KP models with different injection indices and $B = 8.6\,\mu$G, this returns a result of 19.1 Myr for the synchrotron age.

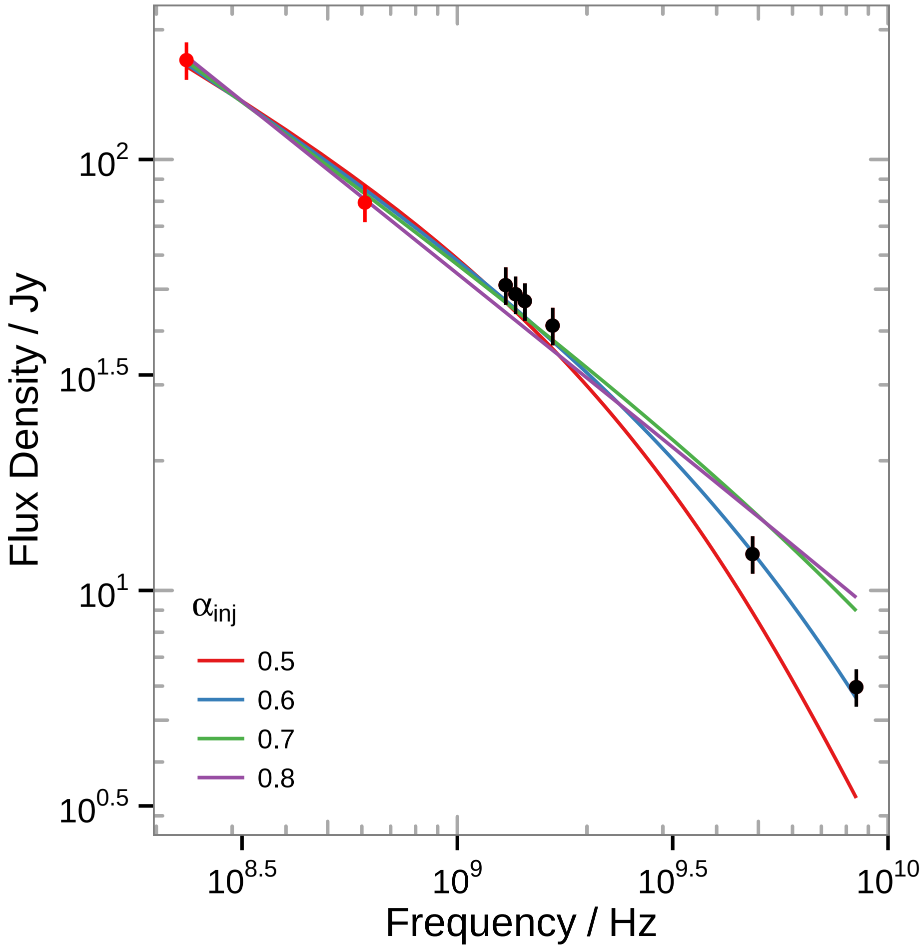

Figure A.9: Hercules A: A sample of KP models with different injection indices and $B = 6.3\,\mu G$, this returns a result of 8.3 Myr for the synchrotron age.

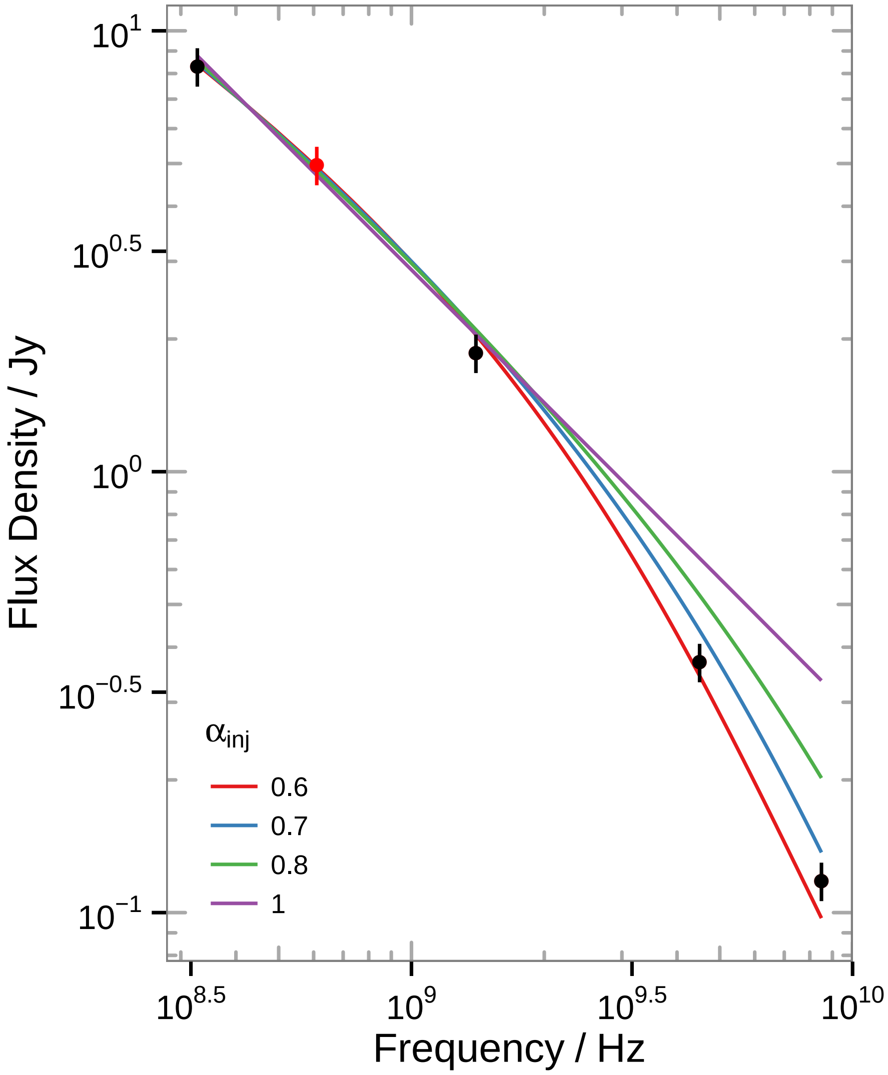

Figure A.10: A2597: A sample of KP models with different injection indices and $B = 12.4\,\mu$G, this returns a result of 11.8 Myr for the synchrotron age.

List of References

M. G. Akritas and M. A. Bershady. Linear Regression for Astronomical Data with Measurement Errors and Intrinsic Scatter. *ApJ*, 470:706, Oct. 1996. doi: 10.1086/177901.

D. M. Alexander and R. C. Hickox. What Drives the Growth of Black Holes? *New Astronomy Reviews*, 56:93–121, June 2012. doi: 10.1016/j.newar.2011.11.003.

M. Alpaslan, A. S. G. Robotham, S. Driver, P. Norberg, I. Baldry, A. E. Bauer, J. Bland-Hawthorn, M. Brown, M. Cluver, M. Colless, C. Foster, A. Hopkins, E. Van Kampen, L. Kelvin, M. A. Lara-Lopez, J. Liske, A. R. Lopez-Sanchez, J. Loveday, T. McNaught-Roberts, A. Merson, and K. Pimbblet. Galaxy And Mass Assembly (GAMA): the large-scale structure of galaxies and comparison to mock universes. *MNRAS*, 438:177–194, Feb. 2014. doi: 10.1093/mnras/stt2136.

R. Antonucci. Unified models for active galactic nuclei and quasars. *ARA&A*, 31:473–521, 1993. doi: 10.1146/annurev.aa.31.090193.002353.

Y. Ascasibar and J. M. Diego. A phenomenological model of galaxy clusters. *MNRAS*, 383:369–374, Jan. 2008. doi: 10.1111/j.1365-2966.2007.12546.x.

R. M. Athreya, V. K. Kapahi, P. J. McCarthy, and W. van Breugel. Steep- spectrum radio cores in high-redshift galaxies. *MNRAS*, 289:525–534, Aug. 1997.

S. A. Balbus and J. F. Hawley. A powerful local shear instability in weakly magnetized disks. I - Linear analysis. II - Nonlinear evolution. *ApJ*, 376:214–233, July 1991. doi: 10.1086/170270.

A. J. Barth. Black Holes in Active Galaxies. *Coevolution of Black Holes and Galaxies*, page 21, 2004.

A. Basu, S. Roy, and D. Mitra. Low frequency radio-FIR correlation in normal galaxies at ˜1 kpc scales. *ArXiv e-prints*, July 2012.

R. Beck and M. Krause. Revised equipartition and minimum energy formula for magnetic field strength estimates from radio synchrotron observations. *Astronomische Nachrichten*, 326:414–427, July 2005. doi: 10.1002/asna.200510366.

R. H. Becker, R. L. White, and D. J. Helfand. The FIRST Survey: Faint Images of the Radio Sky at Twenty Centimeters. *ApJ*, 450:559, Sept. 1995. doi: 10.1086/176166.

M. C. Begelman, R. D. Blandford, and M. J. Rees. Theory of extragalactic radio sources. *Reviews of Modern Physics*, 56:255–351, Apr. 1984. doi: 10.1103/RevModPhys.56.255.

E. F. Bell. Estimating Star Formation Rates from Infrared and Radio Luminosities: The Origin of the Radio-Infrared Correlation. *ApJ*, 586:794–813, Apr. 2003. doi: 10.1086/367829.

E. F. Bell, D. H. McIntosh, N. Katz, and M. D. Weinberg. The Optical and Near-Infrared Properties of Galaxies. I. Luminosity and Stellar Mass Functions. *ApJS*, 149:289–312, Dec. 2003. doi: 10.1086/378847.

A. J. Benson, R. G. Bower, C. S. Frenk, C. G. Lacey, C. M. Baugh, and S. Cole. What Shapes the Luminosity Function of Galaxies? *The Astrophysical Journal*, 599:38–49, Dec. 2003. doi: 10.1086/379160.

P. N. Best. The environmental dependence of radio-loud AGN activity and star formation in the 2dFGRS. *MNRAS*, 351:70–82, June 2004. doi: 10.1111/j.1365-2966.2004.07752.x.

P. N. Best and T. M. Heckman. On the fundamental dichotomy in the local radio-AGN population: accretion, evolution, and host galaxy properties. *MNRAS*, 421:1569–1582, Apr. 2012. doi: 10.1111/j.1365-2966.2012.20414.x.

P. N. Best, G. Kauffmann, T. M. Heckman, J. Brinchmann, S. Charlot, Ž. Ivezić, and S. D. M. White. The host galaxies of radio-loud active galactic nuclei: mass dependences, gas cooling and active galactic nuclei feedback. *MNRAS*, 362:25–40, Sept. 2005a. doi: 10.1111/j.1365-2966.2005.09192.x.

P. N. Best, G. Kauffmann, T. M. Heckman, and Ž. Ivezić. A sample of radio-loud active galactic nuclei in the Sloan Digital Sky Survey. *MNRAS*, 362:9–24, Sept. 2005b. doi: 10.1111/j.1365-2966.2005.09283.x.

P. N. Best, C. R. Kaiser, T. M. Heckman, and G. Kauffmann. AGN-controlled cooling in elliptical galaxies. *MNRAS*, 368:L67–L71, May 2006. doi: 10.1111/j.1745-3933.2006.00159.x.

P. N. Best, A. von der Linden, G. Kauffmann, T. M. Heckman, and C. R. Kaiser. On the prevalence of radio-loud active galactic nuclei in brightest cluster galaxies: implications for AGN heating of cooling flows. *MNRAS*, 379:894–908, Aug. 2007. doi: 10.1111/j.1365-2966.2007.11937.x.

P. N. Best, L. M. Ker, C. Simpson, E. E. Rigby, and J. Sabater. The cosmic evolution of radio-AGN feedback to z = 1. *MNRAS*, 445:955–969, Nov. 2014. doi: 10.1093/mnras/stu1776.

M. Birkinshaw. A deep survey of Abell 2218 at 408 and 1407 MHz - 5C 20. *MNRAS*, 222:731–751, Oct. 1986.

M. Birkinshaw. The Sunyaev-Zel'dovich effect. *Physics Reports*, 310:97–195, Mar. 1999. doi: 10.1016/S0370-1573(98)00080-5.

L. Bîrzan, D. A. Rafferty, B. R. McNamara, M. W. Wise, and P. E. J. Nulsen. A Systematic Study of Radio-induced X-Ray Cavities in Clusters, Groups, and Galaxies. *ApJ*, 607:800–809, June 2004. doi: 10.1086/383519.

L. Bîrzan, B. R. McNamara, P. E. J. Nulsen, C. L. Carilli, and M. W. Wise. Radiative Efficiency and Content of Extragalactic Radio Sources: Toward a Universal Scaling Relation between Jet Power and Radio Power. *ApJ*, 686:859–880, Oct. 2008. doi: 10.1086/591416.

R. D. Blandford and M. C. Begelman. On the fate of gas accreting at a low rate on to a black hole. *MNRAS*, 303:L1–L5, Feb. 1999. doi: 10.1046/j.1365-8711.1999.02358.x.

R. D. Blandford and C. F. McKee. Reverberation mapping of the emission line regions of Seyfert galaxies and quasars. *ApJ*, 255:419–439, Apr. 1982. doi: 10.1086/159843.

E. L. Blanton, S. W. Randall, T. E. Clarke, C. L. Sarazin, B. R. McNamara, E. M. Douglass, and M. McDonald. A Very Deep Chandra Observation of A2052: Bubbles, Shocks, and Sloshing. *ApJ*, 737:99–+, Aug. 2011. doi: 10.1088/0004-637X/737/2/99.

H. Böhringer, K. Matsushita, E. Churazov, Y. Ikebe, and Y. Chen. The new emerging model for the structure of cooling cores in clusters of galaxies. *A&A*, 382:804–820, Feb. 2002. doi: 10.1051/0004-6361:20011708.

B. Boroson, D.-W. Kim, and G. Fabbiano. Revisiting with Chandra the Scaling Relations of the X-ray Emission Components (Binaries, Nuclei, and Hot Gas) of Early-type Galaxies. *ApJ*, 729:12, Mar. 2011. doi: 10.1088/0004-637X/729/1/12.

W. N. Brandt and D. M. Alexander. Supermassive black-hole growth over cosmic time: Active galaxy demography, physics, and ecology from Chandra surveys. *Proceedings of the National Academy of Science*, 107:7184–7189, Apr. 2010. doi: 10.1073/pnas.0914151107.

A. H. Bridle and R. A. Perley. Extragalactic Radio Jets. *ARA&A*, 22:319–358, 1984. doi: 10.1146/annurev.aa.22.090184.001535.

D. Briggs. *High Fidelity Deconvolution of Moderately Resolved Sources.* PhD thesis, The New Mexico Institute of Mining and Technology, Socorro, New Mexico, 1995.

S. Buttiglione, A. Capetti, A. Celotti, D. J. Axon, M. Chiaberge, F. D. Macchetto, and W. B. Sparks. An optical spectroscopic survey of the 3CR sample of radio galaxies with $z < 0.3$. II. Spectroscopic classes and accretion modes in radio-loud AGN. *A&A*, 509:A6, Jan. 2010. doi: 10.1051/0004-6361/200913290.

C. L. Carilli, R. A. Perley, J. W. Dreher, and J. P. Leahy. Multifrequency radio observations of Cygnus A - Spectral aging in powerful radio galaxies. *ApJ*, 383:554–573, Dec. 1991. doi: 10.1086/170813.

J. E. Carlstrom, G. P. Holder, and E. D. Reese. Cosmology with the Sunyaev-Zel'dovich Effect. *ARA&A*, 40:643–680, 2002. doi: 10.1146/annurev.astro.40.060401.093803.

K. W. Cavagnolo, M. Donahue, G. M. Voit, and M. Sun. Intracluster Medium Entropy Profiles for a Chandra Archival Sample of Galaxy Clusters. *ApJS*, 182:12–32, May 2009. doi: 10.1088/0067-0049/182/1/12.

K. W. Cavagnolo, B. R. McNamara, P. E. J. Nulsen, C. L. Carilli, C. Jones, and L. Bîrzan. A Relationship Between AGN Jet Power and Radio Power. *ApJ*, 720:1066–1072, Sept. 2010. doi: 10.1088/0004-637X/720/2/1066.

P. Chandra, A. Ray, and S. Bhatnagar. Synchrotron Aging and the Radio Spectrum of SN 1993J. *ApJL*, 604:L97–L100, Apr. 2004. doi: 10.1086/383615.

J. N. Chengalur, Y. Gupta, and K. S. Dwarakanath. *Low Frequency Radio Astronomy.* 3rd edition, 2007.

E. Churazov, M. Brüggen, C. R. Kaiser, H. Böhringer, and W. Forman. Evolution of Buoyant Bubbles in M87. *ApJ*, 554:261–273, June 2001. doi: 10.1086/321357.

B. G. Clark. Interferometers and Coherence Theory. In J. A. Zensus, P. J. Diamond, and P. J. Napier, editors, *Very Long Baseline Interferometry and the VLBA*, volume 82 of *Astronomical Society of the Pacific Conference Series*, page 3, 1995.

B. G. Clark. Coherence in Radio Astronomy. In G. B. Taylor, C. L. Carilli, and R. A. Perley, editors, *Synthesis Imaging in Radio Astronomy II*, volume 180 of *Astronomical Society of the Pacific Conference Series*, page 1, 1999.

T. E. Clarke, C. L. Sarazin, E. L. Blanton, D. M. Neumann, and N. E. Kassim. Low-Frequency Radio Observations of X-Ray Ghost Bubbles in A2597: A History of Radio Activity in the Core. *ApJ*, 625:748–753, June 2005. doi: 10.1086/429717.

A. S. Cohen, T. E. Clarke, L. Feretti, and N. E. Kassim. Resolving the Steep-Spectrum Emission in the Central Radio Source in ZwCl 0735.7+7421. *ApJL*, 620:L5–L8, Feb. 2005. doi: 10.1086/428572.

J. J. Condon. Radio emission from normal galaxies. *ARAA*, 30:575–611, 1992. doi: 10.1146/annurev.aa.30.090192.003043.

J. J. Condon, W. D. Cotton, E. W. Greisen, Q. F. Yin, R. A. Perley, G. B. Taylor, and J. J. Broderick. The NRAO VLA Sky Survey. *AJ*, 115:1693–1716, May 1998. doi: 10.1086/300337.

J. H. Croston and M. J. Hardcastle. The particle content of low-power radio galaxies in groups and clusters. *MNRAS*, 438:3310–3321, Mar. 2014. doi: 10.1093/mnras/stt2436.

O. Czoske. Wide-field spectroscopy of A1689 and A1835 with VIMOS: first results. In A. Diaferio, editor, *IAU Colloq. 195: Outskirts of Galaxy Clusters: Intense Life in the Suburbs*, pages 183–187, July 2004. doi: 10.1017/S1743921304000390.

C. R. D'Angelo, J. K. Fridriksson, C. Messenger, and A. Patruno. The radiative efficiency of a radiatively inefficient accretion flow. *arXiv*, Oct. 2014.

D. S. De Young. The deflection of cosmic jets. *ApJ*, 371:69–81, Apr. 1991. doi: 10.1086/169871.

D. S. De Young. The Particle Content of Extragalactic Jets. *ApJ*, 648:200–208, Sept. 2006. doi: 10.1086/505861.

A. Del Moro, D. M. Alexander, J. R. Mullaney, E. Daddi, M. Pannella, F. E. Bauer, A. Pope, M. Dickinson, D. Elbaz, P. D. Barthel, M. A. Garrett, W. N. Brandt, V. Charmandaris, R. R. Chary, K. Dasyra, R. Gilli, R. C. Hickox, H. S. Hwang, R. J. Ivison, S. Juneau, E. Le Floc'h, B. Luo, G. E. Morrison, E. Rovilos, M. T. Sargent, and Y. Q. Xue. GOODS-Herschel: radio-excess signature of hidden AGN activity in distant star-forming galaxies. *A&A*, 549: A59, Jan. 2013. doi: 10.1051/0004-6361/201219880.

K. D. Denney, B. M. Peterson, R. W. Pogge, A. Adair, D. W. Atlee, K. Au-Yong, M. C. Bentz, J. C. Bird, D. J. Brokofsky, E. Chisholm, M. L. Comins, M. Dietrich, V. T. Doroshenko, J. D. Eastman, Y. S. Efimov, S. Ewald, S. Ferbey, C. M. Gaskell, C. H. Hedrick, K. Jackson, S. A. Klimanov, E. S. Klimek, A. K. Kruse, A. Ladéroute, J. B. Lamb, K. Leighly, T. Minezaki, S. V. Nazarov, C. A. Onken, E. A. Petersen, P. Peterson, S. Poindexter, Y. Sakata, K. J. Schlesinger, S. G. Sergeev, N. Skolski, L. Stieglitz, J. J. Tobin, C. Unterborn, M. Vestergaard, A. E. Watkins, L. C. Watson, and Y. Yoshii. Reverberation Mapping Measurements of Black Hole Masses in Six Local Seyfert Galaxies. *ApJ*, 721: 715–737, Sept. 2010. doi: 10.1088/0004-637X/721/1/715.

M. Donahue, M. Sun, C. P. O'Dea, G. M. Voit, and K. W. Cavagnolo. Star Formation, Radio Sources, Cooling X-Ray Gas, and Galaxy Interactions in the Brightest Cluster Galaxy in 2A0335+096. *AJ*, 134:14–25, July 2007. doi: 10.1086/518230.

A. Doria, M. Gitti, S. Ettori, F. Brighenti, P. E. J. Nulsen, and B. R. McNamara. A Chandra-VLA Investigation of the X-Ray Cavity System and Radio Mini-Halo in the Galaxy Cluster RBS 797. *ApJ*, 753:47, July 2012. doi: 10.1088/0004-637X/753/1/47.

Y. Dubois, J. Devriendt, A. Slyz, and R. Teyssier. Self-regulated growth of supermassive black holes by a dual jet-heating active galactic nucleus feedback mechanism: methods, tests and implications for cosmological simulations. *MNRAS*, 420:2662–2683, Mar. 2012. doi: 10.1111/j.1365-2966.2011.20236.x.

R. J. H. Dunn and A. C. Fabian. Particle energies and filling fractions of radio bubbles in cluster cores. *MNRAS*, 355:862–873, Dec. 2004. doi: 10.1111/j.1365-2966.2004.08365.x.

R. J. H. Dunn, A. C. Fabian, and G. B. Taylor. Radio bubbles in clusters of galaxies. *MNRAS*, 364:1343–1353, Dec. 2005. doi: 10.1111/j.1365-2966.2005.09673.x.

A. A. Dutton and F. C. van den Bosch. The impact of feedback on disc galaxy scaling relations. *MNRAS*, 396: 141–164, June 2009. doi: 10.1111/j.1365-2966.2009.14742.x.

J. A. Eilek and F. N. Owen. Radio Galaxies in Cooling Cores: Insights from a Complete Sample. In H. Böhringer, G. W. Pratt, A. Finoguenov, and P. Schuecker, editors, *Heating versus Cooling in Galaxies and Clusters of Galaxies*, page 133, 2007. doi: 10.1007/978-3-540-73484-0_26.

S. C. Ellis and E. O'Sullivan. Correlations of near-infrared, optical and X-ray luminosity for early-type galaxies. *MNRAS*, 367:627–645, Apr. 2006. doi: 10.1111/j.1365-2966.2005.09982.x.

A. C. Fabian. Cooling Flows in Clusters of Galaxies. *Annual Review of Astronomy and Astrophysics*, 32:277–318, 1994. doi: 10.1146/annurev.aa.32.090194.001425.

A. C. Fabian. Observational Evidence of Active Galactic Nuclei Feedback. *Annual Review of Astronomy and Astrophysics*, 50:455–489, Sept. 2012. doi: 10.1146/annurev-astro-081811-125521.

A. C. Fabian and P. E. J. Nulsen. Subsonic accretion of cooling gas in clusters of galaxies. *Monthly Notices of the Royal Astronomical Society*, 180:479–484, Aug. 1977.

A. C. Fabian, R. F. Mushotzky, P. E. J. Nulsen, and J. R. Peterson. On the soft X-ray spectrum of cooling flows. *MNRAS*, 321:L20–L24, Feb. 2001. doi: 10.1046/j.1365-8711.2001.04285.x.

B. L. Fanaroff and J. M. Riley. The morphology of extragalactic radio sources of high and low luminosity. *Monthly Notices of the Royal Astronomical Society*, 167:31P–36P, May 1974.

K. Fathi, T. Storchi-Bergmann, R. A. Riffel, C. Winge, D. J. Axon, A. Robinson, A. Capetti, and A. Marconi. Streaming Motions toward the Supermassive Black Hole in NGC 1097. *ApJL*, 641:L25–L28, Apr. 2006. doi: 10.1086/503832.

L. Feretti and G. Giovannini. Galaxy clusters in the radio: Relativistic plasma and icm/radio galaxy interaction processes. *ArXiv e-prints*, 2007. doi: 10.1007/978-1-4020-6941-3_5.

L. Feretti, E. Orrù, G. Brunetti, G. Giovannini, N. Kassim, and G. Setti. Spectral index maps of the radio halos in Abell 665 and Abell 2163. *A&A*, 423:111–119, Aug. 2004. doi: 10.1051/0004-6361:20040316.

L. Feretti, G. Giovannini, F. Govoni, and M. Murgia. Clusters of galaxies: observational properties of the diffuse radio emission. *Astronomy and Astrophysics Review*, 20:54, May 2012. doi: 10.1007/s00159-012-0054-z.

C. A. C. Fernandes, M. J. Jarvis, A. Martínez-Sansigre, S. Rawlings, J. Afonso, M. J. Hardcastle, M. Lacy, J. A. Stevens, and E. Vardoulaki. Black hole masses, accretion rates and hot- and cold-mode accretion in radio galaxies at $z \sim 1$. *MNRAS*, 447:1184–1203, Feb. 2015. doi: 10.1093/mnras/stu2517.

L. Ferrarese and D. Merritt. A Fundamental Relation between Supermassive Black Holes and Their Host Galaxies. *ApJL*, 539:L9–L12, Aug. 2000. doi: 10.1086/312838.

I. Ferrero, M. G. Abadi, J. F. Navarro, L. V. Sales, and S. Gurovich. The dark matter haloes of dwarf galaxies: a challenge for the Λ cold dark matter paradigm? *MNRAS*, 425:2817–2823, Oct. 2012. doi: 10.1111/j.1365-2966.2012.21623.x.

E. Freeland and E. Wilcots. Intergalactic Gas in Groups of Galaxies: Implications for Dwarf Spheroidal Formation and the Missing Baryons Problem. *ApJ*, 738:145, Sept. 2011. doi: 10.1088/0004-637X/738/2/145.

K. Gebhardt, R. Bender, G. Bower, A. Dressler, S. M. Faber, A. V. Filippenko, R. Green, C. Grillmair, L. C. Ho, J. Kormendy, T. R. Lauer, J. Magorrian, J. Pinkney, D. Richstone, and S. Tremaine. A Relationship between Nuclear Black Hole Mass and Galaxy Velocity Dispersion. *ApJL*, 539:L13–L16, Aug. 2000. doi: 10.1086/312840.

A. M. Ghez, S. Salim, N. N. Weinberg, J. R. Lu, T. Do, J. K. Dunn, K. Matthews, M. R. Morris, S. Yelda, E. E. Becklin, T. Kremenek, M. Milosavljevic, and J. Naiman. Measuring Distance and Properties of the Milky Way's Central Supermassive Black Hole with Stellar Orbits. *ApJ*, 689:1044–1062, Dec. 2008. doi: 10.1086/592738.

S. Giacintucci, M. Markevitch, T. Venturi, T. E. Clarke, R. Cassano, and P. Mazzotta. New Detections of Radio Minihalos in Cool Cores of Galaxy Clusters. *ApJ*, 781:9, Jan. 2014. doi: 10.1088/0004-637X/781/1/9.

S. Gillessen, F. Eisenhauer, S. Trippe, T. Alexander, R. Genzel, F. Martins, and T. Ott. Monitoring Stellar Orbits Around the Massive Black Hole in the Galactic Center. *ApJ*, 692:1075–1109, Feb. 2009. doi: 10.1088/0004-637X/692/2/1075.

G. Giovannini and L. Feretti. Halo and relic sources in clusters of galaxies. *New Astronomy*, 5:335–347, Sept. 2000. doi: 10.1016/S1384-1076(00)00034-8.

M. Gitti, L. Feretti, and S. Schindler. Multifrequency VLA radio observations of the X-ray cavity cluster of galaxies RBS797: evidence of differently oriented jets. *A&A*, 448:853–860, Mar. 2006. doi: 10.1051/0004-6361:20053998.

M. Gitti, F. Brighenti, and B. R. McNamara. Evidence for AGN Feedback in Galaxy Clusters and Groups. *Advances in Astronomy*, 2012, 2012. doi: 10.1155/2012/950641.

N. A. B. Gizani and J. P. Leahy. A multiband study of Hercules A - II. Multifrequency Very Large Array imaging. *MNRAS*, 342:399–421, June 2003. doi: 10.1046/j.1365-8711.2003.06469.x.

N. A. B. Gizani, A. Cohen, and N. E. Kassim. First results of the 74-MHz Very Large Array-Pie Town link. Hercules A at low frequencies. *MNRAS*, 358:1061–1068, Apr. 2005. doi: 10.1111/j.1365-2966.2005.08849.x.

F. Govoni, M. Murgia, M. Markevitch, L. Feretti, G. Giovannini, G. B. Taylor, and E. Carretti. A search for diffuse radio emission in the relaxed, cool-core galaxy clusters A1068, A1413, A1650, A1835, A2029, and Ophiuchus. *A&A*, 499:371–383, May 2009. doi: 10.1051/0004-6361/200811180.

D. A. Green. A colour scheme for the display of astronomical intensity images. *Bulletin of the Astronomical Society of India*, 39:289–295, June 2011.

C. P. Haines, M. J. Pereira, A. J. R. Sanderson, G. P. Smith, E. Egami, A. Babul, A. C. Edge, A. Finoguenov, S. M. Moran, and N. Okabe. LoCuSS: A Dynamical Analysis of X-Ray Active Galactic Nuclei in Local Clusters. *ApJ*, 754:97, Aug. 2012. doi: 10.1088/0004-637X/754/2/97.

C. P. Haines, M. J. Pereira, G. P. Smith, E. Egami, A. J. R. Sanderson, A. Babul, A. Finoguenov, P. Merluzzi, G. Busarello, T. D. Rawle, and N. Okabe. LoCuSS: The Steady Decline and Slow Quenching of Star Formation in Cluster Galaxies over the Last Four Billion Years. *ApJ*, 775:126, Oct. 2013. doi: 10.1088/0004-637X/775/2/126.

M. J. Hardcastle, D. A. Evans, and J. H. Croston. The X-ray nuclei of intermediate-redshift radio sources. *MNRAS*, 370:1893–1904, Aug. 2006. doi: 10.1111/j.1365-2966.2006.10615.x.

M. J. Hardcastle, D. A. Evans, and J. H. Croston. Hot and cold gas accretion and feedback in radio-loud active galaxies. *MNRAS*, 376:1849–1856, Apr. 2007. doi: 10.1111/j.1365-2966.2007.11572.x.

J. J. Harwood, M. J. Hardcastle, J. H. Croston, and J. L. Goodger. Spectral ageing in the lobes of FR-II radio galaxies: new methods of analysis for broad-band radio data. *MNRAS*, 435:3353–3375, Nov. 2013. doi: 10.1093/mnras/stt1526.

N. A. Hatch, C. S. Crawford, and A. C. Fabian. Ionized nebulae surrounding brightest cluster galaxies. *MNRAS*, 380:33–43, Sept. 2007. doi: 10.1111/j.1365-2966.2007.12009.x.

T. M. Heckman and P. N. Best. The Coevolution of Galaxies and Supermassive Black Holes: Insights from Surveys of the Contemporary Universe. *ARA&A*, 52:589–660, Aug. 2014. doi: 10.1146/annurev-astro-081913-035722.

R. G. Hine and M. S. Longair. Optical spectra of 3CR radio galaxies. *MNRAS*, 188:111–130, July 1979.

J. A. Högbom. Aperture Synthesis with a Non-Regular Distribution of Interferometer Baselines. *Astronomy and Astrophysics Supplement*, 15:417, June 1974.

D. J. Horner. *X-ray scaling laws for galaxy clusters and groups.* PhD thesis, University of Maryland College Park, 2001.

W. J. Jaffe and G. C. Perola. Dynamical Models of Tailed Radio Sources in Clusters of Galaxies. *A&A*, 26:423, Aug. 1973.

T. W. Jones and F. N. Owen. Hot gas in elliptical galaxies and the formation of head-tail radio sources. *ApJ*, 234: 818–824, Dec. 1979. doi: 10.1086/157561.

W. A. Joye and E. Mandel. New Features of SAOImage DS9. In H. E. Payne, R. I. Jedrzejewski, and R. N. Hook, editors, *Astronomical Data Analysis Software and Systems XII*, volume 295 of *Astronomical Society of the Pacific Conference Series*, page 489, 2003.

N. S. Kardashev. Nonstationarity of Spectra of Young Sources of Nonthermal Radio Emission. *Soviet Astronomy*, 6: 317, Dec. 1962.

S. Kaspi, W. N. Brandt, D. Maoz, H. Netzer, D. P. Schneider, and O. Shemmer. Reverberation Mapping of High-Luminosity Quasars: First Results. *ApJ*, 659:997–1007, Apr. 2007. doi: 10.1086/512094.

G. Kauffmann, T. M. Heckman, C. Tremonti, J. Brinchmann, S. Charlot, S. D. M. White, S. E. Ridgway, J. Brinkmann, M. Fukugita, P. B. Hall, Ž. Ivezić, G. T. Richards, and D. P. Schneider. The host galaxies of active galactic nuclei. *MNRAS*, 346:1055–1077, Dec. 2003. doi: 10.1111/j.1365-2966.2003.07154.x.

K. I. Kellermann and F. N. Owen. *Radio galaxies and quasars*, pages 563–602. 1988.

K. I. Kellermann and G. L. Verschuur. *Galactic and extragalactic radio astronomy (2nd edition).* 1988.

A. King. Black Holes, Galaxy Formation, and the M_{BH}-σ Relation. *ApJL*, 596:L27–L29, Oct. 2003. doi: 10.1086/379143.

J.-P. Kneib, R. S. Ellis, I. Smail, W. J. Couch, and R. M. Sharples. Hubble Space Telescope Observations of the Lensing Cluster Abell 2218. *ApJ*, 471:643–+, Nov. 1996. doi: 10.1086/177995.

J. Kormendy and L. C. Ho. Coevolution (or not) of supermassive black holes and host galaxies. *ARA&A*, 51: 511–653, Aug. 2013. doi: 10.1146/annurev-astro-082708-101811.

J. Kormendy and D. Richstone. Inward Bound—The Search For Supermassive Black Holes In Galactic Nuclei. *ARA&A*, 33:581, 1995. doi: 10.1146/annurev.aa.33.090195.003053.

J. H. Krolik. *Active galactic nuclei : from the central black hole to the galactic environment*. 1999.

B. C. Lacki and R. Beck. The equipartition magnetic field formula in starburst galaxies: accounting for pionic secondaries and strong energy losses. *MNRAS*, 430:3171–3186, Apr. 2013. doi: 10.1093/mnras/stt122.

R. A. Laing, C. R. Jenkins, J. V. Wall, and S. W. Unger. Spectrophotometry of a Complete Sample of 3CR Radio Sources: Implications for Unified Models. In G. V. Bicknell, M. A. Dopita, and P. J. Quinn, editors, *The Physics of Active Galaxies*, volume 54 of *Astronomical Society of the Pacific Conference Series*, page 201, 1994.

W. M. Lane, T. E. Clarke, G. B. Taylor, R. A. Perley, and N. E. Kassim. Hydra A at Low Radio Frequencies. *AJ*, 127: 48–52, Jan. 2004. doi: 10.1086/379858.

A. M. C. Le Brun, I. G. McCarthy, J. Schaye, and T. J. Ponman. Towards a realistic population of simulated galaxy groups and clusters. *MNRAS*, 441:1270–1290, June 2014. doi: 10.1093/mnras/stu608.

J.-T. Li and Q. D. Wang. Chandra survey of nearby highly inclined disc galaxies - II. Correlation analysis of galactic coronal properties. *MNRAS*, Sept. 2013. doi: 10.1093/mnras/stt1501.

Y.-T. Lin and J. J. Mohr. K-band Properties of Galaxy Clusters and Groups: Brightest Cluster Galaxies and Intracluster Light. *ApJ*, 617:879–895, Dec. 2004. doi: 10.1086/425412.

M. S. Longair. *Galaxy Formation*. Springer, 2008.

C.-J. Ma, B. R. McNamara, P. E. J. Nulsen, R. Schaffer, and A. Vikhlinin. Average Heating Rate of Hot Atmospheres in Distant Clusters by Radio Active Galactic Nucleus: Evidence for Continuous Active Galactic Nucleus Heating. *ApJ*, 740:51, Oct. 2011. doi: 10.1088/0004-637X/740/2/51.

J. Machalski, D. Kozieł-Wierzbowska, M. Jamrozy, and D. J. Saikia. J1420-0545: The Radio Galaxy Larger than 3C 236. *ApJ*, 679:149–155, May 2008. doi: 10.1086/586703.

J. Magorrian, S. Tremaine, D. Richstone, R. Bender, G. Bower, A. Dressler, S. M. Faber, K. Gebhardt, R. Green, C. Grillmair, J. Kormendy, and T. Lauer. The demography of massive dark objects in galaxy centres. *AJ*, 115: 2285, 1998. doi: 10.1086/300353.

E. Mandel, S. S. Murray, and J. Roll. Funtools: FITS Users Need Tools, Dec. 2011. Astrophysics Source Code Library.

A. Marconi, G. Risaliti, R. Gilli, L. K. Hunt, R. Maiolino, and M. Salvati. Local supermassive black holes, relics of active galactic nuclei and the X-ray background. *MNRAS*, 351:169–185, June 2004. doi: 10.1111/j.1365-2966.2004.07765.x.

M. Markevitch and A. Vikhlinin. Shocks and cold fronts in galaxy clusters. *Physics Reports*, 443:1–53, May 2007. doi: 10.1016/j.physrep.2007.01.001.

M. Markevitch, A. Vikhlinin, and P. Mazzotta. Nonhydrostatic Gas in the Core of the Relaxed Galaxy Cluster A1795. *ApJL*, 562:L153–L156, Dec. 2001. doi: 10.1086/337973.

P. Martini, J. S. Mulchaey, and D. D. Kelson. The Distribution of Active Galactic Nuclei in Clusters of Galaxies. *ApJ*, 664:761–776, Aug. 2007. doi: 10.1086/519158.

W. G. Mathews, F. Brighenti, A. Faltenbacher, D. A. Buote, P. J. Humphrey, F. Gastaldello, and L. Zappacosta. Large Scatter in X-Ray Emission among Elliptical Galaxies: Correlations with Mass of Host Halo. *ApJL*, 652:L17–L20, Nov. 2006. doi: 10.1086/509915.

P. Mazzotta and S. Giacintucci. Do Radio Core-Halos and Cold Fronts in Non-Major-Merging Clusters Originate from the Same Gas Sloshing? *ApJL*, 675:L9–L12, Mar. 2008. doi: 10.1086/529433.

P. Mazzotta, A. C. Edge, and M. Markevitch. A Chandra Study of the Complex Structure in the Core of 2A 0335+096. *ApJ*, 596:190–203, Oct. 2003. doi: 10.1086/377633.

I. G. McCarthy, A. M. C. Le Brun, J. Schaye, and G. P. Holder. The thermal Sunyaev-Zel'dovich effect power spectrum in light of Planck. *MNRAS*, 440:3645–3657, June 2014. doi: 10.1093/mnras/stu543.

B. R. McNamara and P. E. J. Nulsen. Heating Hot Atmospheres with Active Galactic Nuclei. *Annual Review of Astronomy and Astrophysics*, 45:117–175, Sept. 2007. doi: 10.1146/annurev.astro.45.051806.110625.

B. R. McNamara, M. Wise, P. E. J. Nulsen, L. P. David, C. L. Sarazin, M. Bautz, M. Markevitch, A. Vikhlinin, W. R. Forman, C. Jones, and D. E. Harris. Chandra X-Ray Observations of the Hydra A Cluster: An Interaction between the Radio Source and the X-Ray-emitting Gas. *ApJL*, 534:L135–L138, May 2000. doi: 10.1086/312662.

B. R. McNamara, M. W. Wise, P. E. J. Nulsen, L. P. David, C. L. Carilli, C. L. Sarazin, C. P. O'Dea, J. Houck, M. Donahue, S. Baum, M. Voit, R. W. O'Connell, and A. Koekemoer. Discovery of Ghost Cavities in the X-Ray Atmosphere of Abell 2597. *ApJL*, 562:L149–L152, Dec. 2001. doi: 10.1086/338326.

B. R. McNamara, P. E. J. Nulsen, M. W. Wise, D. A. Rafferty, C. Carilli, C. L. Sarazin, and E. L. Blanton. The heating of gas in a galaxy cluster by X-ray cavities and large-scale shock fronts. *Nature*, 433:45–47, Jan. 2005. doi: 10.1038/nature03202.

B. R. McNamara, D. A. Rafferty, L. Bîrzan, J. Steiner, M. W. Wise, P. E. J. Nulsen, C. L. Carilli, R. Ryan, and M. Sharma. The Starburst in the Abell 1835 Cluster Central Galaxy: A Case Study of Galaxy Formation Regulated by an Outburst from a Supermassive Black Hole. *ApJ*, 648:164–175, Sept. 2006. doi: 10.1086/505859.

B. R. McNamara, F. Kazemzadeh, D. A. Rafferty, L. Bîrzan, P. E. J. Nulsen, C. C. Kirkpatrick, and M. W. Wise. An Energetic AGN Outburst Powered by a Rapidly Spinning Supermassive Black Hole or an Accreting Ultramassive Black Hole. *ApJ*, 698:594–605, June 2009. doi: 10.1088/0004-637X/698/1/594.

A. Merloni. The anti-hierarchical growth of supermassive black holes. *MNRAS*, 353:1035–1047, Oct. 2004. doi: 10.1111/j.1365-2966.2004.08147.x.

B. Mingo, M. J. Hardcastle, J. H. Croston, D. Dicken, D. A. Evans, R. Morganti, and C. Tadhunter. An X-ray survey of the 2 Jy sample - I. Is there an accretion mode dichotomy in radio-loud AGN? *MNRAS*, 440:269–297, May 2014. doi: 10.1093/mnras/stu263.

A. J. Mioduszewski, V. V. Dwarkadas, and L. Ball. Simulated Radio Images and Light Curves of Young Supernovae. *ApJ*, 562:869–879, Dec. 2001. doi: 10.1086/323852.

R. Mittal, D. S. Hudson, T. H. Reiprich, and T. Clarke. AGN heating and ICM cooling in the HIFLUGCS sample of galaxy clusters. *A&A*, 501:835–850, July 2009. doi: 10.1051/0004-6361/200810836.

M. Mościbrodzka and H. Falcke. Coupled jet-disk model for Sagittarius A*: explaining the flat-spectrum radio core with GRMHD simulations of jets. *A&A*, 559:L3, Nov. 2013. doi: 10.1051/0004-6361/201322692.

B. P. Moster, R. S. Somerville, C. Maulbetsch, F. C. van den Bosch, A. V. Macciò, T. Naab, and L. Oser. Constraints on the Relationship between Stellar Mass and Halo Mass at Low and High Redshift. *ApJ*, 710:903–923, Feb. 2010. doi: 10.1088/0004-637X/710/2/903.

R. Narayan and I. Yi. Advection-dominated Accretion: Underfed Black Holes and Neutron Stars. *ApJ*, 452:710, Oct. 1995. doi: 10.1086/176343.

P. E. J. Nulsen, L. P. David, B. R. McNamara, C. Jones, W. R. Forman, and M. Wise. Interaction of Radio Lobes with the Hot Intracluster Medium: Driving Convective Outflow in Hydra A. *ApJ*, 568:163–173, Mar. 2002. doi: 10.1086/338494.

P. E. J. Nulsen, D. C. Hambrick, B. R. McNamara, D. Rafferty, L. Birzan, M. W. Wise, and L. P. David. The Powerful Outburst in Hercules A. *ApJL*, 625:L9–L12, May 2005a. doi: 10.1086/430945.

P. E. J. Nulsen, B. R. McNamara, M. W. Wise, and L. P. David. The Cluster-Scale AGN Outburst in Hydra A. *ApJ*, 628:629–636, Aug. 2005b. doi: 10.1086/430845.

A. Nusser, J. Silk, and A. Babul. Suppressing cluster cooling flows by self-regulated heating from a spatially distributed population of active galactic nuclei. *MNRAS*, 373:739–746, Dec. 2006. doi: 10.1111/j.1365-2966.2006.11061.x.

C. P. O'Dea and F. N. Owen. Astrophysical implications of the multifrequency VLA observations of NGC 1265. *ApJ*, 316:95–112, May 1987. doi: 10.1086/165182.

N. Okabe, M. Takada, K. Umetsu, T. Futamase, and G. P. Smith. LoCuSS: Subaru Weak Lensing Study of 30 Galaxy Clusters. *PASJ*, 62:811–870, June 2010.

C. A. Onken, M. Valluri, J. S. Brown, P. J. McGregor, B. M. Peterson, M. C. Bentz, L. Ferrarese, R. W. Pogge, M. Vestergaard, T. Storchi-Bergmann, and R. A. Riffel. The Black Hole Mass of NGC 4151. II. Stellar Dynamical Measurement from Near-infrared Integral Field Spectroscopy. *ApJ*, 791:37, Aug. 2014. doi: 10.1088/0004-637X/791/1/37.

E. O'Sullivan, S. Giacintucci, L. P. David, M. Gitti, J. M. Vrtilek, S. Raychaudhury, and T. J. Ponman. Heating the Hot Atmospheres of Galaxy Groups and Clusters with Cavities: The Relationship between Jet Power and Low-frequency Radio Emission. *ApJ*, 735:11, July 2011. doi: 10.1088/0004-637X/735/1/11.

M. S. Owers, P. E. J. Nulsen, and W. J. Couch. Minor Merger-induced Cold Fronts in Abell 2142 and RXJ1720.1+2638. *ApJ*, 741:122, Nov. 2011. doi: 10.1088/0004-637X/741/2/122.

A. G. Pacholczyk. *Radio astrophysics. Nonthermal processes in galactic and extragalactic sources.* 1970.

R. A. Perley and B. J. Butler. An Accurate Flux Density Scale from 1 to 50 GHz. *ApJS*, 204:19, Feb. 2013. doi: 10.1088/0067-0049/204/2/19.

B. M. Peterson and K. Horne. Echo mapping of active galactic nuclei. *Astronomische Nachrichten*, 325:248–251, Mar. 2004. doi: 10.1002/asna.200310207.

J. R. Peterson, F. B. S. Paerels, J. S. Kaastra, M. Arnaud, T. H. Reiprich, A. C. Fabian, R. F. Mushotzky, J. G. Jernigan, and I. Sakelliou. X-ray imaging-spectroscopy of Abell 1835. *A&A*, 365:L104–L109, Jan. 2001. doi: 10.1051/0004-6361:20000021.

Planck Collaboration, P. A. R. Ade, N. Aghanim, C. Armitage-Caplan, M. Arnaud, M. Ashdown, F. Atrio-Barandela, J. Aumont, C. Baccigalupi, A. J. Banday, and et al. Planck 2013 results. XX. Cosmology from Sunyaev-Zeldovich cluster counts. *A&A*, 571:A20, Nov. 2014. doi: 10.1051/0004-6361/201321521.

G. W. Pratt, H. Böhringer, and A. Finoguenov. Further evidence for a merger in Abell 2218 from an XMM-Newton observation. *A&A*, 433:777–785, Apr. 2005. doi: 10.1051/0004-6361:20041415.

E. Quataert and A. Gruzinov. Convection-dominated Accretion Flows. *ApJ*, 539:809–814, Aug. 2000. doi: 10.1086/309267.

R Core Team. *R: A Language and Environment for Statistical Computing*. R Foundation for Statistical Computing, Vienna, Austria, 2013. URL `http://www.R-project.org/`. ISBN 3-900051-07-0.

D. A. Rafferty, B. R. McNamara, P. E. J. Nulsen, and M. W. Wise. The Feedback-regulated Growth of Black Holes and Bulges through Gas Accretion and Starbursts in Cluster Central Dominant Galaxies. *ApJ*, 652:216–231, Nov. 2006. doi: 10.1086/507672.

C. Ramos Almeida, C. N. Tadhunter, K. J. Inskip, R. Morganti, J. Holt, and D. Dicken. The optical morphologies of the 2 Jy sample of radio galaxies: evidence for galaxy interactions. *MNRAS*, 410:1550–1576, Jan. 2011. doi: 10.1111/j.1365-2966.2010.17542.x.

C. Ramos Almeida, P. S. Bessiere, C. N. Tadhunter, P. G. Pérez-González, G. Barro, K. J. Inskip, R. Morganti, J. Holt, and D. Dicken. Are luminous radio-loud active galactic nuclei triggered by galaxy interactions? *MNRAS*, 419: 687–705, Jan. 2012. doi: 10.1111/j.1365-2966.2011.19731.x.

C. Ramos Almeida, P. S. Bessiere, C. N. Tadhunter, K. J. Inskip, R. Morganti, D. Dicken, J. I. González-Serrano, and J. Holt. The environments of luminous radio galaxies and type-2 quasars. *MNRAS*, 436:997–1016, Dec. 2013. doi: 10.1093/mnras/stt1595.

T. D. Rawle, A. C. Edge, E. Egami, M. Rex, G. P. Smith, B. Altieri, A. Fiedler, C. P. Haines, M. J. Pereira, P. G. Pérez-González, J. Portouw, I. Valtchanov, G. Walth, P. P. van der Werf, and M. Zemcov. The Relation between Cool Cluster Cores and Herschel-detected Star Formation in Brightest Cluster Galaxies. *ApJ*, 747:29, Mar. 2012. doi: 10.1088/0004-637X/747/1/29.

P. Raybole. External sources of RFI at the GMRT: methods for control and coexistence with commercial users. In *RFI Mitigation Workshop*, May 2010.

M. J. Rees and J. P. Ostriker. Cooling, dynamics and fragmentation of massive gas clouds - Clues to the masses and radii of galaxies and clusters. *MNRAS*, 179:541–559, June 1977.

J. W. Rich, W. J. G. de Blok, T. J. Cornwell, E. Brinks, F. Walter, I. Bagetakos, and R. C. Kennicutt, Jr. Multi-Scale CLEAN: A Comparison of its Performance Against Classical CLEAN on Galaxies Using THINGS. *AJ*, 136: 2897–2920, Dec. 2008. doi: 10.1088/0004-6256/136/6/2897.

G. H. Rieke, E. T. Young, C. W. Engelbracht, D. M. Kelly, F. J. Low, E. E. Haller, J. W. Beeman, K. D. Gordon, J. A. Stansberry, K. A. Misselt, J. Cadien, J. E. Morrison, G. Rivlis, W. B. Latter, A. Noriega-Crespo, D. L. Padgett, K. R.

Stapelfeldt, D. C. Hines, E. Egami, J. Muzerolle, A. Alonso-Herrero, M. Blaylock, H. Dole, J. L. Hinz, E. Le Floc'h, C. Papovich, P. G. Pérez-González, P. S. Smith, K. Y. L. Su, L. Bennett, D. T. Frayer, D. Henderson, N. Lu, F. Masci, M. Pesenson, L. Rebull, J. Rho, J. Keene, S. Stolovy, S. Wachter, W. Wheaton, M. W. Werner, and P. L. Richards. The Multiband Imaging Photometer for Spitzer (MIPS). *ApJS*, 154:25–29, Sept. 2004. doi: 10.1086/422717.

G. H. Rieke, A. Alonso-Herrero, B. J. Weiner, P. G. Pérez-González, M. Blaylock, J. L. Donley, and D. Marcillac. Determining Star Formation Rates for Infrared Galaxies. *ApJ*, 692:556–573, Feb. 2009. doi: 10.1088/0004-637X/692/1/556.

J. Roy, Y. Gupta, U.-L. Pen, J. B. Peterson, S. Kudale, and J. Kodilkar. A real-time software backend for the GMRT. *Experimental Astronomy*, 28:25–60, Aug. 2010. doi: 10.1007/s10686-010-9187-0.

M. P. Rupen. Spectral Line Observing II: Calibration and Analysis. In G. B. Taylor, C. L. Carilli, and R. A. Perley, editors, *Synthesis Imaging in Radio Astronomy II*, volume 180 of *Astronomical Society of the Pacific Conference Series*, page 229, 1999.

M. Ryle. The New Cambridge Radio Telescope. *Nature*, 194:517–518, May 1962. doi: 10.1038/194517a0.

J. S. Sanders, A. C. Fabian, and G. B. Taylor. Feedback through multiple outbursts in the cluster 2A 0335+096. *MNRAS*, 396:1449–1459, July 2009. doi: 10.1111/j.1365-2966.2009.14892.x.

A. J. R. Sanderson and T. J. Ponman. X-ray modelling of galaxy cluster gas and mass profiles. *MNRAS*, 402:65–72, Feb. 2010. doi: 10.1111/j.1365-2966.2009.15888.x.

A. J. R. Sanderson, T. J. Ponman, and E. O'Sullivan. A statistically selected Chandra sample of 20 galaxy clusters - I. Temperature and cooling time profiles. *MNRAS*, 372:1496–1508, Nov. 2006. doi: 10.1111/j.1365-2966.2006.10956.x.

A. J. R. Sanderson, E. O'Sullivan, and T. J. Ponman. A statistically selected Chandra sample of 20 galaxy clusters - II. Gas properties and cool core/non-cool core bimodality. *MNRAS*, 395:764–776, May 2009. doi: 10.1111/j.1365-2966.2009.14613.x.

A. J. R. Sanderson, E. O'Sullivan, T. J. Ponman, A. H. Gonzalez, S. Sivanandam, A. I. Zabludoff, and D. Zaritsky. The baryon budget on the galaxy group/cluster boundary. *MNRAS*, 429:3288–3304, Mar. 2013. doi: 10.1093/mnras/sts586.

C. L. Sarazin, S. A. Baum, and C. P. O'Dea. Unusual Radio Structures in the Cooling Flow Cluster 2A 0335+096. *ApJ*, 451:125, Sept. 1995. doi: 10.1086/176205.

L. Saripalli. Understanding the Fanaroff-Riley Radio Galaxy Classification. *AJ*, 144:85, Sept. 2012. doi: 10.1088/0004-6256/144/3/85.

J. Schaye, C. Dalla Vecchia, C. M. Booth, R. P. C. Wiersma, T. Theuns, M. R. Haas, S. Bertone, A. R. Duffy, I. G. McCarthy, and F. van de Voort. The physics driving the cosmic star formation history. *MNRAS*, 402:1536–1560, Mar. 2010. doi: 10.1111/j.1365-2966.2009.16029.x.

P. A. G. Scheuer. Models of extragalactic radio sources with a continuous energy supply from a central object. *MNRAS*, 166:513–528, Mar. 1974.

A. Schnorr-Müller, T. Storchi-Bergmann, N. M. Nagar, A. Robinson, D. Lena, R. A. Riffel, and G. S. Couto. Feeding and feedback in the inner kiloparsec of the active galaxy NGC 2110. *MNRAS*, 437:1708–1724, Jan. 2014. doi: 10.1093/mnras/stt2001.

U. J. Schwarz. Mathematical-statistical Description of the Iterative Beam Removing Technique (Method CLEAN). *A&A*, 65:345, Apr. 1978.

M. Schwarzschild. A numerical model for a triaxial stellar system in dynamical equilibrium. *ApJ*, 232:236–247, Aug. 1979. doi: 10.1086/157282.

S. S. Shabala, S. Ash, P. Alexander, and J. M. Riley. The duty cycle of local radio galaxies. *MNRAS*, 388:625–637, Aug. 2008. doi: 10.1111/j.1365-2966.2008.13459.x.

N. I. Shakura and R. A. Sunyaev. Black holes in binary systems. Observational appearance. *A&A*, 24:337–355, 1973.

K. Shurkin, R. J. H. Dunn, G. Gentile, G. B. Taylor, and S. W. Allen. Active galactic nuclei-induced cavities in NGC 1399 and NGC 4649. *MNRAS*, 383:923–930, Jan. 2008. doi: 10.1111/j.1365-2966.2007.12651.x.

M. Sikora, Ł. Stawarz, and J.-P. Lasota. Radio Loudness of Active Galactic Nuclei: Observational Facts and Theoretical Implications. *ApJ*, 658:815–828, Apr. 2007. doi: 10.1086/511972.

J. Silk. On the fragmentation of cosmic gas clouds. I - The formation of galaxies and the first generation of stars. *ApJ*, 211:638–648, Feb. 1977. doi: 10.1086/154972.

G. P. Smith, J.-P. Kneib, I. Smail, P. Mazzotta, H. Ebeling, and O. Czoske. A Hubble Space Telescope lensing survey of X-ray luminous galaxy clusters - IV. Mass, structure and thermodynamics of cluster cores at z= 0.2. *MNRAS*, 359:417–446, May 2005. doi: 10.1111/j.1365-2966.2005.08911.x.

G. P. Smith, C. P. Haines, M. J. Pereira, E. Egami, S. M. Moran, E. Hardegree-Ullman, A. Babul, M. Rex, T. D. Rawle, Y.-Y. Zhang, A. Finoguenov, N. Okabe, A. J. R. Sanderson, A. C. Edge, and M. Takada. LoCuSS: Probing galaxy transformation physics with Herschel. *A&A*, 518:L18+, July 2010. doi: 10.1051/0004-6361/201014691.

D. N. Spergel, R. Bean, O. Doré, M. R. Nolta, C. L. Bennett, J. Dunkley, G. Hinshaw, N. Jarosik, E. Komatsu, L. Page, H. V. Peiris, L. Verde, M. Halpern, R. S. Hill, A. Kogut, M. Limon, S. S. Meyer, N. Odegard, G. S. Tucker, J. L. Weiland, E. Wollack, and E. L. Wright. Three-Year Wilkinson Microwave Anisotropy Probe (WMAP) Observations: Implications for Cosmology. *ApJS*, 170:377–408, June 2007. doi: 10.1086/513700.

V. Springel, T. Di Matteo, and L. Hernquist. Black Holes in Galaxy Mergers: The Formation of Red Elliptical Galaxies. *ApJL*, 620:L79–L82, Feb. 2005. doi: 10.1086/428772.

A. Sternberg and N. Soker. Explaining the energetic AGN outburst of MS0735+7421 with massive slow jets. *MNRAS*, 398:422–428, Sept. 2009. doi: 10.1111/j.1365-2966.2009.15155.x.

T. Storchi-Bergmann, R. D. S. Lopes, P. J. McGregor, R. A. Riffel, T. Beck, and P. Martini. Feeding versus feedback in NGC4151 probed with Gemini NIFS - II. Kinematics. *MNRAS*, 402:819–835, Feb. 2010. doi: 10.1111/j.1365-2966.2009.15962.x.

A. Stroe, R. J. van Weeren, H. T. Intema, H. J. A. Röttgering, M. Brüggen, and M. Hoeft. Discovery of spectral curvature in the shock downstream region: CIZA J2242.8+5301. *A&A*, 555:A110, July 2013. doi: 10.1051/0004-6361/201321267.

M. Sun, C. Jones, S. S. Murray, S. W. Allen, A. C. Fabian, and A. C. Edge. Chandra Observations of the Galaxy Cluster A478: The Interaction of Hot Gas and Radio Plasma in the Core, and an Improved Determination of the Compton y-Parameter. *ApJ*, 587:619–624, Apr. 2003. doi: 10.1086/368300.

T. Tamura, J. S. Kaastra, J. R. Peterson, F. B. S. Paerels, J. P. D. Mittaz, S. P. Trudolyubov, G. Stewart, A. C. Fabian, R. F. Mushotzky, D. H. Lumb, and Y. Ikebe. X-ray spectroscopy of the cluster of galaxies Abell 1795 with XMM-Newton. *Astronomy and Astrophysics*, 365:L87–L92, Jan. 2001. doi: 10.1051/0004-6361:20000038.

G. B. Taylor, R. A. Perley, M. Inoue, T. Kato, H. Tabara, and K. Aizu. VLA observations of the radio galaxy Hydra A (3C 218). *ApJ*, 360:41–54, Sept. 1990. doi: 10.1086/169094.

G. B. Taylor, C. L. Carilli, and R. A. Perley, editors. *Synthesis Imaging in Radio Astronomy II*, volume 180 of *Astronomical Society of the Pacific Conference Series*, 1999.

M. B. Taylor. TOPCAT & STIL: Starlink Table/VOTable Processing Software. In P. Shopbell, M. Britton, and R. Ebert, editors, *Astronomical Data Analysis Software and Systems XIV*, volume 347 of *Astronomical Society of the Pacific Conference Series*, page 29, Dec. 2005.

P. Taylor and C. Kobayashi. The effects of agn feedback on present-day galaxy properties in cosmological simulations. Jan. 2015.

T. A. Thompson, E. Quataert, and N. Murray. Radio emission from supernova remnants: implications for post-shock magnetic field amplification & the magnetic fields of galaxies. *MNRAS*, 397:1410–1419, Aug. 2009. doi: 10.1111/j.1365-2966.2009.14889.x.

S. Tremaine, K. Gebhardt, R. Bender, G. Bower, A. Dressler, S. M. Faber, A. V. Filippenko, R. Green, C. Grillmair, L. C. Ho, J. Kormendy, T. R. Lauer, J. Magorrian, J. Pinkney, and D. Richstone. The Slope of the Black Hole Mass versus Velocity Dispersion Correlation. *ApJ*, 574:740–753, Aug. 2002. doi: 10.1086/341002.

P. C. Tribble. Radio spectral ageing in a random magnetic field. *MNRAS*, 261:57–62, Mar. 1993.

T. Venturi, D. Dallacasa, and F. Stefanachi. Radio galaxies in cooling core clusters. Renewed activity in the nucleus of 3C 317? *A&A*, 422:515–522, Aug. 2004. doi: 10.1051/0004-6361:20040089.

G. M. Voit and M. Donahue. An Observationally Motivated Framework for AGN Heating of Cluster Cores. *ApJ*, 634:955–963, Dec. 2005. doi: 10.1086/497063.

H. Wickham. *ggplot2: elegant graphics for data analysis.* Springer New York, 2009. ISBN 978-0-387-98140-6. URL `http://had.co.nz/ggplot2/book`.

R. J. Wilman, A. C. Edge, P. J. McGregor, and B. M. McNamara. Molecular accretion in the core of the galaxy cluster 2A 0335+096. *MNRAS*, 416:2060–2067, Sept. 2011. doi: 10.1111/j.1365-2966.2011.19180.x.

M. W. Wise, B. R. McNamara, P. E. J. Nulsen, J. C. Houck, and L. P. David. X-Ray Supercavities in the Hydra A Cluster and the Outburst History of the Central Galaxy's Active Nucleus. *ApJ*, 659:1153–1158, Apr. 2007. doi: 10.1086/512767.

J.-H. Woo and C. M. Urry. The Independence of Active Galactic Nucleus Black Hole Mass and Radio Loudness. *ApJL*, 581:L5–L7, Dec. 2002. doi: 10.1086/345944.

H. K. C. Yee, E. Ellingson, R. G. Abraham, P. Gravel, R. G. Carlberg, T. A. Smecker-Hane, D. Schade, and M. Rigler. The CNOC Cluster Redshift Survey Catalogs. II. Abell 2390. *ApJS*, 102:289, Feb. 1996. doi: 10.1086/192260.

D. G. York, J. Adelman, J. E. Anderson, Jr., S. F. Anderson, J. Annis, N. A. Bahcall, J. A. Bakken, R. Barkhouser, S. Bastian, E. Berman, W. N. Boroski, S. Bracker, C. Briegel, J. W. Briggs, J. Brinkmann, R. Brunner, S. Burles, L. Carey, M. A. Carr, F. J. Castander, B. Chen, P. L. Colestock, A. J. Connolly, J. H. Crocker, I. Csabai, P. C. Czarapata, J. E. Davis, M. Doi, T. Dombeck, D. Eisenstein, N. Ellman, B. R. Elms, M. L. Evans, X. Fan, G. R. Federwitz, L. Fiscelli, S. Friedman, J. A. Frieman, M. Fukugita, B. Gillespie, J. E. Gunn, V. K. Gurbani, E. de Haas, M. Haldeman, F. H. Harris, J. Hayes, T. M. Heckman, G. S. Hennessy, R. B. Hindsley, S. Holm, D. J. Holmgren, C.-h. Huang, C. Hull, D. Husby, S.-I. Ichikawa, T. Ichikawa, Ž. Ivezić, S. Kent, R. S. J. Kim, E. Kinney, M. Klaene,

A. N. Kleinman, S. Kleinman, G. R. Knapp, J. Korienek, R. G. Kron, P. Z. Kunszt, D. Q. Lamb, B. Lee, R. F. Leger, S. Limmongkol, C. Lindenmeyer, D. C. Long, C. Loomis, J. Loveday, R. Lucinio, R. H. Lupton, B. MacKinnon, E. J. Mannery, P. M. Mantsch, B. Margon, P. McGehee, T. A. McKay, A. Meiksin, A. Merelli, D. G. Monet, J. A. Munn, V. K. Narayanan, T. Nash, E. Neilsen, R. Neswold, H. J. Newberg, R. C. Nichol, T. Nicinski, M. Nonino, N. Okada, S. Okamura, J. P. Ostriker, R. Owen, A. G. Pauls, J. Peoples, R. L. Peterson, D. Petravick, J. R. Pier, A. Pope, R. Pordes, A. Prosapio, R. Rechenmacher, T. R. Quinn, G. T. Richards, M. W. Richmond, C. H. Rivetta, C. M. Rockosi, K. Ruthmansdorfer, D. Sandford, D. J. Schlegel, D. P. Schneider, M. Sekiguchi, G. Sergey, K. Shimasaku, W. A. Siegmund, S. Smee, J. A. Smith, S. Snedden, R. Stone, C. Stoughton, M. A. Strauss, C. Stubbs, M. SubbaRao, A. S. Szalay, I. Szapudi, G. P. Szokoly, A. R. Thakar, C. Tremonti, D. L. Tucker, A. Uomoto, D. Vanden Berk, M. S. Vogeley, P. Waddell, S.-i. Wang, M. Watanabe, D. H. Weinberg, B. Yanny, N. Yasuda, and SDSS Collaboration. The Sloan Digital Sky Survey: Technical Summary. *AJ*, 120:1579–1587, Sept. 2000. doi: 10.1086/301513.

J.-H. Zhao, D. M. Sumi, J. O. Burns, and N. Duric. 3C 317: an Amorphous Radio Source in the Cooling Flow Cluster Abell 2052. *ApJ*, 416:51, Oct. 1993. doi: 10.1086/173214.